UNIVERSITY OF SOUTHAMPTON

FACULTY OF ENGINEERING, SCIENCE AND MATHEMATICS

School of Chemistry

A Comparative Study Of PtCo/C Alloys And Pt/C As Cathode Catalysts For Fuel Cell Applications

by

Sarah Louise Burton

Thesis for the degree of Doctor of Philosophy

November 2009

UNIVERSITY OF SOUTHAMPTON

ABSTRACT

FACULTY OF ENGINEERING, SCIENCE AND MATHEMATICS

School of Chemistry

Doctor of Philosophy

A COMPARATIVE STUDY OF PtCo/C ALLOYS AND Pt/C AS CATHODE CATALYSTS FOR FUEL CELL APPLICATIONS

By Sarah Louise Burton

Commercialisation of fuel cells for automotive applications requires catalysts with both improved activity, particularly for the cathodic oxygen reduction reaction (ORR), and stability over commercial platinum only catalysts. This requires a detailed understanding of both desirable catalyst structure and mechanistic activity. In this work a comparative study is made between commercial Pt/C catalysts and developmental PtCo/C catalysts, with the aim of increasing understanding of the desirable characteristics of improved activity and stability demonstrated for PtCo catalysts.

To explore the origins of activity and stability enhancement for Pt_3Co/C catalysts over Pt/C, the mechanisms of catalyst deactivation have been investigated. In addition, four new $PtCo_3$/C catalyst materials have been prepared and evaluated for ORR activity before and after activation by electrochemical dealloying. Structural changes occurring during these processes have been characterised using cyclic voltammetry, Transmission Electron Microscopy (TEM) and X-ray absorption spectroscopy (XAS).

XAS has also been used to explore the relationship between catalyst activity and structure. This has been achieved by building and validating a specially adapted fuel cell, enabling study of fuel cell catalysts *in situ* under realistic operating conditions. Findings from time resolved potential step experiments with 12 s and 0.1 s time resolution will be presented for catalysts operating at OCV and under load with oxygen cathode gas. In addition, studies have been conducted with nitrogen cathode feed gas to investigate the effect of potential and temperature on the processes of oxide formation and removal on both Pt/C and PtCo/C catalysts.

TABLE OF CONTENTS

DECLARATION OF AUTHORSHIP

I, **Sarah Louise Burton**, declare that the thesis entitled

A Comparative Study Of PtCo/C Alloys And Pt/C As Cathode Catalysts For Fuel Cell Applications

and the work presented in the thesis are both my own, and have been generated by me as the result of my own original research. I confirm that:

- This work was done wholly or mainly while in candidature for a research degree at this University;
- Where any part of this thesis has previously been submitted for a degree or any other qualification at this University or any other institution, this has been clearly stated;
- Where I have consulted the published work of others, this is always clearly attributed;
- Where I have quoted from the work of others, the source is always given. With the exception of such quotations, this thesis is entirely my own work;
- I have acknowledged all main sources of help;
- Where the thesis is based on work done by myself jointly with others, I have made clear exactly what was done by others and what I have contributed myself;
- Parts of this work have been published as:

1. S. C. Ball, S. L. Hudson, J. H. Leung, A. E. Russell, D. Thompsett and B. R. C. Theobald, *ECS Transactions*, **11**, 1247 (2007).
2. S. C. Ball, S. L. Hudson, B. R. C. Theobald and D. Thompsett, *ECS Transactions*, **11**, 1267 (2007).
3. S. L. Hudson, S. C. Ball, K. B. Blaney, G. H. Chouchelamane, S. G. Fiddy, I. Harvey, P. Sivasubramaniam, B. C. Tessier, B. R. C. Theobald, D. Thompsett and A. E. Russell, *ECS Transactions*, **16**, 1395 (2008).

Signed: ……..

Date:…….

ACKNOWLEDGEMENTS

I would like to thank Johnson Matthey and the University of Southampton for the opportunity to conduct this work and acknowledge the financial support of both Johnson Matthey and the Royal Commission for the Exhibition of 1851.

Many people both at Johnson Matthey Technology Centre and the University of Southampton have helped me complete this work and supported me over the last three years, for which I am very grateful. In particular I would like to thank my academic supervisor Professor Andrea Russell for everything she has done, especially her enthusiasm, our scientific discussions and for providing ingenious solutions to the numerous challenges we encountered during beamtimes. I would also like to thank my industrial supervisor Dr. Sarah Ball for enabling me make the most of this opportunity, motivating me (often with chocolate) and for all the advice. I would also like to thank Dr. Dave Thompsett for proposing my research question and the useful discussions on my findings. I would also like acknowledge my advisor Professor Derek Pletcher, Dr. Ed Wright for his help in XAS data manipulation and valuable discussions on cell design, Dr Chan Malde for help with sprayed layers and Dr. Brian Theobald and Elvis Christian for catalyst synthesis.

I would also like to thank the team from Johnson Matthey workshop who built the XAS *in situ* fuel cell, Tony Gartshore, Norman Binstead and the Daresbury helpdesk for IT support and the members of the Johnson Matthey analytical department for sample analysis. In particular, Dr. Sarennah Longworth for her help in generating the TEM images for this document. From Southampton University I would like to say a special thank you to both Béatrice Tessier and Gale Chouchelamane for all their help and dedication, even at 4 a.m. when running the XAS experiments, and I would also like to thank Steven Price, Katie Blaney and Prabalini Sivasupramaniam. From the Daresbury Laboratory and the ESRF I would like to thank station scientists Dr. Ian Harvey and Dr. Mark Newton and the following people who helped make the experimental beamtimes successful: Dr. Steven Fiddy, Chris Corrigan, Dr. Sebastien Pasternak, Dr. Florian Perrin and Dr. Giuliana Aquilanti.

My final thank you goes to my husband Nick for supporting me all the way.

Acronyms, Nomenclature and Units

Term	Description
AC	Alternating current
AFC	Alkaline Fuel Cell
ASAXS	Anomalous Small Angle X-ray Scattering
BOL	Beginning of Life
CCM	Catalyst Coated Membrane
CI	Current Interrupt
CV	Cyclic Voltammetry
DMFC	Direct Methanol Fuel Cell
DoE	Department of Energy (USA)
EDAX	Energy Dispersive X-ray Fluorescence Detection (TEM)
EDE	Energy Dispersive EXAFS
EDXAS	Energy Dispersive X-ray Absorption Spectroscopy
EOL	End of Life
EPMA	Electron Probe Micro Analysis
ESRF	European Synchrotron Radiation Facility, Grenoble, France
EW	Equivalent Weight
EXAFS	Extended X-ray Absorption Fine Structure
FT	Fourier Transform
GDL	Gas Diffusion Layer
HAADF	High Angle Annular Dark field (TEM images)
HRTEM	High Resolution Transmission Electron Microscopy
ICP-MS	Inductively Coupled Plasma Mass Spectrometry
iR	Internal Resistance
LEIS	Low Energy Ion Scattering
MCFC	Molten Carbonate Fuel Cell
MEA	Membrane Electrode Assembly
MSA	Membrane Substrate Assembly

Term	Description
OCV	Open Circuit Voltage
ORR	Oxygen Reduction Reaction
PAFC	Phosphoric Acid Fuel Cell
PEMFC	Proton Exchange Membrane Fuel Cell
RDE	Rotating Disc Electrode
RHE	Reversible hydrogen Electrode
SHE	Standard hydrogen Electrode
SOFC	Solid Oxide Fuel Cell
SRS	Synchrotron Radiation Source, Daresbury laboratory, England
TEM	Transmission Electron Microscopy
XANES	X-ray Absorption Near Edge Structure
XAS	X-ray Absorption Spectroscopy
XPS	X-ray Photoelectron Spectroscopy
XRD	X-ray Diffraction

Term	Description	Unit
A	Area	cm^2
A_j	Amplitude function	-
E	Potential	V
E^0	Cell voltage at standard pressure and temperature and with pure reactants	V
E_0	Binding energy of an absorption edge	eV
ECA	Electrochemical Surface Area	$m^2_{Pt}\, g^{-1}_{Pt}$
E_f	Fermi energy	eV
E_{hv}	Photon energy	eV
EPSA	Electrochemical Platinum Surface area	$cm^2_{Pt}\, cm^{-2}_{geometric}$
EW	Equivalent Weight	g mol^{-1} SO_3^-
F	Faraday Constant = 96485	C mol^{-1}
$F_j(k)$	magnitude of the backscattering amplitude from atom j	-
$\Delta\overline{G}_f$	Change in the molar Gibbs free energy of formation	J mol^{-1}

Term	Description	Unit
$\Delta\overline{H}_f$	Change in the molar enthalpy of formation	kJ mol^{-1}
$\hbar$	Plancks constant, reduced (h/2π) = 1.054×10^{-34}	J s
I	Current	A
I_0	intensity of the incident photons	-
I_f	Final value of the normalised white line intensity	-
I_i	Initial value of the normalised white line intensity	-
I_t	Intensity of the transmitted photons	-
i	current density	A cm^{-2}
i_0	exchange current density	A cm^{-2}
J_{corr}	Hydrogen crossover corrected current density	mA cm^{-2}
j	Co-ordination shell of atoms of type j	-
K_0	Constant associated with the forward or backward reaction, that includes the chemical component of the Gibbs free energy of the transition state	-
k	Wave vector	$Å^{-1}$
k_b	Rate constant for the backward (anodic) reaction	cm s^{-1}
k_f	Rate constant for the forward (cathodic) reaction	cm s^{-1}
k_x	Rate constant for reaction x	cm s^{-1}
m	Number of coordination shells	-
m_e	Mass of an electron = 9.109 x 10^{-31}	kg
N_1	Mean first-nearest-neighbour coordination number of atoms in a cuboctahedral cluster geometry	-
N_j	Coordination number of neighbouring atoms of type j	-
n	Number of electrons involved in an electrode reaction	-
OCV	Open Circuit Voltage	V
$[Ox]$	Concentration of the oxidant species	mol cm^{-3}
P	Pressure	kPa
P_X	partial pressure of X	kPa
Q	Charge	C
q	Charge Density	C cm^{-2}
R	Molar gas constant = 8.314	J K^{-1} mol^{-1}

Term	Description	Unit
R_{EXAFS}	EXAFS Fitting Error	-
$[\mathrm{Re}\,d]$	Concentration of the reductant species	mol cm^{-3}
RH	Relative Humidity	%
R_j	Distance from the absorber atom *j* to neighboring atom	Å
S_0	Amplitude reduction factor (loss of intensity to many body effects)	-
$\Delta\overline{S}_f$	Change in the molar Entropy of formation	J mol^{-1} K^{-1}
T	Temperature	K
t	Time	s
V_a	Activation overvoltage	V
V_r	Ohmic voltage loss	V
x	sample thickness	cm
α	charge transfer coefficient	-
$\chi(k)$	EXAFS function ($\frac{\mu-\mu_0}{\mu_0}$)	-
δ_j	Backscattering phase shift	-
η	Overpotential ($E-E_0$)	V
λ	mean free path of the photoelectron	Å
$1/\tau$	Relaxation time	s^{-1}
$2\sigma_j^2$	Debye-Waller factor: relative mean squared disorder along the distance between the absorbing atom and atom *j* due to thermal and static motions	$Å^2$
μ	X-ray absorption coefficient	cm^{-1}
μ_0	X-ray absorption coefficient of a free atom	cm^{-1}

Sign conventions in cyclic voltammograms:

- Anodic currents are positive
- Cathodic currents are negative

Chapter 1. Introduction

Since their first demonstration in 1839 by Grove, (1, 2), fuel cells have been investigated as a potential alternative power generation method (3). The desire to reduce emissions, preserve finite resources and maintain energy security has resulted in extensive investment and research into fuel cell technologies in recent years (3-5). A number of different fuel cell types exist with varying power output and applications. A summary is provided in Table 1. Fuel cell applications are wide ranging and provide an alternative to batteries, the internal combustion engine, and may be used to provide stationary power on both a domestic and commercial scale (3-6).

Table 1. Summary of fuel cell systems, reactions and applications. From ref. (3)

Fuel cell type	Anode reaction Cathode reaction Overall reaction	Operating temperature and power	Applications
Proton exchange membrane (PEMFC)	$H_2 \rightarrow 2\mathbf{H^+} + 2e^-$ $O_2 + 4\mathbf{H^+} + 4e^- \rightarrow 2H_2O$ $2H_2 + O_2 \rightarrow 2H_2O$	30-100 °C 1-100 kW	1st space vehicles, automotive, portable and Combined heat / power
Alkaline (AFC)	$2H_2 + 4\mathbf{OH^-} \rightarrow 4H_2O + 4e^-$ $O_2 + 4e^- + 2H_2O \rightarrow 4\mathbf{OH^-}$ $2H_2 + O_2 \rightarrow 2H_2O$	50-200 °C 1-10 kW	Apollo space missions vehicles
Direct Methanol (DMFC)	$CH_3OH + H_2O \rightarrow 6\mathbf{H^+} + 6e^- + CO_2$ $3/2O_2 + 6\mathbf{H^+} + 6e^- \rightarrow 3H_2O$ $CH_3OH + 3/2O_2 \rightarrow 2H_2O + CO_2$	20-90 °C 1-100 W	Portable power
Phosphoric acid (PAFC)	$H_2 \rightarrow 2\mathbf{H^+} + 2e^-$ $O_2 + 4\mathbf{H^+} + 4e^- \rightarrow 2H_2O$ $2H_2 + O_2 \rightarrow 2H_2O$	~220 °C 10 kW- 1 MW	Combined heat / power
Molten carbonate (MCFC)	$2H_2 + 2\mathbf{CO_3^{2-}} \rightarrow 2H_2O + 2CO_2 + 4e^-$ $O_2 + 2CO_2 + 4e^- \rightarrow 2\mathbf{CO_3^{2-}}$ $H_2 + 1/2O_2 + CO_2 \rightarrow H_2O + CO_2$	~650 °C 0.1-10 MW	Combined heat / power
Solid oxide (SOFC)	$2H_2 + 2\mathbf{O^{2-}} \rightarrow 2H_2O + 4e^-$ $O_2 + 4e^- \rightarrow 2\mathbf{O^{2-}}$ $2H_2 + O_2 \rightarrow 2H_2O$	500-1000 °C 1 kW-10 MW	Combined heat / power

Fuel cells are electrochemical devices capable of producing electricity via the electrochemical reaction of a fuel (hydrogen) and an oxidant (oxygen) in the presence of a catalyst. The electrochemical reactions for each fuel cell type are shown in Table 1. Key advantages of fuel cells over other alternative power supplies include; high efficiency (Phosphoric acid fuel cells available today, generate electricity at more than 40% efficiency (4)), faster recharging than batteries, potential for zero emissions (when renewable sources are used to generate hydrogen (3, 4)), and few or no moving parts leading to quiet operation, this is of particular importance in portable and domestic power applications (3).

Proton exchange membrane fuel cells (PEMFCs) are the focus of this work and therefore the following discussion will be limited to this type of fuel cell system. For a more detailed overview of the other fuel cells summarised in Table 1 the reader is referred to the following texts (3, 5, 7-12).

1. Proton exchange membrane fuel cells (PEMFCs)

PEMFCs were first developed by General Electric in the United States in the 1960s for use by NASA on their first manned space vehicles, The Gemini spacecraft (3). Today PEMFCs are currently the best candidates for automotive use (3, 5, 13). This is due to: zero emissions at point of use enabling emission reduction since the only by-product is water, low temperature operation allowing rapid start-up, the lack of corrosive fluid hazards associated with other fuel cells and batteries, the compact, thin cell design and that the cell can work in any orientation (3, 13).

The electrolyte in PEMFCs is a solid ion conducting polymer. An example and industry standard is Nafion®, a registered trademark of Dupont which was developed in 1967 (3). The polymer consists of a hydrophobic polytetrafluoroethylene (PTFE) backbone that is sulphonated with side chains ending in SO_3^- H^+. The ionic nature of the sulphonic acid group makes it highly hydrophilic. The differences in hydrophobicity of the backbone and side groups lead to self assembly of the polymer resulting in hydrated regions in which H^+ are weakly bound. This enables proton conduction through the membrane. For efficient fuel cell operation in addition to good proton conductivity, the membrane must also be electronically insulating to prevent a short circuit, prevent

mixing of reactant gases and be both mechanically and chemically durable (3, 14). Since 1967 several variants of Nafion® have been produced and other proton exchange membranes have been developed to decrease cost, improve proton conductivity, resistance to chemical attack, mechanical durability and to enable operation at higher temperatures (> 80 °C) (14-17).

The anode and cathode electrodes are positioned either side of the proton exchange membrane to form the membrane electrode assembly (MEA), often referred to as a single cell. For research purposes single cells are commonly used for evaluating MEA components, however for application, a single MEA will provide insufficient voltage so several are combined in series in a fuel cell stack to achieve the desired power output. A schematic of a fuel cell membrane electrode assembly (MEA) is shown in Figure 1.

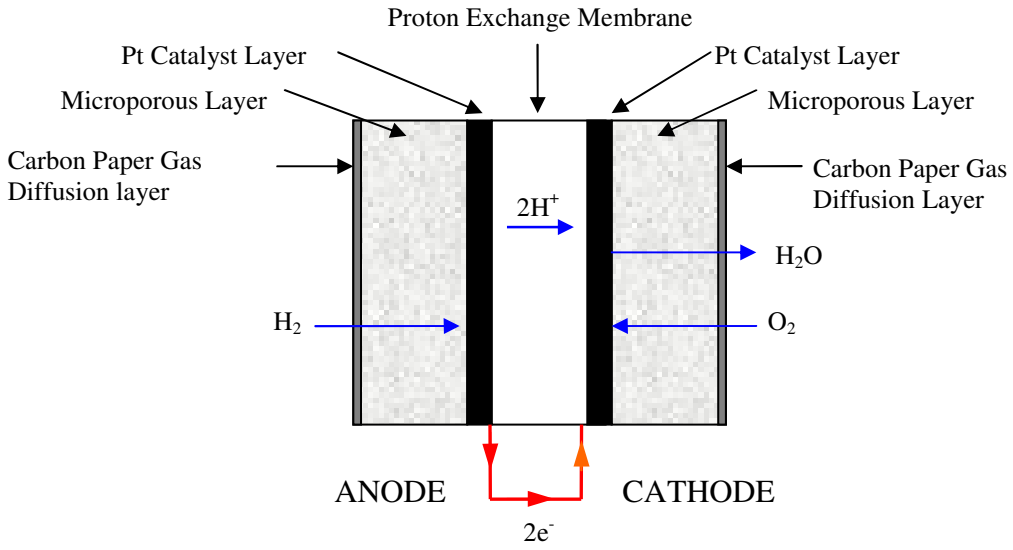

Figure 1. Schematic representation of a fuel cell membrane electrode assembly (note that components are not drawn to scale)

The reactant gases diffuse through a gas diffusion layer before reaching the catalyst layer where reaction occurs. On the anode hydrogen is oxidised to protons and electrons. The electrons pass through the external circuit where useful work can be performed, while the protons pass through the proton exchange membrane to the cathode side. At the cathode oxygen is reduced to water. (See Table 1 for electrochemical reactions). The gas diffusion layer (GDL), as the name suggests, transports reactant gases to the catalyst particles. GDLs are typically a carbon paper

(e.g. Toray™) or cloth that is highly conducting and is often PTFE coated to facilitate water management (3). The gas diffusion layers used in this work are coated with a microporous carbon baselayer. This layer is also conductive, improves water handling and enables efficient adhesion of the catalyst layer to the GDL. The catalyst layer is prepared by forming a mixture the catalyst powder with a soluble version of the electrolyte (ionomer) to improve connectivity. The mixture is then coated either directly onto the membrane or the GDL.

The catalysts used in PEMFCs are normally platinum based and these materials are the subject of this work. Platinum catalysts will be discussed in detail in this and subsequent chapters with particular focus on the catalyst used at the cathode. Commercially available and developmental catalysts on both the anode and cathode contain platinum nanoparticles dispersed on high surface area carbon supports, to give high surface areas for reaction. Depending on the fuel source and power requirements, additional elements may be added to the catalyst to improve activity (18). On the anode, tolerance to impurities such as CO in the hydrogen stream may be required, therefore Ru is commonly added (19), while on the cathode, as will be discussed, addition of extra metals can improve activity. It should be noted that non-platinum catalysts are also under investigation for PEMFC applications, primarily to reduce cost. A review of non-platinum catalysts for fuel cell applications was provided by Wang in 2005 (20). Examples include: non-platinum precious metal containing catalysts, pyrolized metal porphyrins and non-precious metal heteroatomic polymer electrocatalysts (21). To compete with platinum catalysts these materials must exhibit sufficient activity and stability, but as yet have not proved competitive (18), so will not be discussed further.

2. PEMFC commercialisation challenges

Despite the most recent (2009) fuel cell Industry Review (6) reporting a 50% increase in the volume of fuel cell shipments from 2007 to 2008, (mainly as a result of the emerging the portable and stationary markets), with substantial growth anticipated over the next five years, significant challenges still need to be overcome before fuel cells can compete with existing technologies. This is particularly significant for automotive applications where improved efficiency, performance, lifetime, and cost for all fuel cell system components, including balance of plant, are required. In addition the issues

associated with range, hydrogen infrastructure, storage, operation under wide ranging temperature conditions and size and weight of systems need to be addressed (5). Addressing these challenges forms the basis for much of the current fuel cell research with targets being defined by the European, Japanese and US fuel cell funding bodies (22-24).

2.1 The requirement for more active catalysts

The theoretical open circuit voltage, E^0, for a fuel cell undergoing the two electron reaction of hydrogen and oxygen to form water, Equation 1, may be calculated using Equation 2. Where F is the Faraday constant (96485 C mol^{-1}) and $\Delta\overline{G}_f$ is the molar Gibbs free energy change occurring on formation of the product water from the hydrogen and oxygen reactants as described in Equation 3.

$$H_2 + ½\ O_2 \rightleftharpoons H_2O \qquad \textbf{Equation 1}$$

$$E^0 = \frac{-\Delta\overline{G}_f}{2F} \qquad \textbf{Equation 2}$$

$$\Delta\overline{G}_f = \left(\Delta G_f\right)_{H_2O} - \left(\Delta\overline{G}_f\right)_{H_2} - \tfrac{1}{2}\left(\Delta\overline{G}_f\right)_{O_2} \qquad \textbf{Equation 3}$$

The Gibbs free energy terms in Equation 3 vary depending on the change in the molar enthalpy of formation, $\Delta\overline{H}_f$, of X (where X is H_2, O_2 or H_2O), the entropy, $\Delta\overline{S}_f$, associated with the formation of X, and temperature, T, according to Equation 4.

$$\left(\Delta\overline{G}_f\right)_X = \left(\Delta\overline{H}_f\right)_X - T\left(\Delta\overline{S}_f\right)_X \qquad \textbf{Equation 4}$$

Values for H_f and $\overline{S}_f$ at 25 °C, reported in reference (3), are tabulated in Table 2. Using Equation 4 and substituting into Equation 3, a value for $\Delta\overline{G}_f$ of -237.2 kJ mol^{-1} may be calculated (3). Using Equation 2 this gives a value of 1.23 V as the theoretical reversible open circuit voltage of the fuel cell assuming pure hydrogen and oxygen are used at standard pressure (3).

Table 2. Values of $\overline{H}_f$ and $\overline{S}_f$ at 25 °C, for the hydrogen fuel cell at standard pressure (0.1 MPa). From ref. (3)

X	H_f / J mol^{-1}	$\overline{S}_f$ / J mol^{-1} K^{-1}
H_2O (l)	-285,838	70.05
H_2 (g)	0	130.59
O_2 (g)	0	205.14

Using the same process it can be shown that the theoretical cell voltage is ~1.2 V for fuel cells operating up to temperatures of 100 °C at standard pressure using pure reactants. It should be noted however, that the pressure and concentration of the reactants affects the voltage. This relationship is described according to the Nernst equation, which can be given in many forms. For example, if the pressures of the reactants and products are given in bar and the water product is in the form of steam the Nernst equation may be written as in Equation 5. Where E^0 is the cell voltage at standard pressure and temperature and with pure reactants, R, the molar gas constant and P_X the partial pressure of X.

$$E = E^0 + \frac{RT}{2F}\ln\left(\frac{P_{H_2} \times P_{O_2}^{1/2}}{P_{H_2O}}\right) \qquad \textbf{Equation 5}$$

It can be shown that decreasing the partial pressure of the reactants will decrease the cell voltage, while increasing the concentration of the reactants, for example using pure oxygen instead of air, or increasing the system pressure will increase the cell voltage. For low temperature fuel cells the voltage gains observed with increasing pressure or concentration are underestimated by the Nernst equation. This is because increasing the pressure and concentration also reduces the voltage losses observed in real systems by improving occupancy of the catalytic sites (3).

In operational fuel cell systems, the measured potential under typical operating conditions is typically 300-400 mV less than the theoretical potential (3, 18, 25). The cause of the potential drop or overpotential, η, defined as the difference in the measured potential and the theoretical potential, Equation 6**,** is due to four major

irreversibilities, namely: Activation losses, fuel crossover, ohmic losses and mass transport losses (3, 18).

$$\eta = E - E^0$$ **Equation 6**

The activation losses are a consequence of the poor kinetics occurring at the surface of the electrodes. The kinetics of electrochemical reactions, such as those occurring on the anode and cathode fuel cell electrodes, are described by the Butler Volmer equation, given in Equation 13, below (26-28). The Butler-Volmer equation is derived from Transition State theory by consideration of the kinetics of an electrochemical reaction, such as that shown in Equation 7, where k_f and k_b are the rates of the forward (reduction-cathodic) and backward (oxidation-anodic) reactions respectively.

$$[Ox] + n\ e^- \underset{k_b}{\overset{k_f}{\rightleftharpoons}} [\mathrm{Re}\,d]$$ **Equation 7**

At an electrode surface the current is produced from the reactants that reach the surface of the electrode and lose or gain electrons. The magnitude of the current depends on the number of electrons, n, the electrode area, the rate that species reach the electrode surface and react, $k_{f,b}$, and the reactant concentrations, $[Ox]$and $[\mathrm{Re}\,d]$. The net current that flows is the current generated from both the forward and reverse reactions (anodic currents are defined as negative and cathodic currents positive in this illustration). The current density, i, (current per unit area) is therefore described by Equation 8.

$$i = nFk_f[Ox] - nFk_b[\mathrm{Re}\,d]$$ **Equation 8**

The rate of forward and backwards reactions are given the Arrenhius equation and Transition State theory (Equation 9 and Equation 10)**,** where K_0 is a constant associated with the forward or backward reaction, that includes the chemical component of the Gibbs free energy of the transition state. The exponential term refers to the electrical component of the Gibbs free energy of the transition state, where α is the charge

transfer coefficient. α is typically between 0.1 and 0.5 for most materials, is associated with the electrode material properties and depends on the symmetry of the transition state (27). The sum of the charge transfer coefficients for the oxidation and reduction reactions is equal to unity.

$$k_f = K_{0,f} \exp\left(\frac{-n\alpha F\eta}{RT}\right) \qquad \textit{Reduction-cathodic} \qquad \textbf{Equation 9}$$

$$k_b = K_{0,b} \exp\left(\frac{n[1-\alpha]F\eta}{RT}\right) \qquad \textit{Oxidation-anodic} \qquad \textbf{Equation 10}$$

Insertion of Equation 9 and Equation 10 into Equation 8 gives Equation 11.

$$i = nFK_{0,f}[Ox]\exp\left(\frac{-n\alpha F\eta}{RT}\right) - nFK_{0,b}[\mathrm{Re}\,d]\exp\left(\frac{n[1-\alpha]F\eta}{RT}\right) \qquad \textbf{Equation 11}$$

When the electrode is in equilibrium, the overpotential and external current are both zero. In this condition, the exchange current density, i_0, is defined as the current flowing equally in both directions (Equation 12). The larger i_0 the faster the reaction occurs.

$$i_0 = nFK_{0,f}[Ox] = nFK_{0,b}[\mathrm{Re}\,d] \qquad \textbf{Equation 12}$$

After substituting for the exchange current density the final form of the current density is Equation 13**,** which is called the Bulter-Volmer equation.

$$i = i_0\left[\exp\left(\frac{-n\alpha F\eta}{RT}\right) - \exp\left(\frac{n[1-\alpha]F\eta}{RT}\right)\right] \qquad \textbf{Equation 13}$$

Reduction *oxidation*

The equation may be simplified by considering the situation far from equilibrium, where the magnitude of the overpotential is large. In this situation either the term associated with the anodic or cathodic process becomes dominant and the corresponding opposite reaction may be neglected (approximated to be equal to zero). Applying this

simplification, rearranging and taking logs gives Tafel equations for the anodic and cathodic reactions as described in Equation 14 and Equation 15.

$$\log_{10}|i| = \log_{10} i_0 + \frac{n[1-\alpha]F\eta}{2.3RT} \qquad \textit{Oxidation-anodic} \qquad \textbf{Equation 14}$$

$$\log_{10}|i| = \log_{10} i_0 - \frac{n\alpha F\eta}{2.3RT} \qquad \textit{Reduction-cathodic} \qquad \textbf{Equation 15}$$

It can be seen from the Tafel equations that the overpotential approximates to straight line when plotted *vs*. the log of the current density, i, (mA cm^{-2}). The point at which the best fit line intercepts the current density axis corresponds to the exchange current density, i_0 and the charge transfer coefficient and number of electrons transferred in the reaction determine the gradient or Tafel slope. This behaviour was observed and reported by Tafel in 1905 and later was demonstrated to have a theoretical basis in the form of the Butler-Volmer equation (27).

Increasing i_0 will result in a decrease of the over potential from activation loss. i_0 may be increased by: increasing the temperature, (improving turnover on catalytic sites), increasing the reactant concentration and increasing the pressure (improving site occupancy and increasing the theoretical potential as previously described), increasing the surface area (increasing the number of sites), and by using a more effective catalyst (lowering the activation barrier for reaction).

It is the cathodic oxygen reduction reaction (ORR) that is largely responsible for the activation loss observed for hydrogen fuel cells (25). This activation loss accounts for the most significant proportion of the deviation of the cell voltage loss from theoretical values when compared to fuel crossover, resistive and mass transport losses since these losses can be minimised and controlled by optimising experimental parameters. For this reason, a key research target is to develop more active catalysts for the ORR that have improved durability. Improved activity would enable increased performance or maintain equivalent performance while allowing a decrease in metal loading and therefore cost. In addition improved durability would extend operational lifetimes (18).

2.2 The ORR

The ORR is a multi electron reaction, the kinetics and mechanism of which are influenced by both the electrocatalyst and the electrolyte. In acid electrolyte, a general consensus exists that the overall reaction may proceed by two pathways (29), either by: the direct reduction pathway forming water, Equation 16**,** or by indirect reduction, Equation 17, in which hydrogen peroxide is generated. The hydrogen peroxide may then be further electrochemically reduced to water (Equation 18) or undergo chemical decomposition (Equation 19).

$O_2 + 4H^+ + 4e^- \rightarrow 2H_2O$ $\quad E^0{}_{O_2/H_2O} = 1.23$ V **Equation 16**

$O_2 + 2H^+ + 2e^- \rightarrow H_2O_2$ $\quad E^0{}_{O_2/H_2O} = 0.67$ V **Equation 17**

followed by a further reduction via

$H_2O_2 + 2H^+ + 2e^- \rightarrow 2H_2O$ $\quad E^0{}_{O_2/H_2O} = 1.77$ V **Equation 18**

or a chemical decomposition via

$2H_2O_2 \rightarrow 2H_2O + O_2$ **Equation 19**

Extensive experimental (25, 30-50) and theoretical studies (35, 36, 50-59) have been, and continue to be, performed to try to understand which pathway is followed and the mechanistic steps. The rotating ring-disk electrode is commonly employed to provide evidence for the two pathways (34, 44, 60, 61). Depending on the electrode material, oxygen reduction may proceed via either pathway. The direct four electron pathway appears to be predominate on noble metal catalysts, such as Pt, while on carbon, Au and most oxide-covered metals, such as Ni and Co the predominant pathway is via hydrogen peroxide formation (29).

When considering more detailed mechanistic steps for the ORR many possible models for the reaction pathways have been described (29) and the exact mechanism is subject to much debate. These models consider the adsorption of O_2, formation of intermediates, electron transfer steps, decomposition and desorption of products and the associated kinetics. A commonly reported reaction scheme for the ORR is shown in

Figure 2 (32, 46). This is a simplified version of the model proposed by Wroblowa *et al.* (62), in which O_{2ads} is formed from adsorption of O_2 onto the electrode surface in the first step. After adsorption the direct or indirect pathways can be followed as previously described in Equation 16-19 with rate constants k_1 through k_4. The rate determining step has been reported to be the first electron transfer from the $O_{2\ ads}$ (41). k_5 is the rate constant for the desorption of peroxide from the electrode surface. The peroxide may reabsorb and react or diffuse away from the electrode. In the fuel cell this reduces efficiency compared to the four electron route and decomposition of peroxide in the PEMFC can have detrimental effect of the integrity of the membrane (46).

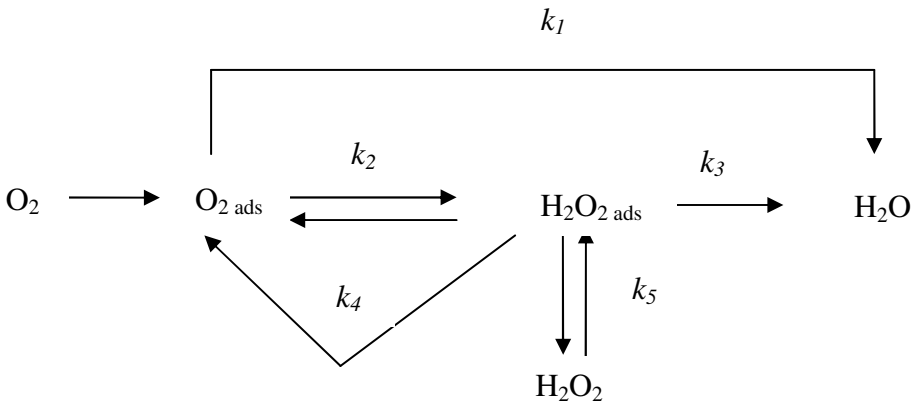

Figure 2. Example of a proposed oxygen reduction reaction pathway (32)

The orientation of the O_2 molecule during adsorption onto the metal surface has been proposed to alter the mechanistic pathway for ORR. Three models for oxygen adsorption modes and corresponding ORR pathways have been proposed by Yeager et al. (63) and are illustrated in Figure 3 (29). The Griffiths model involves edge-wise adsorption. In this synergic bonding interaction electron donation occurs from π orbitals on di-oxygen to empty d orbitals on the metal and back donation occurs from the metal to the empty π^* orbitals of O_2. This weakens the O-O bond and depending on the strength of the interaction may lead to dissociative adsorption of O_2 with simultaneous proton addition and an increase in the oxidation state of the metal as represented in pathway I. The catalyst is subsequently regenerated by reduction and formation of H_2O. If end on adsorption occurs through a single bond to the metal with partial charge transfer (Pauling model), an associative pathway via superoxide and peroxide intermediates is thought to be followed, as shown in pathway II. This can result in both the four electron product, H_2O or H_2O_2 via two electron reduction. The

third mode of binding is described by the bridge model where oxygen is adsorbed across two metal sites. As for pathway I, dissociation can occur and the four electron pathway forming H_2O is followed as shown in pathway 3.

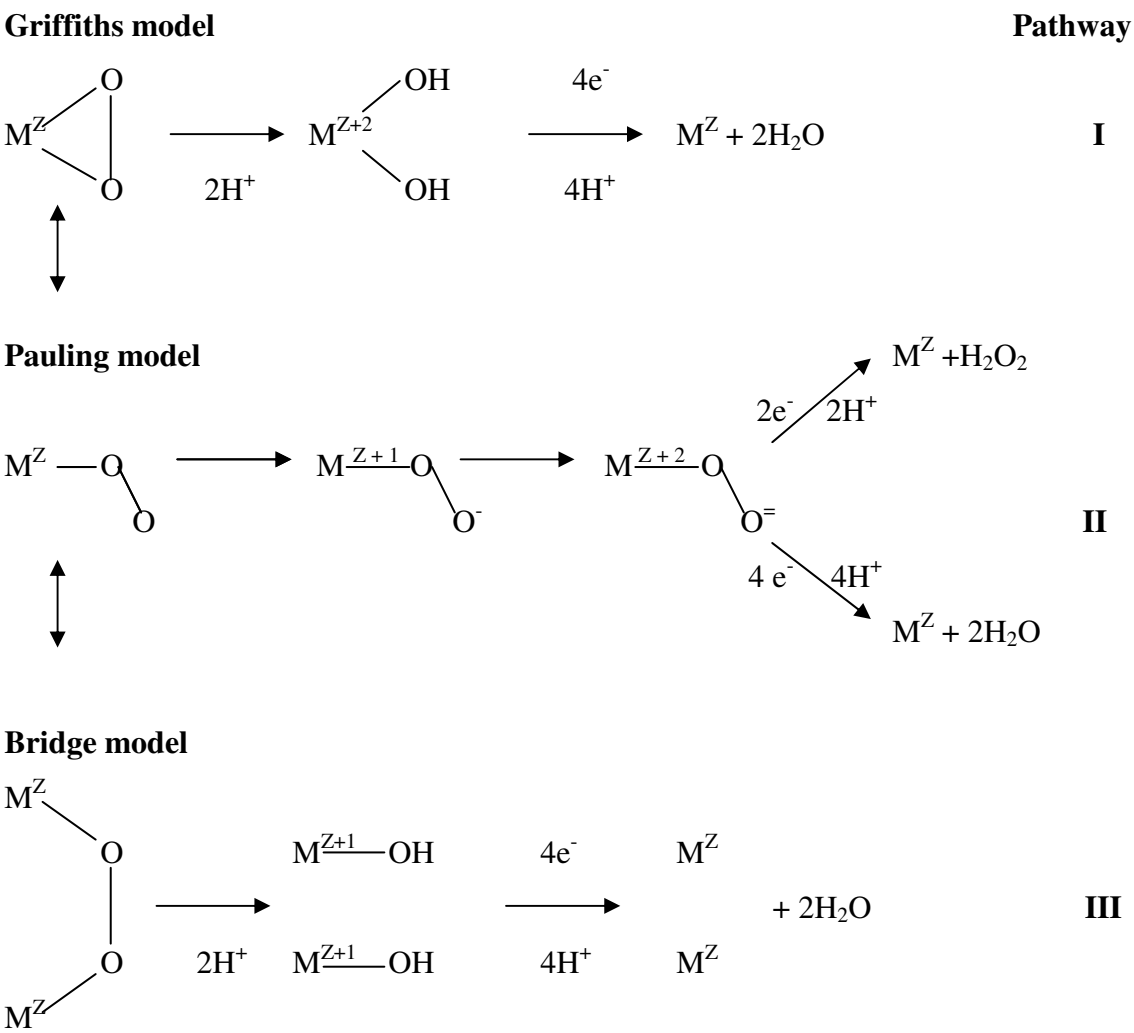

Figure 3. Models for adsorbed oxygen and corresponding reaction pathways for oxygen reduction. (29)

It is evident from Figure 3 that both the geometric and electronic properties of the catalyst are important factors in allowing favourable binding of reactants and subsequent reaction. An electronic effect arises due to differences in local electronic structure at the surface leading to different interactions with adsorbates/blocking species and intermediates (64). During interaction of an adsorbate with a transition metal, the sp

band of the transition metal causes a lowering and broadening of the adsorbate levels and the strong interaction of the d-band results in formation of bonding and antibonding orbitals (65). The Fermi energy, filling, d-band centre and width of the metal d-band all play an important role in enabling orbital overlap. Going across the periodic table from left to right increases filling of the d-band. This results in a decreasing width of the d-band and the position of the d-band centre shifting to lower energy. When the d-band is completely filled a further decrease in energy is observed as the d-band effectively becomes a core level. Going down a series from 3d to 5d results in broadening of the d-band due to increased orbital size and overlap (65). A high lying d-band results in a stronger chemisorption interaction with an adsorbate (64). If the electronic configuration of the metal leads to the antibonding orbital of the adsorbate lying below the metal Fermi level dissociation will occur. It is noted that this may result in a strong stabilisation effect of the dissociated state that may in turn prevent subsequent reaction. For optimum activity this implies a balance is required in the adsorption of reactants and formation of intermediates and the ability to dissociate products (65).

The surface geometry of the metal providing different configurations to the molecule for bonding is described as a purely geometric effect (64), for example a different crystallographic face or step site will induce a different geometric effect. The electronic and geometric effects are often difficult to separate since different geometries of the site (step *vs*. close packed) alter the position of the d-band (steps have higher-lying d-states than close packed surfaces) and simultaneously present different binding configurations to the adsorbate (64).

2.2.1 Platinum catalysts

For optimum catalytic activity, a catalyst must be selective for the reaction of interest since activity is governed by a balance between adsorption energies of reactive intermediates and surface coverage by spectator (blocking) species (44, 65). The catalyst should enable bond breaking and intermediate formation, without interacting so strongly with intermediates as to prevent further reaction and block adsorption sites (Sabatier's principle) (65). In addition the number of sites available for reaction and the turn over frequency of each site (kinetics), must be maximised.

Compared to other noble metals, platinum shows the highest turn over frequency, reacts mainly via the four electron pathway and therefore has a comparably low overpotential (29). For these reasons platinum is used as a cathode catalyst for fuel cell applications. To further optimise activity, the platinum is typically dispersed on a high surface area carbon to increase the metal surface area and therefore number of sites for reaction. However, ever decreasing particle size does not necessarily correlate with maximum specific activity (rate per unit area), as shown in studies by Kinoshita (29, 66). In these studies it was demonstrated that a particle size effect was involved for the ORR due to the structure sensitivity of the reaction.

Assuming a cubooctahedral model for platinum crystallites with (1 1 1) and (1 1 0) faces and edge and corner sites, Kinoshita calculated the effect of particle size on the distribution of surface atoms of each type, normalised to both the total number of atoms (mass average) and the number of surface atoms (surface average). The maximum mass averaged distribution was found to occur at 2 nm and 3.5 nm diameter on the (1 1 1) and (1 1 0) faces respectively, the surface averaged distribution was found to decrease with decreasing particle size on both faces, and the number of corner and edge sites decreases with increasing particle size (29, 66). These calculated results showed good correlation with mass and specific activity results reported in the literature by Ross and Settler, and Peuckert *et al.* for platinum catalysts (66). In assuming that the edge and corner sites were not active for reaction, Kinoshita concluded that that no benefit in mass or specific activity could be obtained by decreasing particle size below the limit of 2 nm (29).

Contrary to the work of Kinoshita, the results of others showed no clear evidence of the maximum in mass activity with particle size (29, 45) for example Yamamoto *et al.* recently published (67) ORR activity results for colloidal platinum particles of < 2 nm containing only 12, 28 and 60 platinum atoms. A 13 fold activity enhancement over a commercially available 2.5 nm diameter Pt/C catalyst was reported for the smallest particle size in RDE measurements. However, a direct comparison with a non-carbon supported 2.5 nm diameter catalyst prepared by the same route was not made. It is therefore not possible to tell if the activity enhancement is solely a consequence of the particle size, or a consequence of the differences in the oxygen diffusion properties of the carbon supported catalyst layer on the RDE disk.

Studies on platinum single crystals by Marković et al. (32) showed structure sensitivity by differences in the order of activity for the ORR on different Pt(h k l) crystal faces, in different electrolytes. In $HClO_4$ activity increases in the sequence Pt(1 0 0) < Pt(1 1 1) < Pt(1 1 0) while in H_2SO_4 all crystallite faces are less active and a different order of activity is observed where Pt(1 1 1) << Pt(1 0 0) < Pt(1 1 0). This is due to the strong anion adsorption of the (bi)sulphate anion that is thought to block the adsorption of O_2 in the first step of the ORR (32). For the Pt(1 1 1) face, the symmetry match for (bi)sulphate binding is most favoured and accounts for the significant deactivation of this face. Competitive binding of other species has also been reported to reduce the activity for ORR (32), with the adsorption of oxygen containing species, such as OH, surface oxide and water molecules playing an important role in the deactivation process (38). It has been shown that oxide covered surfaces exhibit different Tafel slopes and lower reaction rates than oxide free surfaces (31, 32, 35, 38). The difference in the Tafel slope (60 mV/decade oxide covered vs 120 mV/decade oxide free) may either be a consequence of a change in the charge transfer coefficient, α, or if α remains the same, then the change in Tafel slope may arise from a change in the number of electrons transferred in the limiting step of the reaction mechanism. It has also been reported that the adsorption of OH (45, 46, 68), and Cl^- (42, 49) also limits the kinetics and coverage of these species is important. When considering the possible binding modes for O_2 in Figure 3, it can be seen how site blocking by OH and other competitive binding species could result in a change of reaction pathway by reducing the number of sites available for bridge binding.

2.2.2 Strategies for improving activity

To improve the activity of platinum for the ORR a number of strategies have been reported. It has been demonstrated, in both phosphoric acid fuel cells and more recently in PEMFCs (69), that activity may be increased by alloying platinum with secondary metal (M) forming mixed Pt-M nanoalloys that may either be random or ordered (70, 71). Equally, ternary systems have also been studied (69). A wide variety of metals have been used as the alloying components including; Fe, Ni, Ir, V, Cr, Mn, Ti, Cu, and Co and a range of atomic compositions have been used (37, 69, 72-80).

More recently the use of alternative bimetallic architectures has been shown to improve activity and depending on M and the preparation route, these structures can enable an additional cost reduction, by allowing more efficient use of the platinum within the particle. All examples form a core shell type structure with an outer platinum shell surrounding an M containing core. Three different preparation routes have been reported to achieve this structure. In the first instance, it was shown that platinum could undergo surface segregation to form a shell or 'skin' around the M core (43, 44, 56, 81, 82). Next, based on d-band centre trends, it was shown that a layer of platinum deposited as an overlayer on a metal with different lattice constant could result in stress or strain in the platinum overlayer and change the catalytic activity (47, 65). Depositing platinum onto a surface with a larger lattice constant, pulls the platinum atoms apart, decreasing the average coordination number and d-orbital overlap and consequently the d-band narrows. To maintain the degree of filling, the centre of the band moves up in energy (65). This, as previously mentioned, will increase the binding interaction with an adsorbate. This effect was demonstrated for deposition of a platinum monolayer onto a single crystals of M (50, 61) and later for dispersed particles where platinum was deposited as an overlayer onto a preformed core using under potential deposition methods, forming so called 'core shell' particles (47, 70, 71, 83, 84). The third method to form the platinum shell is to chemically leach or electrochemically dealloy to remove M from the outerlayers of a preformed PtM material (81, 85-92). In these works M includes: Ni (50, 56, 73) , Co, Ti, V (44, 56, 81) Cu, (85-92) and equally ternary metal systems have also been reported (93-95).

In parallel, there has been a recent focus in preparing catalysts to maximise favourable geometries to enhance activity. To this end platinum nanoparticles of different shapes and sizes have been synthesised. The wide range of possible nanostructures have been recently reviewed by Peng and Yang (70) and include: cubes, tetrahedrons, tripods, cubooctahedron, nanorods, wires and tubes. In addition, nanostructured thin film catalysts prepared by sputter deposition of platinum on organic whiskers by 3M company (96-99) have been shown to result in defined crystal face orientations (96). These geometries are now also being combined with the desirable properties seen for PtX containing materials in attempts to further improve activity.

The improvements in activity for PtM materials have been attributed and or correlated to various changes caused by alloying/interaction of M including:

1. **The effect of Pt-Pt interatomic distance**: Alloying with elements smaller than platinum results in lattice contraction, which in turn corresponds with an increase in electrocatalytic activity. Jalan and Taylor (100, 101) proposed this effect was attributed to the smaller Pt-Pt interatomic bond distances resulting in more favourable sites that enhance the dissociative adsorption of oxygen. This view is supported by Mukerjee *et al.* who correlated Pt-Pt bond length (or d-band vacancy) measured during XAS studies with ORR activity (33).

2. **The proportion of low index planes**: Alloying is also known to increase the proportion of the more reactive, low index crystal planes of platinum compared to pure platinum. This may in part due to a particle size effect since alloys are often larger than high surface area platinum catalysts due to the high temperature heat treatment required for formation (48, 75).

3. **Inhibition of OH_{ads} and oxide formation**: Alloying or use of bimetallic catalysts has been shown to inhibit OH_{ads} anion adsorption on platinum. This has been observed experimentally in cyclic voltammograms (25, 38, 40, 41, 44, 50, 102) and during X-ray absorption Spectroscopy studies (33, 35, 103). The delayed onset of OH_{ads} (and oxide) thus reduces the amount of competitive binding that occurs, keeps the surface oxide free over a larger potential window and therefore more sites are available for ORR (50, 102). It has also been suggested that if OH preferentially binds to X, then Pt sites are less likely to be blocked (47).

4. **Surface roughening**: Other studies (80, 104) suggest that surface roughening of alloys occurs as a result of leaching of the secondary metal leaving Raney surfaces with higher surface area and hence higher activity.

5. **Alloying atoms involved in the ORR**: It is been suggested that alloying elements such as Cr can act as a redox mediator facilitating the ORR (80).

6. **Electronic effects:** Alloying with different metals results in changes in electronic structure of the Pt 5d-band vacancy (33). The position of the d-band centre effects the ability of the metal to bind desired (O_2) species, generate intermediates and also effects the subsequent release of intermediates from the surface (58, 59). The degree of filling of the d-bands is also important as this interaction determines the adsorption strength of oxygenated intermediate species and facilitates their conversion to final products. The coupling of the d-metal states and competing adsorbates (OH_{ads}) must also be considered. Several experimental and modelling studies (33, 58, 61), including recent work by Markovic et al. (44, 56) have shown Pt alloy and bimetallic catalysts exhibit a 'Volcano-type' behaviour with an optimum electronic structure correlating to optimum activity. This is shown in Figure 4 where the d-band centre is correlated with activity. Compared to polycrystalline platinum the alloys have a lower d-band centre. This leads to a weaker interaction with adsorbates. On the left hand side of the volcano the rate is limited by insufficient adsorption of O_2 due to the low lying d-states, while on the right hand side desorption of products limits the reaction (44). An optimum is observed were sufficient adsoption of reactants and desorption of products occurs. As previously mentioned, the effects of stress and strain also alter the electronic configuration, which in turn modifies activity (47, 65).

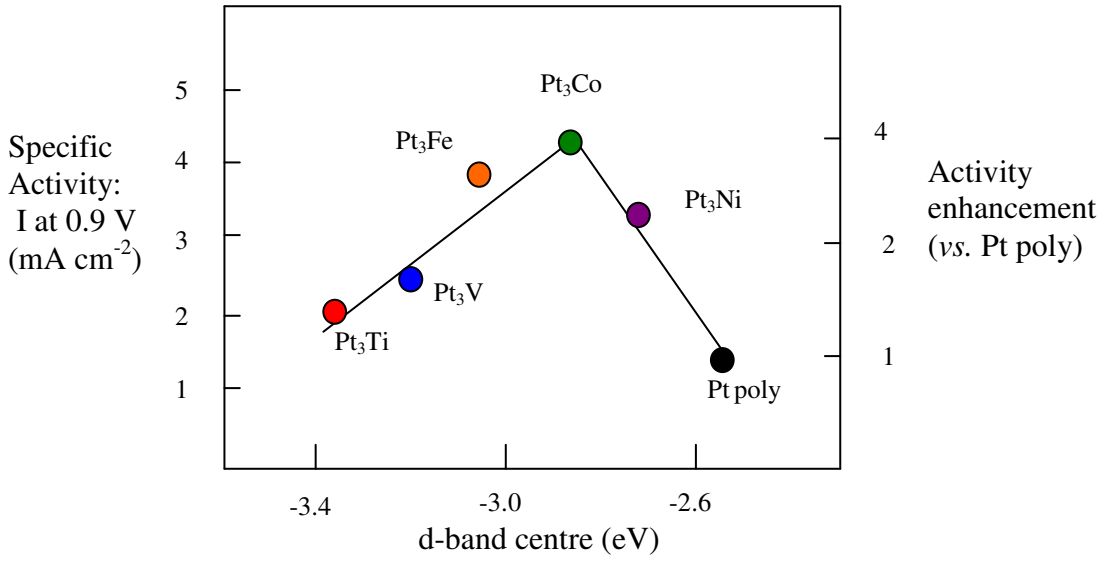

Figure 4. **Relationships between the catalytic properties and electronic structure of Pt_3M alloys [adapted from reference (44)]**

2.3. Stability of ORR catalysts

As well as demonstrating enhanced activity, new candidate cathode catalyst materials must meet demanding durability targets. Catalysts must survive repeated potential cycling and exposure to high potentials (105). This can result in corrosion of the carbon support (13, 106-109) and loss of electrochemically active metal area (ECA) (13, 110-113), which may in turn lead to loss in fuel cell performance. When compared to platinum alone PtCo, PtNi and PtFe catalysts have been reported to be more stable to platinum electrochemical area loss (72, 73, 76, 77, 114, 115). The improved stability has been attributed to the fact the second metal helps anchor the platinum to the carbon support and the larger particle size of alloy catalysts (13, 77). The use of alloys and bimetallics however, has lead to additional stability considerations regarding the additional metal/s. Base metals are known to undergo indirect reduction of oxygen forming peroxide, which can lead to membrane degradation (46). In addition, leaching of the alloying metal under operating conditions has been observed in both PEMFCs (13, 76, 114) and DMFCs (116) resulting in loss of the alloying activity benefit over time. More detailed discussions regarding these mechanisms and the impact of activity loss will be presented in Chapter 3.

3. Project Aims and Objectives

This chapter highlights poor cathode performance and catalyst stability as major factors limiting fuel cell commercialisation. Bimetallic and alloy catalysts have been identified as a means of improving both activity and stability. The numerous theories for the observed activity enhancements have been described. The aim of this work is to test these theories by comparison of a Pt/C catalyst, typical of commercially available materials, with a series of PtCo/C catalysts, with a view to gaining an increased understanding of desirable catalytic features for enhanced ORR activity. A range of techniques will be used to characterise catalyst structure including: X-ray absorption spectroscopy (XAS), X-ray diffraction (XRD), Transmission Electron Microscopy (TEM) and Cyclic Voltammetry. Correlation of catalyst structural properties will be made to both catalytic activity and durability. Catalyst performance and stability will be assessed using cyclic voltammetry and polarisation measurements.

Deactivation of platinum and bimetallic catalysts occurs over time. By understanding the processes that cause deactivation, favourable catalytic activity and stability properties may be identified. Chapter 3 aims to study catalyst deactivation by quantifying metal leaching, accessing the impact of leaching on catalyst structure and probing the mechanisms of performance loss during stability tests.

In chapters 4 and 5, the relationship between cathode catalyst activity and structure is explored using X-ray absorption spectroscopy (XAS) to provide element specific information on the arrangement of atoms and their nearest neighbours (117, 118). Although XAS studies of catalyst powders and electrodes (119-122) have proved instructive, the optimum environment for characterisation is *in situ* under realistic fuel cell operating conditions, now known as *operando* studies. The design and operation of a fuel cell to enable *operando* XAS measurements to be conducted on the cathode will be presented, together with findings from investigation into the mechanism of oxide growth and removal during potential steps, and catalyst structure during the ORR.

Favourable geometric effects are claimed to explain the activity enhancement of electrochemical dealloyed $PtCu_3$/C catalysts that have been demonstrated to meet automotive targets (87). In light of these results, chapter 6 presents the preparation, characterisation and activity of electrochemically dealloyed $PtCo_3$/C catalysts.

Overall conclusions will be provided in chapter 7, with the differences observed in this work between PtCo alloys and platinum discussed in relation to literature theories for activity enhancement.

References

1. W. R. Grove, *Philosophical Magazine and Journal of Science*, **XIV**, 127 (1839).
2. W. R. Grove, *Philosophical Magazine and Journal of Science*, **XXI**, 417 (1842).
3. J. Larminie and A. Dicks, *Fuel Cell Systems Explained*, Wiley (2003).
4. M. S. Dresselhaus and I. L. Thomas, *Nature*, **414**, 332 (2001).
5. B. C. H. Steele and A. Heinzel, *Nature*, **414**, 345 (2001).
6. *Platinum Metals Review*, **53**, 104 (2009).
7. K. Kinoshita, in *Electrochemical Oxygen Technology, Chapter 4 Fuel cells*, p. 163, John Wiley & Sons (1992).
8. K. Kordesch, V. Hacker, K. Strasser and M. Cifrain, in *Handbook of Fuel Cells, Volume 4: Fuel Cell Technology and Applications, Part 2, Chapters, Part 4: Alkaline fuel cells and systems*, W. Vielstich, A. Lamm and H. A. Gasteiger Editors, p. 763, John Wiley & Sons (2003).
9. R. D. Breault, D. A. Lansdman, F. J. Luczak, J. M. King and B. McDonald, in *Handbook of Fuel Cells, Volume 4: Fuel Cell Technology and Applications, Part 2, Chapters 59-61, Part 5: Phosphoric acid fuel cells and systems*, W. Vielstich, A. Lamm and H. A. Gasteiger Editors, p. 795, John Wiley & Sons (2003).
10. J. Muller, G. Frank, K. Colbow, D. Wilkinson, M. Neergat, K. A. Friedrich, U. Stimming, A. Lamm, S. R. Narayanan, T. I. Valdez and N. Rohatgi, in *Handbook of Fuel Cells, Volume 4: Fuel Cell Technology and Applications, Part 2, Chapters 62-65, Part 6: Direct methanol fuel cells and systems*, W. Vielstich, A. Lamm and H. A. Gasteiger Editors, p. 845, John Wiley & Sons (2003).
11. Y. Mugikura, J. Hoffmann, C.-Y. Yuh and A. Godula Jopek, in *Handbook of Fuel Cells, Volume 4: Fuel Cell Technology and Applications, Part 2, Chapters 66-69, Part 7: Molten carbonate fuel cells and systems*, W. Vielstich, A. Lamm and H. A. Gasteiger Editors, p. 905, John Wiley & Sons (2003).
12. T. Kawada, J. Mizusaki, O. Yamamoto, D. Stover, H. P. Buchkremer, J. P. P. Huijsmans, M. Suzuki, K. Hilpert, W. J. Quaddakkers and L. Singheiser, in *Handbook of Fuel Cells, Volume 4: Fuel Cell Technology and Applications, Part 2, Chapters 70-79, Part 8: Solid oxide fuel cells and systems*, W. Vielstich, A. Lamm and H. A. Gasteiger Editors, p. 983, John Wiley & Sons (2003).
13. R. Borup, J. Meyers, B. Pivovar, Y. S. Kim, R. Mukundan, N. Garland, D. Myers, M. Wilson, F. Garzon, D. Wood, P. Zelenay, K. More, K. Stroh, T. Zawodzinski, J. Boncella, J. E. McGrath, M. Inaba, K. Miyatake, M. Hori, K. Ota, Z. Ogumi, S. Miyata, A. Nishikata, Z. Siroma, Y. Uchimoto, K. Yasuda, K. I. Kimijima and N. Iwashita, *Chemical Reviews*, **107**, 3904 (2007).
14. M. Doyle and G. Rajendran, in *Handbook of Fuel Cells, Volume 4: Fuel Cell Technology and Applications, Part 2, Chapter 30, Perfluorinated membranes*, W. Vielstich, A. Lamm and H. A. Gasteiger Editors, p. 351, John Wiley & Sons (2003).
15. J. Peron, Y. Nedellec, D. J. Jones and J. Roziere, *Journal of Power Sources*, **185**, 1209 (2008).
16. K. D. Kreuer, in *Handbook of Fuel Cells, Volume 4: Fuel Cell Technology and Applications, Part 2, Chapter 33 Hydrocarbon membranes*, W. Vielstich, A. Lamm and H. A. Gasteiger Editors, p. 420, John Wiley & Sons (2003).
17. D. J. Jones and J. Roziere, *Journal of Membrane Science*, **185**, 41 (2001).

18. H. A. Gasteiger, S. S. Kocha, B. Sompalli and F. T. Wagner, *Applied Catalysis B-Environmental*, **56**, 9 (2005).
19. C. Roth, N. Benker, M. Mazurek, F. Scheiba and H. Fuess, *Applied Catalysis A-General*, **319**, 81 (2007).
20. B. Wang, *Journal of Power Sources*, **152**, 1 (2005).
21. R. Bashyam and P. Zelenay, *Nature*, **443**, 63 (2006).
22. HFP, European Technology Platform for Hydrogen and Fuel Cells, www.HFPeurope.org, in (2007).
23. NEDO, http://www.nedo.go.jp/nenryo/gijutsu/index.html, in (2007).
24. DoE, WWW.eere.energy.gov/hydrogenandfuelcells/mypp/pdfs/fuel_cells.pdf, in (2006).
25. U. A. Paulus, A. Wokaun, G. G. Scherer, T. J. Schmidt, V. Stamenkovic, N. M. Markovic and P. N. Ross, *Electrochimica Acta*, **47**, 3787 (2002).
26. E. Chen, in *Fuel Cell Technology Handbook*, G. Hoogers Editor, CRC Press (2003).
27. A. J. Bard and L. R. Faulkner, *Electrochemical Methods, Fundamentals and Applications, 2nd Edition*, John Wiley & Sons (2001).
28. D. Pletcher, in *A First Course In Electrode Processes, Chapter 1, The Nature of Electrode Reactions*, E.C.C., p. 1, (1991).
29. K. Kinoshita, in *Electrochemical Oxygen Technology, Chapter 2, Oxygen Electrochemistry*, p. 19, John Wiley & Sons (1992).
30. T. Zambelli, J. V. Barth, J. Wintterlin and G. Ertl, *Nature*, **390**, 495 (1997).
31. S. L. Chen and A. Kucernak, *Journal of Physical Chemistry B*, **108**, 3262 (2004).
32. N. M. Markovic and P. N. Ross, *Surface Science Reports*, **45**, 121 (2002).
33. S. Mukerjee, S. Srinivasan, M. P. Soriaga and J. McBreen, *Journal of the Electrochemical Society*, **142**, 1409 (1995).
34. U. A. Paulus, T. J. Schmidt, H. A. Gasteiger and R. J. Behm, *Journal of Electroanalytical Chemistry*, **495**, 134 (2001).
35. J. Roques, A. B. Anderson, V. S. Murthi and S. Mukerjee, *Journal of the Electrochemical Society*, **152**, E193 (2005).
36. A. B. Anderson, J. Roques, S. Mukerjee, V. S. Murthi, N. M. Markovic and V. Stamenkovic, *Journal of Physical Chemistry B*, **109**, 1198 (2005).
37. B. C. Beard and P. N. Ross, *Journal of the Electrochemical Society*, **137**, 3368 (1990).
38. A. Kuzume, E. Herrero and J. M. Feliu, *Journal of Electroanalytical Chemistry*, **599**, 333 (2007).
39. M. D. Macia, J. M. Campina, E. Herrero and J. M. Feliu, *Journal of Electroanalytical Chemistry*, **564**, 141 (2004).
40. D. S. Strmcnik, P. Rebec, M. Gaberscek, D. Tripkovic, V. Stamenkovic, C. Lucas and N. M. Markovic, *Journal of Physical Chemistry C*, **111**, 18672 (2007).
41. V. Stamenkovic, T. J. Schmidt, P. N. Ross and N. M. Markovic, *Journal of Electroanalytical Chemistry*, **554**, 191 (2003).
42. V. Stamenkovic, N. M. Markovic and P. N. Ross, *Journal of Electroanalytical Chemistry*, **500**, 44 (2001).
43. V. R. Stamenkovic, B. S. Mun, K. J. J. Mayrhofer, P. N. Ross and N. M. Markovic, *Journal of the American Chemical Society*, **128**, 8813 (2006).
44. V. R. Stamenkovic, B. S. Mun, M. Arenz, K. J. J. Mayrhofer, C. A. Lucas, G. F. Wang, P. N. Ross and N. M. Markovic, *Nature Materials*, **6**, 241 (2007).

45. K. J. J. Mayrhofer, B. B. Blizanac, M. Arenz, V. R. Stamenkovic, P. N. Ross and N. M. Markovic, *Journal of Physical Chemistry B*, **109**, 14433 (2005).
46. N. Ramaswamy, N. Hakim and S. Mukerjee, *Electrochimica Acta*, **53**, 3279 (2008).
47. R. R. Adzic, J. Zhang, K. Sasaki, M. B. Vukmirovic, M. Shao, J. X. Wang, A. U. Nilekar, M. Mavrikakis, J. A. Valerio and F. Uribe, *Topics in Catalysis*, **46**, 249 (2007).
48. M. Teliska, V. S. Murthi, S. Mukerjee and D. E. Ramaker, *Journal of the Electrochemical Society*, **152**, A2159 (2005).
49. T. M. Arruda, B. Shyam, J. M. Ziegelbauer, S. Mukerjee and D. E. Ramaker, *Journal of Physical Chemistry C*, **112**, 18087 (2008).
50. V. R. Stamenkovic, B. Fowler, B. S. Mun, G. F. Wang, P. N. Ross, C. A. Lucas and N. M. Markovic, *Science*, **315**, 493 (2007).
51. Z. H. Gu and P. B. Balbuena, *Journal of Physical Chemistry C*, **112**, 5057 (2008).
52. Z. H. Gu and P. B. Balbuena, *Journal of Physical Chemistry C*, **111**, 9877 (2007).
53. Z. H. Gu and P. B. Balbuena, *Journal of Physical Chemistry C*, **111**, 17388 (2007).
54. Y. Ma and P. B. Balbuena, *Chemical Physics Letters*, **447**, 289 (2007).
55. H. A. Hansen, J. Rossmeisl and J. K. Norskov, *Physical Chemistry Chemical Physics*, **10**, 3722 (2008).
56. V. Stamenkovic, B. S. Mun, K. J. J. Mayrhofer, P. N. Ross, N. M. Markovic, J. Rossmeisl, J. Greeley and J. K. Norskov, *Angewandte Chemie-International Edition*, **45**, 2897 (2006).
57. J. Roques and A. B. Anderson, *Surface Science*, **581**, 105 (2005).
58. A. Ruban, B. Hammer, P. Stoltze, H. L. Skriver and J. K. Norskov, *Journal of Molecular Catalysis A-Chemical*, **115**, 421 (1997).
59. B. Hammer and J. K. Norskov, *Surface Science*, **343**, 211 (1995).
60. T. J. Schmidt, H. A. Gasteiger, G. D. Stab, P. M. Urban, D. M. Kolb and R. J. Behm, *Journal of the Electrochemical Society*, **145**, 2354 (1998).
61. J. L. Zhang, M. B. Vukmirovic, Y. Xu, M. Mavrikakis and R. R. Adzic, *Angewandte Chemie-International Edition*, **44**, 2132 (2005).
62. H. S. Wroblowa, Y. C. Pan and G. Razumney, *Journal of Electroanalytical Chemistry*, **69**, 195 (1976).
63. E. Yeager, *Journal of Molecular Catalysis*, **38**, 5 (1986).
64. J. K. Norskov, T. Bligaard, B. Hvolbaek, F. Abild-Pedersen, I. Chorkendorff and C. H. Christensen, *Chemical Society Reviews*, **37**, 2163 (2008).
65. I. Chorkendorff and J. W. Niemantsverdriet, *Concepts of Modern Catalysis and Kinetics*, WILEY-VCH (2003).
66. K. Kinoshita, *Journal of the Electrochemical Society*, **137**, 845 (1990).
67. K. Yamamoto, T. Imaoka, W. J. Chun, O. Enoki, H. Katoh, M. Takenaga and A. Sonoi, *Nature Chemistry*, **1**, 397 (2009).
68. V. S. Murthi, R. C. Urian and S. Mukerjee, *Journal of Physical Chemistry B*, **108**, 11011 (2004).
69. D. Thompsett, in *Handbook of Fuel cells,Volume 3: Fuel Cell Technology and Applications, Chapter 37, Pt Alloys as oxygen reduction catalysts*, W. Vielstich, H. A. Gasteiger and A. Lamm Editors, p. 467, John Wiley & Sons, Ltd (2003).
70. Z. M. Peng and H. Yang, *Nano Today*, **4**, 143 (2009).
71. R. Ferrando, J. Jellinek and R. L. Johnston, *Chemical Reviews*, **108**, 845 (2008).

72. Z. D. Wei, H. T. Guo and Z. Y. Tang, *Journal of Power Sources*, **62**, 233 (1996).
73. H. R. Colon-Mercado, H. Kim and B. N. Popov, *Electrochemistry Communications*, **6**, 795 (2004).
74. S. Mukerjee and S. Srinivasan, *Journal of Electroanalytical Chemistry*, **357**, 201 (1993).
75. C. W. B. Bezerra, L. Zhang, H. S. Liu, K. C. Lee, A. L. B. Marques, E. P. Marques, H. J. Wang and J. J. Zhang, *Journal of Power Sources*, **173**, 891 (2007).
76. P. Yu, M. Pemberton and P. Plasse, *Journal of Power Sources*, **144**, 11 (2005).
77. H. R. Colon-Mercado and B. N. Popov, *Journal of Power Sources*, **155**, 253 (2006).
78. A. Witkowska, S. Dsoke, E. Principi, R. Marassi, A. Di Cicco and V. R. Albertini, *Journal of Power Sources*, **178**, 603 (2008).
79. P. P. Wells, Y. D. Qian, C. R. King, R. J. K. Wiltshire, E. M. Crabb, L. E. Smart, D. Thompsett and A. E. Russell, *Faraday Discussions*, **138**, 273 (2008).
80. M. T. Paffett, K. A. Daube, S. Gottesfeld and C. T. Campbell, *Journal of Electroanalytical Chemistry*, **220**, 269 (1987).
81. S. Chen, W. C. Sheng, N. Yabuuchi, P. J. Ferreira, L. F. Allard and Y. Shao-Horn, *Journal of Physical Chemistry C*, **113**, 1109 (2009).
82. K. J. J. Mayrhofer, V. Juhart, K. Hartl, M. Hanzlik and M. Arenz, *Angewandte Chemie-International Edition*, **48**, 3529 (2009).
83. J. Zhang, Y. Mo, M. B. Vukmirovic, R. Klie, K. Sasaki and R. R. Adzic, *Journal of Physical Chemistry B*, **108**, 10955 (2004).
84. J. Luo, L. Wang, D. Mott, P. N. Njoki, Y. Lin, T. He, Z. Xu, B. N. Wanjana, I. I. S. Lim and C. J. Zhong, *Advanced Materials*, **20**, 4342 (2008).
85. R. Srivastava, P. Mani and P. Strasser, *Journal of Power Sources*, **190**, 40 (2009).
86. S. Koh, N. Hahn, C. F. Yu and P. Strasser, *Journal of the Electrochemical Society*, **155**, B1281 (2008).
87. P. Mani, R. Srivastava and P. Strasser, *Journal of Physical Chemistry C*, **112**, 2770 (2008).
88. P. Strasser, *Advanced Materials & Processes*, **166**, 13 (2008).
89. S. Koh, C. Yu and P. Strasser, *ECS Transactions*, **11**, 205 (2007).
90. S. Koh and P. Strasser, *Journal of the American Chemical Society*, **129**, 12624 (2007).
91. R. Srivastava, P. Mani, N. Hahn and P. Strasser, *Angewandte Chemie-International Edition*, **46**, 8988 (2007).
92. P. Strasser, S. Koh and C. Yu, *ECS Transactions*, **11**, 167 (2007).
93. K. C. Neyerlin, R. Srivastava, C. F. Yu and P. Strasser, *Journal of Power Sources*, **186**, 261 (2009).
94. M. Shao, K. Sasaki, N. S. Marinkovic, L. Zhang and R. R. Adzic, *Electrochemistry Communications*, **9**, 2848 (2007).
95. J. Shim, D. Y. Yoo and J. S. Lee, *Electrochimica Acta*, **45**, 1943 (2000).
96. L. Gancs, T. Kobayashi, M. K. Debe, R. Atanasoski and A. Wieckowski, *Chemistry of Materials*, **20**, 2444 (2008).
97. J. B. Stahl, M. K. Debe and P. L. Coleman, in *42nd National Symposium of the American-Vacuum-Society*, p. 1761, Minneapolis, Mn (1995).
98. M. K. Debe and R. J. Poirier, *Journal of Vacuum Science & Technology A-Vacuum Surfaces and Films*, **12**, 2017 (1994).

99. K. M. Debe, in *Handbook of Fuel Cells, Volume 3: Fuel Cell Technology and Applications, Part 3, Chapter 45, Novel catalysts, catalysts support and catalysts coated membrane methods*, W. Vielstich, A. Lamm and H. A. Gasteiger Editors, p. 576, John Wiley & Sons (2003).
100. V. Jalan and E. J. Taylor, *Journal of the Electrochemical Society*, **130**, 2299 1983).
101. V. Jalan and E. J. Taylor, *Journal of the Electrochemical Society*, **130**, C125 (1983).
102. V. Stamenkovic, T. J. Schmidt, P. N. Ross and N. M. Markovic, *Journal of Physical Chemistry B*, **106**, 11970 (2002).
103. S. Mukerjee and J. McBreen, *Journal of Electroanalytical Chemistry*, **448**, 163 (1998).
104. M. T. Paffett and S. Gottesfeld, *Journal of the Electrochemical Society*, **135**, C348 (1988).
105. DoE, Research and Development of Fuel Cell Technology for the Hydrogen Economy Funding opportunity Number: DE-PS36-06GO96017, in (2006).
106. Kinoshit.K and J. A. S. Bett, *Carbon*, **11**, 403 (1973).
107. P. L. Antonucci, F. Romeo, M. Minutoli, E. Alderucci and N. Giordano, *Carbon*, **26**, 197 (1988).
108. K. H. Kangasniemi, D. A. Condit and T. D. Jarvi, *Journal of the Electrochemical Society*, **151**, E125 (2004).
109. S. Maass, F. Finsterwalder, G. Frank, R. Hartmann and C. Merten, *Journal of Power Sources*, **176**, 444 (2008).
110. Y. Shao-Horn, W. C. Sheng, S. Chen, P. J. Ferreira, E. F. Holby and D. Morgan, *Topics in Catalysis*, **46**, 285 (2007).
111. P. J. Ferreira, G. J. la O, Y. Shao-Horn, D. Morgan, R. Makharia, S. Kocha and H. A. Gasteiger, *Journal of the Electrochemical Society*, **152**, A2256 (2005).
112. K. I. Ota, S. Nishigori and N. Kamiya, *Journal of Electroanalytical Chemistry*, **257**, 205 (1988).
113. W. Bi, G. E. Gray and T. F. Fuller, *Electrochemical and Solid State Letters*, **10**, B101 (2007).
114. S. Ball, S. Hudson, B. Theobald and D. Thompsett, *ECS Transactions*, **1**, 141 (2006).
115. M. F. Mathais, R. Makharia, H. A. Gasteiger, J. J. Conley, T. J. Fuller, C. J. Gittleman, S. S. Kocha, D. P. Miller, C. K. Mittelsteadt, T. Xie, G. S. Yan and P. T. Yu, *Interface, Electrochemical Society*, 24 (2005).
116. P. Piela, C. Eickes, E. Brosha, F. Garzon and P. Zelenay, *Journal of the Electrochemical Society*, **151**, A2053 (2004).
117. A. E. Russell and A. Rose, *Chemical Reviews*, **104**, 4613 (2004).
118. J. McBreen, W. E. Ogrady and K. I. Pandya, *Journal of Power Sources*, **22**, 323 (1988).
119. R. A. Lampitt, L. P. L. Carrette, M. P. Hogarth and A. E. Russell, *Journal of Electroanalytical Chemistry*, **460**, 80 (1999).
120. W. E. O'Grady and D. C. Koningsberger, *Electrochemical Society Extended Abstracts*, **88-1**, 513 (1988).
121. J. McBreen, W. E. O'Grady, K. I. Pandya, R. W. Hoffman and D. E. Sayers, *Langmuir*, **3**, 428 (1987).
122. S. Maniguet, R. J. Mathew and A. E. Russell, *Journal of Physical Chemistry B*, **104**, 1998 (2000).

Chapter 2. Experimental Methods and Techniques

The theoretical and practical aspects of the catalyst preparation and testing by electrochemical and spectroscopic techniques used in this work will be discussed in this chapter.

1. Catalysts under investigation, reagents and materials

The carbon supported catalyst materials used in this work include; Pt/C reference materials, PtCo/C and Pd/C catalysts. Assay compositions, mean crystallite sizes determined by XRD and the chapters where the catalysts have been used are reported in Table 1.

Table 1. Catalysts used in this study

Catalyst	Chapter	Assay composition / wt %	XRD mean crystallite size / nm
60%Pt/C	3,4,5	57 % Pt	2
40%Pt/C	3, 4,5,6	38.2 % Pt	2.2
40%Pt/C 600 °C	3,4	42.8% Pt	4.7
40%Pt/C 900 °C	3,4,5,6	40.9 % Pt	5.0
40%Pt/C 1000 °C	3,4	40.0 % Pt	7.7
40%Pt/C 1000 °C II	4	-	5.6
40%Pt/C 1200 °C	3,4	41.4 % Pt	15.6
40% Pt_3Co/C 600 °C	3	41.7 % Pt, 4.3 % Co	3.6
40% Pt_3Co/C 1000 °C	3,6 4,5 3	39.5 % Pt, 4.02 % Co batch 1 40.6 % Pt, 4.04 % Co batch 2 41.9 % Pt, 4.2 % Co batch 3	5.9 batch 1 5.8 batch 2 5.0 batch 3
40% Pt_3Co/C 1000 °C Acid leached	3,4,5,6	40.5 % Pt, 3.12 % Co	5.9
40% Pt_3Co/C 1200 °C Acid leached	3	42.7 % Pt, 4.11 % Co	12.9
40% Pt_3Co/C 900 °C	3	38.5 % Pt, 3.96 % Co	3.7
40% Pt_3Co/C 1200 °C	3	39.8 % Pt, 4.08 % Co	12.6
Catalyst 1 $PtCo_3$/C 600 °C	6	22.4 % Pt, 19.4 % Co	amorphous
Catalyst 2 $PtCo_3$/C 950 °C	6	23.3 % Pt, 20.2 % Co	16 and 3.3
Catalyst 3 $PtCo_3$/C 600 °C Acid leached	6	27.4 % Pt, 1.38 % Co	2.2
Catalyst 4 $PtCo_3$/C 950 °C Acid leached	6	27.8 % Pt, 3.31 % Co	2.4
10% Pd/C	4, 5	10.26 % Pd	-

A list of the reagents and materials, excluding catalysts, used in this work and source information is shown in Table 2.

Table 2. Reagent and materials used in this study		
Reagent/material Category	**Reagent/material description**	**Reagent/material Supplier/Source**
Metal salts	K_2PtCl_4 $CoCl_2.6H_2O$	Johnson Matthey Alfa Aesar
Carbon	Ketjen Graphite for cell plates	Akzo Nobel Ralph Coidan Limited
Gas Diffusion Layer	TGPH60 with carbon microporous layer at 0.4 mg C cm-2	Johnson Matthey Fuel Cells Ltd.
Ionomer (aq)	Nafion®	Dupont
Acid (l)	H_2SO_4	VW International Limited
Base (l)	NaOH	Fluka
Electrolyte (s) (Perfluorinated membranes)	Flemion® SH-30 (30 µm) Nafion® 115 (127 µm) NRE211CS (25 µm chemically stabilised) V3 (Johnson Matthey proprietary 30 µm membrane)	Asahi Glass Dupont Dupont Johnson Matthey Fuel Cells Ltd.
Electrolyte (l)	H_2SO_4	VW International Limited
Gases	H_2, N_2, O_2 Cylinders for use during XAS measurements H_2, N_2, O_2, Ar, CO for electrochemical testing	BOC/Air products Johnson Matthey Technology Centre in house electrolyser (H_2 and O_2), BOC/Air products
Electrodes	40% Pt/C Anode electrodes	Johnson Matthey Fuel Cells Ltd.
Catalysts and inks	60% Pt/C	Johnson Matthey Fuel Cells Ltd.

1.1 Catalyst preparation and characterisation

The Pt/C and Pt_3Co/C catalysts used in this study were prepared by Dr. B.R.C. Theobald, Johnson Matthey, using proprietary methods that have previously been described (1-3). Briefly, the carbon is slurried in weakly basic water before addition of the metal salts. On complete deposition of the metal, the metal was reduced either by chemical methods or by heat treatment. Different heat treatment temperatures and conditions have been used to provide Pt/C catalyst with a range of particle sizes. Alloying of the Pt_3Co catalysts was confirmed by the presence of a Pt_3Co phase using XRD analysis with a BrukerAXS D-500 Diffractometer. Where applicable chemical acid leaching was conducted in 0.5 M H_2SO_4, 80 ºC for 24 hrs. The Pt and Co content of the resulting leachate was determined using ICP-MS.

With guidance from Dr. B.R.C. Theobald and E. Christian, Johnson Matthey, four new $PtCo_3$/C catalysts have also been prepared. Chapter 6. These materials were based on the PtCu/C catalysts reported by Strasser *et al*. (4-10) that were shown to have enhanced activity after an electrochemical de-alloying procedure. $PtCo_3$/C catalysts were

synthesised as to target the $Pt_{25}M_{75}$ composition reported by Strasser *et al*.. However, instead of using the reported route of impregnation, the PtCo catalysts were prepared using the proprietary co-deposition route (1-3). The carbon (36 g) was slurried in water at elevated temperature before stepwise addition of 32.11g K_2PtCl_4 and 54.88 g $CoCl_2.6H_2O$ metal salts. The pH was maintained by addition of NaOH facilitating the complete deposition of the metal as described by Equation 1 and Equation 2 (11). The approximate total volume in the reaction flask was 7.4 L. After deposition the catalyst was separated by filtration, washed and dried. The dried catalyst weight was 74.70 g.

$$K_2PtCl_4 + 2NaOH \rightarrow PtO.H_2O + 2NaCl + 2KCl \qquad \textbf{Equation 1}$$

$$CoCl_2 + 2NaOH \rightarrow Co(OH)_2 + 2NaCl \qquad \textbf{Equation 2}$$

The catalyst was then annealed at 600 and 950 °C in 5% H_2/N_2 to form two precursor materials with a nominal composition of 23.6 wt% Pt / 21.4 wt% Co/C (Pt25:Co75 atomic). NB. To prevent combustion, the reduced precursor materials must be carefully exposed to air using an evacuation and air bleed method to achieve controlled passivation. 10 g of each precursor materials were chemically acid leached with 250 ml of 0.5 M H_2SO_4 for 24 hrs in a 3-neck 500 ml flask equipped with a magnetic stirrer, reflux condenser and thermometer. After acid addition the suspension was heated to 80 °C. After 24 hrs at ~80 °C the heating was switched off and the suspension was allowed to cool to ~50 °C. The suspension was filtered using a Buchner funnel and vacuum. The dark pink filtrate was collected and submitted for metal assay and the solid was washed copiously until the washings were pH neutral. The washed material was sucked dry on the filter before transferring to a drying oven and dried overnight at 105 °C in air. The leaching procedure was repeated until the leachate was colourless by visual inspection. The Pt and Co content of the resulting leachate was determined using ICP-MS. The new materials were characterised by assay, CO chemisorption, XRD and TEM and were subsequently electrochemically de-alloyed as described in section 2.2.4.

1.2 Sample preparation

To enable electrochemical characterisation and testing the catalyst powders were made into inks by addition of aqueous ionomer (Nafion®). Typically 125 wt % Nafion® was

added with respect to the wt% carbon in the catalyst. To achieve optimum mixing, inks were processed either by using a Silverson mixer or a Speedy Mixer DAC150 FVZ-K with ceramic processing beads. Depending on the coating technique that was to be employed for fabricating electrodes from the ink, the ink solids were reduced by addition of deionised water. Typically solid fractions of 10% were required for hand painted and spray coated electrodes while inks with a solid content of up to 28% were used for fabricating screen printed electrodes. To enable fuel cell testing the corresponding anode and cathode electrode layers were fabricated into MEAs.

1.2.1 Electrode fabrication

Electrodes were fabricated by hand painting, screen-printing or spray coating an aqueous nafion ink of the catalyst of interest onto a gas diffusion layer (GDL, Toray TGPH-60 carbon paper coated with a microporous carbon layer). The fabrication method used depended on both the electrode area and the required catalyst loading.

Hand painting was used for small areas, < 8 cm^2 and low loadings, typically 0.3-0.5 $mg_{Pt}\,cm^{-2}$. Using a paintbrush the ink was applied evenly to pre-cut carbon fibre paper that was larger than the required test electrode area. A larger area was used as catalyst applied on edges sometimes exhibits poor adhesion and can become uneven in this region. Before addition of the first coat of ink 35% IPA/H_2O was sprayed onto the microporous layer to ensure good wetting. Thin coats of ink were added with drying on a hotplate at 90 °C between each addition. The electrode was rotated before addition of each subsequent layer to ensure an even coating. Addition continued until the desired loading was reached. The metal loading was calculated using Equation 3. The electrodes used in the electrochemical tests were cut from the larger painted areas.

$$\text{Pt loading}\,(g_{Pt}cm^{-2}) = \frac{\text{ink weight (g)} \times \%\ \text{cat. in dried layer} \times \%\ \text{Pt in cat.}}{\text{Electrode area}\,(cm^2)} \qquad \textbf{Equation 3}$$

Screen printing or spray coating were used for fabrication of electrodes with larger areas (up to 500 cm^2). For MEA activity testing typically a loading of 0.2 - 0.4 $mg_{Pt}cm^{-2}$ was used on the anode and cathode. For these relatively low loadings screen printing was used. The catalyst ink is smoothly spread across a mesh screen covering the IPA wetted

gas diffusion layer. The loading can be varied by changing the mesh size used. After application the catalyst layers were allowed to dry in air. The loading was calculated using Equation 3. For some tests catalyst coated membranes (CCM) were used. These were prepared by screen printing onto clean PTFE instead of gas diffusion layer.

For preparing electrodes with either thick catalyst layers (0.24 $mg_{Pd}cm^{-2}$) and / or high loadings > 1.5 $mg_{Pt}cm^{-2}$ enough catalyst can not be physical applied via the screen printing method due mesh size limitations. In this instance spray coating is used. This technique applied the catalyst ink to the gas diffusion layer as a fine spray. The ink is forced though a fine nozzle using compressed air. This can be achieved using a hand held spray gun or more sophisticatedly, using a Johnson Matthey built automatic spraying rig in which the gun position is fixed at a constant height above the GDL. Spray overlap is optimised and the GDL heated from below to allow contact drying. Addition of more layers occurs until the desired loading is reached. Loadings were calculated as previously described. In this instance IPA spraying prior to catalyst coating is not required.

1.2.2 MEA fabrication

MEAs were fabricated by accurately aligning pre-cut anode and cathode electrodes (or PTFE layers in the case of CCM fabrication) on either side of a proton conducting membrane. The resultant assembly was placed between filter paper, PTFE sheets and Titanium pressing plates, as shown in Figure 1, before hot pressing for 2 minutes. The assembly was then cooled to < 60 °C under pressure before removal from the press and allowing cooling to room temperature. The pressing conditions varied depending on the membrane used. Membrane substrate assembles (MSA) for gas humidification in the XAS transmission cell were made by hot pressing Nafion 115 membrane to Toray carbon fibre paper. The typical conditions used for bonding were 150-180 °C and 200-400 psi sample pressure.

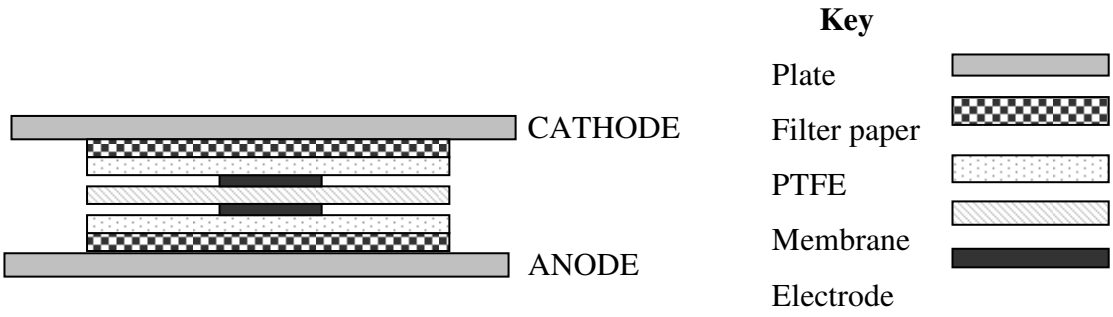

Figure 1. Arrangement of components used during MEA fabrication

2. Electrochemical characterisation and testing

Detailed understanding of the electrocatalysis reactions occurring on catalyst materials is critical to development and commercialisation of fuel cells. Electrochemical techniques are therefore a central component of this work. Both potential sweep and potential stepping and potential hold experiments have been employed to characterise surface processes providing mechanistic insight, to determine active metal areas, and catalytic activity and to study catalyst degradation and stability. Testing has been conducted in both liquid electrolyte and MEA environments.

2.1 Electrochemical testing in liquid electrolyte

Cyclic voltammetry has been used to study fuel cell catalyst materials in liquid electrolyte. Cyclic voltammetry allows the characterisation of redox processes occurring at electrode solution interfaces for both homogeneous and heterogeneous reactions. A three electrode set-up was used comprising of a working electrode (the electrode at which the reaction of interest occurs), a counter electrode (the electrode that undergoes the charge balancing reaction to that occurring on the working electrode), and a reference electrode (used to define zero volts within the system). By convention the absolute potential of 0.0 V is defined by the standard hydrogen electrode (SHE). Equation 4.

Pt (s) H_3O^+ (a =1) H_2 (1013.25 mbar) 298 K **Equation 4**

For practical reasons the reference electrode used in this work for studying reaction in acid environment is a Pd (s) H_2SO_4 (1 M) H_2 at a range of temperatures, (analogous to

the reversible hydrogen electrode RHE where Pt is used instead of Pd). All potentials are reported *vs*. the Pd/H reference electrode (+ 5 mV *vs*. RHE (12)). The electrodes are immersed in a solvent to provide a media for diffusional mass transport of reactants to and products away from the electrode surface. To ensure efficient ion conductivity and low internal resistance (iR) drop a highly conducting supporting electrolyte is required. In this work the solvent system used was water and the supporting electrolyte H_2SO_4 at 1 M concentration. The electrolyte was purged with inert gas, N_2 or Ar, to exclude O_2 before and during voltammetry experiments. The electrodes and electrolyte are contained within a jacketed electrochemical cell designed to minimise resistance (iR drop). Figure 2 shows a schematic representation of the electrochemical cell used in this work. The cell has a low volume of electrolyte (100 ml) to allow detection of dissolved species during testing by electrolyte sampling and measurement by ICP-MS. See section 2.1.2. The working electrode used was made by attaching a clip made from Au wire to catalyst coated carbon fibre paper electrode (section 1.2.1). The catalyst coated side faced up, parallel to the reference and counter electrodes that were each contained inside individual electrolyte filled fritted compartments.

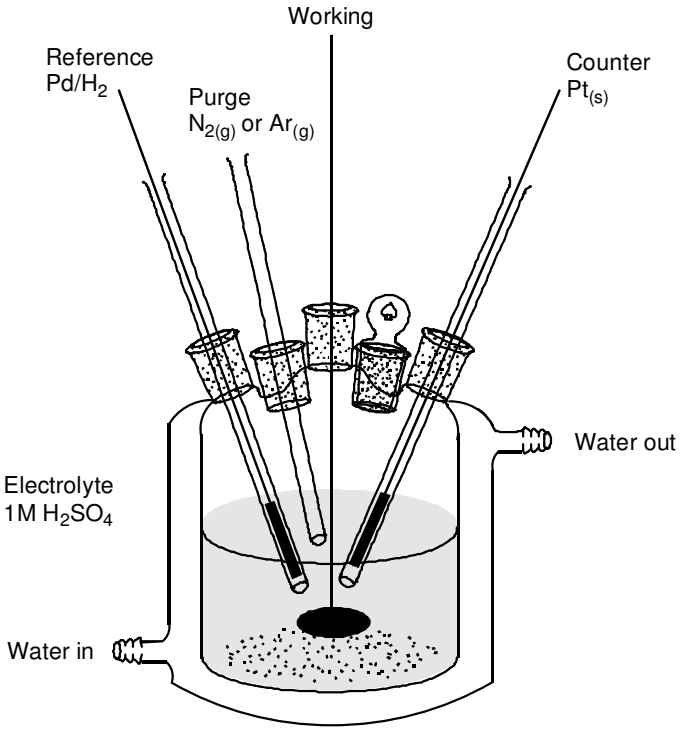

Figure 2. Schematic representation of the electrochemical cell used for testing fuel cell catalysts

The electrodes are connected to a potentiostat to form an electrical circuit. The potentiostat used in this work was an EcoChemie PGSTAT 30 Autolab. The potentiostat controls the experiment, ensuring the current flow through the reference electrode is zero and holds the potential of the working electrode constant with respect to a reference electrode by controlling the current flowing through the counter electrode. If the current between the working and reference electrodes is zero then the iR drop is also zero and the potential of the working electrode versus the reference may be measured.

During cyclic voltammetry experiments the potential of the working electrode is swept linearly between two limits and the current response recorded by the potentiostat. The important variables are the starting potential, the potential limits and the sweep rate.

The current response is characteristic of the oxidative, reductive and capacitive processes occurring at the working electrode solution interface, and is sweep rate dependent. The focus of this work is the study of heterogeneous reactions of fuel cell catalyst materials therefore the following discussion will be limited to the study of absorbed species on electrode surfaces. In this instance the current response is governed by the number of electrons transferred in the reaction and the number and type of active sites on the electrode surface. This is clearly illustrated in the cyclic voltammetry profiles of Pt single crystals where each absorption site (111, 100, step and terrace sites) gives rise to a unique current response both in terms of onset potential and peak shape (13). Peak position is a measure of the adsorption strength. Strongly bound species require higher potentials for removal from the electrode surface. For heterogeneous systems the peak current density is directly proportional to scan rate and the charge required to oxidise an absorbed layer is equal to the area under the redox peak associated with that process. This peak area is independent of scan rate and therefore integration of peak area provides a useful measure of electroactive surface area.

In this work polycrystalline Pt and Pt based catalysts have been studied, all these materials display characteristic features corresponding to the electrochemical processes occurring at the Pt : solution interface. These features are shown in Figure 3 for a polycrystalline Pt/C electrode undergoing a potential sweep from 0.05 V to 1.4 V and back to 0.05 V *vs.* Pd/H in 1M H_2SO_4 supporting electrolyte at 80 °C.

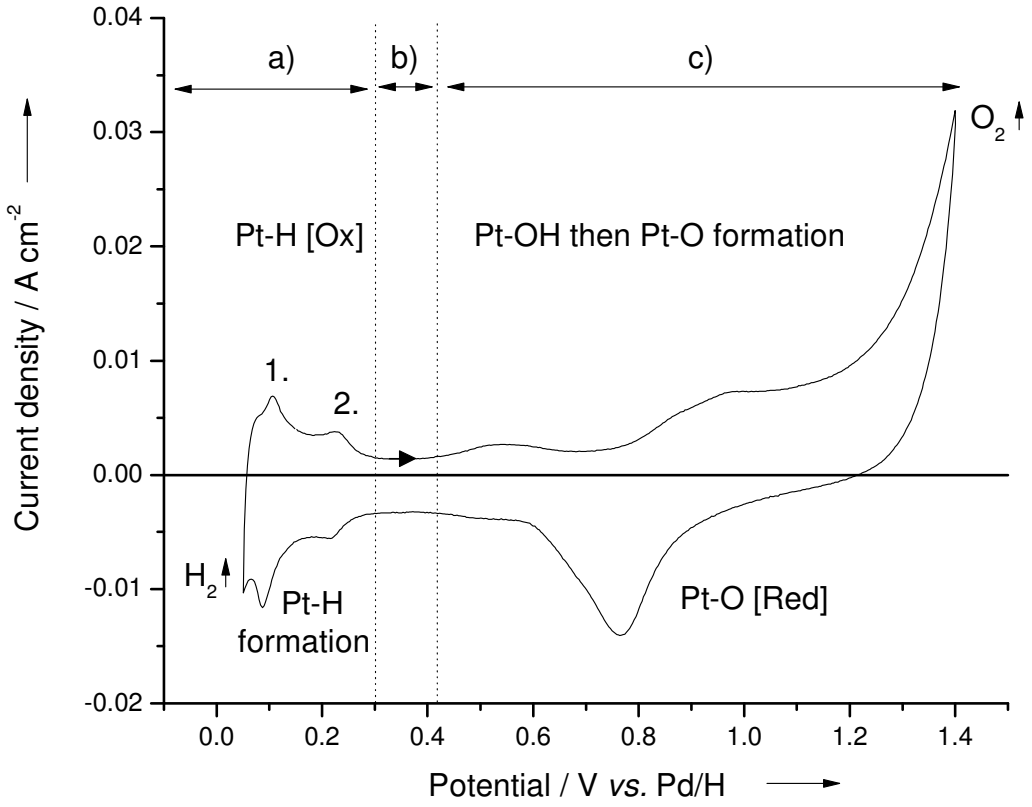

Figure 3. Cyclic voltammogram of a polycrystalline Pt/C electrode at 10 mVs^{-1} in 1 M H_2SO_4 supporting electrolyte at 80 °C

The voltammetry profile may be split into three regions a) the hydrogen region, b) The double layer region and c) the oxide region. The electrochemical processes occurring in each of these regions will now be discussed.

The hydrogen region contains two pairs of peaks. These peaks are assigned to absorption/desorption of hydrogen on the platinum surface described by Equation 5. The shape of the individual cathodic/anodic peaks arises due to progressive vacant site filling/emptying during the adsorption/desorption process until a maximum/minimum is reached and no further current flows (apart from the double layer a charging current). The reversible nature of the adsorption/desorption processes leads to the adsorption and corresponding desorption peak occurring at very similar potentials. Compared to platinum single crystal data the peaks are broader as the voltammetric response corresponds to the superposition of the numerous different adsorption sites on polycrystalline Pt/C. The two pairs of peaks occur at different overpotentials, corresponding to different Pt-H bond energies. Considering the desorption peaks (anodic scan) we observe peak 1 at low overpotentials ~0.10 V *vs.* Pd/H indicating that

the bound hydrogen atom is easily removed. This feature is known as the weakly bound hydrogen. Peak 2, at higher overpotenitals ~ 0.25 V vs. Pd/H, corresponds to strongly bound hydrogen.

$$Pt + H_3O^+ + e^- \rightleftharpoons Pt\text{-}H_{ads} + H_2O \qquad \textbf{Equation 5}$$

For platinum, the adsorption of hydrogen obeys the Langmuir isotherm, consequently the maximum coverage is a monolayer (14). The area under the adsorption peaks, (Charge associated with the peak in the cathodic scan), corrected for the double layer contribution can therefore be used to determine the electrochemical Pt surface area (EPSA in $cm^2_{Pt}\,cm^{-2}_{geo}$). As described in Equation 6.

$$EPSA\ (cm^2_{Pt}\ cm^{-2}_{geo}) = \frac{\text{Charge (C)}}{\text{Charge density (C cm}^{-2}) \times \text{Area(cm}^2)} \qquad \textbf{Equation 6}$$

The measured charge (C) is converted to a surface area using the charge density ($\mu C\ cm^{-2}$) of Pt and normalised by the area of the electrode under test ($cm^2_{geometric}$). The theoretical charge density of a material for a one electron process on a fcc crystal (hkl) face is the product of the number of atoms in one square centimetre of this face and the charge of one electron. The number of atoms per square centimetre $N_{(hkl)}$ depends on the interatomic distance *a* (in cm) which is 2.776×10^{-8} cm for Pt and the crystallographic plane. This leads to three values of charge density for Pt associated with each crystallographic face (111 = 240 $\mu C\ cm^{-2}$, 100 = 208 $\mu C\ cm^{-2}$, 110 = 147 $\mu C\ cm^{-2}$) (15, 16). Due to the polycrystalline nature of the catalyst materials studied, this work uses the commonly reported value of 210 $\mu C\ cm^{-2}$ for the charge density of polycrystalline platinum (17, 18). The EPSA value is converted to an ElectroChemical Surface Area, in $m^2_{Pt}\,g_{Pt}^{-1}$ using Equation 7 to enable direct comparison of different catalyst materials tested with different electrode loadings.

$$ECA\ (m^2_{Pt}\ g^{-1}_{Pt}) = \frac{EPSA\ (cm^2_{Pt}\ cm^{-2}_{geo})}{\text{Loading (mg cm}^{-2}) \times 10} \qquad \textbf{Equation 7}$$

Close to the thermodynamic potential of 0 V hydrogen evolution occurs. Equation 8. This process is facilitated by the adsorption of hydrogen on the Pt surface. The mechanistic steps are described in Equation 9 and Equation 10 (19).

$2H^+ + e^- \rightarrow H_2 \uparrow \qquad E = 0.0\ V$ **Equation 8**

$H^+ + Pt + e^- \rightarrow Pt\text{-}H_{ads}$ **Equation 9**

$2Pt\text{-}H_{ads} \rightarrow 2Pt + H_2 \uparrow$ **Equation 10**

The current response in region b), known as the double layer region, is dominated by the charging current at the electrode/electrolyte interface. In this region, unlike regions a) and c), no Faradaic electron transfer processes occur at the electrode/solution interface. The current response is a consequence of the change in surface charge on the electrode i.e. double layer charging of both the Pt surface and, dominating the response, the carbon support. For a Pt wire the double layer region is found to extend to higher potentials (up to ~0.6 V), however, in the voltammogram of Pt/C shown in Figure 3 a redox feature is observed at ~0.5 V vs. Pd/H. This feature is not present in the voltammetry of a Pt wire and is therefore assigned to redox processes occurring on the carbon support (quinone/hydroquinone redox couple (20)). This feature is observed for all carbon supported catalysts used in this work.

Region c is where platinum oxidation/reduction and oxygen evolution occurs. Unlike the reversible adsorption of hydrogen onto the Pt surface, oxide formation is an irreversible process as shown by the shape of the peaks in the anodic scan and high overpotentials required to remove the Pt oxide in the cathodic scan. This hysteresis suggests that a form of irreversible structural change occurs during the anodic sweep resulting in a more stable surface. The mechanism of oxide formation is still under debate with several mechanistic pathways proposed (21). A general consensus exists where $Pt\text{-}OH_{ads}$ forms at low overpotentials (< 0.8 V *vs*. RHE) followed by Pt-O and PtO_2 formation at higher potentials. At potentials corresponding to a critical surface coverage of oxygen species (~ 1.0 V *vs*. RHE) the formation of subsurface oxygen species occurs and leads to the hysteresis observed. This process, first proposed by Reddy *et al*. in 1968, is known as place exchange (14). A more detailed discussion on

proposed oxide formation and removal mechanisms can be found in chapter 5. In addition to oxide formation the other voltammetric feature in the anodic scan of region c is the steep increase in anodic current at ~1.23 V. This corresponds to the onset of oxygen evolution, where water is oxidised to molecular oxygen. Equation 11.

$2H_2O \rightarrow 4H^+ + 4\,e^- + O_2 \uparrow$ $\quad E^\circ = 1.23$ V **Equation 11**

The adsorption of CO on Pt surfaces has also been used as a means of measuring the electroactive surface area. In the CO oxidation experiment the Pt/C electrode is exposed to CO saturated electrolyte at 0.125 V *vs*. Pd/H. While still under potential control the electrolyte was subsequently saturated with N_2 before 3 x cyclic voltammetry sweeps were performed. Scan 1 starts anodically from 0.125 V to 1.0 V, the sweep is reversed and the cathodic response recorded from 1.0 V to 0.05 V.

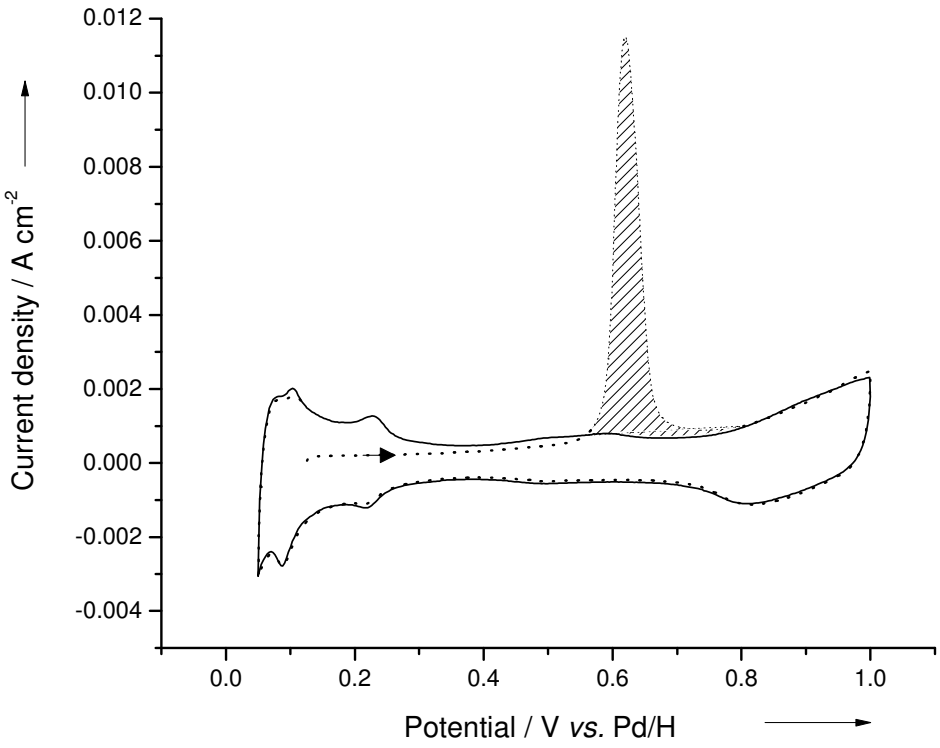

Figure 4. CO Oxidation voltammetry a polycrystalline Pt/C electrode at 10 mV s^{-1} in 1M H_2SO_4 supporting electrolyte at 80 °C. Scan 1 dashed line, solid line scan 2, shaded area corresponds to the oxidation of CO according to Equation 12

Figure 4 shows the cyclic voltammetry profile. CO adsorption on Pt blocks the sites used for Pt-H adsorption and, therefore, no features are observed in the hydrogen region in the first anodic scan. The oxidation feature with onset at ~0.5 V *vs*. Pd/H (shaded area) corresponds to CO oxidation to CO_2 as described in Equation 12. The charge associated with this two electron process can be used to determine the electrochemical surface area as described in Equation 6 and Equation 7. The charge density value used in this instance is doubled from 210 μC cm^{-2} to 420 μC cm^{-2} to account for additional transfer of electrons. At 0.8 V all CO is oxidised from the catalyst surface and therefore the characteristic Pt features previously described are observed in the voltammetry in subsequent scans.

$$Pt\text{-}CO + H_2O \rightarrow Pt + CO_2 + 2H^+ + 2\,e^- \qquad \textbf{Equation 12}$$

2.1.1 Working electrode sample preparation

Before testing, the large area catalyst coated electrodes (see section 1.2.1) were cut into circular 1.0 cm^2 or 3.14 cm^2 buttons, heat treated at 177 °C in air and fully flooded. Initially wetting of the electrodes was conducted by boiling in acidified deionised water, however, significant leaching was found to occur for base metals such as Co. To minimise leaching subsequent testing used a vacuum filling technique to ensure the electrode was fully wetted before testing. The electrode was placed in a beaker of deionised water and prevented from floating. The beaker was then transferred to a Struers Epovac to allow evacuation. Evacuation of the beaker to 200 mbar caused air trapped within the electrode to be replaced by water, fully flooding the electrode without the need to use an acidic environment. It will be made clear in each chapter where wetting was achieved by acid boiling or vacuum filling.

2.1.2 Stability testing procedure

The stability of the catalyst to repeated potential cycling in 1M H_2SO_4 between either 0.6 - 1.0 V or 0.6 - 1.2 V *vs.* Pd/H at 50 mVs^{-1} was investigated by periodic ECA measurement and electrolyte sampling. 5 ml of electrolyte was removed after 0, 50, 150, 250, 500, 750 & 1000 cycles and analysed for Pt and Co content by ICP-MS analysis. The total electrolyte volume was kept constant by replenishment with fresh electrolyte.

Experiments reported in Chapter 3 were run in duplicate on each catalyst with the same trends in changes in voltammetry, ECA loss and metal loss observed for each repeat. No repeat measurements were performed on the catalyst studied in Chapter 6.

2.1.3 Window opening procedure

A potential window opening test was conducted to investigate the ability of the catalyst to grow and remove oxide at 80 °C. A cyclic voltammogram was run between 0.01-0.6 V *vs*. Pd/H at 10 mV s^{-1}, then repeated with 0.1 V incremental increases in upper potential limit up to 1.4 V. This experiment was also conducted after the 0.6-1.2 V cycling experiment to investigate the effect of cycling on the catalyst. Repeat testing was not conducted.

2.2 Electrochemical testing in MEAs

In addition to the electrochemical testing in liquid electrolyte the fuel cell catalyst materials have also been characterised within the MEA environment under fuel cell operating conditions. The catalytic activity of the oxygen reduction reaction has been measured for 49 cm^2 active area MEAs using Johnson Matthey single cell test stands and at synchrotron sources with simultaneous collection of X-ray absorption data in a specially designed fuel cell with 12.56 cm^2 active area MEAs. A detailed discussion on the cell design can be found in chapter 4. Catalyst stability has also been investigated within the MEA environment and an electrochemical de-alloying cycling protocol used to activate Co rich catalysts *in situ*.

2.2.1 Oxygen reduction reaction activity measurement

Measurement of catalytic activity for the oxygen reduction reaction was conducted to evaluate catalyst materials with respect to commercial targets by determining the difference in the thermodynamic cell voltage (~1.23 V) and the measured cell voltage (oxygen polarisation). In this work oxygen polarization measurements have been conducted both potentiostatically (A potential is applied to the electrode and the current measured after a fixed time period) and galvanostatically (A current is applied and the potential is measured after a fixed time period) depending on the test equipment used. In

this work deviation from the theoretical cell voltage as a consequence of activation losses on the cathode is of particular interest.

To determine the cathode activation losses from the measured cell performance and allow direct comparison between catalyst materials the other losses within the system, such as anode activation, resistance and mass transport losses, must be accounted and compensated for (22). This is achieved by use of appropriate anode catalyst materials and, test conditions and making suitable measurements to quantify the losses.

When Pt/C is used as the hydrogen oxidation catalyst for anode electrodes the kinetics of hydrogen electrooxidation are very facile. Due to these rapid kinetics Gasteiger *et al*. report that Pt loadings as low as 0.05 mg Pt cm^{-2} on the anode may be used without the need to compensate the measured cell performance for contributions from anode polarisation (23). The loss associated with the oxidation current generated by fuel crossover via diffusion through the membrane (hydrogen crossover) can be compensated for by addition of the current measured when the N_2 purged cathode compartment at 0.5 V with respect to the H_2 purged anode compartment to the cell current density to give J_{corr} / mA cm^{-2}.

Ohmic losses associated with the conductivity of protons through the membrane and electronic contact resistances between plate and MEA components (iR drop) may be determined by using the potentiostat to perform current interrupt measurements. The current at a given cell voltage is briefly (1 ms) switched off and the potential monitored during the relaxation to OCV. A characteristic response is observed, a sharp increase in voltage occurs at short times corresponding to removal of the ohmic contribution V_r followed by a slower decay corresponding to the capacitive component of the circuit V_a. During the polarisation tests the current interrupt measurement is performed for each applied voltage value and V_r is measured, knowing the current at the applied cell potential and the cell active area, a resistance value in Ohm cm^2 is determined. This value is then used to correct the applied voltage at each current density for resistance within the cell.

Mass transport losses corresponding to the access of reactant to and products away from catalyst active sites are only significant at high current densities so may be neglected

when using pure oxygen and conducting experiments in the kinetic region as done in this work. After correction of all the losses described this leaves the corrected cell performance giving a measure of the activation loss for the oxygen reduction reaction on the cathode. To allow direct comparison between different MEA samples typically the performance values are correct for the mass of platinum on the electrode to give a mass activity (A mg_{Pt}^{-1}) or by correction of catalyst ECA to give a specific activity (A cm_{Pt}^{-2}).

2.2.2 49 cm^2 single cell testing procedure

Measurement of catalytic activity for the oxygen reduction reaction was conducted on cathode catalysts in 49 cm^2 active area MEAs. MEAs were fabricated with cathode and anode loadings of 0.2-0.4 mg_{Pt} cm^{-2} and Flemion® SH-30 membrane as described in section 1.2.2. Single cell testing was performed in 50 cm^2 hardware at 100% RH using external contact humidifiers. After initial safety tests, to ensure the integrity of the fuel cell assembly to gas leaks, samples were conditioned in the single cell for at least 8 hrs on H_2/Air at 80 °C, 150 kPa_{abs} and ≥ 0.5 Acm^{-2}. Oxygen polarization measurements were conducted galvanostatically using a 15 minute hold equilibration time after each incremental current increase from 0.05 to 1.5 A cm^{-2}. Temperature and pressures were 80 °C and 150 kPa_{abs} and gas stoichiometries were 2:10 H_2:O_2 for oxygen polarization. In addition oxygen polarizations were also conducted at 270 kPa_{abs} from 1.5 to 0.05 A cm^{-2} with a 3 minute equilibration time. Membrane resistance was measured at each current density using the current interrupt technique, and measured currents were corrected for H_2 crossover, measured *in situ* for each MEA at 270 kPa_{abs}. Specific activity at 900 mV at the different pressures was also determined by correcting for cathode Pt surface area measured *in situ* based on CO oxidation voltammetry. CO area was measured at 80 °C in the MEA by poisoning the cathode with CO at 0.15 V (*vs.* anode), purging with N_2 at 0.15 V, then cycling from 0.15 to 1.0 V and integrating the area of the CO peak, using a correction factor of 420 μC cm^{-2}. Typically experiments were run in duplicate on each catalyst. An error of ± 5 mV determined from multiple measurements on standard samples is typical, therefore differences in performance of > 5 mV should be considered significant.

2.2.3 Electrochemical de-alloying

An electrochemical dealloying process similar to that described by Strasser *et al*. (4-10) was used on the $PtCo_3$ catalysts. A 49 cm^2 catalyst coated membrane (CCM) was fabricated and loaded into the test cell. The beginning of life performance was measured at 270 kPa_{abs} before the cathode was electrochemically cycled from 0.5-1.0 V at 100 mV s^{-1} 1000 times. The CCM was then removed from the cell and place in 1 M H_2SO_4 overnight. The CCM was then washing by boiling in 1 M H_2SO_4 for 3 hrs in an attempted to remove dissolved Co from the membrane. The CCM was then allowed to cool in the acid overnight before removing from the acid and rinsing in 2 x ~250 ml of deionised water. The washings were combined and the Co and Pt content measured by ICP-MS. The washed MEA was then refabricated before de-alloyed performance testing was conducted at 270 kPa_{abs}. In addition to the four PtCo catalysts a Pt standard catalyst was also tested for comparative purposes and a PtCo catalyst was also tested without the cycling step to ascertain whether the de-alloying procedure is required for performance enhancement. In all cases no duplicate measurements were conducted. Results are discussed in chapter 6.

2.2.4 12.56 cm^2 transmission XAS cell testing

In this work a fuel cell to enable time resolved *operando* XAS studies of cathode catalysts has been designed to allow catalyst structure to be probed during operation. The cell design is discussed in Chapter 4. Here the MEA testing procedure is reported. Measurement of catalytic activity for the oxygen reduction reaction and potential step and potential hold experiments to study catalyst structure under operating conditions and oxide growth and removal were conducted on cathode catalysts in 12.56 cm^2 active area MEAs. In evaluating the new cell design catalyst loadings of 0.4 mg_{Pt} cm^{-2} were used. For the *operando* XAS experiments loadings of 2.0 mg_{Pt} cm^{-2} or higher were used at the cathode to give sufficient absorbance for transmission EXAFS of sufficient signal to noise (24). To provide an X-ray transparent anode, 10% Pd/C at 0.24 mg_{Pd} cm^{-2}, was used. MEAs were fabricated by positioning two centimetre diameter circular anode and cathode electrodes on either side of a Nafion 115 membrane and hot pressing according to the procedure described in section 1.1.2. MEAs of the catalyst of interest were loaded into the cell and the cell was connected to a gas control box and water bath. The integrity of the cell to gas and water leaks was determined. The cell was heated to 65 °C

and incoming gases humidified by MSAs and use of a circulating waterbath at 80 °C set point. H_2 at 140 or 60 ml min^{-1} and N_2 or O_2 or air at 60 ml min^{-1} was flowed to the anode and cathode respectively. At 0.5 A cm^{-2} with H_2 and O_2, the flows correspond to stoichiometry 3.2 and 2.7 respectively. The gas was supplied to the cell and the cell pressure was maintained at 10 psi for activity testing. The cell potential was controlled using a PGSTAT 30 Autolab with 10/20 A Booster. For activity measurement the MEA was conditioned potentiostatically by cycling the cathode ten times to and from 0.95 V to 0.6 V with a 0.05 V increment and 5 s stabilisation at each potential. The cell was then held at 0.6 V for 150 s before oxygen polarisation curves were measured potentiostatically from 0.95 V to 0.6 V and back to 0.95 V with a 0.025 V increment and 30 s stabilisation time. The iR resistance was determined from current interrupt measurements. During cell validation duplicate MEAs were tested of each catalyst type, a typical error of ± 5 mV was observed between samples.

In addition to activity measurement, potential stepping and potential holding experiments have been conducted under N_2 (half cell) and O_2 (fuel cell) atmospheres with simultaneous collection of X-ray absorption spectra to investigate the effect of applied potential on catalyst structure. Chapters 4 and 5. The voltage time profile of a combined potential stepping and holding experiment where the potential is stepped from 1.25 V to 1.0 V and back to 1.25 V after a potential hold at 1.0 V for 10 s is show in Figure 5. During the potential steps the voltage of the working electrode is rapidly, (ideally instantaneously), changed. The current response is recorded with time (chronoamperometry). The current corresponds to both the double layer charging and also the electrochemical Faradic processes occurring at the electrode electrolyte interface. N_2 potential step experiments were conducted from 0.125 V to a range of upper potential limits and back to 0.125 V at 35 and 65°C before exposure of the cathode to oxygen. O_2 potential stepping experiments were conducted after MEA conditioning (previously described) from OCV to at range of applied potentials from 0.9 to 0.6 V and back to OCV. Typically duplicate measurements for each potential step experiment were made on individual MEAs and as beamtime allocation allowed repeat measurements were made on MEAs of the same catalyst. The gas flows, cell pressures and hold duration times varied. The exact experimental conditions used will be made clear within individual results chapters.

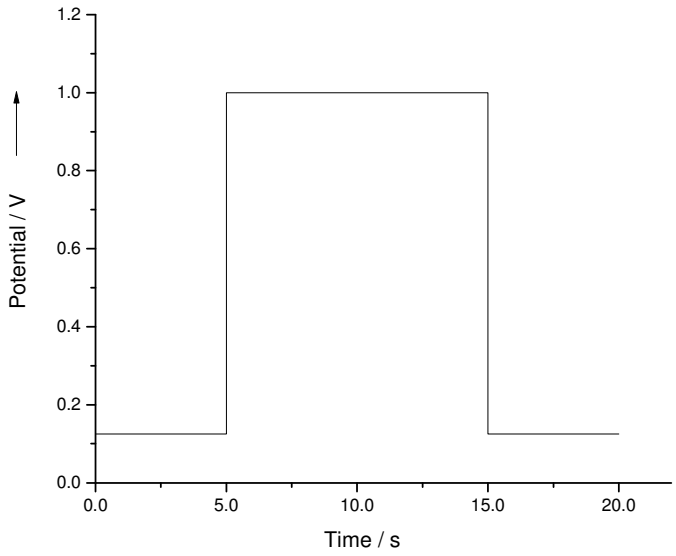

Figure 5. Potential time profile of a potentiostatic stepping experiment from 0.125 V to 1.0 V and back to 0.125 V

3. X-Ray Absorption Spectroscopy

X-ray absorption spectroscopy (XAS) has been shown to be a powerful technique for providing electronic and structural information. The oxidation state, orbital occupancy and local coordination (numbers and identity of neighbours) of the absorbing atom may be determined by analysis of both the X-ray Absorption Near Edge Structure (XANES) and Extended X-ray Absorption Fine structure (EXAFS) (25). For these reasons XAS has been increasingly applied to the study of fuel cell catalysts. (24, 26-37). The theoretical basis of X-ray absorption spectroscopy, including data processing and the experimental methods will be discussed.

3.1 Theory

XAS provides element specific information about the local environment of an atom by excitation of core electrons within the atom by X-ray radiation, typically from a synchrotron source. X-ray interaction with a sample results in the intensity of the transmitted photons I_t being altered compared to the intensity of the incident photons I_0 according the Beer Lambert equation, Equation 13, where x is the sample thickness and μ, the X-ray absorption coefficient.

$\mu x = \log(I_0/I_t)$ **Equation 13**

Figure 6 shows a typical XAS spectrum through an absorption edge. The observed absorption, μx, above the pre-edge region is a consequence of sample irradiation by photons with energies corresponding to quantised transitions from core levels (s, p) to vacant states of appropriate symmetry (according to Fermi's golden rule) and, at energies approximately 50 eV higher than the absorption edge, electron ejection from core levels into the continuum via the photoelectric effect. The structure observed within the spectra corresponds to electron transitions within the atom (XANES) and the superposition of the interference patterns of outgoing photoelectrons (viewed as spherical waves) and the electron density surrounding the absorbing atom (EXAFS). The EXAFS region can extend up to 1000 eV past the edge. The spectrum is therefore representative of the local electronic environment of, and surrounding the absorbing atom.

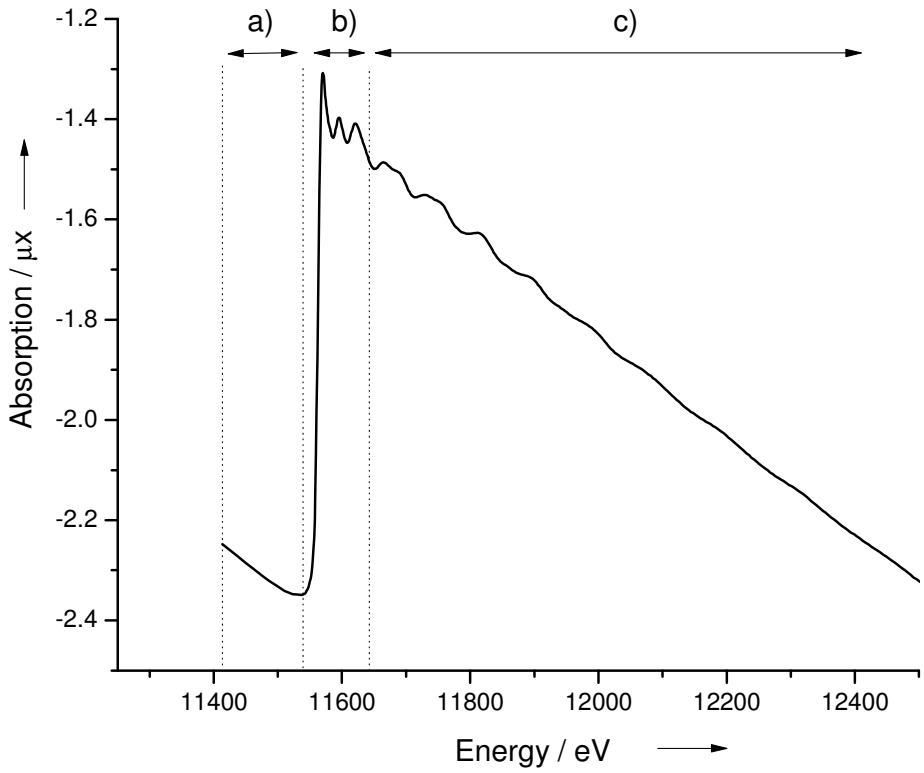

Figure 6. XAS Spectrum of Pt/C in H_2 atmosphere at the Pt L_{III} edge showing: a) pre-edge region, b) edge and XANES region, c) EXAFS region

In this work XAS at the Pt L_{III} edge and Co K edge absorption edges has been used to study catalysts containing Pt and Co. The Co K adsorption edge (at 7.709 keV) arises from transitions from the $1s_{1/2}$ core states. The Pt L_{III} adsorption edge (at 11.564 keV), shown in Figure 6, arises from transitions from the $2p_{3/2}$ core states. A characteristic feature of the Pt L_{III} adsorption edge spectrum is the enhanced X-ray adsorption or "white line". This features arises as a consequence of the symmetry allowed transitions ($\Delta J = 0 \pm 1$) into vacant 5d states that have J = 5/2 character (38). Lytle *et al*. have shown that the intensity of the peak at the L_{III} absorption edge is proportional to the d-electron vacancies (39, 40), while Mansour *et al*. (38) have demonstrated a quantitative method for determining the number of unoccupied d-electron states in Pt from both L_{II} and L_{III} X-ray absorption edge spectra. Such information on the electronic configuration of atoms can provided insight into the bonding interactions during catalytic reactions.

Interpretation of the EXAFS region of the X-ray absorption spectrum gives structural information about atoms of type *j*, such as the coordination number, N_j, and the distance, R_j, from the absorber atom. This information is extracted from the data by fitting the EXAFS function $\chi(k)$, Equation 14, to the EXAFS equation, Equation 15.

$$\chi(k) = \frac{\mu - \mu_0}{\mu_0} \qquad \textbf{Equation 14}$$

$$\chi(k) = \sum_{j=1}^{shells} A_j(k) \sin \delta_j(k) \qquad \textbf{Equation 15}$$

with the amplitude function

$$A_j(k) = \frac{N_j}{kR_j^2} S_0^2 F_j(k) e^{-2k^2\sigma j^2} e^{-2Rj/\lambda(k)} \qquad \textbf{Equation 16}$$

and the phase function

$$\sin \delta(k) = \sin(2kR_j + \varphi_j(k)) \qquad \textbf{Equation 17}$$

Where μ_0 is the smoothly varying portion of μ past the edge and corresponds to the absorption coefficient of a free atom, $F_j(k)$ is the magnitude of the backscattering from atom j, $\delta_j(k)$ is the backscattering phase shift resulting from scattering off atom j, S_0 is the amplitude reduction factor and reflects multielectron effects and central atom shake-up and shake-off due to the relaxation process after photoionization, $e^{-2k^2\sigma j^2}$ accounts for the finite lifetime of the excited state, σ_j^2 is the relative mean squared disorder along the distance between the absorbing atom and atom j due to thermal and static motions, and λ is the mean free path of the electron.

Equation 15 is derived by considering interaction of the outgoing photoelectron wave, with wave vector k, with the electron density of neighboring atoms. Interactions produce backscattered waves that may interfere either constructively or destructively with the outgoing wave. The final state wavefunction is a superposition of all the outgoing and backscattered waves from each co-ordination shell j. This gives rise to the oscillations observed above the absorption edge. The oscillations are unique to the absorber environment since the number and type of neighbour atoms and their distance from the absorber atom will modulate both the amplitude (Equation 16) and phase (Equation 17) of the final state wavefunction.

To allow fitting to Equation 15 the following general procedure is used. Firstly the raw data must be converted to an energy scale in eV from a position of the monochromator in mdeg. At this stage several spectra may be combined to improve signal to noise. Next the data is subjected to determination of the zero point of the energy E_0, normalization and background subtraction. The zero point of the energy scale is set to be the point of inflection in the absorption edge. This allows the energy of the incident photon, E_{hv}, to be converted to k-space ($Å^{-1}$) as described in Equation 18:

$$k = \left(\frac{2m_e}{\hbar} (E_{hv} - E_0) \right)^{1/2} \qquad \textbf{Equation 18}$$

Background subtraction removes both the variation in the absorbance with energy caused by the other atoms in the sample and the smooth variation in μ_0 past the absorption edge. The data is then normalized, placing the measured spectra on a per absorber atom basis.

The oscillatory EXAFS component is then isolated. The EXAFS $\chi(k)$ data may then be fitted to the EXAFS equation (Equation 15) using fitting software such as EXCURV98, a least squares fitting programme based on curved-wave theory, using a Z + 1 2p core hole approximation (41).

In this work 3 different types of XAS experiments have been conducted at two different synchrotron sources leading to differing requirements for data manipulation. The experiments and the data fitting methods employed will now be described along with an example of how the data was processed for a Pt/C catalyst.

3.2 XAS measurements on MEAs

XAS measurements were made on MEAs using a specially design XAS fuel cell to enable *operando* measurements. (Chapter 4) All measurements were made in transmission mode as the MEA underwent potential steps in different gas atmospheres (section 2.2.5). XAS data was collected on two different timescales and therefore required two different optical modes. Conventional point-by-point scanning of the energy range by a Si (111) single crystal monochromator on station 9.3 at the SRS Daresbury laboratory, Warrington, England, allowed XAS scans to be collected with a 10 s scan duration followed by a 2 s delay to allow the position of the monochromator to change before the next scan commenced. For data collection at faster timescales Energy Dispersive EXAFS (EDE) was used. In this technique a 'bent' monochromator is used to instantaneously illuminate the sample with a focussed X-ray beam containing the desired spread of energies. Data acquisition on the milli second time scale is therefore possible (42, 43). EDE experiments were conducted on beamline ID24 at the ESRF, Grenoble, France. To achieve synchronisation potentiostat triggering was used to commence the XAS data acquisition. The optical set-up allowed collection of a XAS spectrum every 6.6 ms, 15 spectra were summed to give a data set every 0.1 s.

Data collected at the SRS was analysed according the following procedure. The experimentally measured XAS data were analysed using the Daresbury suite of analysis programs after energy calibration using the 1st maximum of the derivative of the corresponding Pt foil internal standard spectra. The corrected absorption spectra for XANES analysis were processed using EXBROOK. The zero point of the energy scale

was taken to be the point of inflection in the absorption edge. The pre-edge region was fitted by a straight line and extrapolated to zero energy. A polynomial spline was fitted to the non-oscillatory component of the post-edge region and was extrapolated back to zero energy. The difference between the extrapolated values was taken to be the step height and the spectrum was normalised to this value. For EXAFS analysis EXSPLINE was used to remove the background from the corrected data to ensure reproducible removal for all spectra. The EXAFS components, $\chi(k)$, were then isolated from the absorption spectra and subsequently analysed using EXCURV98.

The energy calibration of EDE collected at the ESRF was conducted using the XOP 2.3 software (44) by reference with Pt foil data collected both during the EDE experiments and during scanning experiments at the SRS Daresbury UK. Data handling and cropping was completed using the xmult software (45) developed by Norman Binstead. No background subtraction was applied to the data.

3.3 XAS measurements on catalyst powder and electrodes

XAS measurements were performed on both catalyst powders, in pellet form by mixture with boronitride, and on electrode samples of new catalyst materials and catalysts that had undergone electrochemical cycling. The samples were mounted in a gas treatment cell, that was a simplified version of a design that previously been described (25, 27, 46) enabling operation at only ambient temperature. The cell design enabled data collection in both transmission and fluorescence mode and in a hydrogen atmosphere. Typically three scans of 5 minute duration were recorded for each sample, however, depending the sample concentration and data quality more scans were run as required. Measurement in a hydrogen atmosphere required the pre-loaded sample to be exposed to flowing hydrogen for at least 30 minutes at atmospheric pressure before the cell was sealed for data collection.

The XAS data were collected at the SRS Daresbury laboratory, Warrington, England using station 9.3. In addition, data collection of some samples discussed in this thesis was conducted by other members of the research group on stations 7.1 (Co K edge), 16.5 (Pt L_{III} edge). The XAS data were analysed using the Daresbury suite of analysis programmes: EXCALIB for energy calibration and scan summation, EXBROOK for E_0

determination, normalisation and background subtraction and EXCURV98 for EXAFS fitting.

3.4 Example of data processing for Pt/C

The method of data processing to allow determination of E_0, normalization and background subtraction using EXBROOK will now be demonstrated for an example spectrum of Pt/C. This method was used during analysis of catalyst powders and electrodes. Figure 7 shows the energy calibrated output file from EXCALIB for a Pt/C catalyst, initialized in EXBROOK. The zero point of the energy scale is set to be the point of inflection in the absorption edge (taken from the maximum in the first derivative), as shown in Figure 8.

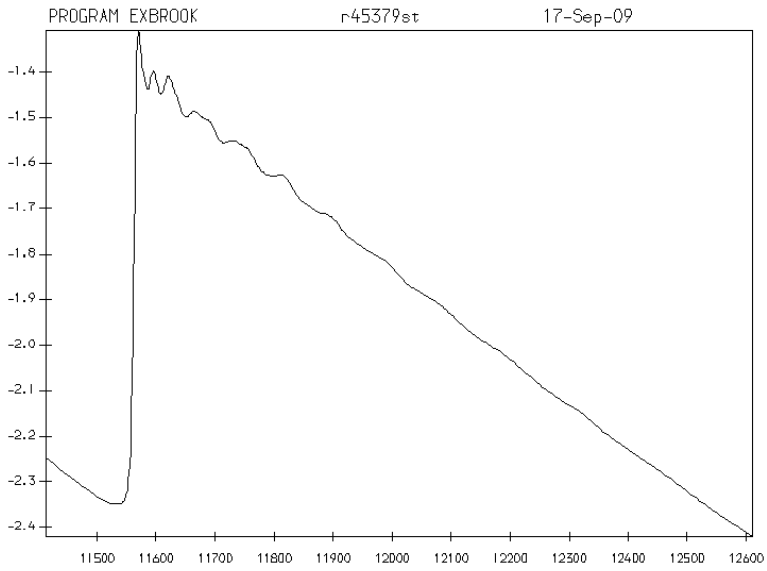

Figure 7. Energy calibrated output file from EXCALIB for a Pt/C catalyst

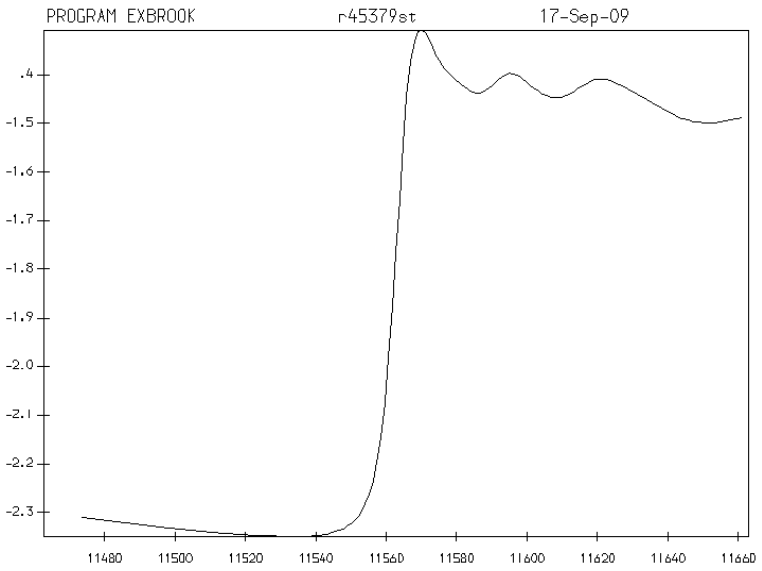

Figure 8. ***E_0*** **determination**

Next, the pre-edge region is fitted to a quadratic equation and subtracted from the data as shown in Figure 9. Figure 10 shows the XANES plotting. In this step the XANES region (from 50 eV before to 100 eV after the edge) is plotted with the spectrum normalised to give an edge jump of 1.

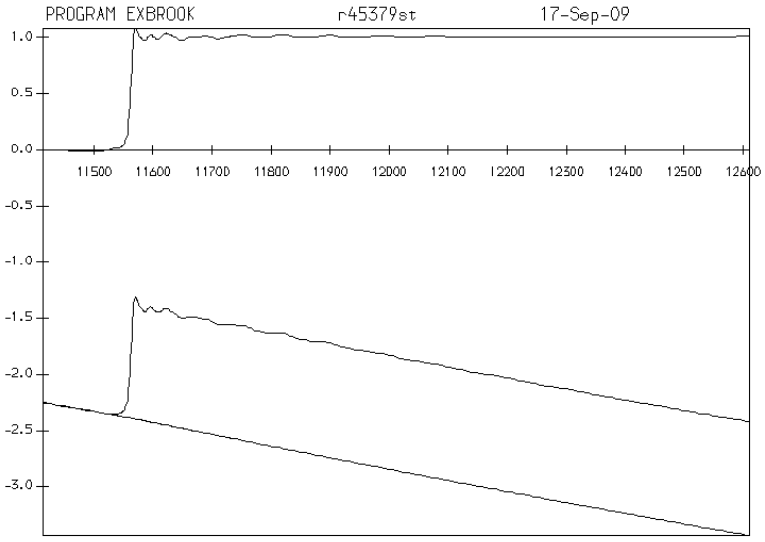

Figure 9. **Fitting and subtraction of pre-edge region**

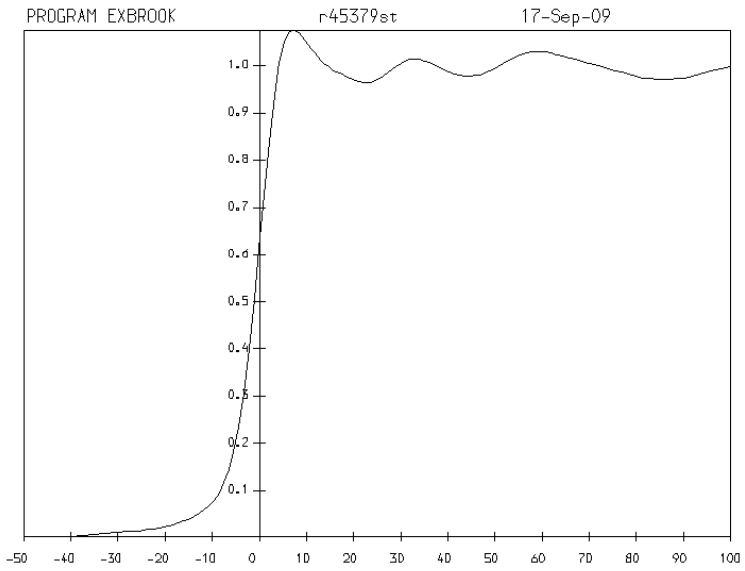

Figure 10. XANES plotting and normalisation

To allow background removal, the EXAFS region > 40 eV past the adsorption edge is isolated then the background removal is optimized such that a smooth post-edge background is applied to the pre-edge subtracted spectrum. The post-edge background spectrum should be a smooth line such that the EXAFS oscillations are not removed. In addition the corresponding Chi plot (EXAFS in *k*-space) should show equal amplitude above and below the x-axis and the Fourier transform of the EXAFS should be optimised such that the peak height below 2 Å is minimised and the 1st peak > 2 Å is maximised. The optimum post-edge fitting for the Pt/C catalyst is shown in Figure 11 Following background removal the data may be fitted using EXCURV. Using EXCURV, coordination shells are added sequentially to build a structural model, the coordination numbers, distances, Debye-Waller factors are automatically refined by the software. The software then generates values and errors of fitted parameters, Chi and FT plots and also provides an indication of fit quality (R_{EXAFS}). If shell addition resulted in an error larger than the parameter or addition of additional shells did not significantly improve R_{EXAFS} (> 2 unit improvement) the shell was removed from the fitting model. R_{EXAFS} values and fitting errors for each parameter are reported in individual chapters.

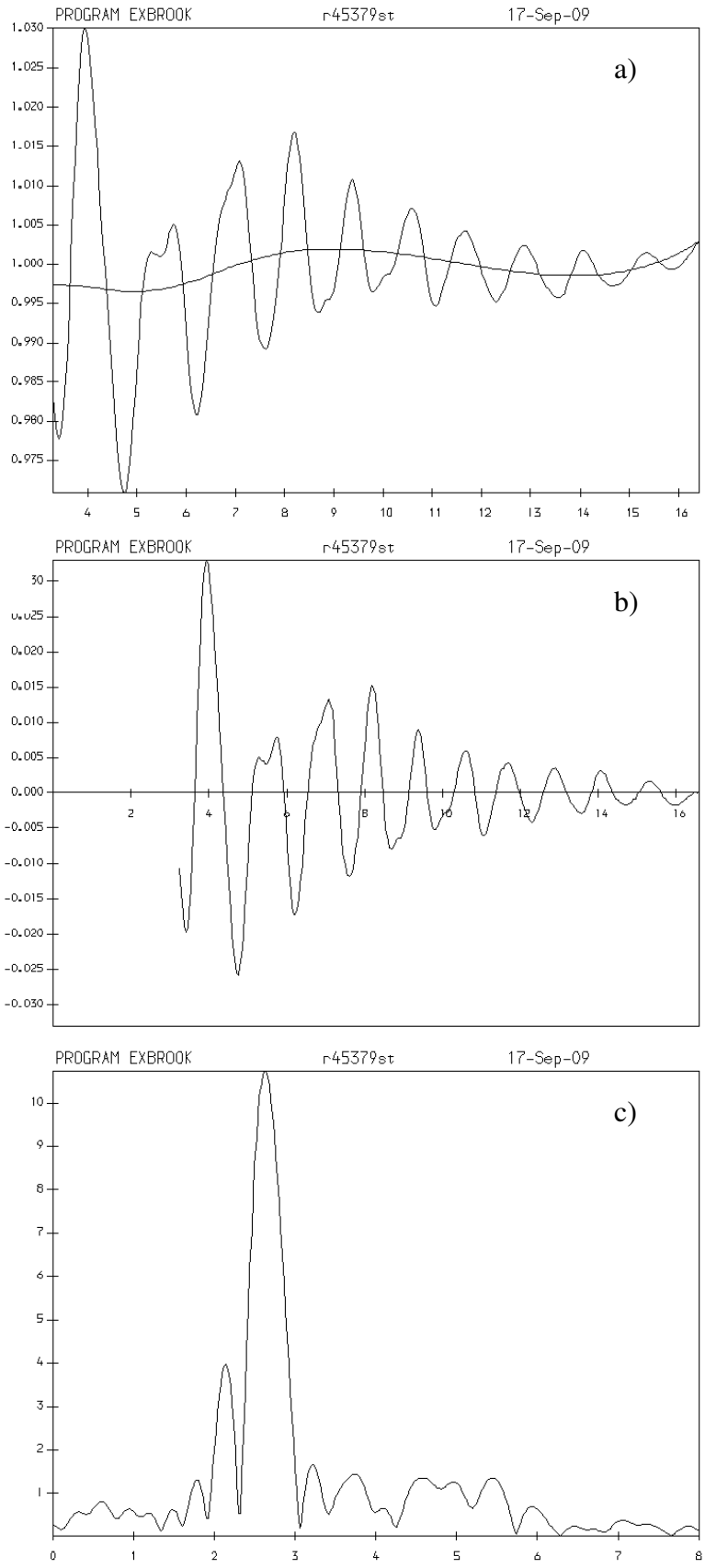

Figure 11. Optimised post-edge background removal of the pre-edge subtracted spectrum a) and corresponding Chi b) and FT plots c)

4. Characterisation of catalyst materials

In addition to electrochemical methods and XAS the following techniques have been used to characterise the catalyst materials used in this study. With the exception of CO chemisorption, scientists in the Johnson Matthey analytical department performed the measurements.

4.1 XRD

The XRD uses Bragg diffraction to determine the crystal lattice parameters of a specimen. In a collimated X-ray beam a crystalline material gives rise to reflections at specific angles depending on the geometry and spacing of the lattice. The pattern of peaks obtained can be matched against a library of standards to determine the phases present. Alloying can be detected by shifting of peaks from the position of the pure material and crystallite size can be determined from the peak broadening**.** In this work XRD analysis with a BrukerAXS D-500 Diffractometer was used to determine the phases present in the catalyst and the crystallite sizes of these materials.

4.2 Transmission Electron Microscopy (TEM) and Electron Probe Micro Analysis (EPMA)

Transmission Electron Microscopy (TEM) is a high magnification imaging technique allowing the observation of features of nearly atomic size. An electron beam is directed through a thin specimen and the image is focused and magnified by a series of electron lenses. Both bright and dark field optical arrangements can be used to optimise the contrast in the image. Elemental analysis of the sample is achieved using an energy-dispersive X-ray (EDAX) detector. In addition particle size analysis can be performed. In this work samples were studied using a Tecnai F20 Transmission Electron Microscope. TEM analysis was performed on powder samples, electrode samples pre and post electrochemical cycling and MEAs. The sample preparation for electrode samples required the catalyst to be scraped off the electrode to give a powder. The powder was then deposited onto a holey carbon film supported by a copper grid. Catalyst powders were also deposited onto a holey carbon film supported by a copper grid before analysis. The sample preparation for MEAs required incasing the MEA in resin and microtone slicing to produce a cross section. In addition to TEM, Electron

Probe Micro Analysis (EPMA) studies were also conducted on MEAs using a Cameca SX51N Electron Probe Micro Analyser. This technique, like EDAX, uses X-ray fluorescence to determine the elemental compositions within the sample.

4.3 Inductively Coupled Plasma - Mass Spectrometry ICP-MS

ICP-MS combines the use of an argon plasma and quadropole mass spectrometer to allow the identification and concentration of elements in samples to be determined. ICP-MS was used to quantify the amount of platinum and base metal leaching occurring during chemical leaching and the electrochemical testing. Samples were analysed using a Perkin Elmer Elan 6100DRC ICP-MS using ppb level Pt and Co standards matrix matched to the ten times diluted electrolyte samples.

4.4 CO Chemisorption

The metal surface area of the catalysts were measured by CO chemisorption assuming a one to one binding ratio of CO to Pt and that no adsorption of CO onto Co occurs. Samples were reduced in 100% H_2 at 50°C for 30 minutes prior to measurement. CO was added to the sample, and the volumetric uptake of CO was measured and converted to a metal area.

References

1. J. S. Buchanan, R. J. Potter and T. R. Ralph, in, Johnson Matthey Public Limited Company, London, England, US Patent 5,759,944 (1998).
2. J. S. Buchanan, G. A. Hards and S. J. Cooper, in, Johnson Matthey Public Limited Company, London, England, GB Patent 2,242,203 (1991).
3. L. Keck, J. Buchanan and G. A. Hards, in, Johnson Matthey Public Limited Company, London, England, US Patent 5,068,161 (1991).
4. P. Mani, R. Srivastava and P. Strasser, *Journal of Physical Chemistry C*, **112**, 2770 (2008).
5. P. Strasser, *Advanced Materials & Processes*, **166**, 13 (2008).
6. P. Mani, R. Srivastava, C. Yu and P. Strasser, *ECS Transactions*, **11**, 933 (2007).
7. P. Strasser, S. Koh and C. Yu, *ECS Transactions*, **11**, 167 (2007).
8. S. Koh and P. Strasser, *Journal of the American Chemical Society*, **129**, 12624 (2007).
9. S. Koh, N. Hahn, C. F. Yu and P. Strasser, *Journal of the Electrochemical Society*, **155**, B1281 (2008).

10. Z. C. Liu, S. Koh, C. F. Yu and P. Strasser, *Journal of the Electrochemical Society*, **154**, B1192 (2007).
11. F. A. Cotton and G. Wilkinson, *Advanced Inorganic Chemistry 5th Edition*, Wiley-Interscience (1998).
12. M. J. Vasile and C. G. Enke, *Journal of the Electrochemical Society*, **112**, 865 (1965).
13. G. A. Attard, A. Ahmadi, D. J. Jenkins, O. A. Hazzazi, P. B. Wells, K. G. Griffin, P. Johnston and J. E. Gillies, *Chemphyschem*, **4**, 123 (2003).
14. P. A. Christensen and Hamnett, *Techniques and Mechanisms in Electrochemistry*, Chapman and Hall (1994).
15. F. G. Will, *Journal of The Electrochemical Society*, **112**, 451 (1965).
16. M. W. Breiter, *Electrochemical Processes in Fuel Cells*, Springer, Berlin (1969).
17. J. Shim, D. Y. Yoo and J. S. Lee, *Electrochimica Acta*, **45**, 1943 (2000).
18. S. Chen, W. C. Sheng, N. Yabuuchi, P. J. Ferreira, L. F. Allard and Y. Shao-Horn, *Journal of Physical Chemistry C*, **113**, 1109 (2009).
19. D. Pletcher, *A First Course In Electrode Processes*, Alresford Press Ltd (1991).
20. K. H. Kangasniemi, D. A. Condit and T. D. Jarvi, *Journal of the Electrochemical Society*, **151**, E125 (2004).
21. G. Jerkiewicz, G. Vatankhah, J. Lessard, M. P. Soriaga and Y. S. Park, *Electrochimica acta*, **49**, 1451 (2004).
22. H. A. Gasteiger, S. S. Kocha, B. Sompalli and F. T. Wagner, *Applied Catalysis B-Environmental*, **56**, 9 (2005).
23. H. A. Gasteiger, J. E. Panels and S. G. Yan, *Journal of Power Sources*, **127**, 162 (2004).
24. R. J. K. Wiltshire, C. R. King, A. Rose, P. P. Wells, M. P. Hogarth, D. Thompsett and A. E. Russell, *Electrochimica Acta*, **50**, 5208 (2005).
25. A. E. Russell and A. Rose, *Chemical Reviews*, **104**, 4613 (2004).
26. W. E. O'Grady and D. C. Koningsberger, *Electrochemical Society Extended Abstracts*, **88-1**, 513 (1988).
27. R. A. Lampitt, L. P. L. Carrette, M. P. Hogarth and A. E. Russell, *Journal of Electroanalytical Chemistry*, **460**, 80 (1999).
28. C. Roth, N. Benker, M. Mazurek, F. Scheiba and H. Fuess, *Applied Catalysis A-General*, **319**, 81 (2007).
29. J. McBreen, W. E. O'Grady, K. I. Pandya, R. W. Hoffman and D. E. Sayers, *Langmuir*, **3**, 428 (1987).
30. M. E. Herron, S. E. Doyle, S. Pizzini, K. J. Roberts, J. Robinson, G. Hards and F. C. Walsh, *Journal of Electroanalytical Chemistry*, **324**, 243 (1992).
31. S. Maniguet, R. J. Mathew and A. E. Russell, *Journal of Physical Chemistry B*, **104**, 1998 (2000).
32. E. Principi, A. Di Cicco, A. Witkowska and R. Marassi, *Journal of Synchrotron Radiation*, **14**, 276 (2007).
33. C. Roth, N. Martz, T. Buhrmester, J. Scherer and H. Fuess, *Physical Chemistry Chemical Physics*, **4**, 3555 (2002).
34. P. G. Allen, S. D. Conradson, M. S. Wilson, S. Gottesfeld, I. D. Raistrick, J. Valerio and M. Lovato, *Electrochimica Acta*, **39**, 2415 (1994).
35. R. Viswanathan, G. Y. Hou, R. X. Liu, S. R. Bare, F. Modica, G. Mickelson, C. U. Segre, N. Leyarovska and E. S. Smotkin, *Journal of Physical Chemistry B*, **106**, 3458 (2002).

36. S. L. Hudson, S. C. Ball, K. B. Blaney, G. H. Chouchelamane, S. G. Fiddy, I. Harvey, P. Sivasubramaniam, B. C. Tessier, B. R. C. Theobald, D. Thompsett and A. E. Russell, *ECS Transactions*, **16**, 1395 (2008).
37. A. Witkowska, S. Dsoke, E. Principi, R. Marassi, A. Di Cicco and V. R. Albertini, *Journal of Power Sources*, **178**, 603 (2008).
38. A. N. Mansour, J. W. Cook and D. E. Sayers, *Journal of Physical Chemistry*, **88**, 2330 (1984).
39. F. W. Lytle, *Journal of Catalysis*, **43**, 376 (1976).
40. F. W. Lytle, P. S. P. Wei, R. B. Greegor, G. H. Via and J. H. Sinfelt, *Journal of Chemical Physics*, **70**, 4849 (1979).
41. N. Binstead, EXCURV98, CCLRC, Daresbury Laboratory, in (1998).
42. M. A. Newton, A. J. Dent and J. Evans, *Chemical Society Reviews*, **31**, 83 (2002).
43. M. A. Newton, *Journal of Synchrotron Radiation*, **14**, 372 (2007).
44. M. Sanchez del Rio and R. J. Dejus, *SPIE Proceedings*, **5536**, 171 (2004).
45. N. Binstead, XMULT, University of Southampton, in (2006).
46. M. Vaarkamp, B. L. Mojet, M. J. Kappers, J. T. Miller and D. C. Koningsberger, *Journal of Physical Chemistry*, **99**, 16067 (1995).

Chapter 3. Deactivation of Pt_3Co

Some of the results presented in this chapter were previously presented in ECS Transactions manuscripts in 2007 (1, 2).

1. Introduction

The activity and stability of Pt_3Co/C alloy catalysts reported in the literature and experiments that were conducted on Johnson Matthey materials prior to commencing this work, in which the author was involved, will be described in the introduction (sections 1.1 to 1.3) to provide the background as to why the work in this chapter was conducted. In light of these results, the mechanisms of activity loss in Pt_3Co/C alloy systems have been investigated by accelerated durability testing in liquid electrolyte using a cell designed to enable quantification of dissolved species. By combining electrochemical, TEM and XAS results, the origins for the observed activity enhancement of Pt_3Co/C alloys over Pt/C catalysts and mechanisms that account for the deactivation of these materials will be proposed.

1.1 Activity and stability of PtCo alloy catalysts

To meet automotive targets for fuel cell operation, cathode catalysts must demonstrate both enhanced activity and stability over the current commercially available platinum catalysts (3). The activity requirements have recently been defined by the US Department of Energy (DoE) (4). For economically viable automotive application cathode catalysts must show a mass activity of 0.44 A mg^{-1}_{Pt} at 900 mV and 150 kPa_{abs} when operated using oxygen. This corresponds to 3-4 times the activity shown by the current state-of-the-art monometallic carbon supported platinum catalysts.

PtCo alloys have been demonstrated to show an activity benefit over commercial Pt/C catalysts, both historically in phosphoric acid fuel cells (PAFCs) (5) and, more recently, in PEMFCs. In RDE experiments , Paulus *et al.* (6) showed a 1.3 to 3 times mass activity benefit for carbon supported PtCo alloys over a Pt/C catalyst in 0.1 M $HClO_4$ at 60 °C with a comparable particle diameter, and a 2 times mass times activity benefit was reported by Colón-Mercado and Popov (7) and Chen *et al*. (8). Enhanced performance for PtCo/C catalysts has also been demonstrated in MEA tests by Mathias *et al.* (9) and Yu *et al.* (10) in 2005. At the same time PtCo alloys were under

investigation at Johnson Matthey, with activity and stability results for 40% Pt_3Co/C catalysts with a range of particle sizes being reported in 2006 (11, 12). A significant performance enhancement of around 25 mV in the kinetic region was observed over Pt and annealed Pt reference catalysts. Figure 1 shows that this 25 mV enhancement is translated to a two times mass activity benefit over Pt only catalysts irrespective of particle size, which is inversely proportional to the CO area. It was also demonstrated that the observed mass activity benefit for Pt_3Co/C could be exploited as a cost reduction; equivalent performance was obtained for a Pt_3Co/C cathode catalyst with nearly half the loading of a Pt/C cathode (0.25 *vs.* 0.4 $mg_{Pt}\,cm^{-2}$) (11).

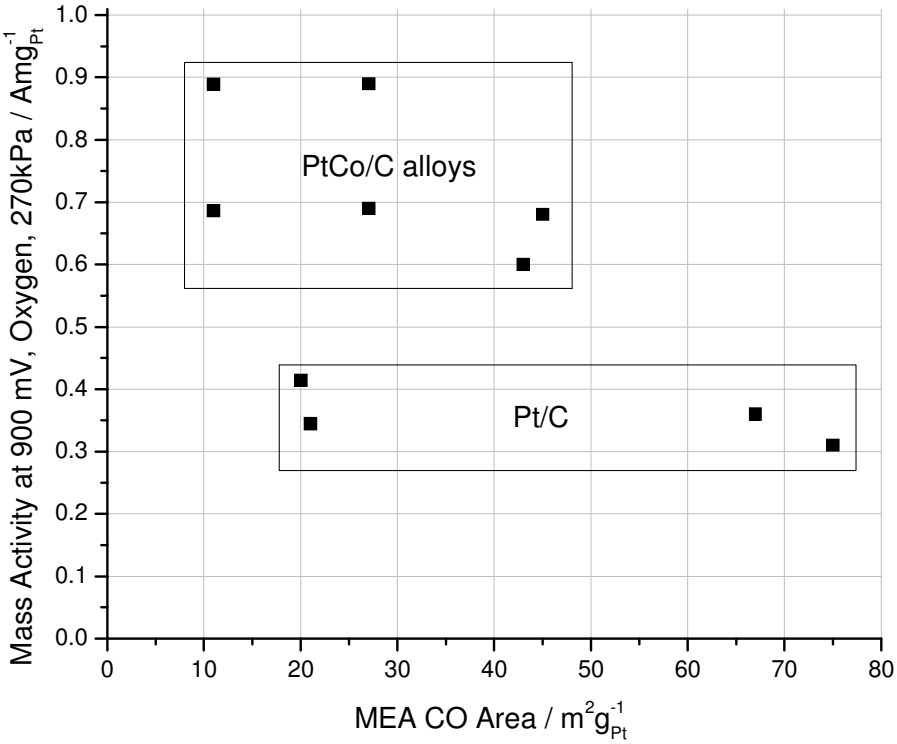

Figure 1. Oxygen reduction mass activity at 900 mV, as a function of *in situ* MEA Pt area for a series of Pt_3Co/C and Pt/C catalysts using O_2 feed at 270 kPa (11)

Until 2004, improving the beginning of life (BOL) catalytic performance was a major focus in the fuel cell literature with fewer publications considering PEMFC degradation and durability. Since then, the issue of degradation and durability has become a key area of fuel cell research and durability targets have been set by the US, Japanese and European fuel cell funding bodies (13). In addition to enhanced BOL activity, catalysts must also retain activity for more than the 5000 hrs lifetime of the automotive fuel cell

stack (equivalent to 150,000 driven miles) to allow direct comparison with the durability and reliability of current automotive engines (4). In this time 30,000 start up / shut down cycles and 300,000 large voltage transients (caused by load cycling leading to a change in cell potential) during operation of the fuel cell stack are expected. Under these conditions the catalyst will repeatedly experience high voltages (up to 1.4 V) and large voltage transients (for example a load change may result in voltage step change from 0.7 V to 0.9 V), both of which can significantly impact catalytic activity by reducing the active surface area. Idle and start up / shut down conditions have been equated to an accelerated potentiostatic hold test of 100 hrs at 1.2 V and suggested targets of < 40% of the initial mass activity and ECA lost over 300,000 large voltage transients with a low activity degradation rate of < 3 $\mu V\ hr^{-1}$ have been proposed by the DoE for these tests (4, 13).

In terms of electrochemical area stability PtCo alloys have shown significant improvement over platinum only catalysts under potentiostatic hold and cycling regimes (7, 9-12, 14). Work by Yu *et al.* (10) showed that a Pt_3Co alloy maintained superior mass activity compared to platinum over 2400 cycles from 0.87-1.2 V *vs*. RHE and application of accelerated durability tests by Popov *et al*. (7) comparing a 20% Pt/C and a 20% Pt_3Co/C alloy showed enhanced catalyst particle stability upon addition of the alloying element. The stability of two Johnson Matthey Pt_3Co/C catalysts to voltage cycles were studied in both the MEA and in liquid electrolyte environments (11, 12). It was found that in the MEA, the Pt/C catalyst lost surface area and mass and specific activity after 1000 cycles, while the PtCo alloy catalysts retained surface area and at least a two times mass activity benefit (at 900 mV and 230 kPa), over platinum during 10,000 voltage cycles from 0.6-1.0 V. (Note these experiments were conducted using different cell hardware and experimental conditions, including lower pressure, to those in Figure 1, leading to lower absolute performance values than those previously shown in Figure 1) During the cycling experiment, the activity of one PtCo alloy increased after 3000 cycles from 0.26 A mg^{-1}_{Pt} to 0.46 A mg^{-1}_{Pt}, then the performance decreased to 0.37 A mg^{-1}_{Pt} after 10,000 voltage cycles. The second PtCo alloy tested showed the same trend in activity. The activity increased from 0.34 A mg^{-1}_{Pt} to 0.36 A mg^{-1}_{Pt} up to 3000 cycles then the activity decreased to 0.30 A mg^{-1}_{Pt} at the end of the cycling test. The same surface area loss trends were observed during cycles in liquid electrolyte, however, degradation rates were found to be accelerated compared to MEA testing. The

test that was conducted, was a prerequisite to the results presented in this chapter. The Johnson Matthey Pt_3Co/C and Pt/C catalysts were electrochemically cycled as electrode layers 10,000 times at 50 mV s^{-1} from 0.6-1.0 V in 1 M H_2SO_4 at 80 ºC (11). The change in hydrogen adsorption area and the cyclic voltammetric profile for each catalyst with cycle number is presented in Figure 2.

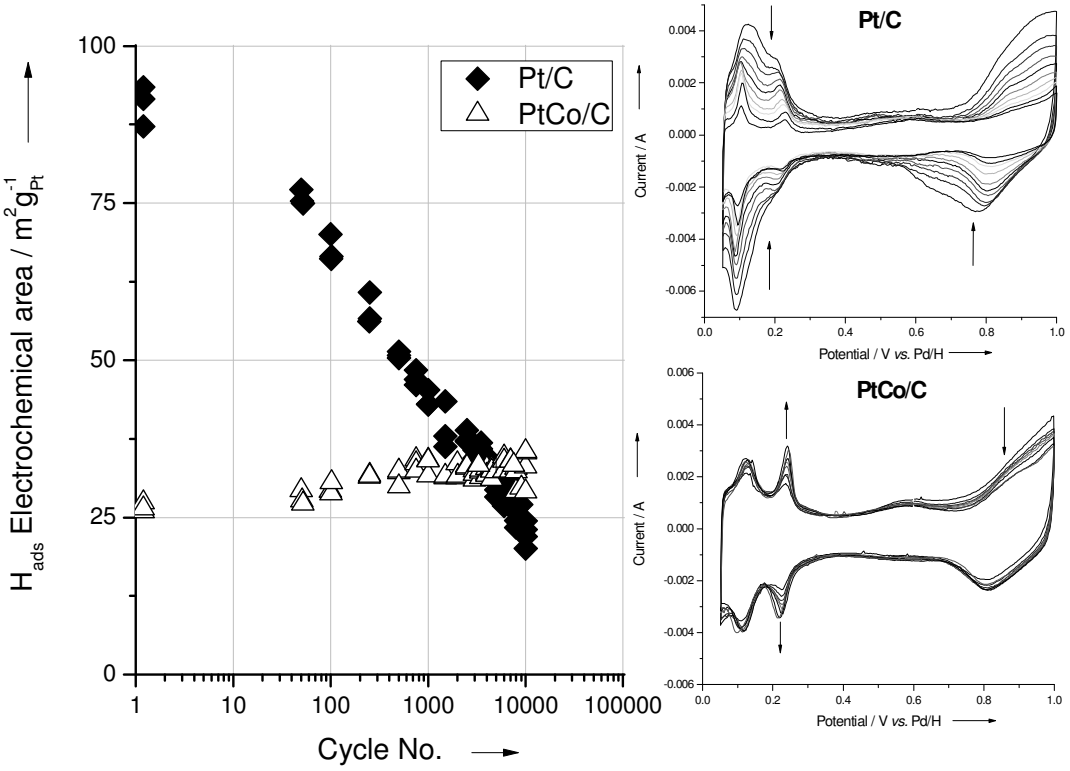

Figure 2. Changes in electrochemical area as a function of cycle number for Pt and Pt_3Co catalysts in N_2 purged 1M H_2SO_4, 80 ºC, cycling 0.6-1.0 V *vs*. Pd/H at 50 mV s^{-1} (11) and corresponding CV profiles (previously unpublished). Arrows indicate trend with increasing cycle number

A large decrease in surface area (~60%) was found for the Pt/C catalyst during the course of cycling, and very little change was found for the Pt_3Co alloy. With cycles the voltammetry of the Pt/C catalyst showed the features in the hydrogen region becoming more well defined and less broad, indicating formation of more well-defined surface sites, which is consistent with the formation of larger platinum crystallites. A decrease in the magnitude of current in the Faradaic regions of the voltammetry was also observed, which is consistent with the surface area loss. The voltammetry of the Pt_3Co catalyst showed a slight sharpening of hydrogen features, but no change in the Pt-H absorption area or position of the oxide reduction peak was found during the cycling.

Post mortem TEM on samples cycled in 1 M H_2SO_4 showed little change in the size or morphology of the Pt_3Co alloy particles, but significant particle growth and agglomeration was found for the cycled Pt electrode, along with areas of bare carbon support implying some dissolution or detachment of catalyst particles had occurred. The 1 M H_2SO_4 solutions used were analysed at the end of testing to determine the levels of dissolved Pt and Co, but the amounts could not be quantified due to the low concentrations of metals present. It was known from this work and that of Popov *et al*. and Yu *et al*. that the rapid performance decay for the Pt/C catalysts was accompanied by surface area loss (7, 10-12). For PtCo alloys deactivation and loss of fuel cell performance also occurred, but over longer times (7, 10-12), despite the observed low surface area losses under potentiostatic cycling regimes. This indicated other factors were influencing deactivation of PtCo alloy catalysts.

1.2 Mechanisms of catalyst deactivation

In 2007, fuel cell durability and degradation literature including: durability testing methods, performance losses associated with operating conditions, and losses associated with MEA components (membranes, electrocatalysts, catalyst supports and GDLs), was extensively reviewed by Borup *et al*. (13). Similarly a review of the impact of accelerated stress tests was conducted in 2009 Zang *et al.* (15). All but performance losses associated with the durability and degradation of electrocatalysts fall beyond the scope of this work. Processes that cause performance loss via catalyst degradation can be grouped into two general areas, either processes that result in loss of or modify the electrochemically active surface area (reducing the number of sites available for reaction or changing the nature of active sites), or by processes that change the mass transport properties of the MEA and therefore hinder the transportation of reactants to and products away from the active sites.

1.2.1 Mechanisms of electroactive surface area loss

The Pourbaix diagram for platinum (16) shows that Pt electrocatalysts are thermodynamically unstable in the fuel cell operational window. This instability with time leads to performance loss. A comprehensive discussion of the instability of Pt/C electrocatalysts in MEAs may be found in a recent paper by Ferreira *et al*. (17) and

review by Shao-Horn *et al.,* (18), in which platinum surface area losses have been grouped into three different processes, based on experimental evidence.

i) Platinum particle agglomeration triggered by corrosion of the carbon support. This is significant under start/stop conditions where catalysts are exposed to high potentials, but is not limited to potentiostatic hold conditions. Online mass spectrometry measurements by Ball *et al*. and Maass *et al.* also report evidence for carbon support oxidation occurring during potential cycling (12, 19).

ii) Platinum dissolution and redeposition as a nanoscale Ostwald-ripening process; smaller platinum particles dissolve in the ionomer phase and redeposit on larger platinum particles that are separated by a few nanometers. This dissolution may be electrochemical, Equation 1, or chemical via platinum oxide film formation. Equation 2 and Equation 3 (17).

Electrochemical platinum dissolution $Pt_{(s)} \rightarrow Pt^{2+}_{(aq)} + 2e^-_{(aq)}$ **Equation 1**

Chemical dissolution

Step 1 $Pt_{(s)} + H_2O_{(l)} \rightarrow PtO_{(s)} + 2H^+_{(aq)} + 2e^-_{(aq)}$ **Equation 2**

Step 2 $PtO_{(s)} + 2H^+_{(aq)} \rightarrow Pt^{2+}_{(aq)} + H_2O_{(l)}$ (slow) **Equation 3**

These two processes have been used in the kinetic modelling work of Darling and Meyers (20) to describe oxidation and dissolution of platinum in PEMFCs. They assumed platinum dissolution is determined by potential, particle size and fraction of the surface covered by oxide. In the model, which also allows redeposition of platinum, the oxide layer can protect the platinum from dissolution. However, the kinetics of oxide formation are slow relative to the rate of electrochemical dissolution. Rapid changes in potential can therefore leave unprotected platinum subject to electrochemical dissolution before the protective surface oxide can form.

iii) Coalescence of platinum nanoparticles via nanocrystallite migration on the carbon support. This is a micrometre-scale diffusion process, where dissolved

platinum ions diffuse towards the anode and are reduced from the anode in regions of low potential (17).

Experimental evidence for mechanisms ii) and iii) have been provided using post mortem electron probe microanalysis (EPMA) and TEM of MEAs. Post mortem EPMA results reported by Yu *et al*. (10) and Bi *et al.* (21) showed that platinum migrated into the membrane forming a band of particles parallel to the catalyst layer, and TEM evidence from Guilminot *et al*. (22) and Yasuda *et al*. (23) indicated that the Pt particles in the membrane did not originate from migration of particles from the catalyst layer, but instead were the consequence of nucleation and atomic growth of the particles following reduction (by H_2 from the anode) of the dissolved Pt species (Pt^{z+} where z = 2,4). The position of the band of Pt particles was shown by Bi *et al*. to be correlated with the position of the hydrogen front from crossover from the anode which resulted in a low potential (reducing) environment in the membrane (21). TEM results of a post cycled Pt/C catalyst, as shown in Figure 3, was also reported by Johnson Matthey (11). The cycled MEA reveals clear evidence of Pt dissolution on the cathode, migration and precipitation in the membrane. The Pt crystallites within the membrane were up to 90 nm across (see Figure 3(b)). TEM also revealed Pt particle growth within the catalyst layer from 2 nm average diameter particles for the uncycled catalyst to 5-9 nm for the post cycled sample.

Cross-section EPMA measurements on the Johnson Matthey cycled samples showed leaching of Co into the membrane for MEAs containing PtCo/C cathodes (11). An example EPMA cross section image of a Pt_3Co/C catalyst after operation is shown in Figure 4. The line scan clearly shows the presence of Co within the membrane. Co leaching was also reported by Yu *et al*. (10) and others have also reported leaching of alloying metals under operating conditions in both PEM fuel cells (7, 10, 11, 24) and in direct methanol fuel cell (DMFC) environments (25). *In situ* metal leaching of this type can degrade catalytic performance by modifying the nature of active sites and the changing the mass transport properties of the MEA.

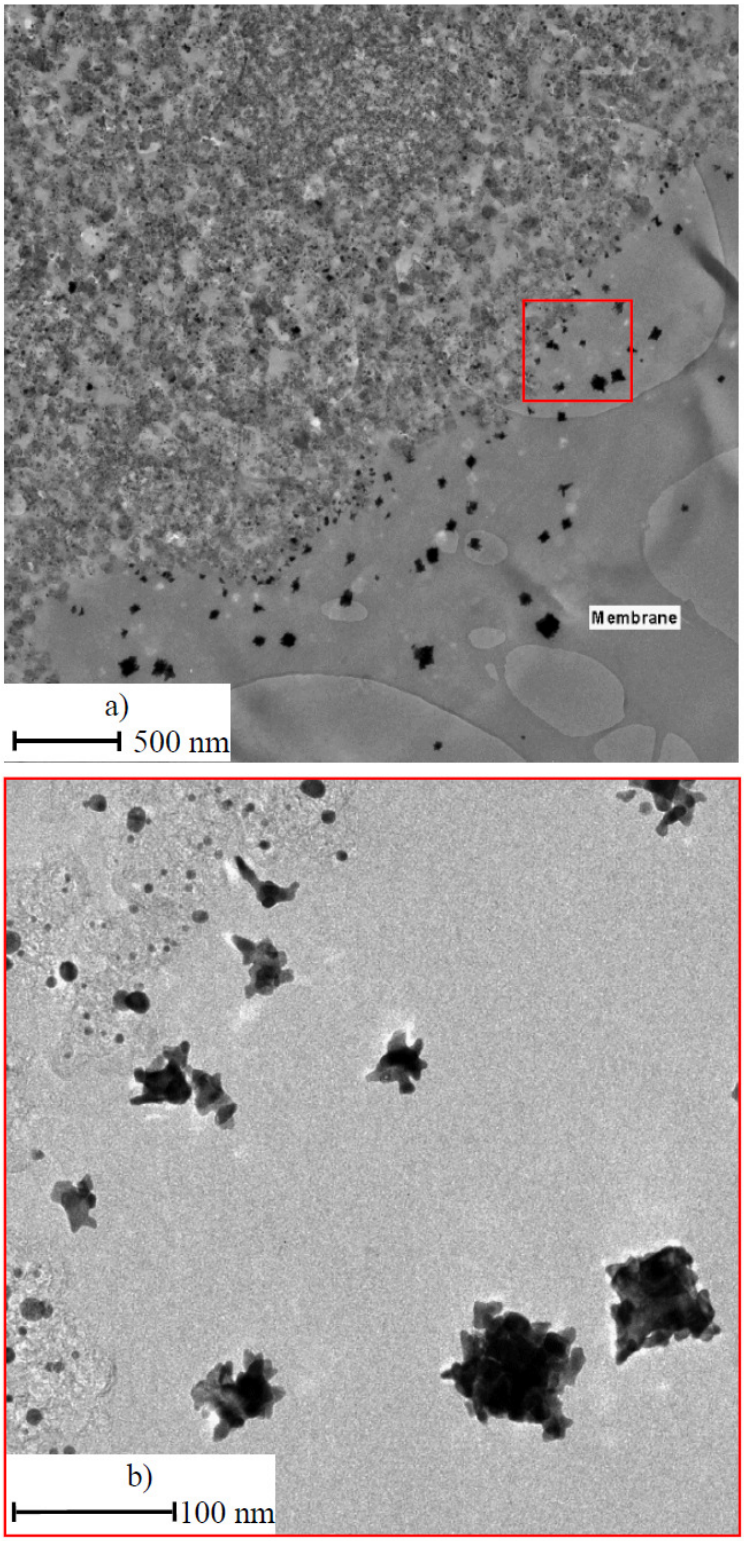

Figure 3. **TEM cross sectional image of a Pt/C cathode cycled 10,000 times under N_2 from 0.6-1.0 V *vs*. Pt/H_2 anode membrane catalyst layer interface region (a) overview (b) interface detail from marked area (11)**

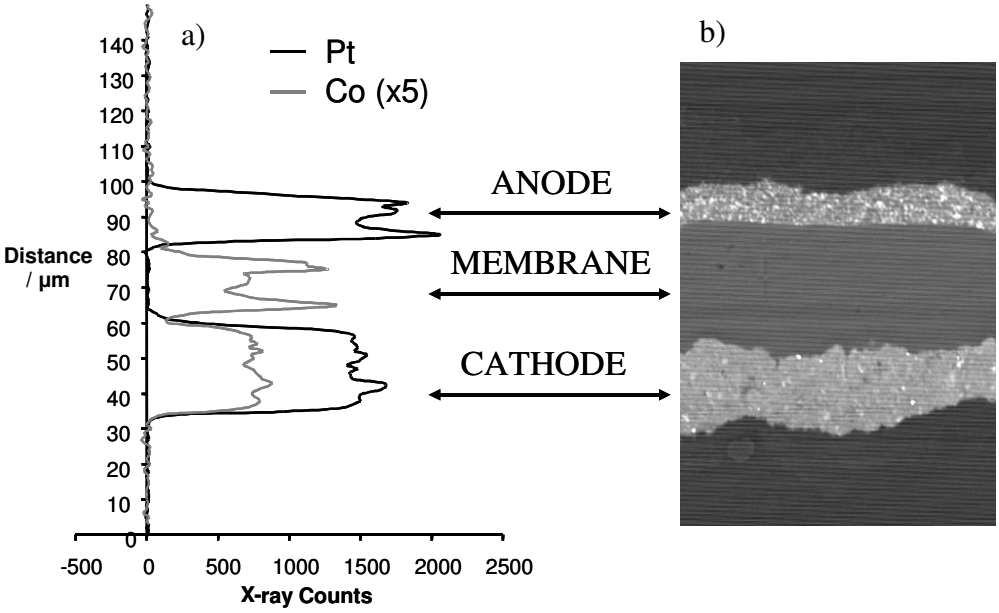

Figure 4. **Electron probe micro analysis on a MEA cross-section after operation a) line scan analysis showing the distribution of Pt and Co within the MEA from cathode side to anode side the corresponding MEA cross section is shown in b)**

1.2.2 Performance loss induced by changes in mass transport

The strong affinity of metal cations for the sulphonic acid groups in PFSA membrane/ionomer results in the likely exchange of metal cations (including dissolved Pt species) with the membrane bound protons. This would result in a loss in fuel cell performance by decreasing membrane/ionomer conductivity (H^+ transport through the membrane), reducing water content by dehydrating the membrane, and/or suppressing oxygen reduction kinetics by decreasing oxygen content in the ionomer film (3). In addition, dissolved metal ions in the membrane may facilitate membrane degradation and, therefore, performance degradation by increasing chemical radical attack, mechanically weakening the membrane and increasing the chance of pinholing, increasing H_2 crossover, and/or shorting (3, 26). Also, precipitated platinum in the membrane has been reported to increase peroxide radical formation leading to membrane degradation (27, 28).

It has also been reported that platinum alloy catalysts have a tendency to flood more easily than platinum catalysts under air and at high current densities, reducing MEA

performance. This phenomenon was attributed to the hydrophilic nature of the hydrous oxides formed on the base metal surface of the catalyst particles (3). It has been suggested by Gasteiger *et al*. that a pre-leaching treatment of the alloy catalyst could be beneficial, since readily leached base metal could be removed preventing mass transport issues within the MEA (3).

Change or loss of the carbon support structure, via partial or total electrochemical oxidation of carbon functionalities is the other major mechanism that has been shown lead to performance degradation by changing the mass transport properties of the MEA (13, 15).

1.3 Aims of this work

Previous work (11, 12), conducted on Johnson Matthey materials, has shown that performance degradation can occur as a consequence of electrochemical cycling. The aim of the work presented in this chapter is to understand the mechanisms of activity loss in Pt/C and Pt_3Co/C and to study the effect of chemical acid leaching on the activity of Pt_3Co/C catalysts. In light of the good stability trend correlation between liquid electrolyte testing and MEA cycling tests, the observed acceleration of degradation in liquid electrolyte, and the difficulty associated with quantification of the amount of Co removed within the MEA environment, the investigation reported here was conducted in liquid electrolyte. An electrochemical cell with a smaller electrolyte volume than the cell previously reported (11) (100 ml *vs.* 250 ml) was used to allow improved quantification of dissolved species by ICP-MS analysis. Results of an accelerated cycling protocol to two different upper potential limits will be presented for Pt and Pt_3Co alloy catalysts. In addition, changes in catalyst morphology post cycling will be investigated by TEM. To understand the cause of deactivation for post cycled catalysts and to characterise chemically acid leached catalysts, XAS measurements at the Pt L_{III} and Co K edges will be presented to determine the effect of Co removal on catalyst structure. Changes associated with ability of the catalyst to grow and remove oxide pre- and post-cycling and the effects of acid leaching on oxide growth will also be discussed. By combining these results an insight into the different mechanisms that result in loss of Pt_3Co/C alloy activity and stability will be provided.

2. Experimental detail

The Pt/C and PtCo/C catalysts used in this study, and the tests that were conducted are detailed in Table 1, together with a summary of the catalyst particle sizes determined from XRD. All catalysts were prepared and characterised as described in Chapter 2 1.1. Electrodes of the catalysts were fabricated by screen printing (Chapter 2 1.2) at loadings of 0.4-0.6 $mg_{Pt}\,cm^{-2}$.

Table 1. Summary of Catalysts and testing conducted

Catalyst	Testing conducted				XRD mean crystallite size / nm
	MEA activity	Stability 0.6-1.0 V and 0.6-1.2 V	Window Opening	XAS	
60%Pt/C	-	Yes	Yes	-	2
40%Pt/C	Yes	-	-	-	2.2
40%Pt/C 600 °C	Yes	-	-	Yes	4.7
40%Pt/C 900 °C	-	Yes	-	-	5.0
40%Pt/C 1000 °C	Yes	1.2 V only		Yes	7.7
40%Pt/C 1200 °C	Yes	-	-	-	15.6
40% Pt_3Co/C 600 °C	Yes	-	-	-	3.6
40% Pt_3Co/C 1000 °C	Yes	Yes	Yes	Yes batch 1	5.9 batch 1 and 5.0 batch 2
40% Pt_3Co/C 1000 °C Acid leached	Yes	-	Yes	Yes	5.9
40% Pt_3Co/C 1200 °C Acid leached	Yes	-	-	-	12.9
40% Pt_3Co/C 900 °C	Yes	-	-	-	3.7
40% Pt_3Co/C 1200 °C	Yes	Yes	-	-	12.6

MEAs of the catalysts were fabricated with Flemion® SH-30 membrane and 40% Pt/C anode (Chapter 2 section 1.2.2), and MEA activity measurements were performed as described in Chapter 2 section 2.2.

The catalysts were subjected to stability testing in liquid electrolyte (Chapter 2 section 2.1). The 3.14 cm^2 working electrode button of the catalyst of interest was fully flooded by boiling in acidified water prior to testing. The boiling solution was analysed for Pt and Co by ICP-MS. The stabilities of Pt/C and Pt_3Co/C alloy catalysts under different cycling regimes were investigated using a 100 ml volume three-electrode electrochemical cell (Chapter 2, Figure 2.) potentiostatically controlled with an Eco Chemie Autolab PGSTAT 20 potentiostat. A Pd/H reference, platinum mesh/wire counter, each contained in a fritted compartment, and 1 M H_2SO_4 supporting electrolyte were used in all experiments. The jacketed cell was operated at a constant temperature of 80 ºC maintained by use of a circulating water bath. The 0.6-1.0 V and 0.6-1.2 V *vs*.

Pd/H at 50 mV s^{-1} stability test procedures (Chapter 2 section 2.1.2) and window opening (Chapter 2 section 2.1.3) procedure were performed. Determination of the catalyst electrochemical surface area was conducted at both the beginning and end of each test using the charge associated with H_{ads} or oxidation of an adsorbed monolayer of CO to CO_2. Analysis of dissolved species (ppb quantities) in the electrolyte during the stability test procedure was conducted by ICP-MS. For the 60% Pt/C catalyst, the electrolyte was replaced after 250 and 500 cycles to keep the levels of Pt in solution < 500 ppb so that saturation, limiting further dissolution, did not occur. The stability test was conducted in duplicate under each regime for each catalyst while the window opening procedure was only conducted once. TEM analysis of the pre and post cycled electrodes was conducted as described in Chapter 2 section 4.2.

XAS data was obtained for both powder samples (fresh catalyst) and post cycled electrodes using the gas treatment cell and spectra were collected in both air and H_2 atmospheres (Chapter 2 3.3). Measurements were conducted on stations 7.1, 16.5 and 9.3 at the SRS Daresbury laboratory, which operated at 2.0 GeV ring energy and 100-250 mA ring current. Spectra were obtained at the Pt L_{III} edge and Co K edge. All the powder samples (fresh catalyst) spectra were collected in October 2006, in transmission mode by other members of Prof. Russell's research group using samples that I supplied. I was present during the beamtime in June 2007 and June 2008, when the spectra of the electrode button samples were obtained in fluorescence mode. I completed all of the XAS data analysis using the methods described in Chapter 2 section 3.3. Briefly, individual scans for each sample were summed and XANES spectra were acquired after pre-edge subtraction. The background was then removed to obtain EXAFS spectra and the data were fitted to a three, four, five or six shell model, as appropriate. In the instances where oxygen neighbours were present an additional shell was added to the model as shown:

Structural Models used at the Pt L_{III} edge:

Four/Three shell: Pt-Pt_1 Pt-Co Pt-Pt_2 Pt-Pt_3 or Pt-Pt_1 Pt-Pt_2 Pt-Pt_3

Five/Four shell: Pt-Pt_1 Pt-Co Pt-Pt_2 Pt-O Pt-Pt_3 or Pt-O Pt-Pt_1 Pt-Pt_2 Pt-Pt_3

Structural Models used at the Co K edge:

Five shell: Co-Pt_1 Co-Co Co-Pt_2 Co-Pt_3 Co-Pt-Pt

Six shell: Co-Pt_1 Co-Co Co-Pt_2 Co-Pt_3 Co-O Co-Pt-Pt

3. Results

3.1 Effect of chemical acid leaching on the activity of Pt_3Co/C

The effect of Co removal on the activities of the Pt_3Co/C catalysts were investigated in light of the cycle stability results that indicated a correlation between activity and Co removal (11, 12). A chemical acid leaching treatment (Chapter 2 1.1) was performed on two 40% Pt_3Co/C catalysts to remove Co from the catalysts. The chemical leaching treatment removed 13% of the Co from the 12.9 nm catalyst and 27% of the Co from the 5.9 nm catalyst (by ICP-MS).

XRD analysis (Figure 5) showed no change in crystallite size on leaching and only a small change in lattice parameter (3.848 to 3.856 Å) suggesting that Co remained within the bulk of the particles or that the Co that was removed was not originally present as part of the crystalline component of the catalysts. As compared to pure Pt (3.911 Å (29)) the acid leached catalyst retains a contacted lattice parameter.

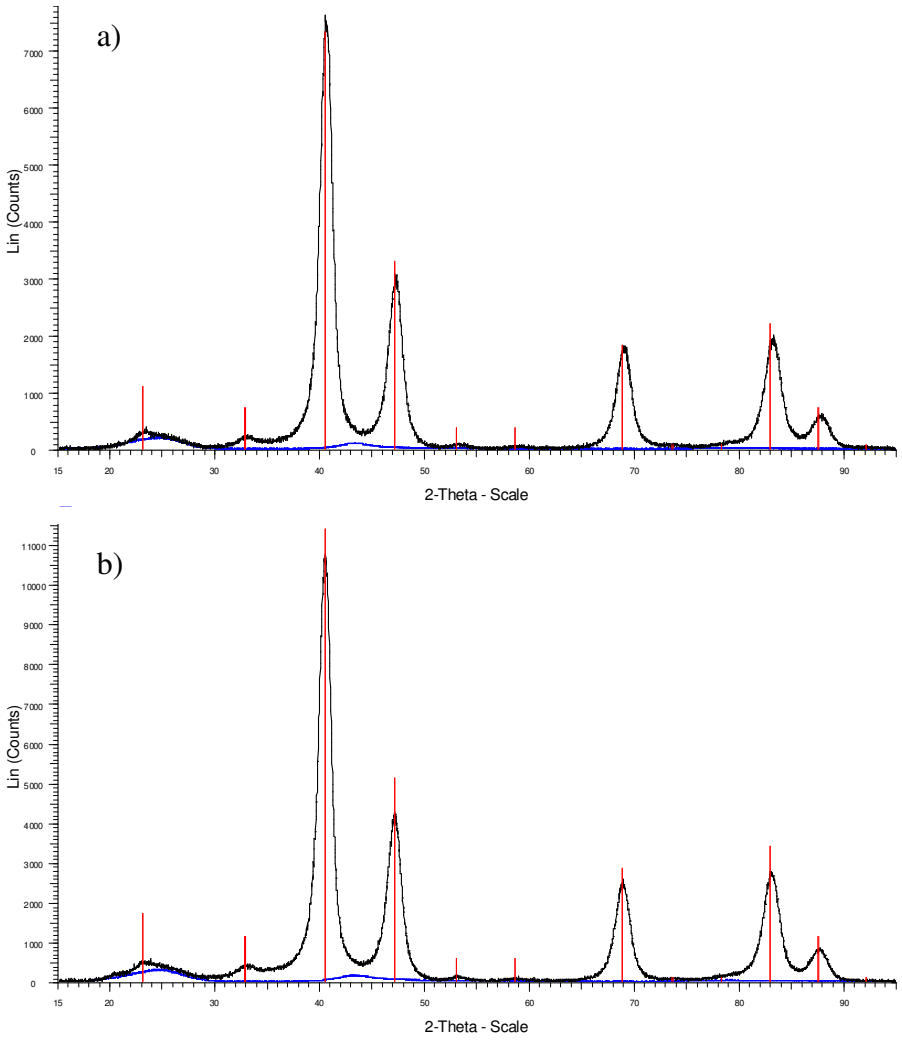

Figure 5. **XRD patterns for 40% Pt_3Co/C a) before and b) after acid leaching. (Black line – catalyst trace, Blue line – experimentally determined reference pattern for the carbon support, Diffraction pattern bars: Red– Cubic Platinum Cobalt Pt_3Co ICDD data base PDF No. 29-0499)**

The MEA performance of the leached catalysts was measured and the results are presented in Figure 6. It has been reported by Gasteiger *et al*. (3) and others (8) that the mass activity of a chemically acid leached PtCo/C alloy catalyst was 2.5 times that of a platinum reference catalyst. The mass activities at 900 mV measured for PtCo/C and Pt/C catalysts with a range of particle sizes are shown in Figure 6, together with the mass activity of the acid leached PtCo alloys. It can be seen that acid leaching of the catalysts results in loss of the activity benefit observed for the as-prepared alloys. Contrary to the reports of others (3, 8) the activity of the acid leached PtCo alloys show comparable performance to that expected for a platinum catalyst of comparable particle size.

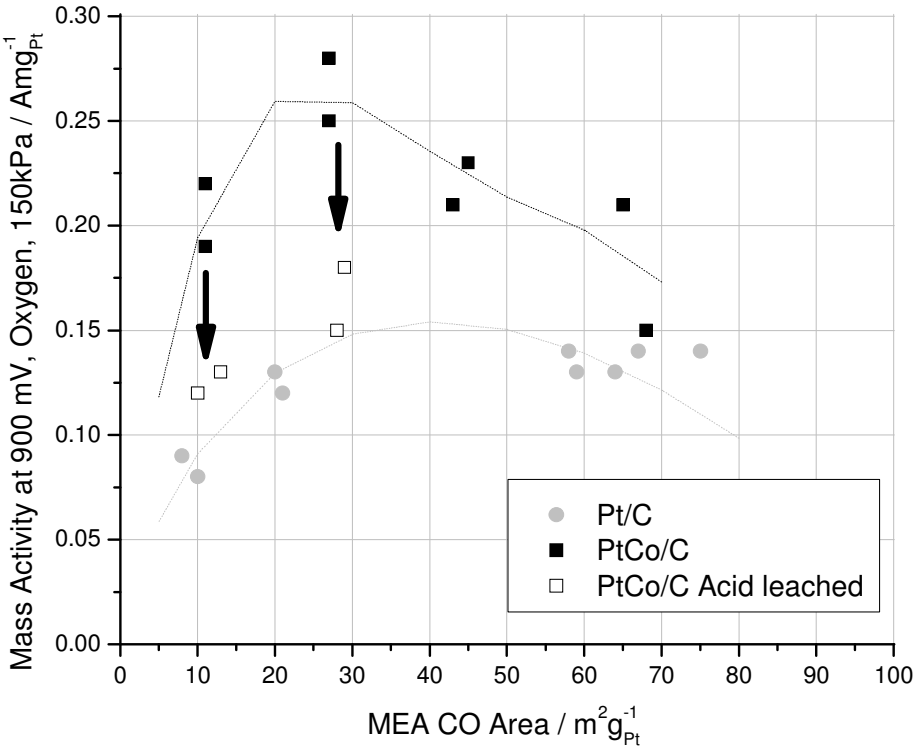

Figure 6. **Mass activity on O_2 at 900 mV, as a function of *in situ* MEA Pt area for a series of Pt_3Co and Pt catalysts. Lines show the trend in performance with electrochemical area and arrows show the effect of chemical acid leaching on performance (2)**

3.1 Characterisation of as prepared catalysts by cyclic voltammetry

Figure 7 shows a comparison plot of the cyclic voltammetry of the 60% Pt/C, 40% Pt_3Co/C and acid leached 40% Pt_3Co/C catalysts with an upper potential limit of 1.0 V normalised to the platinum loading of each electrode. A clear shift in the position for the hydrogen adsorption/desorption features is observed for the alloy catalysts compared to that of the Pt catalyst. This shift is consistent across repeat measurements and is considered to be significant. Differences are also observed in the oxide removal peak positions and the double layer region, where all catalysts show a redox feature associated with oxidation/reduction of the carbon support. For the alloys this feature is consistently observed at high potentials than for the Pt/C catalyst. It has been reported by others, (30-33), that the onset of OH_{ads} requires higher overpotentials on alloys compared to platinum. In contrast, in Figure 7 the onset of oxide formation appears to be very similar for all three catalysts, at approximately 0.7 V. However it is noted that

the redox feature associated with carbon support makes it difficult to determine the onset of oxide formation for the catalysts.

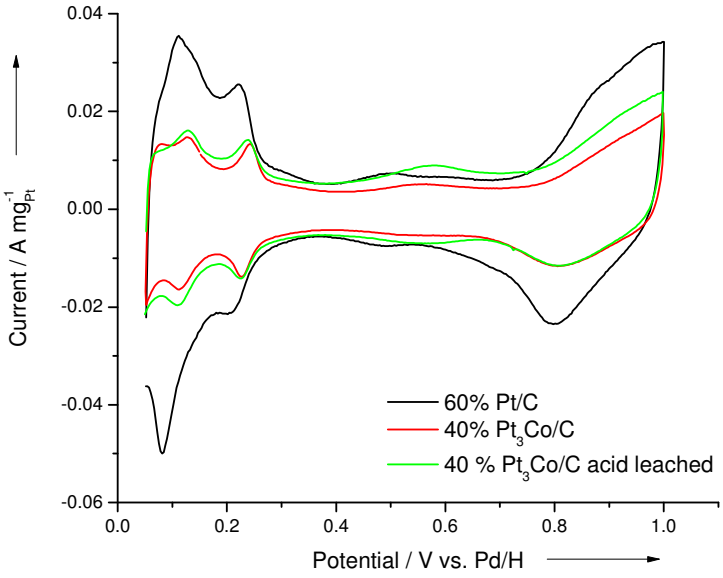

Figure 7. **Comparison plot of 60% Pt/C, 40% Pt_3Co/C and 40% Pt_3Co/C acid leached catalysts at 1.0 V *vs.* Pd/H upper potential limit in 1 M H_2SO_4 at 80 °C at 10 mV s^{-1}**

The beginning of life window opening cyclic voltammetry profiles to a range of upper potential limits for the 60% Pt/C, 40% Pt_3Co/C and 40% Pt_3Co/C acid leached catalyst electrodes are shown in Figure 8. As the potential of the upper limit is increased the voltammetry profiles of all catalysts exhibit increased oxide formation. At potentials > 1.2 V a sharp increase in current was found for all the catalysts, corresponding to oxygen evolution. The irreversibility of the oxide formation is seen in the increasing overpotential required to remove the oxide in on the cathodic sweep. The oxide removal peak positions, charges associated with H_{ads} and oxide removal for each catalyst are summarised in Table 2. The oxide growth per unit area of the catalysts at each upper potential limit was determined by normalising the oxide removal charge to the hydrogen adsorption charge. The 40% Pt_3Co/C and 40% Pt_3Co/C acid leached catalysts were found to have grown more oxide at a given potential than 60% Pt/C. A higher coverage of adsorbed oxygen species on PtCo relative to bulk Pt has also been reported by Chen *et al.* (8). The oxide removal peak position was found to occur at a lower overpotentials (higher measured potentials) for the alloy catalysts, despite the fact that they have more oxide per unit area than the 60% Pt/C catalyst.

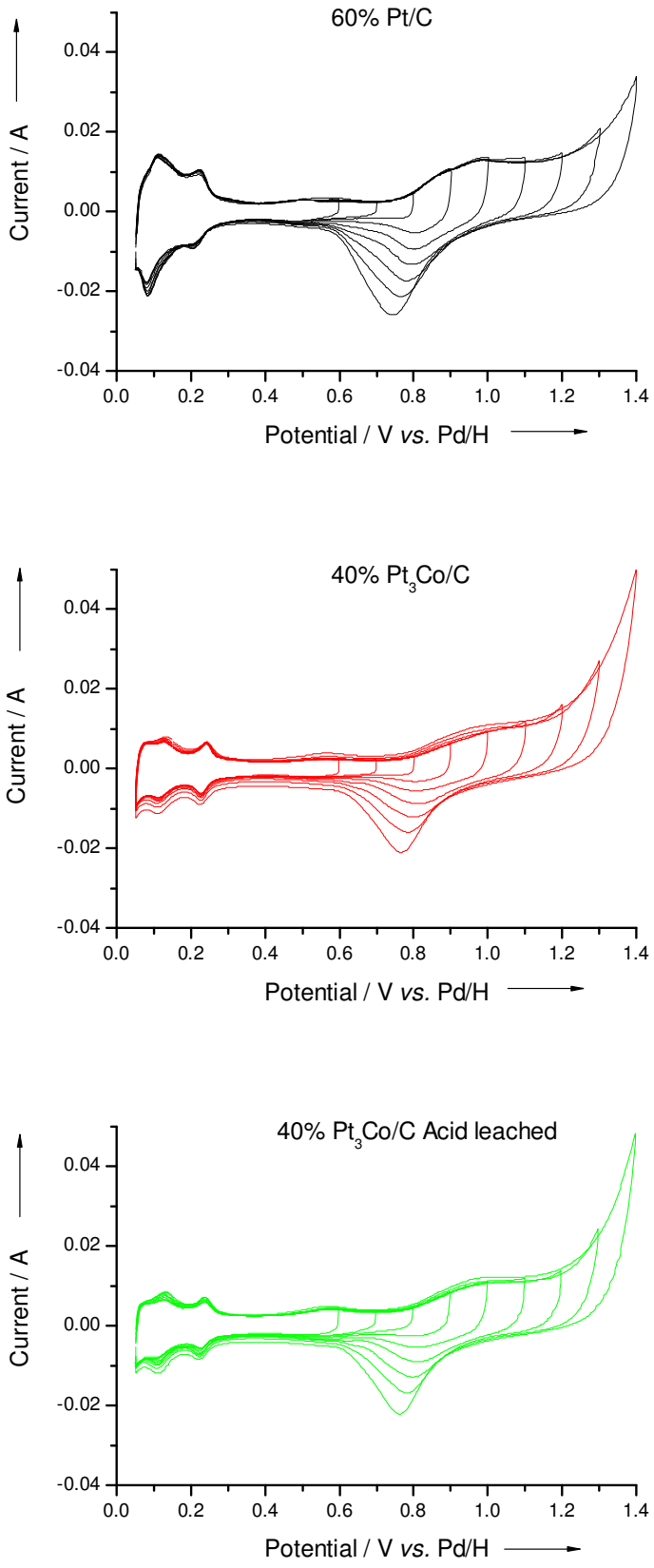

Figure 8. **Cyclic voltammetry of the as prepared 60% Pt/C, 40% Pt_3Co/C and 40% Pt_3Co/C acid leached catalysts to a range of upper potential limits *vs.* Pd/H in 1 M H_2SO_4 at 80 °C at 10 mV s^{-1}. The CVs were collected sequentially, starting for cycles between 0.05 and 0.6 V and increasing to 0.05 to 1.4 V in 0.1 V increments**

Table 2. Electrochemical parameters taken from CVs in Figure 8

Catalyst	Upper limit / V	Oxide reduction peak position / V *vs.* Pd/H	Oxide removal charge / C x 10^2	H_{ads} charge / C x 10^2	ECA / $m^2\ g_{Pt}^{-1}$	Oxide removal charge / H_{ads} charge
60% Pt/C	0.6	-	-	17.5	66	-
	0.7	-	-	19.0	72	-
	0.8	-	-	18.1	69	-
	0.9	0.802	3.59	18.2	69	0.20
	1.0	0.798	12.9	18.6	71	0.69
	1.1	0.793	24.8	18.7	71	1.32
	1.2	0.783	32.9	18.6	70	1.77
	1.3	0.765	39.8	18.4	70	2.17
	1.4	0.745	44.9	17.5	66	2.57
40% Pt_3Co/C	0.6	-	-	6.83	22	-
	0.7	-	-	6.59	21	-
	0.8	-	-	6.91	22	-
	0.9	0.800	2.47	6.99	22	0.35
	1.0	0.805	68.8	6.98	22	0.99
	1.1	0.813	14.1	7.25	23	1.94
	1.2	0.803	20.0	7.62	24	2.63
	1.3	0.784	24.0	7.94	25	3.02
	1.4	0.765	27.6	8.43	27	3.27
40% Pt_3Co/C Acid leached	0.6	-	-	6.54	21	-
	0.7	-	-	6.53	21	-
	0.8	-	-	6.87	22	-
	0.9	0.800	1.54	7.33	24	0.21
	1.0	0.808	6.83	7.80	25	0.88
	1.1	0.813	13.6	8.38	27	1.63
	1.2	0.799	22.4	8.57	28	2.61
	1.3	0.782	27.6	8.79	28	3.14
	1.4	0.762	31.5	9.22	30	3.42

3.2 The effect of potential cycling on the stability of 60% Pt/C

The 60% catalyst was cycled between 0.6-1.0 V for 1000 cycles and the CO oxidation voltammetry were obtained periodically. Using a fresh sample, the procedure was repeated for cycles between 0.6-1.2 V. The electrochemical areas calculated from the charge associated with CO oxidation during both cycling regimes are tabulated in Table 3. As can be seen during the 0.6-1.0 V cycling test 53 % of the initial ECA was lost. Cycling from 0.6-1.2 V was found to be more damaging resulting in 75 % ECA loss. In both tests, the ECA was progressively lost throughout the test with the rate of ECA loss slowing with cycle number. For 0.6-1.2 V cycling, during the first 50 cycles the ECA loss rate was 0.4 ECA units ($m^2\ g^{-1}_{Pt}$) per cycle, from 50 to 250 cycles the rate of loss decreased to 0.1 ECA units per cycle and between 500 and 1000 cycles 0.012 ECA units were lost per cycle.

Table 3. Changes in electrochemical surface area during cycling of 60% Pt/C

Cycling regime	Pt loading / mg_{Pt} cm^{-2}	Cycle No.	Oxide reduction peak position / V *vs.* Pd/H	CO oxidation charge / C	CO ECA Surface area / m^2 g_{Pt}^{-1}	% ECA loss
0.6-1.0 V	0.32	0	0.798	3.05×10^{-1}	72	0
		50	0.800	2.69×10^{-1}	64	12
		250	0.807	2.12×10^{-1}	50	31
		500	0.807	1.84×10^{-1}	43	40
		1000	0.809	1.44×10^{-1}	34	53
0.6-1.2 V	0.49	0	0.796	4.67×10^{-1}	72	0
		50	0.805	3.36×10^{-1}	52	28
		250	0.808	2.08×10^{-1}	32	55
		500	0.811	1.54×10^{-1}	24	67
		1000	0.815	1.17×10^{-1}	18	75

The effect of cycling between 0.6-1.2 V on the CO oxidation voltammetry is shown in Figure 9. As cycle number increases the magnitude of the current across the voltammogram decreases and both the CO oxidation onset potential and peak shift to lower overpotentials, while the shift in the onset is small ~15 mV, this trend was consistently observed during repeat testing and is therefore thought to be significant. This indicates that as the catalyst is cycled it becomes easier to oxidise adsorbed CO on the surface. In addition a decrease in the potential window for CO oxidation is observed along with development of a shoulder on the high overpotential end of the CO oxidation peak. It has been shown by Maillard *et al.* that the CO oxidation peak is sensitive to the particle size distribution. The peak shape was shown to be broad and symmetrical for Pt nanoparticles with narrow particle size distribution consisting of catalyst particles less than 3 nm, as seen at the start of the cycling experiment. In addition, Maillard *et al.* showed that wider particle size distributions consisting of larger particles exhibit a narrower oxidation peak potential window with a tail at high overpotenials and such distributions require a lower overpotential for CO oxidation (34), as was observed for in the voltammetry post cycling. The voltammetry is therefore consistent with cycling causing an increase in average particle size and a wider particle size distribution. A shift to lower overpotentials (higher measured potentials) is also seen in the oxide reduction peak potential with increasing cycle number, but no change in position of the hydrogen adsorption/desorption features or significant change in the onset of oxide formation is observed in Figure 9. The same observations, but to a lesser extent, are seen in the voltammetry for the 0.6-1.0 V cycling for this catalyst.

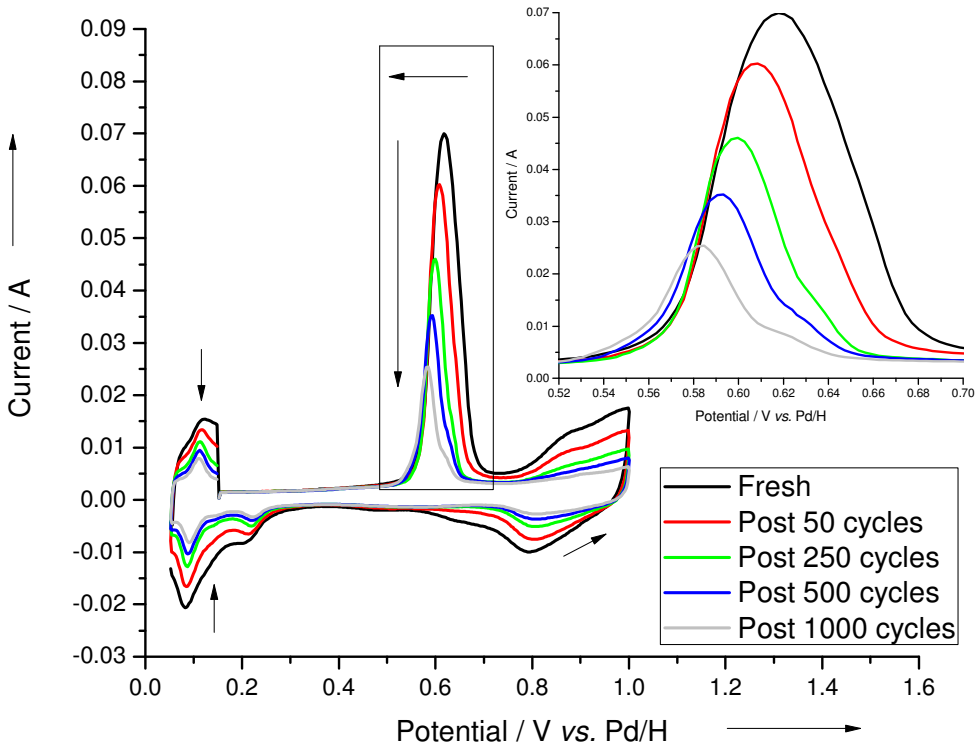

Figure 9. **The effect of number of cycles from 0.6-1.2 V *vs.* Pd/H on the CO oxidation voltammetry of 60% Pt/C at 10 mV s^{-1} in 1 M H_2SO_4 at 80 °C. Arrows indicate trend with increasing cycle number. Inset expanded CO oxidation peak**

To investigate the mechanism of ECA loss TEM images, Figure 10, were obtained and the particle size distributions were measured, Figure 11, for the as prepared and post-cycled electrodes. In comparison to the as prepared catalyst, which had particle sizes between 2-6 nm, the particle sizes of the post cycled catalysts were much larger. The particle size distributions remained symmetrical, but shifted to larger sizes and became broader with the increased upper cycling potential limit. The TEM evidence is, therefore, consistent with the CO oxidation voltammetry.

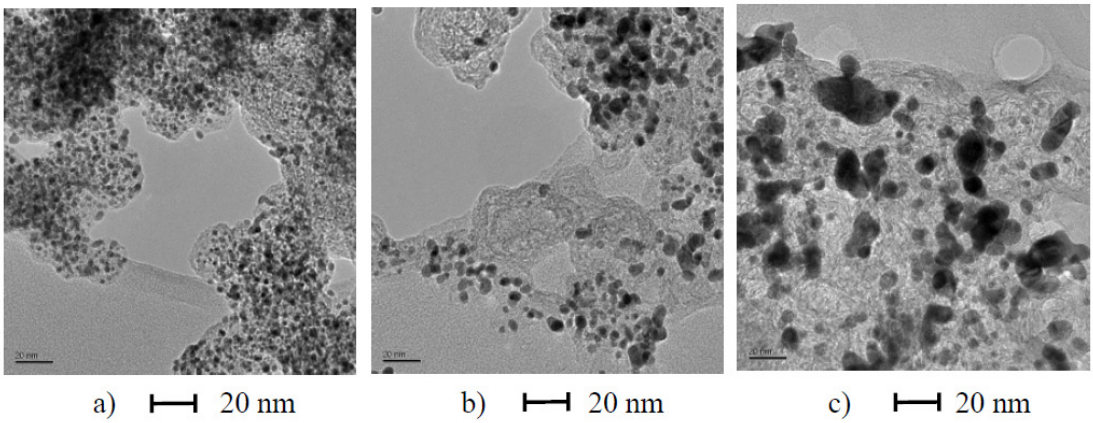

Figure 10. **TEM images of a) as prepared 60% Pt/C b) 60% Pt/C post 0.6-1.0 V cycling and c) 60% Pt/C post 0.6-1.2 V cycling**

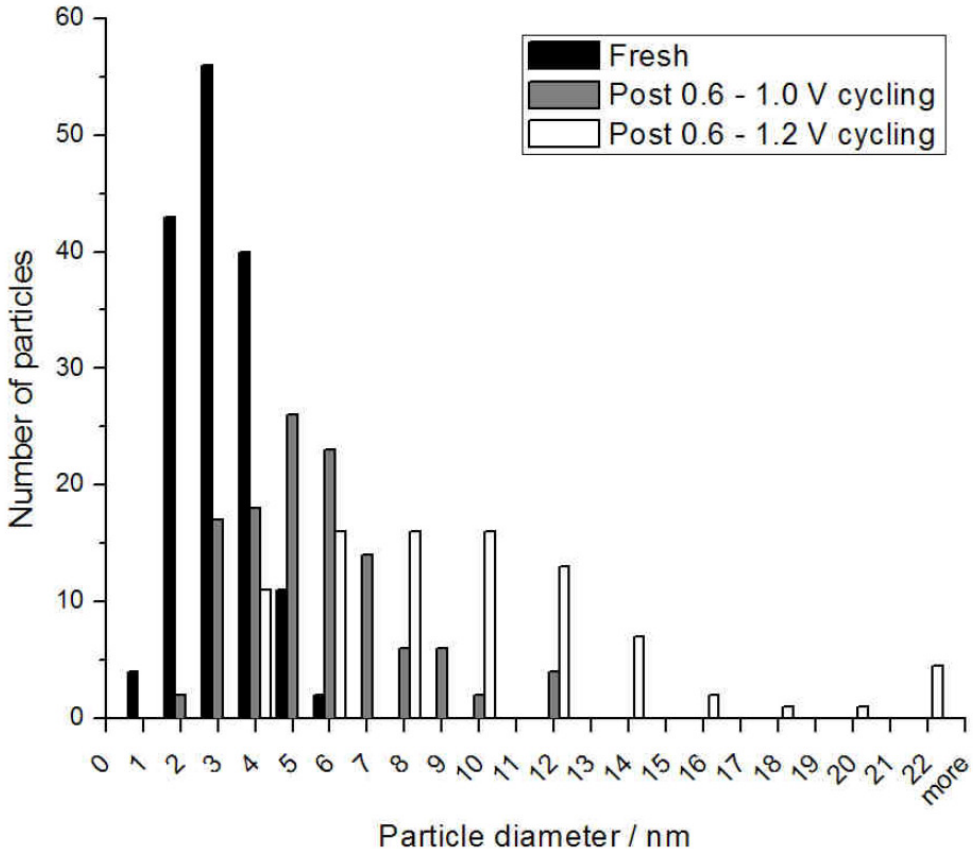

Figure 11. **Particle size analysis of 60% Pt/C pre and post cycling. Total number of particles measured: fresh 156, post 0.6-1.0 V cycling 118 and post 0.6-1.2 V cycling 88**

To investigate platinum dissolution the amount of platinum in the electrolyte was determined as a function of cycle number by ICP-MS, ppb quantities of platinum were found in the electrolyte. Figure 12 shows the variation in the amount of platinum measured in the electrolyte as a % of platinum within the catalyst for each cycling regime based on data from one test. 1% of the platinum in the catalyst was found to have dissolved into the electrolyte after cycling 1000 times from 0.6-1.0 V, while cycling from 0.6-1.2 V resulted in more platinum dissolution with a concentration in solution equivalent to removal of 10% of platinum in the catalyst after 750 cycles. Repeat testing also showed the % Pt loss. A linear increase in dissolved platinum with cycle number was observed in both cycling experiments. This is in good agreement with recent work by Ota *et al.* (35) where a linear consumption of Pt wire was observed during potential cycling to a range of upper potential limits up to 1.8 V. Pt dissolution studies using Pt/C electrodes by Myers *et al*. (36) also show a linear trend in dissolution of Pt during 0.9 V potentiostatic hold tests. It is known that metal dissolution often increases ECA by formation of Raney surfaces, however, in this instance a decrease in ECA is observed. This may occur if the dissolution of Pt into the electrolyte occurs from the smallest platinum particles (largest contributors to the ECA area), as the TEM evidence suggests.

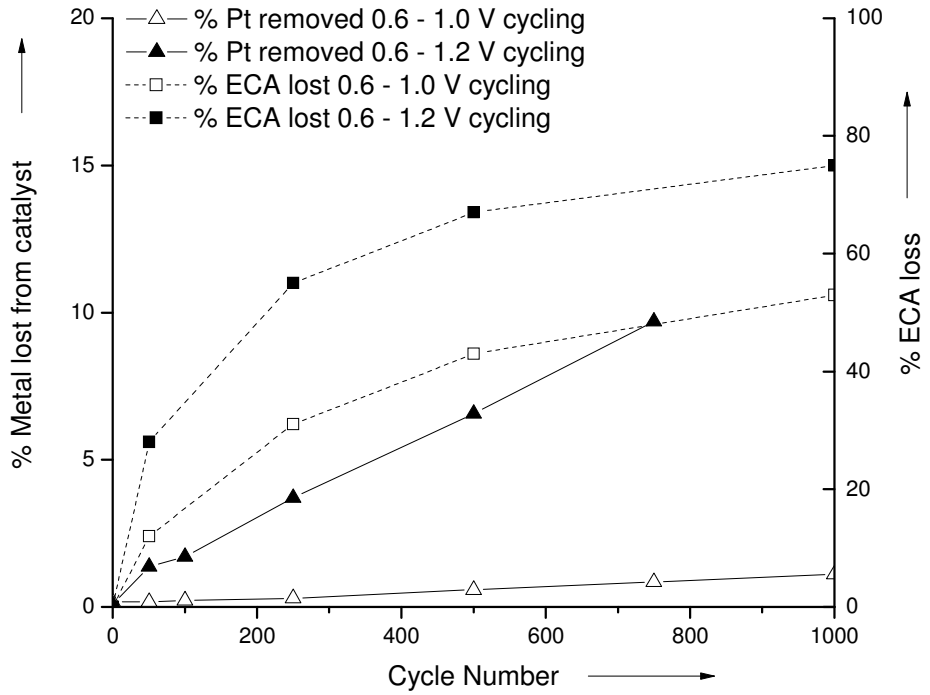

Figure 12. Effect of cycling on platinum dissolution for 60% Pt/C

3.3 The effect of potential cycling on the stability of Pt_3Co/C

The effect of the potential cycling regime on the stability of a Pt_3Co/C alloy was also investigated. Electrochemical areas calculated from the charge associated with CO oxidation during both cycling regimes are tabulated in Table 4.

Table 4. Changes in electrochemical surface area during cycling of 40% Pt_3Co/C 1000 °C /C

Cycling regime	Pt loading / mg_{Pt} cm^{-2}	Cycle No.	Oxide reduction peak position / V *vs.* Pd/H	CO oxidation charge / C	CO ECA Surface area / m^2 g_{Pt}^{-1}	% ECA loss
0.6-1.0 V	0.49	0	0.812	2.03×10^{-1}	31	0
		50	0.797	2.12×10^{-1}	33	0
		250	0.802	2.14×10^{-1}	33	0
		500	0.799	2.06×10^{-1}	32	0
		1000	0.809	1.96×10^{-1}	30	3
0.6-1.2 V	0.56	0	0.826	2.51×10^{-1}	34	0
		50	0.814	2.58×10^{-1}	35	0
		250	0.808	2.41×10^{-1}	33	4
		500	0.805	2.14×10^{-1}	29	15
		1000	0.808	1.87×10^{-1}	25	25

For both tests the ECA was found to increase slightly to a maximum after 50 cycles then decrease during the remaining part of the test. The alloy was found to be more stable than 60% Pt/C, losing 3% ECA in the 0.6-1.0 V cycling and 25% in the 0.6-1.2 V cycling. ECA loss was shown in the CO oxidation voltammetry by a decrease in charge. In both the cycling regimes the CO oxidation peak shifted to higher overpotentials and sharpened after the first 50 cycles, then no further shift was observed. The oxide reduction peak position showed little change in position during the 0.6-1.0 V cycling test and shifted to ~20 mV to higher overpotentials during the 0.6-1.2 V cycling test. Figure 13 shows the CO oxidation voltammetry during the 0.6-1.0 V cycling test and Figure 14 shows the CO oxidation voltammetry during the 0.6-1.2 V cycling test. The same shift in CO oxidation peak was observed for batch 2 of the 40% Pt_3Co/C with 5 nm particle size during 0.6-1.2 V cycling but little change in The oxide reduction peak position was observed for this catalyst (see Figure 27).

TEM shows that the relatively large 4-12 nm particles in the fresh catalyst are little changed by cycling,
Figure 15, with the exception that the smallest particles that are lost from the particle size distribution in Figure 16.

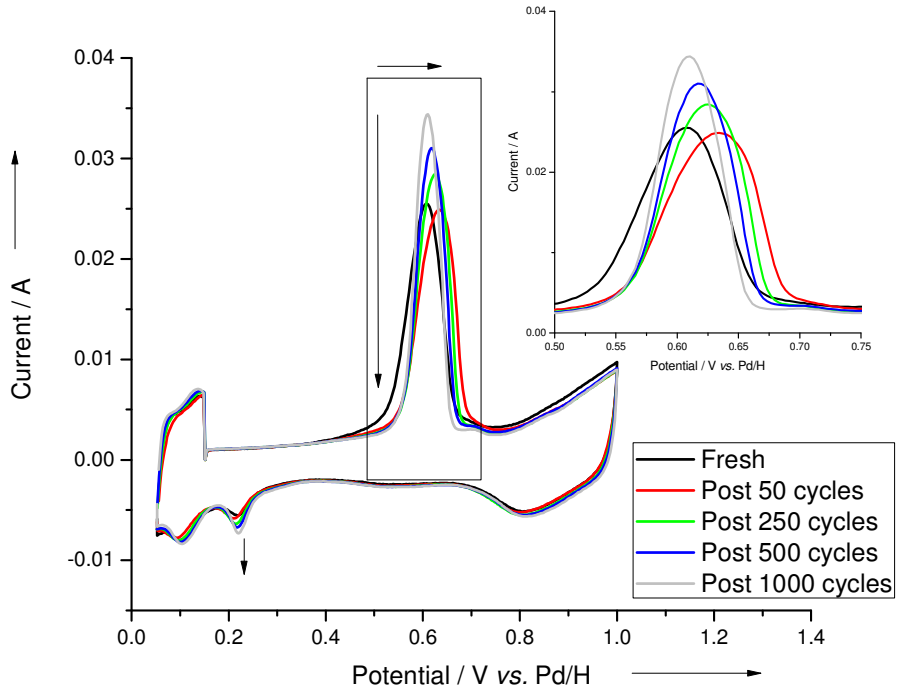

Figure 13. **The effect of number of cycles from 0.6-1.0 V *vs.* Pd/H on the CO oxidation voltammetry of Pt_3Co/C at 10 mV s^{-1} in 1 M H_2SO_4 at 80 ºC. Arrows indicate trend with increasing cycle number. Inset expanded CO oxidation peak**

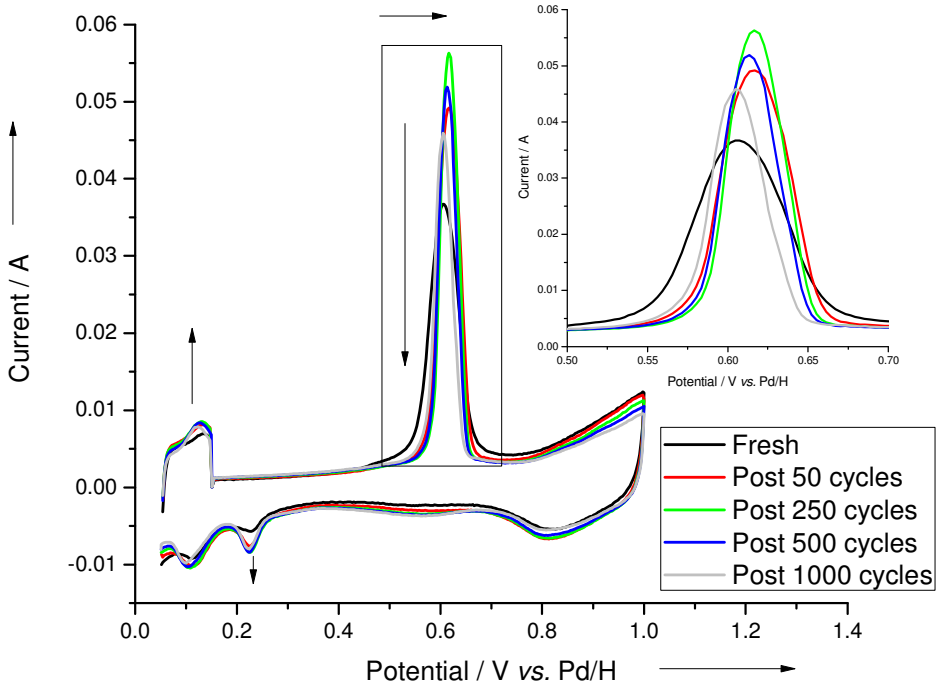

Figure 14. **The effect of number of cycles from 0.6-1.2 V *vs.* Pd/H on the CO oxidation voltammetry of Pt_3Co/C at 10 mV s^{-1} in 1 M H_2SO_4 at 80 ºC. Arrows indicate trend with increasing cycle number. Inset expanded CO oxidation peak**

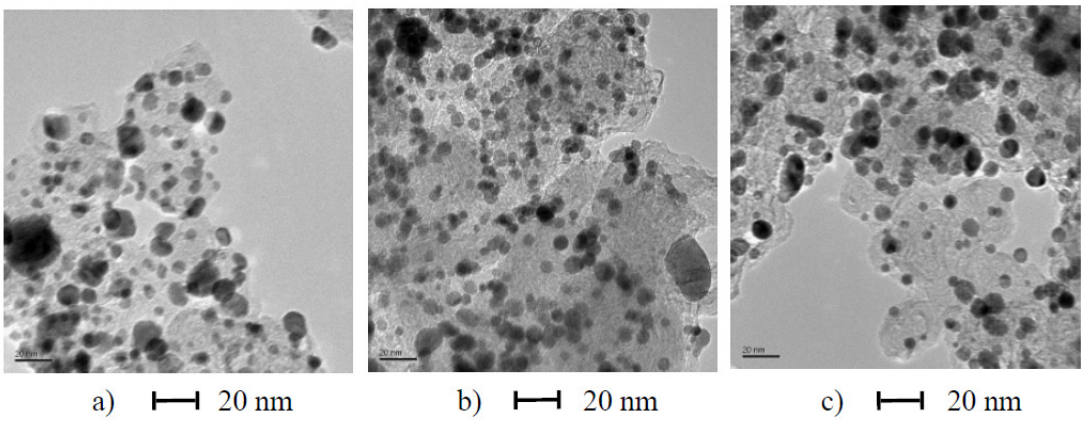

Figure 15. **TEM images of a) as prepared Pt_3Co/C b) Pt_3Co/C post 0.6-1.0 V cycling and c) Pt_3Co/C post 0.6-1.2 V cycling**

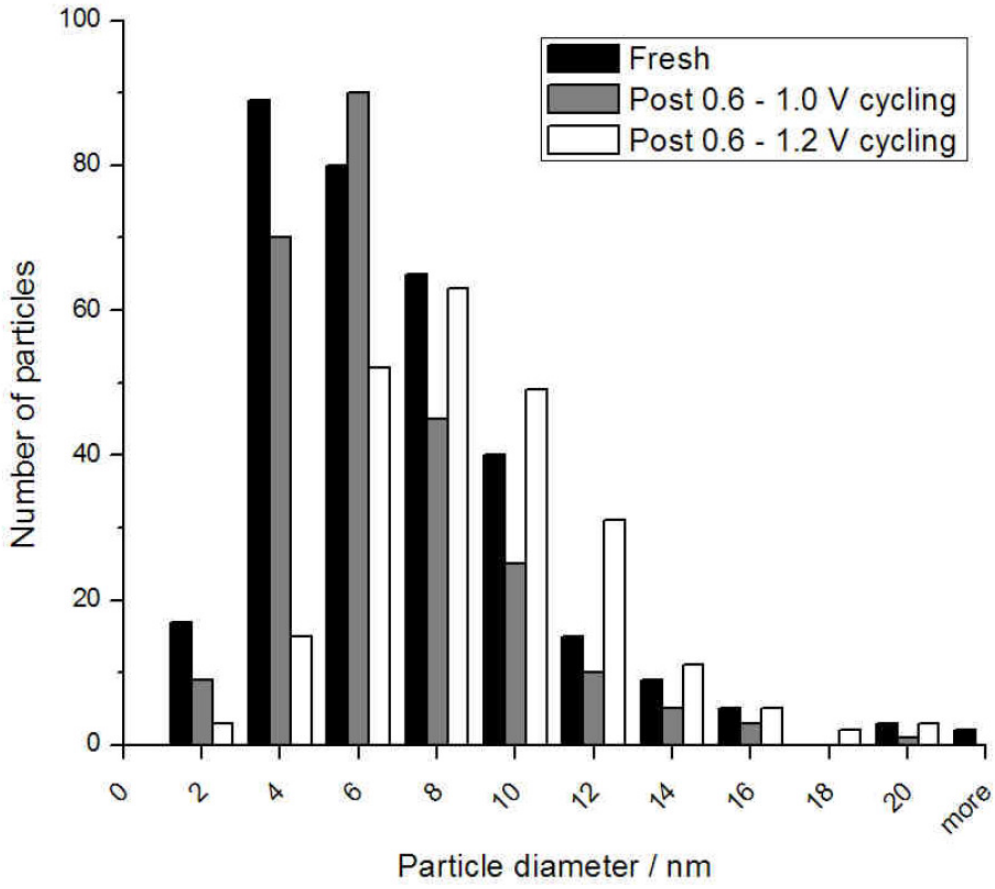

Figure 16. **Particle size analysis of Pt_3Co/C pre and post cycling. Total number of particles measured: fresh 325, post 0.6-1.0 V cycling 258 and post 0.6-1.2 V cycling 237**

ECA loss by platinum dissolution into the electrolyte was confirmed by ICP-MS and found to be potential dependent, as reported by Myers et al. (36). The equivalent of < 1% platinum from the catalyst was found in the electrolyte after 0.6-1.0 V cycling while 4% platinum from the catalyst was found in the electrolyte after 0.6-1.2 V cycling as shown in Figure 17.

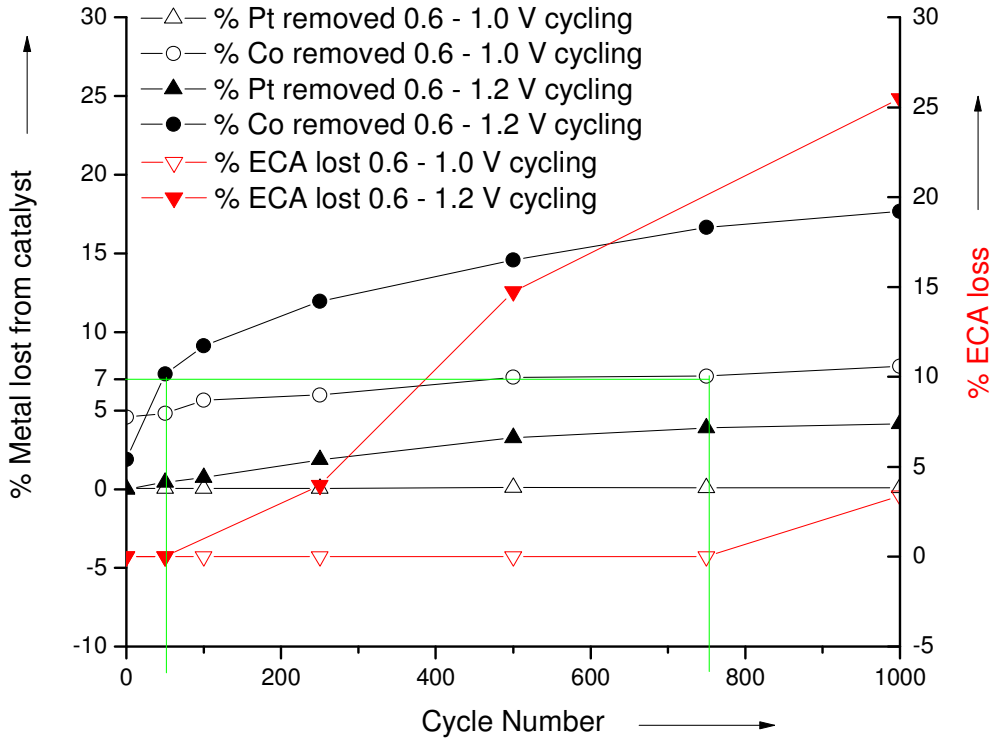

Figure 17. Correlation of dissolved metal and ECA loss for Pt_3Co/C alloy. Green line denotes the cycle number where the onset of ECA loss occurs for each cycling regime and the corresponding % Co loss (7% Co loss in both cases)

The Pourbaix diagram for Co shows that in the potential and pH region of both the electrode acidic boiling pretreatment and cycling test cobalt is soluble (37). Therefore any Co removed from the catalyst will not be redeposited as Co metal and will remain in the electrolyte. Using ICP-MS Co loss was found to occur during both the electrode wetting pretreatment (18% Co removed from the catalyst) and further Co was removed during cycling. Most Co was removed during the first 50 cycles with the rate of loss slowing with increasing cycle number. This initial loss of Co from the particle may be responsible for the ECA increase seen in the voltammetry, as removal of surface Co may expose underlying platinum (surface roughening). After 1000 0.6-1.2 V cycles a

further 18% of the Co from the catalyst was found to be dissolved in the electrolyte. The amount of base metal loss was found to be lower, only 8%, in the 0.6-1.0 V cycling test. However, in both cases a critical Co loss of 25% (18% from pre treatment + 7% from cycling) correlates with the point at which ECA loss is observed as shown by the green line in Figure 17. Repeat testing on the smaller particle sized batch 2 40% Pt_3Co/C catalyst showed the same trend on onset of ECA loss and the same % Pt and Co loss with cycles but increased ECA loss (see Figure 28).

In addition, oxide formation and removal after the 0.6-1.2 V cycling study was investigated using cyclic voltammetry. The cyclic voltammetric profiles to a range of upper limits (window opening CVs) are shown in Figure 18 and the oxide removal peak positions, charges associated with H_{ads}, oxide growth and removal for each catalyst are summarised in Table 5. Comparing with the data presented in Table 2, it can be seen that cycling results in a change in both the amount of oxide grown per unit area and the position of the oxide removal peak. After cycling the 40% Pt_3Co/C alloy less oxide is formed per unit area and the oxide removal peak occurs at a lower overpotential when compared to the as prepared and the acid leached 40% Pt_3Co/C catalysts.

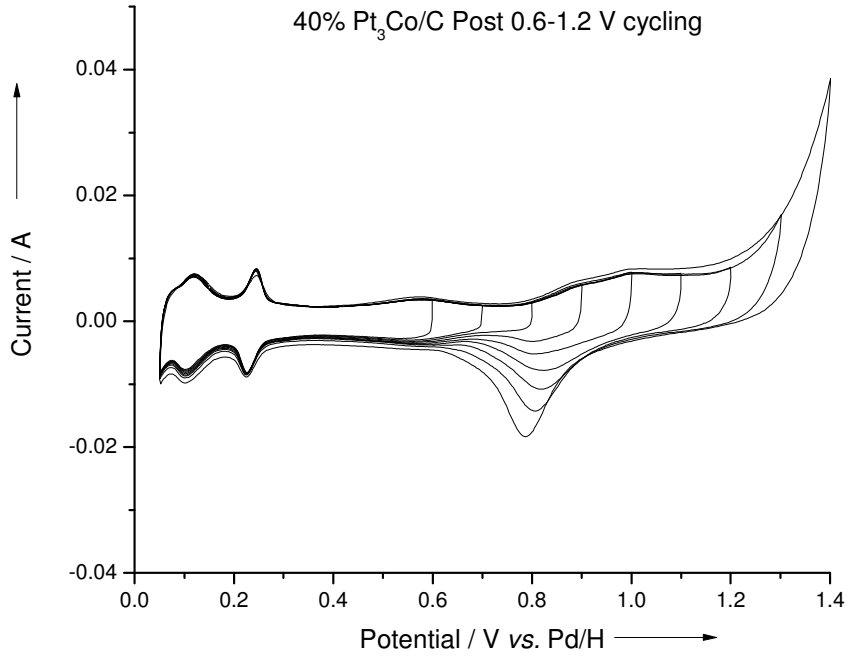

Figure 18. Cyclic voltammetry profiles of 40% Pt_3Co/C at 10 mV s^{-1} post cycling at a range of upper potential limits *vs.* Pd/H in 1 M H_2SO_4 at 80 °C. The CVs were collected sequentially, starting for cycles between 0.05 and 0.6 V and increasing to 0.05 to 1.4 V in 0.1 V increments

Table 5. Electrochemical parameters taken from CVs in Figure 18

Catalyst	Upper limit / V	Oxide reduction peak position / V *vs.* Pd/H	Oxide removal charge / C x 10^2	H_{ads} charge / C x 10^2	ECA / $m^2\ g_{Pt}^{-1}$	Oxide removal charge / H_{ads} charge
40% Pt_3Co/C post 1000 0.6-1.2 V cycles	0.6	-	-	6.93	22	-
	0.7	-	-	6.79	21	-
	0.8	-	-	6.52	21	-
	0.9	0.802	1.57	6.79	21	0.23
	1.0	0.807	57.9	6.66	21	0.87
	1.1	0.824	99.3	6.90	22	1.44
	1.2	0.820	14.4	7.06	22	2.03
	1.3	0.807	18.1	7.10	22	2.55
	1.4	0.787	20.1	7.45	24	2.69

3.4 XAS characterisation of 40% Pt_3Co/C pre and post cycling and post chemical acid leaching

XAS has been used to investigate the effect of both electrochemical cycling and chemical acid leaching in 0.5 M H_2SO_4 on the structure of the Pt_3Co/C alloy. For comparative purposes two Pt/C catalysts (4.7 nm and 7.7 nm) were also studied. The chi and Fourier transform plots for all catalysts in air and H_2 at both the Pt L_{III} and Co K edges are shown in Figure 19 to Figure 23. The fits for all catalysts were in good agreement with the experimental data, with all fits having R_{EXAFS} values < 30 at the Pt L_{III} edge. The fit quality at the Co K edge was good (R_{EXAFS} values < 32) for the powder samples however, a lower quality fit was obtained for the post cycled electrodes especially in H_2, for this reason analysis will focus on the data obtained in air. The lower quality fits for the electrode samples are likely to be the consequence of the low concentration of Co in these samples due to the low electrode loading used in the experiment. The corresponding parameters obtained by fitting the data are detailed in Table 6 and Table 7.

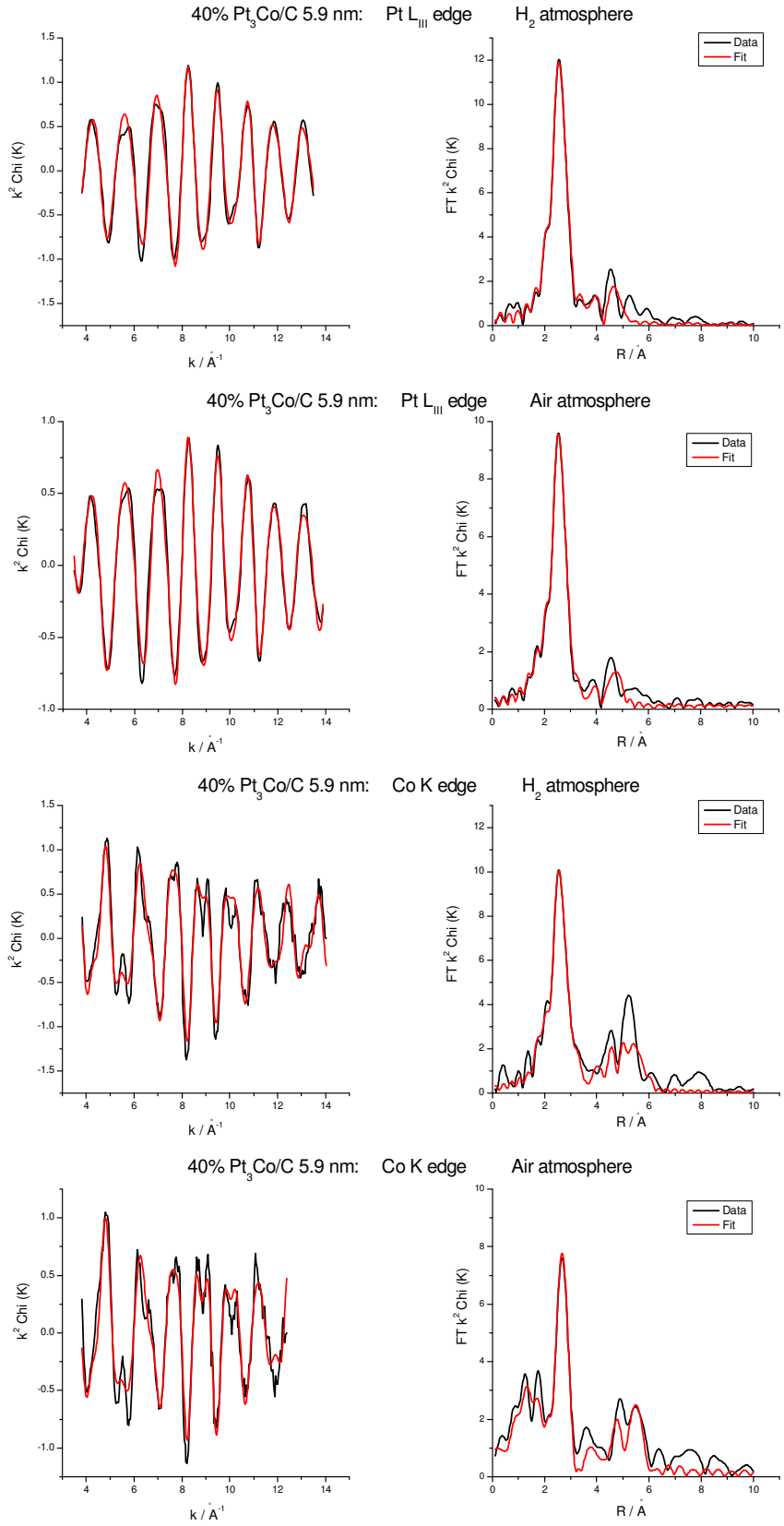

Figure 19. **k^2 weighted experimental chi data (black) and theoretical fit (red) plot and k^2 weighted experimental Fourier transform data (black) and theoretical fit (red) plot for 40% Pt_3Co/C catalyst at the Pt L_{III} and Co K edge in H_2 and air**

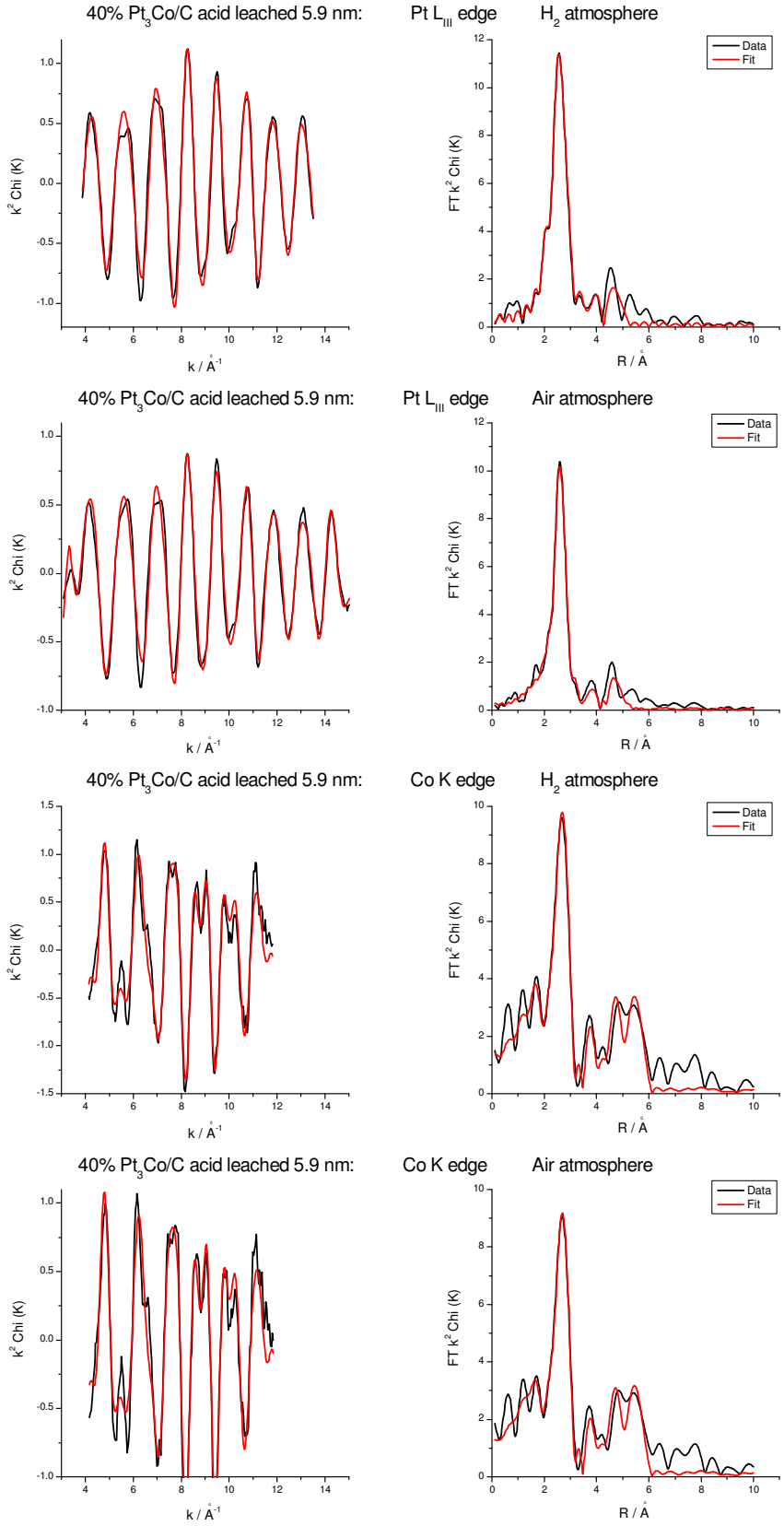

Figure 20. **k^2 weighted experimental chi data (black) and theoretical fit (red) plot and k^2 weighted experimental Fourier transform data (black) and theoretical fit (red) plot for 40% Pt_3Co/C acid leached catalyst at the Pt L_{III} and Co K edge in H_2 and air**

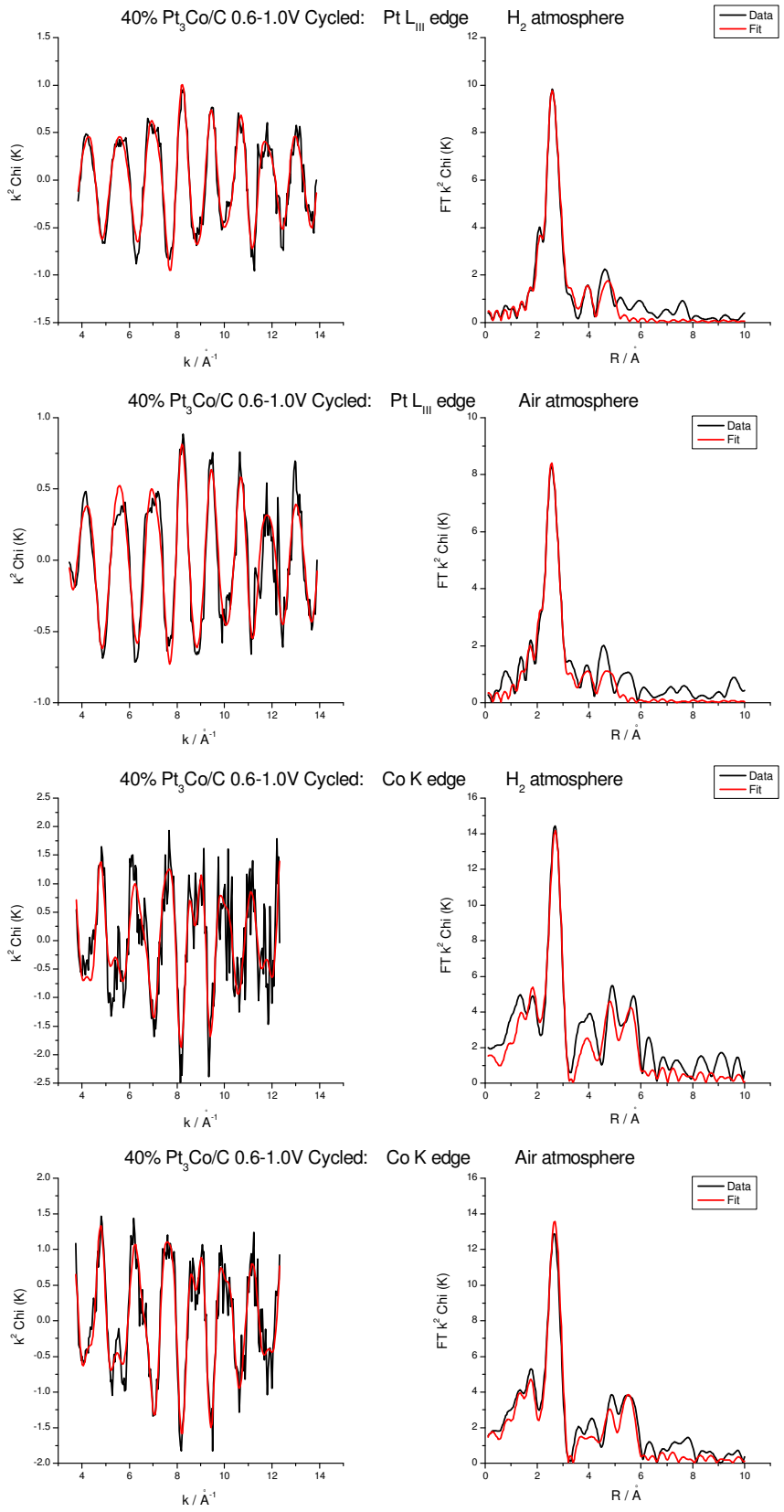

Figure 21. **k^2 weighted experimental chi data (black) and theoretical fit (red) plot and k^2 weighted experimental Fourier transform data (black) and theoretical fit (red) plot for 40% Pt_3Co/C catalyst post 0.6-1.0 V cycling at the Pt L_{III} and Co K edge in H_2 and air**

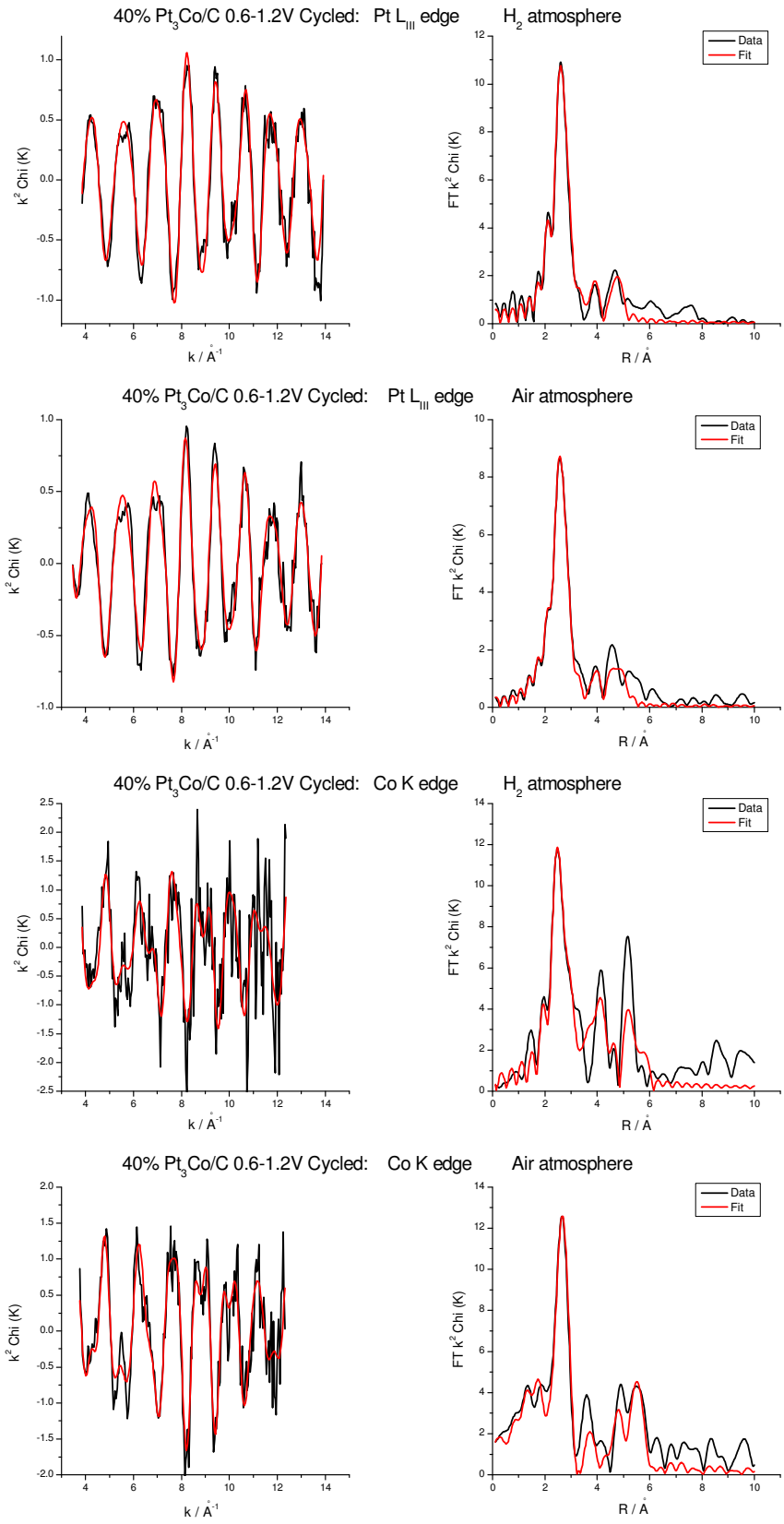

Figure 22. **k^2 weighted experimental chi data (black) and theoretical fit (red) plot and k^2 weighted experimental Fourier transform data (black) and theoretical fit (red) plot for 40% Pt_3Co/C catalyst post 0.6-1.2 V cycling at the Pt L_{III} and Co K edge in H_2 and air**

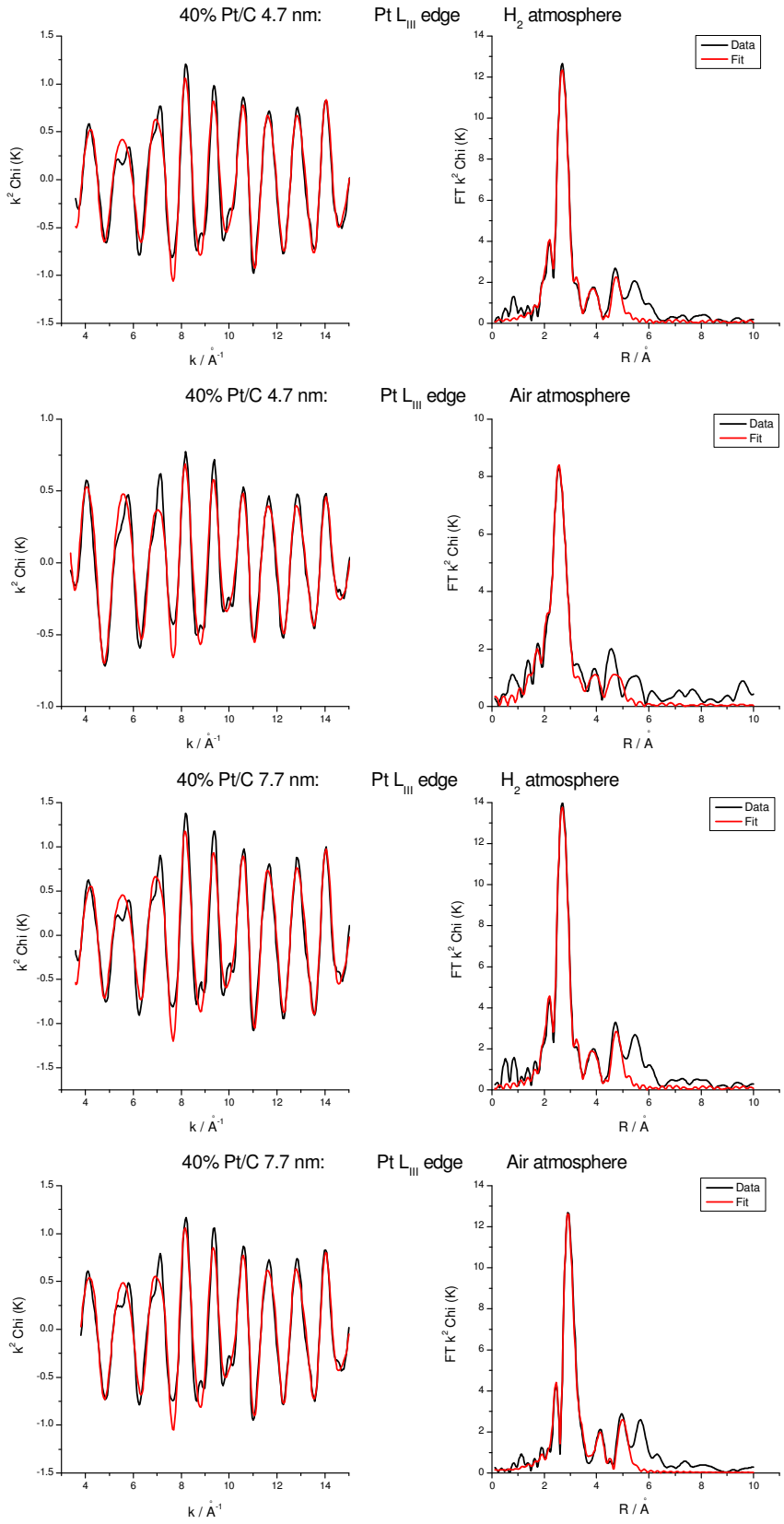

Figure 23. **k^2 weighted experimental chi data (black) and theoretical fit (red) plot and k^2 weighted experimental Fourier transform data (black) and theoretical fit (red) plot for the 40% Pt/C 4.7 nm and 7.7 nm catalysts at the Pt L_{III} in H_2 and air**

Table 6. Structural parameters for Pt_3Co/C alloy and Pt/C catalysts obtained by fitting the Pt L_{III} and Co K edges EXAFS data in Air.

Edge	Catalyst	Absorber neighbour	N	R (Å)	$2\sigma^2$ (Å^2)	E_f (eV)	R_{exafs} (%)
Pt L_{III}	40% Pt_3Co/C 1000 °C	Pt-Pt_1	5.9 (± 0.7)	2.72 (± 0.01)	0.011 (± 0.001)	- 13.2 (± 0.6)	14.8
		Pt-Co	1.2 (± 0.4)	2.68 (± 0.04)	0.010 (± 0.001)		
		Pt-Pt_2	0.6 (± 0.3)	3.85 (± 0.13)	0.004 (± 0.002)		
		Pt-O	0.9 (± 0.3)	2.03 (± 0.04)	0.034 (± 0.007)		
		Pt-Pt_3	5.3 (± 1.6)	4.73 (± 0.08)	0.014 (± 0.002)		
Co K	40% Pt_3Co/C 1000 °C	Co-Pt_1	4.0 (± 0.1)	2.70 (± 0.01)	0.012 (± 0.001)	- 4.7 (± 1.0)	31.5
		Co-Co	0.8 (± 0.2)	2.67 (± 0.02)	0.011 (± 0.001)		
		Co-Pt_2	1.5 (± 0.9)	3.91 (± 0.04)	0.016 (± 0.002)		
		Co-Pt_3	3.7 (± 0.8)	4.72 (± 0.01)	0.007 (± 0.002)		
		Co-O	1.0 (± 0.2)	1.99 (± 0.02)	0.020 (± 0.007)		
		Co-Pt-Pt	4.0 (± 0.1)	5.51 (± 0.02)	0.010 (± 0.003)		
Pt L_{III}	40% Pt_3Co/C 1000 °C acid leached	Pt-Pt_1	5.9 (± 0.3)	2.73 (± 0.01)	0.012 (± 0.001)	-15.0 (± 0.6)	16.2
		Pt-Co	1.1 (± 0.3)	2.68 (± 0.01)	0.010 (± 0.001)		
		Pt-Pt_2	0.8 (± 0.2)	3.85 (± 0.01)	0.004 (± 0.002)		
		Pt-O	1.1 (± 0.2)	2.02 (± 0.02)	0.032 (± 0.006)		
		Pt-Pt_3	5.2 (± 0.9)	4.73 (± 0.01)	0.014 (± 0.002)		
Co K	40% Pt_3Co/C 1000 °C acid leached	Co-Pt_1	4.8 (± 0.4)	2.70 (± 0.01)	0.013 (± 0.001)	- 6.6 (± 1.0)	27.2
		Co-Co	1.1 (± 0.2)	2.65 (± 0.02)	0.007 (± 0.003)		
		Co-Pt_2	2.1 (± 1.1)	3.92 (± 0.03)	0.018 (± 0.008)		
		Co-Pt_3	5.9 (± 0.9)	4.72 (± 0.01)	0.006 (± 0.002)		
		Co-O	0.5 (± 0.3)	2.03 (± 0.05)	0.011 (± 0.009)		
		Co-Pt-Pt	4.8 (± 0.4)	5.53 (± 0.02)	0.011 (± 0.002)		
Pt L_{III}	40% Pt_3Co/C 1000 °C post 0.6-1.0 V cycling	Pt-Pt_1	4.7 (± 0.4)	2.73 (± 0.01)	0.011 (± 0.001)	-13.5 (± 1.2)	29.1
		Pt-Co	1.1 (± 0.2)	2.69 (± 0.01)	0.011 (± 0.002)		
		Pt-Pt_2	2.0 (± 0.7)	3.90 (± 0.01)	0.012 (± 0.004)		
		Pt-O	0.5 (± 0.2)	2.01 (± 0.04)	0.012 (± 0.009)		
		Pt-Pt_3	3.7 (± 1.2)	4.75 (± 0.02)	0.011 (± 0.003)		
Co K	40% Pt_3Co/C 1000 °C post 0.6-1.0 V cycling	Co-Pt_1	7.0 (± 0.1)	2.71 (± 0.01)	0.012 (± 0.001)	- 6.7 (± 1.0)	30.8
		Co-Co	1.0 (± 0.3)	2.66 (± 0.02)	0.010 (± 0.003)		
		Co-Pt_2	1.8 (± 1.6)	3.98 (± 0.05)	0.014 (± 0.010)		
		Co-Pt_3	5.5 (± 1.4)	4.72 (± 0.01)	0.006 (± 0.002)		
		Co-O	1.1 (± 0.4)	2.09 (± 0.03)	0.022 (± 0.014)		
		Co-Pt-Pt	7.0 (± 0.1)	5.53 (± 0.02)	0.014 (± 0.003)		
Pt L_{III}	40% Pt_3Co/C 1000 °C post 0.6-1.2 V cycling	Pt-Pt_1	5.3 (± 0.3)	2.75 (± 0.01)	0.011 (± 0.001)	-14.4 (± 0.9)	25.6
		Pt-Co	1.0 (± 0.2)	2.70 (± 0.01)	0.010 (± 0.002)		
		Pt-Pt_2	0.8 (± 0.2)	3.91 (± 0.01)	0.002 (± 0.002)		
		Pt-O	0.7 (± 0.3)	2.05 (± 0.05)	0.039 (± 0.018)		
		Pt-Pt_3	8.3 (± 1.6)	4.77 (± 0.01)	0.017 (± 0.002)		
Co K	40% Pt_3Co/C 1000 °C post 0.6-1.2 V cycling	Co-Pt_1	6.9 (± 0.9)	2.71 (± 0.01)	0.012 (± 0.002)	- 7.0 (± 1.4)	39.2
		Co-Co	1.2 (± 0.4)	2.65 (± 0.02)	0.010 (± 0.005)		
		Co-Pt_2	2.7 (± 2.0)	3.87 (± 0.05)	0.017 (± 0.010)		
		Co-Pt_3	6.3 (± 1.8)	4.74 (± 0.02)	0.007 (± 0.003)		
		Co-O	1.2 (± 0.6)	2.08 (± 0.04)	0.025 (± 0.025)		
		Co-Pt-Pt	6.6 (± 0.9)	5.53 (± 0.02)	0.012 (± 0.003)		
Pt L_{III}	Pt/C 4.7 nm	Pt-O	1.3 (± 0.1)	2.01 (± 0.01)	0.023 (± 0.004)	-13.4 (± 0.6)	22.4
		Pt-Pt_1	6.3 (± 0.2)	2.76 (± 0.01)	0.012 (± 0.001)		
		Pt-Pt_2	3.2 (± 0.7)	3.90 (± 0.01)	0.018 (± 0.003)		
		Pt-Pt_3	4.1 (± 0.8)	4.80 (± 0.01)	0.011 (± 0.001)		
Pt L_{III}	Pt/C 7.7 nm	Pt-O	0.4 (± 0.2)	1.96 (± 0.06)	0.021 (± 0.017)	-13.1 (± 0.7)	23.0
		Pt-Pt_1	8.8 (± 0.3)	2.76 (± 0.01)	0.011 (± 0.001)		
		Pt-Pt_2	4.7 (± 0.9)	3.90 (± 0.01)	0.010 (± 0.002)		
		Pt-Pt_3	6.3 (± 1.0)	4.80 (± 0.01)	0.002 (± 0.001)		

Table 7. Structural parameters for Pt_3Co/C alloy and Pt/C catalysts obtained by fitting the Pt L_{III} and Co K edges EXAFS data in H_2.

Edge	Catalyst	Absorber neighbour	N	R (Å)	$2\sigma^2$ (Å^2)	E_f (eV)	R_{exafs} (%)
Pt L_{III}	40% Pt_3Co/C 1000 °C	Pt-Pt_1	7.2 (± 0.3)	2.72 (± 0.01)	0.011 (± 0.001)	-13.5 (± 0.6)	16.2
		Pt-Co	1.7 (± 0.2)	2.68 (± 0.01)	0.012 (± 0.001)		
		Pt-Pt_2	2.0 (± 0.4)	3.86 (± 0.01)	0.010 (± 0.001)		
		Pt-Pt_3	5.3 (± 0.9)	4.73 (± 0.01)	0.011 (± 0.002)		
Co K	40% Pt_3Co/C 1000 °C	Co-Pt_1	6.0 (± 0.1)	2.71 (± 0.01)	0.014 (± 0.001)	-4.5 (± 0.7)	30.0
		Co-Co	0.6 (± 0.1)	2.67 (± 0.02)	0.010 (± 0.003)		
		Co-Pt_2	2.6 (± 1.1)	3.89 (± 0.03)	0.019 (± 0.006)		
		Co-Pt_3	2.8 (± 0.6)	4.73 (± 0.01)	0.006 (± 0.010)		
		Co-O	0.5 (± 0.2)	2.05 (± 0.03)	0.010 (± 0.009)		
		Co-Pt-Pt	6.0 (± 0.1)	5.52 (± 0.01)	0.018 (± 0.003)		
Pt L_{III}	40% Pt_3Co/C 1000 °C acid leached	Pt-Pt_1	7.1 (± 0.7)	2.73 (± 0.01)	0.011 (± 0.001)	-11.3 (± 0.7)	16.1
		Pt-Co	1.6 (± 0.2)	2.68 (± 0.01)	0.013 (± 0.002)		
		Pt-Pt_2	2.0 (± 0.4)	3.86 (± 0.01)	0.010 (± 0.002)		
		Pt-Pt_3	5.2 (± 0.9)	4.73 (± 0.01)	0.011 (± 0.002)		
Co K	40% Pt_3Co/C 1000 °C acid leached	Co-Pt_1	5.4 (± 0.5)	2.71 (± 0.01)	0.014 (± 0.001)	-6.4 (± 1.0)	26.5
		Co-Co	1.0 (± 0.2)	2.66 (± 0.01)	0.006 (± 0.002)		
		Co-Pt_2	2.1 (± 1.3)	3.92 (± 0.04)	0.017 (± 0.008)		
		Co-Pt_3	5.9 (± 0.9)	4.73 (± 0.01)	0.005 (± 0.001)		
		Co-O	0.5 (± 0.2)	2.07 (± 0.04)	0.007 (± 0.008)		
		Co-Pt-Pt	5.4 (± 0.5)	5.53 (± 0.01)	0.013 (± 0.002)		
Pt L_{III}	40% Pt_3Co/C 1000 °C post 0.6-1.0 V cycling	Pt-Pt_1	6.7 (± 0.4)	2.74 (± 0.01)	0.012 (± 0.001)	-12.4 (± 0.9)	23.8
		Pt-Co	0.8 (± 0.2)	2.68 (± 0.01)	0.010 (± 0.003)		
		Pt-Pt_2	2.1 (± 0.5)	3.89 (± 0.01)	0.010 (± 0.002)		
		Pt-Pt_3	3.0 (± 1.2)	4.74 (± 0.01)	0.012 (± 0.002)		
Co K	40% Pt_3Co/C 1000 °C post 0.6-1.0 V cycling	Co-Pt_1	6.4 (± 1.0)	2.72 (± 0.01)	0.009 (± 0.001)	-7.1 (± 1.5)	50.1
		Co-Co	1.4 (± 0.8)	2.64 (± 0.04)	0.016 (± 0.009)		
		Co-Pt_2	1.5 (± 1.0)	3.98 (± 0.04)	0.003 (± 0.007)		
		Co-Pt_3	6.8 (± 2.2)	4.73 (± 0.02)	0.005 (± 0.003)		
		Co-Pt-Pt	6.4 (± 1.0)	5.56 (± 0.03)	0.013 (± 0.002)		
Pt L_{III}	40% Pt_3Co/C 1000 °C post 0.6-1.2 V cycling	Pt-Pt_1	7.6 (± 0.4)	2.74 (± 0.01)	0.012 (± 0.001)	-11.7 (± 0.9)	23.9
		Pt-Co	0.8 (± 0.3)	2.69 (± 0.02)	0.013 (± 0.001)		
		Pt-Pt_2	2.2 (± 0.5)	3.87 (± 0.01)	0.010 (± 0.002)		
		Pt-Pt_3	6.1 (± 1.2)	4.75 (± 0.01)	0.011 (± 0.002)		
Co K	40% Pt_3Co/C 1000 °C post 0.6-1.2 V cycling	Co-Pt_1	6.0 (± 0.1)	2.68 (± 0.01)	0.010 (± 0.003)	-4.5 (± 2.0)	62.7
		Co-Co	1.5 (± 0.9)	2.67 (± 0.04)	0.015 (± 0.014)		
		Co-Pt_2	3.2 (± 1.2)	3.94 (± 0.02)	0.002 (± 0.003)		
		Co-Pt_3	3.3 (± 2.8)	4.71 (± 0.05)	0.005 (± 0.008)		
		Co-Pt-Pt	6.0 (± 0.1)	5.48 (± 0.04)	0.012 (± 0.006)		
Pt L_{III}	Pt/C 4.7 nm	Pt-Pt_1	8.6 (± 0.3)	2.76 (± 0.01)	0.011 (± 0.001)	-11.9 (± 0.6)	22.5
		Pt-Pt_2	2.9 (± 0.6)	3.90 (± 0.01)	0.011 (± 0.002)		
		Pt-Pt_3	5.7 (± 1.1)	4.79 (± 0.01)	0.011 (± 0.002)		
Pt L_{III}	Pt/C 7.7 nm	Pt-Pt_1	9.5 (± 0.3)	2.76 (± 0.01)	0.011 (± 0.001)	-12.4 (± 0.7)	25.5
		Pt-Pt_2	3.8 (± 0.9)	3.91 (± 0.01)	0.011 (± 0.002)		
		Pt-Pt_3	7.4 (± 1.4)	4.79 (± 0.01)	0.011 (± 0.002)		

The coordination numbers of the metal neighbours provides useful information when considering the degree of segregation within the catalyst particles. For a completely mixed particle with no segregation, the ratio of Pt to Co coordination numbers ($N_{Pt/Co}$) would be equal to the atomic ratio. In the case of the 40% Pt_3Co/C catalysts $N_{Pt/Co}$ will equal 3 if there is no segregation. Using the fitted EXAFS parameters in Table 7 $N_{Pt/Co}$ for this catalyst is 4.2 ± 0.5 as shown in Equation 4**:**

$$\frac{7.2 \pm 0.3}{1.7 \pm 0.2} = 4.2 \pm 0.5 \qquad \textbf{Equation 4}$$

This value is close to the atomic ratio, indicating a high degree of alloying. However, the deviation from the atomic ratio of 3 suggests that there is some degree of segregation within the structure. This is expected since it is known that heat treatments such as those used to form alloys result in Pt skin formation (33) (segregation of Pt to the surface). After acid leaching $N_{Pt/Co}$ is the same within the fitting error, 4.4 ± 0.9, indicating that acid leaching does change the bulk alloying of the particles. After electrochemical cycling to 1.0 V and 1.2 V $N_{Pt/Co}$ increases significantly to 8.4 ± 0.6 and 9.5 ± 0.7 respectively. This indicates the cycling significantly changes the particle composition, increasing the proportion of Pt within the structure. At the Pt L_{III} edge all catalysts are fully reduced under H_2 while at the Co K edge Co-O neighbours are present for both the Pt_3Co/C and acid leached Pt_3Co/C catalysts indicating that a fraction of Co remains oxidized. This could either be Co at the particle surface or a separate Co oxide phase on the carbon support. It is noted that the post cycled catalysts are fully reduced.

Figure 24 shows the effect of cycling and acid leaching on the Pt-Pt bond length obtained from the fits. Compared to the as prepared Pt_3Co/C alloy, electrochemical cycling results in an increase in Pt-Pt bond length to values more similar to that seen for the Pt/C catalysts. No change in the Pt-Pt bond length is observed following chemical acid leaching and little change in the Pt-Co bond length is observed upon cycling or leaching, however the fitting error increased post-cycling, reflecting the reduced Pt-Co coordination number.

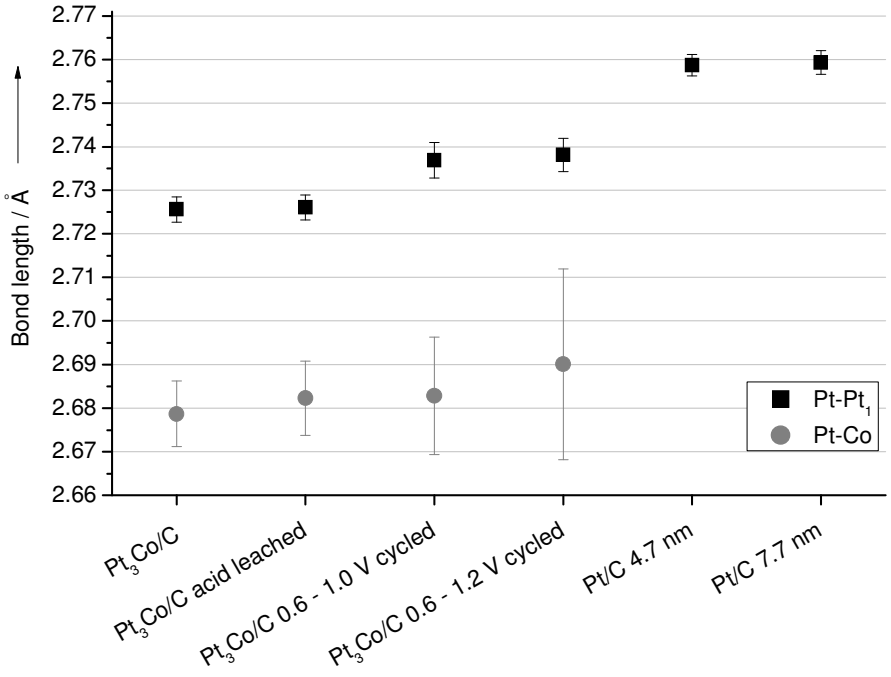

Figure 24. The effect of cycling and acid leaching on the fitted bond lengths for Pt_3Co/C with comparison to Pt/C in H_2

A summary of the first shell coordination numbers in both H_2 and air at the Pt L_{III} edge is shown in Figure 25. In H_2, chemical leaching does not change the number of Pt-Pt or Pt-Co neighbours. This is in agreement with XRD analysis of the fresh and leached catalysts that showed little change in lattice parameter, indicating that the bulk alloy structure was retained and therefore it is concluded that acid leaching primarily affected the surface of the particle. However, electrochemical cycling results in a decrease in the Pt-Co coordination, which is in contrast to the ICP-MS results that showed that both leaching and cycling to 1.0 V remove similar amounts of Co. This suggests that Co removal by electrochemical cycling affects catalyst structure differently to Co removal by chemical leaching. Cycling to 1.0 V or 1.2 V does not change the Pt-Co coordination number despite more Co being removed when cycling to 1.2 V as indicated by the ICP-MS data. A slight increase in Pt-Pt coordination number is observed after 0.6-1.2 V cycling, which may be related to either Co removal or some particle size growth. All catalysts are oxidised in air atmosphere as indicated by the presence of Pt-O neighbours and a reduction in the Pt-Pt coordination number. Post-cycling fewer Pt-O neighbours can be fitted, this is possibly the consequence of particle growth during cycling as fewer Pt-O neighbours are present on the larger particle sized Pt catalyst. A decrease in Pt-Pt

coordination in air compared to H_2 atmosphere is observed for all catalysts as a consequence of the presence of Pt-O neighbours.

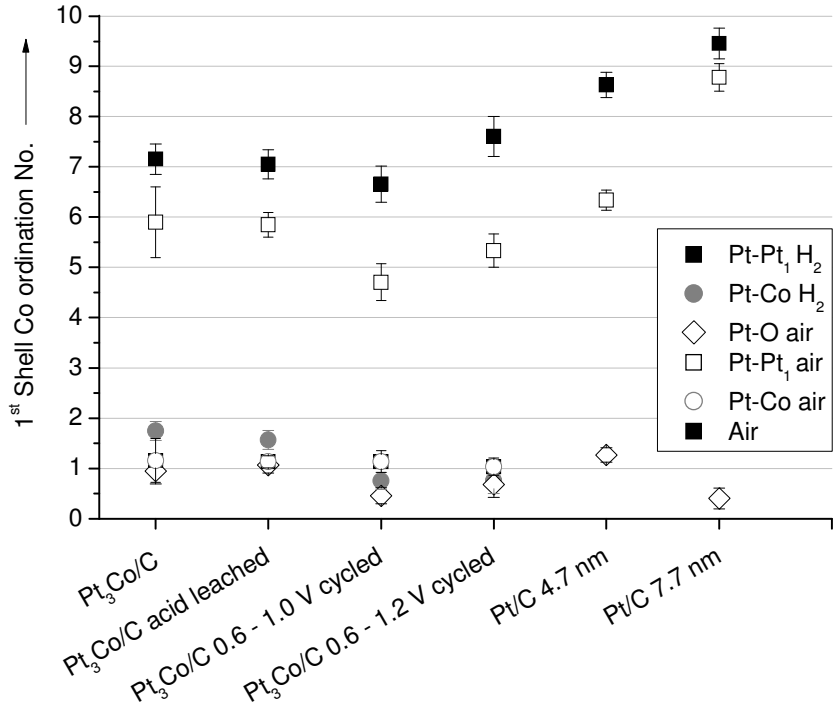

Figure 25. Summary of the fitted coordination number of first shell neighbours at the Pt L_{III} edge

At the Co K edge in H_2 both the 40% Pt_3Co/C and acid leached catalysts are not fully reduced, however, for the post cycled samples the addition of oxygen neighbours did not improve the fit. In air Co-O neighbours could be fitted for all catalysts indicating that after leaching or cycling Co is present at / or sufficiently near the surface of the catalyst to enable oxidation. Within the error of the fit, acid leaching or electrochemical cycling did not change the number of Co-Co neighbours or Co-Co bond length. Acid leaching halved the number of Co-O neighbours indicating removal of surface or unalloyed Co, however, electrochemical cycling did not change the number of Co-O neighbours fitted and the Co-O bond length showed an increase. In contrast to the Pt L_{III} edge data the number of Co-Pt neighbours increased slightly after chemical leaching and significantly after electrochemical cycling as shown in Figure 26. This result indicates that leaching and cycling both change the Co distribution within the sample and the effect is more significant after cycling.

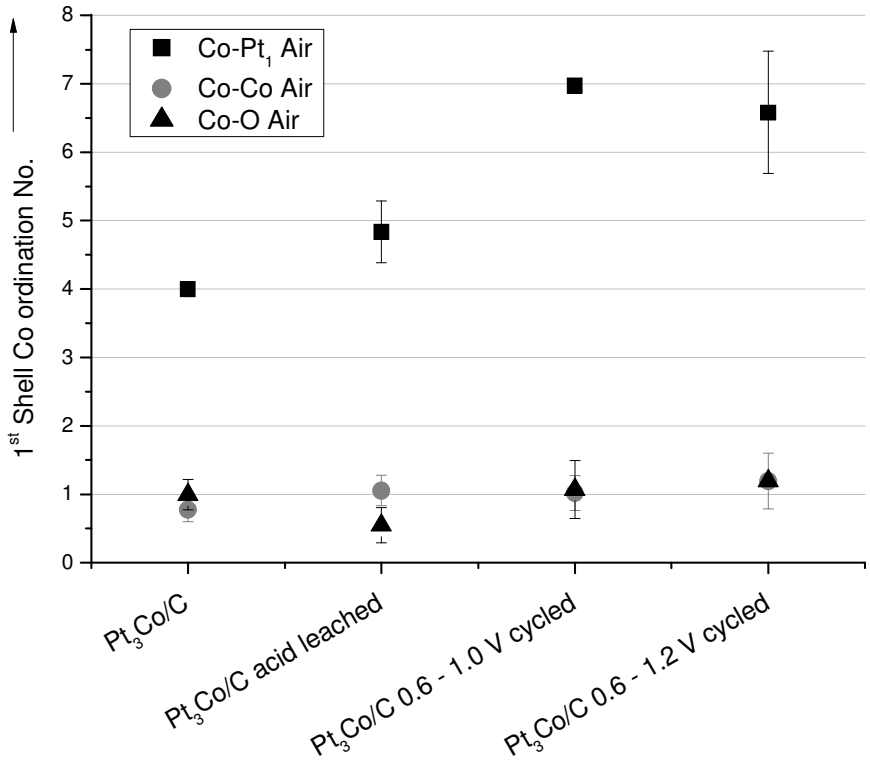

Figure 26. Summary of the fitted coordination number of first shell neighbours at the Co K edge in air

3.5 The effect of particle size on cycle stability

To determine if the increased ECA stability observed for the 40% Pt_3Co/C alloy is a consequence of alloying or merely the result of increased particle size, the stability tests from 0.6-1.0 V and 0.6-1.2 V were also conducted on a range of Pt/C and Pt_3Co/C alloy catalysts with different particle sizes, as detailed in Table 1. For each catalyst tested, the cyclic voltammetric profiles with cycle number are shown in Figure 27. Similar trends to those previously discussed are observed. A summary of the ECA loss and % metal removed during cycles is shown in Table 8.

Table 8. Summary of ECA loss and % metal removed during cycles

Catalyst	XRD mean crystallite size / nm	Cycling regime	% ECA loss after 1000 cycles	%Pt removed	%Co removed
40%Pt/C 900 °C	5.0	0.6-1.0 V	14	< 1	-
		0.6-1.2 V	44	7.3	-
40%Pt/C 1000 °C	7.7	0.6-1.2 V	11	4	-
40% Pt_3Co/C 1000 °C	5.0	0.6-1.2 V	27	4	38
40% Pt_3Co/C 1200 °C	12.6	0.6-1.2 V	0	5	18

40% Pt/C 5 nm 0.6-1.0 V Cycling

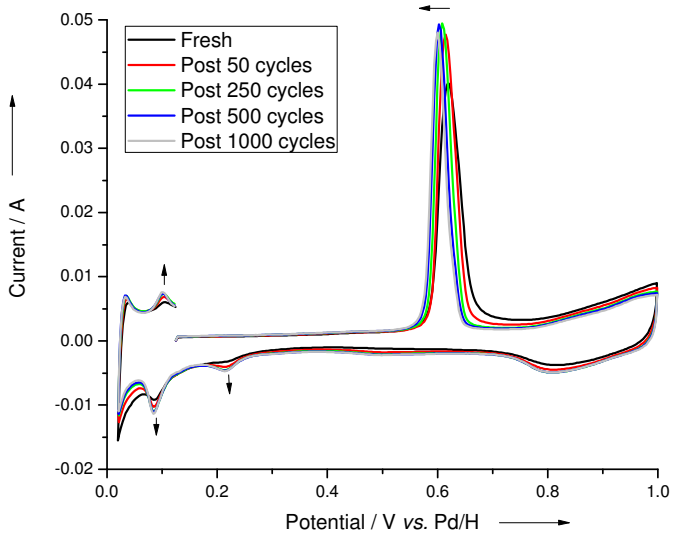

40% Pt/C 5 nm 0.6-1.2 V Cycling

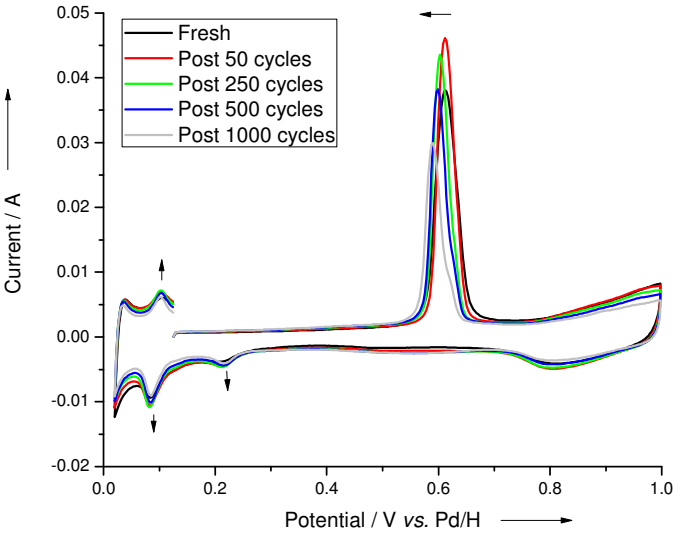

40% Pt/C 7.7 nm 0.6-1.2 V Cycling

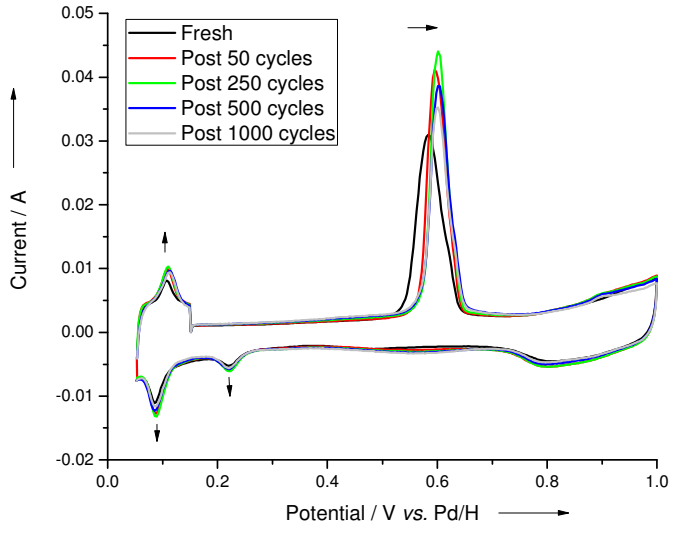

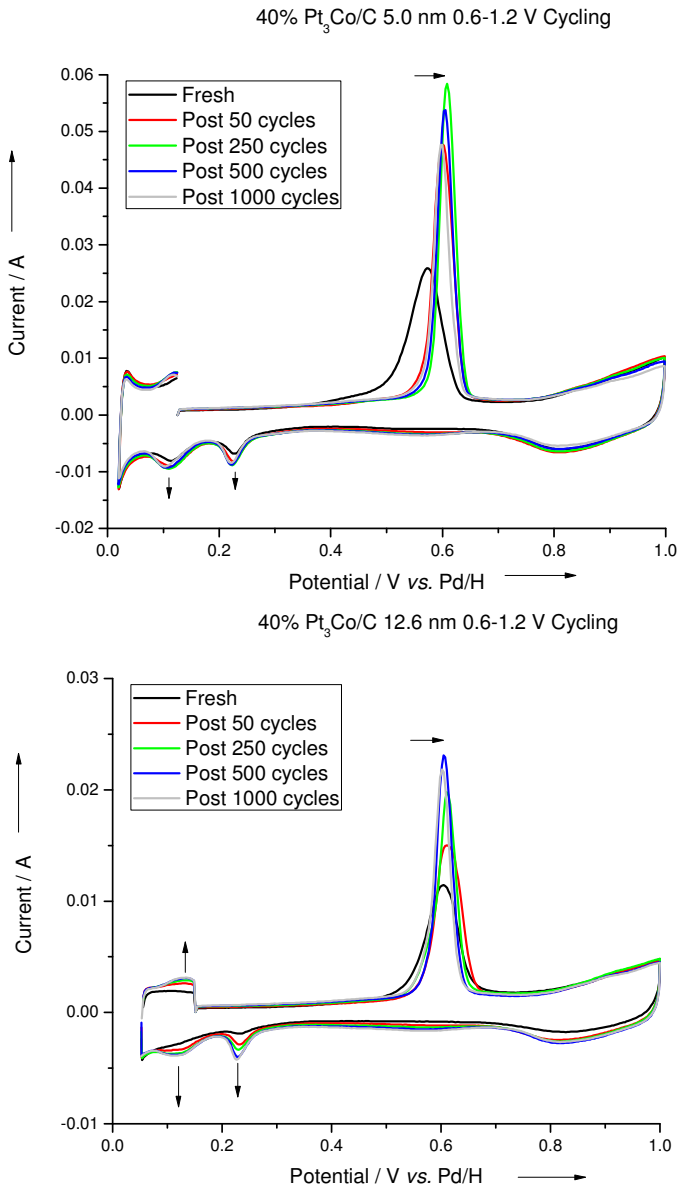

Figure 27. **The effect of number of cycles from 0.6-1.0 V and 0.6-1.2 V *vs.* Pd/H on the CO oxidation voltammetry of Pt/C and Pt_3Co/C catalysts with a range of particle sizes at 10 mV s^{-1} in 1 M H_2SO_4 at 80 ºC. Arrows indicate trend with increasing cycle number**

The % ECA loss after 1000 cycles was determined from the voltammetry for each catalyst and was used to demonstrate the effect of particle size on ECA stability for each cycling regime (Figure 28). The results obtained demonstrate that particle size alone cannot account for the increased stability benefit observed for 40% Pt_3Co/C alloy over 60% Pt/C (2 nm). It was found that if the catalyst particles were large enough, the ECA stability could be dramatically improved even for Pt/C. However, for a given particle size, the corresponding alloy catalysts were more stable, indicating an additional

alloying benefit. ICP-MS analysis of the electrolyte was conducted on samples cycled to 1.2 V. Results indicate that sacrificial removal of the base metal retains ECA for alloys, however, once a critical level of base metal is removed from the catalyst the enhanced catalyst stability is removed. The Pt_3Co/C catalyst that did not exhibit ECA loss during the 0.6-1.2 V cycling (12.6 nm particle size), lost 24% Co.

Figure 28 also illustrates the effect of the upper potential limit on catalyst stability. For both Pt and Pt_3Co/C alloy catalysts the 0.6-1.2 V cycling was found to be more aggressive than cycling from 0.6-1.0 V.

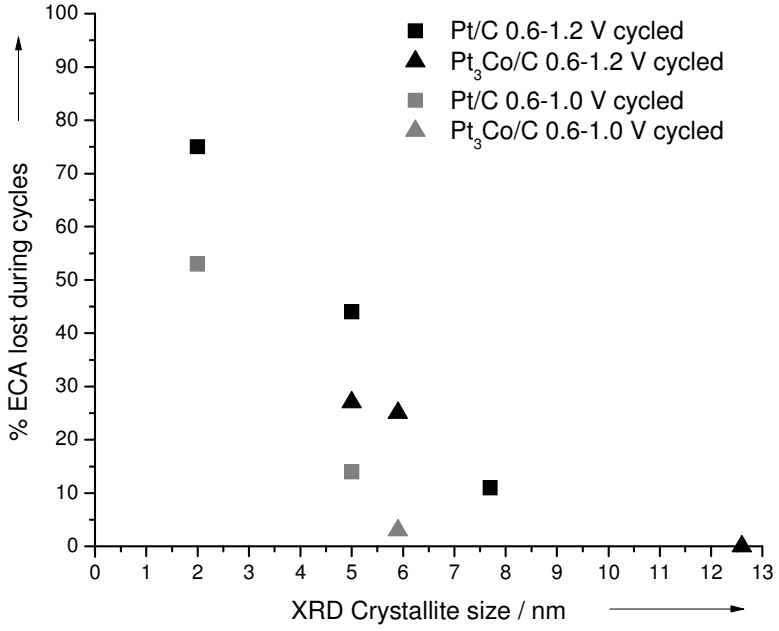

Figure 28. The effect of particle size on the %ECA lost during 0.6-1.0 V and 0.6-1.2 V cycles for Pt/C and Pt_3Co/C alloy catalysts

4. Discussion

4.1 Mechanisms of surface area loss for Pt/C and Pt_3Co/C

Under both electrochemical cycling regimes 40% Pt_3Co/C was found to be more stable than 60% Pt/C (2 nm), although in all tests some electrochemical surface area loss has been observed. Evidenced by the cyclic voltammetry, TEM and ICP-MS results, the dominant mechanisms for the observed ECA loss during cycling for 60% Pt/C (2 nm) and 40% Pt_3Co/C are different.

For 60% Pt/C (2 nm) the ECA loss, progressive change in overpotential of the CO oxidation peak and the appearance of the shoulder at higher overpotentials with increasing cycle number indicate that the catalyst particles grow throughout the test. The slowing rate of ECA loss observed with cycle number suggests that the ECA loss mechanism is more damaging to small particles. This is supported by the TEM particle size analysis, where under both cycling regimes, the smaller particles in the fresh catalyst are lost and larger particles form. The change in the particle size distribution of the catalyst post-cycling is to increase the % of large particles with a decrease in the relative fraction of small particles and a broadening of the size distribution. It has been reported that if coalescence were the mechanism of ECA loss, a log normal distribution with an overall increase in average particle size would be expected as particles close together sinter together to form larger particles (13). Since this is not observed in the TEM images reported in this work, the dominant mechanism for the ECA loss is not considered to be the result of coalescence.

To understand the experimental observations, the processes occurring in both cycling regimes are considered. During cycling, an oxide layer is repeatedly grown and removed. The proportion of Pt atoms as oxide (as opposed to metal) is higher for small particles than larger ones and for particles cycled to the higher potential limit. During the formation of platinum oxide, it is known that (16, 20, 22, 35, 36, 38, 39) soluble Pt^{z+} species can form from either direct electrochemical oxidation of Pt (s) or by chemical dissolution from the platinum oxide layer. Evidence for dissolved platinum was found in this work by analysis of the electrolyte during the cycling tests. A mechanism for particle growth can therefore be proposed in which the anodic sweep oxidises platinum and dissolved Pt^{z+} species are formed, but before the dissolved ions are able to diffuse away from particles the potential is swept cathodically and Pt^{z+} is reduced to platinum metal which deposits on a neighbouring particle. Repeated cycling would result in a progressive increase in particle size. Small particles would be expected to be lost in preference to larger ones, in good agreement with predictions of Darling's model (20) and higher potential limits would be more damaging. This mechanism is described in the literature as the Ostwald-ripening process (17) and is reported (13, 17) to give the observed change in particle size distribution and voltammetry as observed in this work. If this were the sole mechanism of ECA loss it can be calculated that a spherical 2 nm platinum particle would need to grow to 10 nm to account for an 80% ECA loss. Whilst

this result is in good agreement with the TEM particle size analysis, it should be noted that the assumption of spherical particles is inconsistent with the TEM images post cycling. It is therefore concluded that for Pt/C Ostwald ripening is a dominant mechanism accounting of ECA loss during cycling for 60% Pt/C.

However, ICP-MS results confirm that not all dissolved Pt is redeposited by Ostwald ripening. Some dissolved Pt is lost to the electroyte and is therefore no longer able to contribute to the measured ECA. Dissolution of Pt into the electrolyte is most significant when cycling to 1.2 V. After 750 cycles to 1.2 V a concentration in solution equivalent to removal of 10% of platinum in the catalyst was measured. Compared to the MEA environment where dissolved Pt^{z+} can migrate and be reduced in the membrane (10, 11, 17, 18, 21-23, 40), no subsequent reduction and deposition of dissolved Pt can occur in this experiment. The larger electrolyte volume and concentration gradient in the liquid cell may account for the observation that cycling in liquid electrolyte accelerates the ECA loss compared to the MEA environment as dissolution and migration can occur more readily.

In contrast, the cyclic voltammetry and TEM of the Pt_3Co/C alloy showed little evidence that ECA loss via the Ostwald-ripening mechanism was a dominant process. The particle size distribution was relatively unchanged by cycling with only the smallest particles being lost. Post 1.2 V cycling a slight shift in the whole distribution to larger particle size is observed, but without significant broadening of the distribution. It is therefore difficult to separate ECA loss via Ostwald-ripening and by coalescence.

Dissolution of Pt was also found for the Pt_3Co/C catalyst and, therefore, accounts for a proportion of the observed ECA loss. Compared with 60% Pt/C, half as much Pt dissolution occurred for the Pt_3Co alloy during 0.6-1.2 V cycling. Compared to a similar particle sized Pt/C catalyst, the amount of Pt dissolution is similar to but still lower for the alloy. Both the increased size of the alloy particles and the addition of the base metal are thought to enhance the stability of alloy catalysts over platinum only materials (3, 28, 29). Significantly, dissolution of Co occurred during cycling of the Pt_3Co/C alloy. In both cycling regimes a correlation between the initiation of ECA loss and loss of a critical fraction (25%) of the Co was observed. The 12.7 nm Pt_3Co/C catalyst that did not exhibit ECA loss during the 0.6-1.2 V cycling, lost 24% Co. This evidence suggests

that Co is sacrificially lost in preference to Pt, helping maintain ECA and that Co loss from the surface may explain the observed small increase in ECA at start of cycling test.

For both Pt and Pt_3Co/C alloy catalysts 0.6-1.2 V cycling is found to be more aggressive than cycling from 0.6-1.0 V. This is thought to be due to the different amounts of oxide grown at 1.0 V *vs*. 1.2 V. Analysis of the oxide growth per unit H_{ads} area from Figure 8 shows that approximately 2.5 times more oxide is grown at 1.2 V than that grown at 1.0 V. The time spent at high potentials is also increased during cycles to 1.2 V and it is also known that the place exchange mechanism becomes more significant at higher potentials (36) causing particle disruption. All these factors influence the dissolution of Pt and therefore increase ECA loss. The fact that more Co dissolution is observed when cycling to high potentials is also thought to be a consequence of these factors facilitating Co moving to the particle surface where exposure to acid will result in dissolution.

4.2 Comparison of chemical acid leaching and electrochemical cycling

Activity measurements on the Pt_3Co/C alloy catalyst after cycling (11, 12) and chemical leaching have shown a performance decrease that is thought to correlate with Co removal from the catalyst. Chemical leaching and 0.6-1.0 V and 0.6-1.2 V electrochemical cycling removed 25 %, 26% and 36% Co from the catalyst, respectively.

The effect of acid leaching and 0.6-1.2 V electrochemical cycling on the cyclic voltammetry of the 40% Pt_3Co/C catalyst were investigated in this work. Figure 29 summaries the oxide formation of the PtCo alloy catalysts at a range of upper potential limits. The corresponding data for the 2 nm 60% Pt/C catalyst is also shown for comparison. It can be seen that acid leaching the catalyst decreases the amount of oxide formation at potentials up to 1.0 V, then at higher upper potential limits, leaching has little effect on the oxide formation compared to the as prepared 40% Pt_3Co/C catalyst. However, electrochemical cycling from 0.6-1.2 V is found to reduce the extent of oxide formation at all potentials. The extent of oxide formation after cycling was found to be similar to that observed for the 60% Pt/C catalyst. This result indicates that electrochemical cycling results in formation of a surface with platinum like properties,

while acid leaching partially removes the alloy characteristic of increased oxide formation per unit electrochemical area compared to Pt/C. This result is consistent with less Co removal from the alloy after acid leaching compared to 0.6-1.2 V cycling.

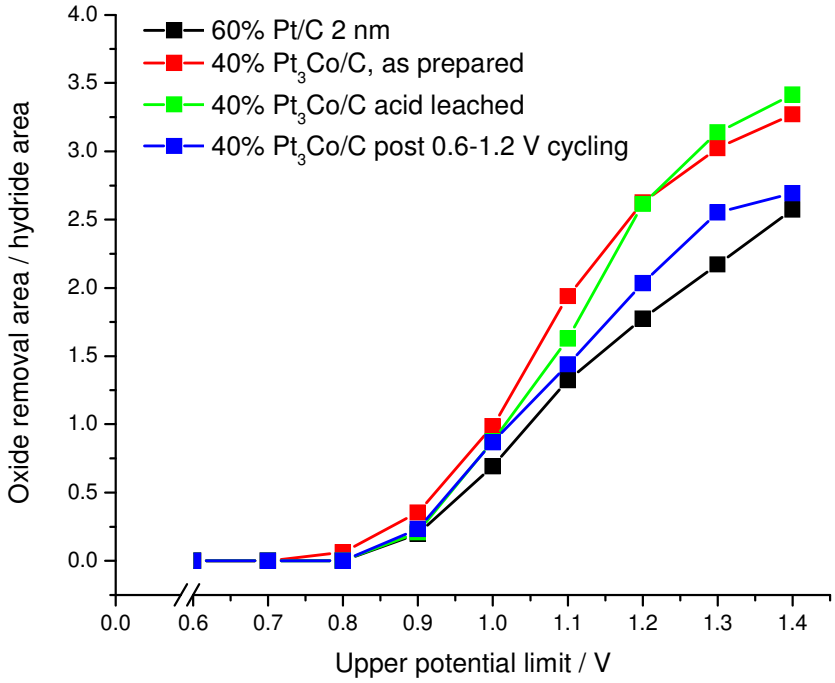

Figure 29. Summary of extent of oxide formation with increasing upper potential limit determined from cycling voltammograms of 60% Pt/C, 40% Pt_3Co/C, as prepared, acid leaching and post 0.6-1.2 V electrochemical cycling

From XAS analysis both electrochemical cycling and acid leaching were shown to change the structure of the catalyst. At the Pt L_{III} edge no significant variations in the EXAFS parameters were found upon acid leaching, indicating that any Co removed was only from the surface layers. This result was consistent with XRD analysis. At the Co K edge acid leaching resulted in a halving of the Co-O neighbors as compared to the as prepared catalyst, indicating Co removal from the outer most layers of the particle. The presence of some Co-O neighbours suggests either a catalyst structure that still has exposed Co at the surface, or dissolved Co in oxidised form remains tapped within the electrode structure, or that the particle structure is such that the Co within the particle may be oxidised. In contrast EXAFS analysis at the Pt L_{III} edge showed the average Pt-Pt bond length increased to more Pt like values and a decrease in the Pt-Co coordination number occurred at the after electrochemical cycling. After 0.6-1.2 V

cycling an increase in the Pt-Pt coordination number also occurred. This indicates that cycling results in a more dramatic change in catalyst structure with removal of Co disrupting a larger proportion of the particle. This effect was most pronounced during cycles to the higher upper potential limit of 1.2 V, correlating with the increased Co dissolution and place exchange under these conditions. At the Co K edge, electrochemical cycling was shown not to alter the number of Co-O neighbours indicating, as for acid leaching, that the cycled catalyst structure still has exposed Co at the surface, or dissolved Co in oxidised form remains tapped within the electrode structure, or the particle structure is such that the Co within the particle may be oxidised. In addition, cycling was found to give a large increase in Co-Pt neighbours when compared to the as prepared catalyst. This indicates cycling causes a rearrangement of the catalyst structure.

In recent work by Chen *et al.* (8) a percolated structure for an acid leached Pt_3Co/C catalyst has been proposed based on characterization by high resolution TEM and aberration-corrected high-angle annular dark-field scanning transmission microscopy, XAS and XRD. It is thought that the dissolution of Co is not confined near the surface and on average, near surface regions are Pt-rich relative to the particle interior. The percolated structure is shown in Figure 30 and it can be seen that this structure differs from a core shell structure since the Pt-enriched regions can extend from surface regions into the particle core.

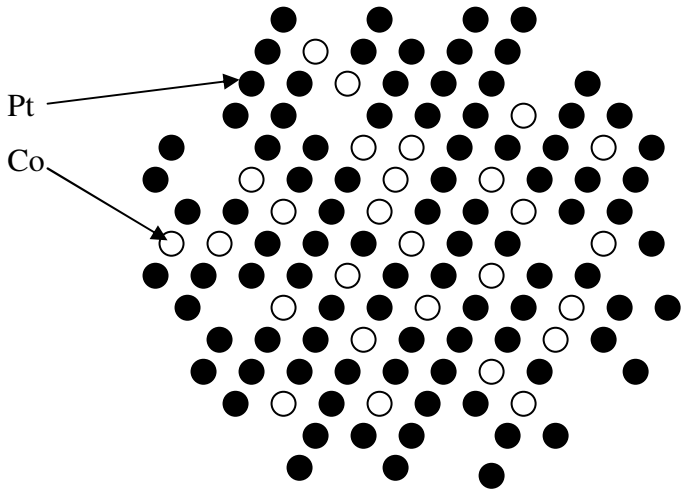

Figure 30. Percolated structure of Pt_3Co/C acid leached adapted from ref (8)

The formation of a percolated structure would allow the presence of oxidised Co within the catalyst structure as observed for the acid leached and electrochemically cycled 40% Pt_3Co/C catalysts studied in this work. However, the presence of trapped Co within the electrode structure cannot be discounted and it is thought that electrochemical cycling will also modify the catalyst structure due to place exchange and the possibility of Oswald ripening occurring under these conditions.

The observed structural changes compared to the as prepared 40% Pt_3Co/C catalyst, may therefore help explain the activity loss observed for Pt_3Co/C alloy catalysts post cycling and leaching. These results strongly indicate that Co within the outmost layers is a requirement for enhanced activity over platinum only catalysts. It has been proposed that one of the primary effects of the alloying element is to modify the electronic properties of platinum, which in turn leads to enhanced activity (8, 41, 42). It is therefore possible that sufficient removal of the alloying element can remove the beneficial change in electronic properties and hence the activity returns to that of platinum only catalyst as observed in this work upon acid leaching. Measurement of the d-band centre of Pt/C, for reference, and the PtCo/C alloys before and after acid leaching and electrochemical cycling would be required to verify this proposal. A method by which this may be achieved is to conduct XAS measurements of the catalysts on both the Pt L_{II} and L_{III} edges and use the method demonstrated by Mansour *et al*. (43) for determining the number of unoccupied d-electron states.

5. Conclusions

The stability of Pt/C and Pt_3Co/C alloy catalysts under 0.6-1.0 and 0.6-1.2 V potentiostatic cycling regimes has been investigated. Cycling to higher upper potential limits was found to be more damaging to the catalyst particles. Significant ECA area loss was observed for the 2 nm Pt/C catalyst while the 5 nm Pt_3Co/C alloy displayed enhanced stability. The mechanisms of ECA loss were found to be different for the two materials. For 60% Pt/C the Ostwald-ripening mechanism could account for a significant proportion of ECA loss observed, however, evidence of platinum dissolution into the electrolyte was also found. For 40% Pt_3Co/C ECA loss occurred via dissolution. ECA loss via Ostwald-ripening or coalescence occurred, but the mechanism could not be distinguished. Enhanced ECA stability was correlated to increasing particle size for

both Pt and PtCo alloy catalysts. At a given particle size PtCo alloy catalysts were shown to be more stable than Pt/C catalysts indicating an additional alloying benefit. Potential dependent Co dissolution from 40% Pt_3Co/C occurred during cycling. Loss of critical levels of Co, defined the onset of Pt ECA loss. Co loss by chemical leaching and cycling has been shown to result in different catalyst structures despite similar amounts of Co removal. Cycling disrupts more of the catalyst structure with more dramatic effects observed for the high potential limit. Leaching and cycling are thought to remove Co from within the outer most layers of the catalyst particle and the presence of sufficient Co in this position seems critical to maintaining activity enhancement over Pt/C.

References

1. S. C. Ball, S. L. Hudson, J. H. Leung, A. E. Russell, D. Thompsett and B. R. C. Theobald, *ECS Transactions*, **11**, 1247 (2007).
2. S. C. Ball, S. L. Hudson, B. R. C. Theobald and D. Thompsett, *ECS Transactions*, **11**, 1267 (2007).
3. H. A. Gasteiger, S. S. Kocha, B. Sompalli and F. T. Wagner, *Applied Catalysis B-Environmental*, **56**, 9 (2005).
4. DoE, WWW.eere.energy.gov/hydrogenandfuelcells/mypp/pdfs/fuel_cells.pdf, in (2006).
5. D. Thompsett, in *Handbook of Fuel cells - Fundamentals, Technology and Applications*, W. Vielstich, H. A. Gasteiger and A. Lamm Editors, John Wiley & Sons, Ltd (2003).
6. U. A. Paulus, A. Wokaun, G. G. Scherer, T. J. Schmidt, V. Stamenkovic, V. Radmilovic, N. M. Markovic and P. N. Ross, *Journal of Physical Chemistry B*, **106**, 4181 (2002).
7. H. R. Colon-Mercado and B. N. Popov, *Journal of Power Sources*, **155**, 253 (2006).
8. S. Chen, W. C. Sheng, N. Yabuuchi, P. J. Ferreira, L. F. Allard and Y. Shao-Horn, *Journal of Physical Chemistry C*, **113**, 1109 (2009).
9. M. F. Mathais, R. Makharia, H. A. Gasteiger, J. J. Conley, T. J. Fuller, C. J. Gittleman, S. S. Kocha, D. P. Miller, C. K. Mittelsteadt, T. Xie, G. S. Yan and P. T. Yu, *Interface, Electrochemical Society*, 24 (2005).
10. P. Yu, M. Pemberton and P. Plasse, *Journal of Power Sources*, **144**, 11 (2005).
11. S. Ball, S. Hudson, B. Theobald and D. Thompsett, *ECS Transactions*, **1**, 141 (2006).
12. S. C. Ball, S. L. Hudson, B. R. C. Theobald and D. Thompsett, *ECS Transactions*, **3**, 595 (2006).
13. R. Borup, J. Meyers, B. Pivovar, Y. S. Kim, R. Mukundan, N. Garland, D. Myers, M. Wilson, F. Garzon, D. Wood, P. Zelenay, K. More, K. Stroh, T.

Zawodzinski, J. Boncella, J. E. McGrath, M. Inaba, K. Miyatake, M. Hori, K. Ota, Z. Ogumi, S. Miyata, A. Nishikata, Z. Siroma, Y. Uchimoto, K. Yasuda, K. I. Kimijima and N. Iwashita, *Chemical Reviews*, **107**, 3904 (2007).
14. S. C. Ball, S. L. Hudson, D. Thompsett and B. Theobald, *Journal of Power Sources*, **171**, 18 (2007).
15. S. S. Zhang, X. Z. Yuan, H. J. Wang, W. Merida, H. Zhu, J. Shen, S. H. Wu and J. J. Zhang, *International Journal of Hydrogen Energy*, **34**, 388 (2009).
16. J. Van Muylder, N. De Zoubov and M. Pourbaix, in *Atlas of Electrochemical Equilibra in Aqueous Solutions*, M. Pourbaix Editor, p. 378, National Association of Corrosion Engineers, Texas, USA (1974).
17. P. J. Ferreira, G. J. la O, Y. Shao-Horn, D. Morgan, R. Makharia, S. Kocha and H. A. Gasteiger, *Journal of the Electrochemical Society*, **152**, A2256 (2005).
18. Y. Shao-Horn, W. C. Sheng, S. Chen, P. J. Ferreira, E. F. Holby and D. Morgan, *Topics in Catalysis*, **46**, 285 (2007).
19. S. Maass, F. Finsterwalder, G. Frank, R. Hartmann and C. Merten, *Journal of Power Sources*, **176**, 444 (2008).
20. R. M. Darling and J. P. Meyers, *Journal of the Electrochemical Society*, **150**, A1523 (2003).
21. W. Bi, G. E. Gray and T. F. Fuller, *Electrochemical and Solid State Letters*, **10**, B101 (2007).
22. E. Guilminot, A. Corcella, F. Charlot, F. Maillard and M. Chatenet, *Journal of the Electrochemical Society*, **154**, B96 (2007).
23. K. Yasuda, A. Taniguchi, T. Akita, T. Ioroi and Z. Siroma, *Physical Chemistry Chemical Physics*, **8**, 746 (2006).
24. H. R. Colon-Mercado, H. Kim and B. N. Popov, *Electrochemistry Communications*, **6**, 795 (2004).
25. P. Piela, C. Eickes, E. Brosha, F. Garzon and P. Zelenay, *Journal of the Electrochemical Society*, **151**, A2053 (2004).
26. N. Ramaswamy, N. Hakim and S. Mukerjee, *Electrochimica Acta*, **53**, 3279 (2008).
27. J. Peron, Y. Nedellec, D. J. Jones and J. Roziere, *Journal of Power Sources*, **185**, 1209 (2008).
28. T. Madden, D. Weiss, N. Cipollini, D. Condit, M. Gummalla, S. Burlatsky and V. Atrazhev, *Journal of the Electrochemical Society*, **156**, B657 (2009).
29. W. B. Pearson, *A Handbook of Lattice Spacings and Structures of Metals and Alloys*, Pergamon Press (1964).
30. U. A. Paulus, A. Wokaun, G. G. Scherer, T. J. Schmidt, V. Stamenkovic, N. M. Markovic and P. N. Ross, *Electrochimica Acta*, **47**, 3787 (2002).
31. A. Kuzume, E. Herrero and J. M. Feliu, *Journal of Electroanalytical Chemistry*, **599**, 333 (2007).
32. D. S. Strmcnik, P. Rebec, M. Gaberscek, D. Tripkovic, V. Stamenkovic, C. Lucas and N. M. Markovic, *Journal of Physical Chemistry C*, **111**, 18672 (2007).
33. V. Stamenkovic, T. J. Schmidt, P. N. Ross and N. M. Markovic, *Journal of Electroanalytical Chemistry*, **554**, 191 (2003).
34. F. Maillard, M. Eikerling, O. V. Cherstiouk, S. Schreier, E. Savinova and U. Stimming, *Faraday Discussions*, **125**, 357 (2004).
35. S. Mitsushima, S. Kawahara, K. I. Ota and N. Kamiya, *Journal of the Electrochemical Society*, **154**, B153 (2007).
36. X. P. Wang, R. Kumar and D. J. Myers, *Electrochemical and Solid State Letters*, **9**, A225 (2006).

37. E. Deltombe and M. Pourbaix, in *Atlas of Electrochemical Equilibra in Aqueous Solutions*, M. Pourbaix Editor, p. 378, National Association of Corrosion Engineers, Texas, USA (1974).
38. K. I. Ota, S. Nishigori and N. Kamiya, *Journal of Electroanalytical Chemistry*, **257**, 205 (1988).
39. M. Azaroual, B. Romand, P. Freyssinet and J. R. Disnar, *Geochimica Et Cosmochimica Acta*, **65**, 4453 (2001).
40. T. Akita, A. Taniguchi, J. Maekawa, Z. Sirorna, K. Tanaka, M. Kohyama and K. Yasuda, *Journal of Power Sources*, **159**, 461 (2006).
41. V. R. Stamenkovic, B. S. Mun, M. Arenz, K. J. J. Mayrhofer, C. A. Lucas, G. F. Wang, P. N. Ross and N. M. Markovic, *Nature Materials*, **6**, 241 (2007).
42. V. Stamenkovic, B. S. Mun, K. J. J. Mayrhofer, P. N. Ross, N. M. Markovic, J. Rossmeisl, J. Greeley and J. K. Norskov, *Angewandte Chemie-International Edition*, **45**, 2897 (2006).
43. A. N. Mansour, J. W. Cook and D. E. Sayers, *Journal of Physical Chemistry*, **88**, 2330 (1984).

Chapter 4. Probing the structure of Operating Fuel Cell Cathode Catalysts Using XAS – Part I

Some of the results presented in this chapter were previously presented in ECS Transactions, 16 (2) 1395-1401 (2008) (1).

1. Introduction

Fuel cell catalyst development increasingly relies on the ability to prepare structured nanoparticles of platinum and platinum alloys. Specific arrangements of surface and bulk atoms are necessary to optimise catalytic activity and selectivity (2-5). Determination of the detailed structure of catalyst particles is therefore essential to understand the relationship between structure and catalytic activity and to identify the optimum particle structure.

X-ray absorption spectroscopy (XAS) has been shown to be a powerful technique for providing electronic and structural information such as the oxidation state and local coordination (numbers and identity of neighbours) of the absorbing atom. For these reasons XAS has been increasingly applied to the study of fuel cell catalysts. Studies have been reported using three different *in situ* environments; (i) of catalyst powders in gas treatment cells (2, 3), (ii) of electrode layers in three electrode electrochemical cells with liquid electrolyte (4-6) and (iii) of membrane electrode assemblies (MEAs) mounted in fuel cells (7-11). Whilst the first two environments provide useful information for characterising fuel cell catalysts, the optimum *in situ* environment to enable correlation of catalytic activity with structural insights provided by XAS is as an MEA under realistic fuel cell operating conditions (7, 9), know as *operando* studies.

To enable XAS in an operating fuel cell, some unavoidable modifications of the cell design are required. Such modifications include replacing standard MEA components with elements that do not absorb the X-rays or removing interfering elements from the electrode in the region of the window. The detrimental absorption of the graphite flow field plates must also be addressed. These modifications can result in deviation from real world fuel cell operation. For example, in order to achieve sufficient signal in transmission mode relatively high catalyst loadings, on the order of 1-2 mg_{Pt} cm^{-2}, need

to be used, as demonstrated by the work of Viswanathan *et al.* (11) and Roth *et al*. (8). These high loadings result in thick catalyst layers and can lead to poor utilisation of the catalyst. More realistic catalyst loadings (0.8 mg_{Pt} cm^{-2}) were used by Wiltshire *et al*. (9) who used fluorescence detection. Wiltshire *et al*. also reduced the graphite flow field plate thickness to less than half of that used in the transmission experiments of Viswanathan *et al.* and Roth *et al*. Recent work by Witkowska *et al.,* who reported a cell designed for both fluorescence and transmission XAS at low energy edges, e.g. the Co K edge, demonstrates the advantage of further reducing the graphite absorption (7, 12). However, data acquisition times of 1 hr were required and therefore only steady state information was obtained. To achieve optimum catalyst activity pressurised fuel cell systems are commonly used, however, the *in situ* designs previously described all operate at atmospheric or low pressures.

This work aims to explore the relationship between fuel cell cathode catalyst activity and structure using X-ray absorption spectroscopy (XAS) to provide element specific information on the arrangement of atoms and their nearest neighbours (13, 14). To achieve this aim an *operando* XAS fuel cell system has been designed that enables transmission XAS measurements to be conducted on cathode catalysts operating at 10 psig. Validation of the cell design for measuring catalytic activity and findings for Pt/C and Pt_3Co/C catalysts during time resolved potential step measurements using XAS data acquisition times of 12 s will be presented.

1.1. Designing a Fuel Cell to enable time resolved *operando* XAS studies of cathode catalysts

Current conventional fuel cell design incorporates key features that enable optimum performance to be achieved from fuel cell catalyst materials. Typically an MEA is compressed between two solid, highly conducting graphite flow field plates that transport reactant gases to and product water away from the MEA. Cells generally operate at elevated pressures (e.g. 150 kPa_{abs}) and temperatures, (80 °C with current research focusing on increasing the temperature of operation to 120 °C to improve performance and system efficiency). Sufficient reactant gas stoichiometries are required and gases are often humidified in order to help hydrate the MEA and therefore decrease resistive losses of the proton exchange membrane. Sufficient cell compression is needed

to minimise electronic contact resistances between the bipolar plates and gas diffusion media and between the gas diffusion media and catalyst layers, however, the compression used needs to be optimal to prevent damage of the MEA components that may result in restricted gas/water access or pinholing of the membrane resulting in a cell short circuit.

State of the art commercial MEAs often use thin membranes (~25 µm) to lessen resistive losses. Pt/C is used as the hydrogen oxidation catalyst for anode electrodes since the kinetics of hydrogen electrooxidation are very facile on Pt. Due to these rapid kinetics Gasteiger *et al*. report that Pt loadings as low as 0.05 $mg_{Pt}\,cm^{-2}$ on the anode may be used without the need to compensate the measured cell performance for contributions from anode polarisation (15). On the cathode Pt/C or carbon supported Pt alloy catalysts are used with loadings in the region of 0.4 $mg_{Pt}\,cm^{-2}$. In addition, careful optimisation of the catalyst layer structure and global MEA structure is required to attain optimum cell performance. The exact structures required are still a source of much research and depend strongly on the cell operating conditions.

Despite the aforementioned engineering and materials solutions, voltage losses in the fuel cell are still observed and need to be corrected for when reporting catalyst activity. These include hydrogen crossover, ohmic losses associated with the conductivity of protons through the membrane and electronic contact resistances between plate and MEA components, and mass transport losses. The corrected cell performance is, thus, a measure of the activation loss attributed to the poor activity of Pt for the oxygen reduction reaction on the cathode.

In this work a fuel cell to enable time resolved *operando* XAS studies of cathode catalysts has been designed to allow catalyst structure to be probed during operation. Ideally the cell would include all the beneficial engineering and materials properties of the conventional fuel cell described above so that the studies probe a realistic representation of the catalyst under typical operating conditions. The fuel cell design for this work was based on the research group's cell used for fluorescence XAS investigations conducted at elevated temperatures and ambient pressures (9). The cell active area is 12.57 cm^2. To enable XAS to be collected in transmission mode the cell needed modification to include thinned graphite windows on both the anode and

cathode sides of the cell. In addition it was found that the window dimensions needed to be reduced from 60 mm x 40 mm (in the fluorescence cell and version I transmission cell design) to 16 mm x 6 mm in the version II transmission cell. To further improve the structural rigidity of the cell, the thickness of the perspex end plates was also doubled. These modifications were found to provide improved electrical contact and MEA compression in the region of the X-ray window. A gas control box was also added to the system to enable operation at elevated pressures with regulated gas flows. Unlike experiments conducted with the fluorescence cell design, the additional gas control systems enabled 100% H_2 feed gas to be used at the anode during experiments facilitating reduced anode polarisation. The transmission XAS cell (version II) is shown in Figure 1. Technical drawings of the cell may be found in the Electronic Appendix.

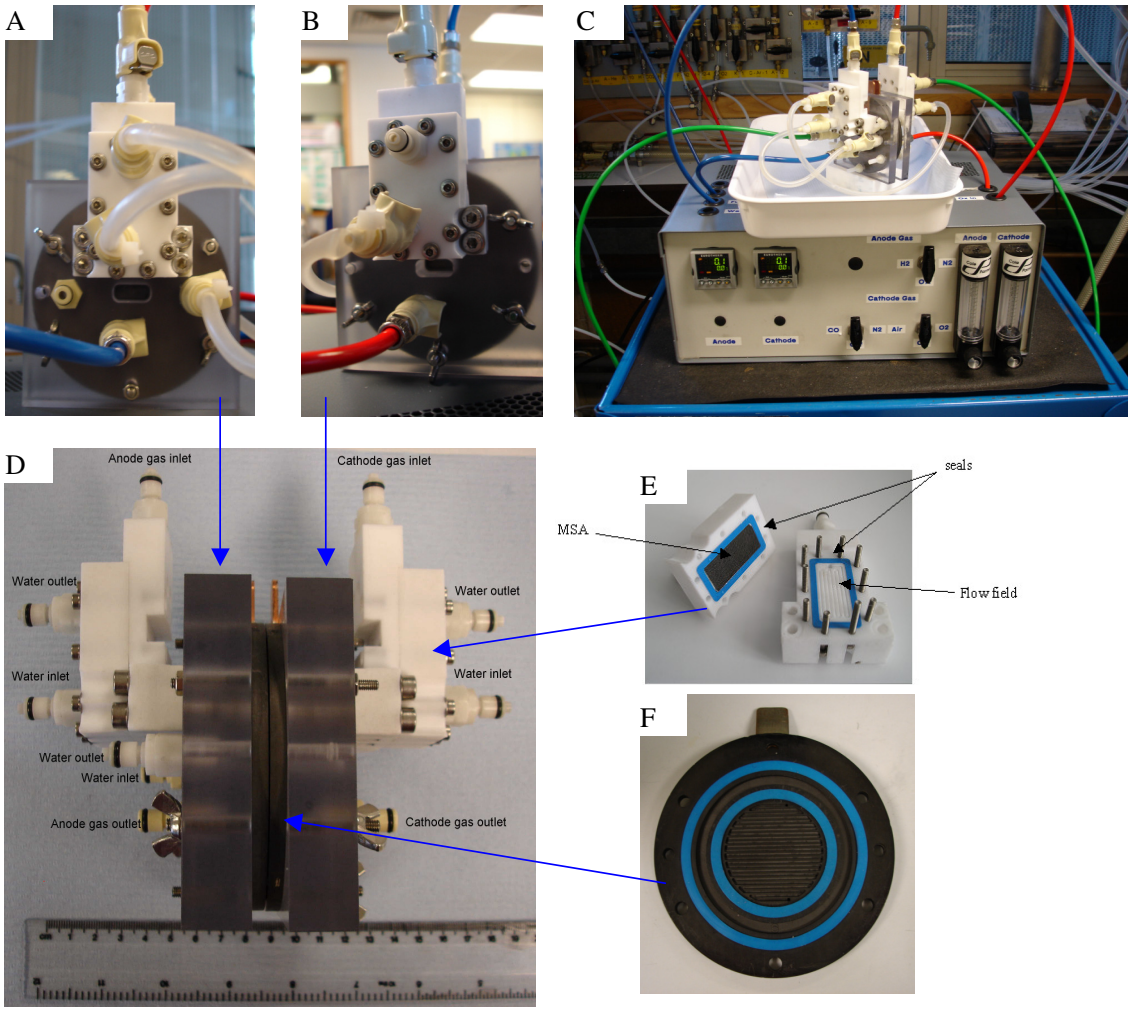

Figure 1. **XAS transmission Fuel cell. (A) Anode side (B) Cathode side (C) Cell connected to gas control box (D) Side view (E) Humidifiers (F) Graphite flow field plate with thinned 16 mm x 6 mm window on anode and cathode sides and water heating channel (version II)**

As for conventional fuel cells, the transmission XAS cell operates at elevated pressure (10 psi) and elevated temperature (65 °C, maximum temperature obtainable using a circulating water bath to pump hot water through the water channel in the graphite plate). The MEA is compressed between two graphite flow field plates surrounded by perspex compression plates using six threaded screws. The incoming reactant gases are humidified by flowing over a membrane substrate assembly (MSA) that is in contact with hot water. Gas flow rates of 60 ml min^{-1} on both the anode and cathode were chosen to provide sufficient stoichiometry for reaction. However, unlike conventional fuel cells the *operando* XAS cell also has to allow time resolved X-ray Absorption Spectroscopy data to be collected. The cell therefore has to incorporate a low absorbance X-ray path and have the catalyst of interest in sufficient concentration to obtain a high signal to noise response. These XAS requirements lead to some unavoidable modifications of the conventional fuel cell design.

To incorporate a low absorbance X-ray pathway the humidifiers were attached to the cell so as to be out of the way of the incoming beam. Standard MEA components such as a Pt/C anode contain interfering elements, therefore either the Pt had to be removed from the electrode in the region of the window, the approach taken by Roth *et al.* (8), or the anode catalyst had to be replaced with a non-interfering element such as Pd/C. Due to possible problems with current distribution in the region of the window caused by removing Pt in this area a Pd/C anode was used for all *operando* XAS measurements. The detrimental absorption of the graphite flow field plates was also addressed. This was achieved by thinning to form graphite windows 16 mm x 6 mm and 1.5 mm thick on both the anode and cathode sides of the cell. This same approach was used by Viswanathan *et al.* (11) and Roth *et al.* (8), however, in the XAS Transmission cell the total graphite thickness was further reduced by 1 mm to reduce graphite absorbance. For *operando* experiments conducted at the Co K edge and to obtain sufficient data quality at ms time resolution the plate design was modified further (version III) to completely remove the graphite from the window area and the resultant hole was sealed with Kapton film to form a gas and water tight seal (see section 4.4 and Chapter 5).

In order to achieve sufficient signal in transmission mode relatively high catalyst loadings need to be used (8, 11), loadings of 2.0-3.3 $mg_{Pt}\,cm^{-2}$ were used in these

experiments. These high loadings result in thick catalyst layers that have a very different structure to the conventional 0.4 $mg_{Pt}\,cm^{-2}$ layers.

The other main way in which the *operando* XAS cell differs from conventional designs is that the thin membranes typically used in conventional cells were not able to be used as problems were encountered with sealing the cell quickly and easily as is required when conducting experiments on the beamline, therefore a thicker membrane Nafion 115 (125 µm) was used. In light of these modifications away from conventional fuel cell designs, the Transmission XAS fuel cell has been evaluated to determine if the *operando* studies will probe a realistic representation of the catalyst under typical operating conditions.

2. Validation of Cell design

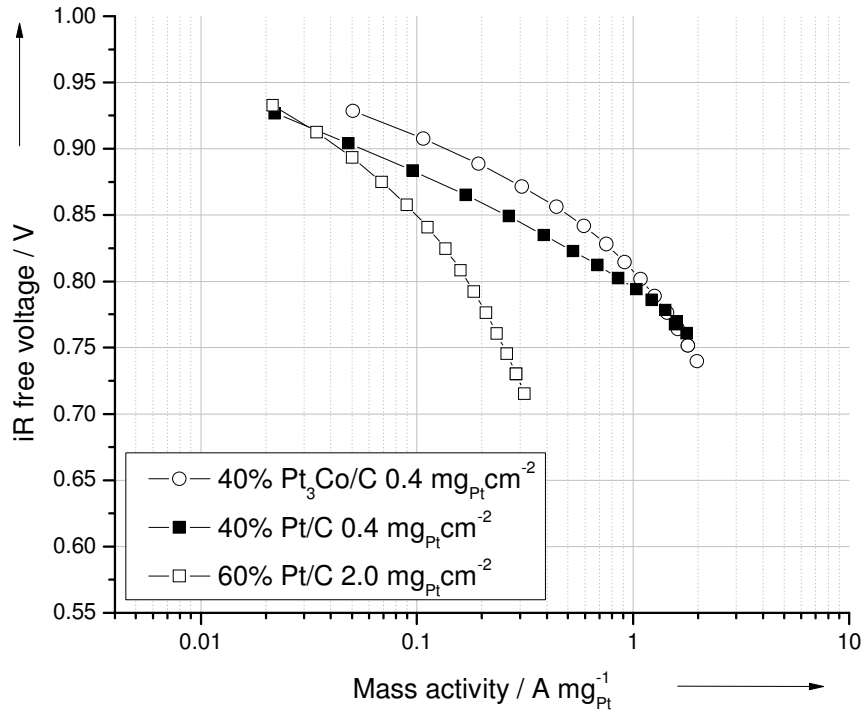

Figure 2. **iR free fuel cell mass activity performance of MEAs with 40% Pt/C and 40% Pt_3Co/C cathodes with 0.4 $mg_{Pt}\,cm^{-2}$ loading and 0.4 $mg_{Pt}\,cm^{-2}$ 40% Pt/C anodes in the transmission XAS cell. For comparison the mass activity of a 2.0 $mg_{Pt}\,cm^{-2}$ 60% Pt/C MEA, with 10 % Pd/C anode as used in the *operando* XAS measurements is also plotted (open squares). All MEAs were prepared with Nafion 115 and tested with H_2 anode gas and O_2 cathode gas at 60 ml min^{-1}, 10 psig, 65 ºC**

The cell design was validated by conducting activity measurements using both Pt/C and Pt_3Co/C catalysts. The experimental procedure used is described in Chapter 2 section 2.2.5. The iR and hydrogen crossover corrected activities of Pt/C only and Pt_3Co/C alloy catalysts at 0.4 $mg_{Pt}\,cm^{-2}$ tested in the XAS transmission fuel cell are shown in Figure 2.

The Pt_3Co alloy shows a two times improvement in activity at 900 mV over the Pt catalyst at the same mass loading. This trend is in good agreement with MEA activity that has previously been reported for these catalysts tested in fuel cells of more conventional design (16). However, the absolute activity values obtained for the catalysts in the XAS transmission cell are lower by a factor of two compared to the reported values. This discrepancy may be accounted for by differences in testing conditions between the two systems such as lower operating temperature and less efficient humidification in the transmission XAS cell. The measured cell resistance for the 0.4 $mg_{Pt}\,cm^{-2}$ MEAs using the current interrupt technique is on average 0.2 $\Omega\,cm^{-2}$. This value is two times higher than for more conventional cells using equivalent MEAs. Pressure sensitive paper has shown that the compression of the assembled XAS transmission cell is less efficient in the region of the thinned graphite transmission windows compared to conventional solid plate designs. This is thought to be the significant factor contributing to the higher measured cell resistance.

To consider the effect of the increased Pt loading (and layer thickness) required for *operando* XAS measurement an MEA comparable to those to be used at the synchrotron was also tested. The MEA contained 2.0 $mg_{Pt}\,cm^{-2}$ Pt/C cathode and a 10 % Pd/C anode. The iR corrected mass activity is also shown in Figure 2. Despite the increased thickness of the catalyst layer and the Pd/C anode, the iR corrected mass activity is comparable to the thinner 0.4 $mg_{Pt}\,cm^{-2}$ loaded Pt/C MEA in the kinetic region > 0.85 V. At lower potentials, corresponding to higher currents, poorer correlation due to increased mass transport with the thicker layer is observed. This may be a catalyst utilisation effect. At these higher currents, the additional polarisation due to the anode will also become more important and is not corrected for here. This, in addition to the layer thickness may help explain the deviation observed at higher current densities. The measured cell resistance of the thicker layer was comparable to the low loaded layer. These results demonstrate that the XAS transmission cell design allows the same

catalytic trends to be observed as in conventional fuel cells and that the requirement to use thicker catalyst layers and the Pd anode for XAS measurements does not adversely affect the catalyst utilisation in the kinetic region (the main region of interest for study of the ORR in this work) under these operating conditions. Assuming the same results can be obtained at the synchrotron the structural parameters obtained from XAS measures can be considered representative of the catalyst operating under realistic fuel cell conditions.

3. Experimental

3.1 Catalyst preparation, characterisation and MEA fabrication

60% Pt/C (2.0 $mg_{Pt}\,cm^{-2}$), 40% Pt/C (2.4 $mg_{Pt}\,cm^{-2}$), 10% Pd/C (0.24 $mg_{Pd}\,cm^{-2}$), 40% Pt_3Co/C (3.3 $mg_{Pt}\,cm^{-2}$) and 40% Pt_3Co/C acid leached (3.3 $mg_{Pt}\,cm^{-2}$) catalysts were prepared and characterised as described in Chapter 2 section 1.1. Electrodes at 0.4 $mg_{Pt}\,cm^{-2}$ used in cell validation were prepared by screen printing (with some layers sourced from Johnson Matthey Fuel Cells, Swindon) while high loaded layers used in XAS measurements were prepared by spray coating as described in Chapter 2 section 1.1.2. MEAs were fabricated by positioning four centimetre diameter circular anode and cathode electrodes on either side of a Nafion 115 membrane and hot pressing as detailed in Chapter 2 section 2.2.5.

3.2 XAS data collection and analysis during electrochemical measurements

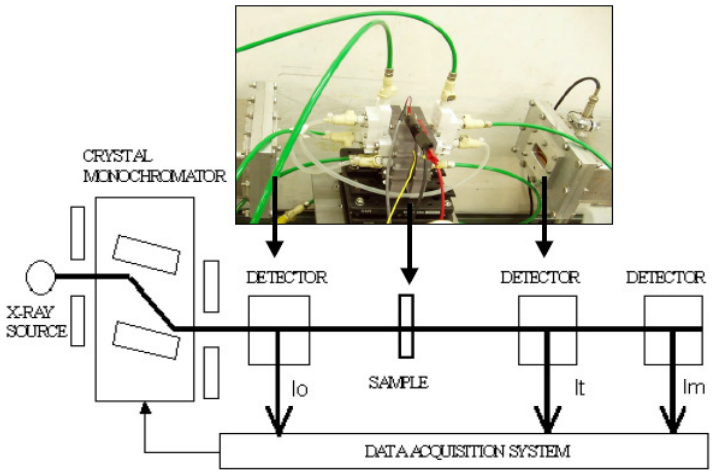

Figure 3. Experimental set-up showing transmission fuel cell on station 9.3

The cell potential was controlled using an Eco chemie Autolab PGSTAT 30 in conjunction with an Eco chemie 10 Amp Booster during electrochemical measurements. The cell was heated to 65 °C and incoming gases humidified by use of MSAs and a circulating waterbath set at 80 °C. All oxygen polarisation curves and potential step measurements to and from 0.125 V or OCV, were conducted at 10 psi with 60 ml min^{-1} H_2 at the anode and N_2 or O_2 at the cathode regulated by use of the gas control box.

All X-ray data were collected on station 9.3 at Daresbury Laboratory, Warrington, UK. The ring is operated at 2.0 GeV energy and 100–250 mA ring current. XAS measurements were conducted at the Pt L_{III} edge (11.564 keV) using a double crystal Si(111) monochromator. The experimental set-up for *operando* XAS measurements is shown in Figure 3. During testing the fuel cell was operated as previously described with H_2 anode gas and N_2 or O_2 cathode gas. The cell was situated between two ionization chambers I_0 and I. A Pt foil monitor spectrum was also simultaneously recorded as an internal standard for energy calibration using a third ion chamber. XAS data was acquired as a function of time following potential steps. During the time resolved experiments in nitrogen the cathode potential was held at 0.125 V for the duration of ten XAS scans before the potential was stepped to 0.6, 0.7, 0.8, 0.9 or 1.0 V vs. the Pd/C anode in H_2. The potential was held at the upper limit for 25 XAS scans before a potential step back to 0.125 V. The duration of each XAS scan was 10 s with a total of 12 s between scans to allow for the changes in position of the monochromator. Similarly time resolved experiments with oxygen at the cathode were conducted from OCV (typically 1.1 V) to 0.9, 0.8, 0.7 and 0.6 V to back to OCV to investigate the effect of applied voltage and therefore load drawn from cell on the catalyst structure. The experimentally measured XAS data were analysed using the Daresbury suite of analysis programs as described in Chapter 2 section 3.2. The EXAFS data was theoretically fitted to a two shell model for Pt/C and three shell model for Pt_3Co/C to acquire the number of neighbours, bond distances, Debye-Waller factors and E_f. In the instances where oxygen neighbours were present an additional shell was added to the model. The four models used are described below:

Structural Models used at the Pt L_{III} edge for Pt/C and Pt_3Co/C catalysts:

Two/Three shell:	$Pt\text{-}Pt_1$	$Pt\text{-}Pt_2$		or	$Pt\text{-}Pt_1$	Pt-O	$Pt\text{-}Pt_2$	
Three/Four shell:	$Pt\text{-}Pt_1$	Pt-Co	$Pt\text{-}Pt_2$	or	$Pt\text{-}Pt_1$	Pt-Co	$Pt\text{-}Pt_2$	Pt-O

3.3 XAS data collection of Pt/C powder samples

To consider the effect of particle size on EXAFS fitting parameters, a series of Pt/C catalysts with a range of particle sizes from 2 nm to 15.9 nm were studied. The catalysts were derived from the same 2 nm average particle diameter precursor catalyst by heat treatment (Chapter 2 section 1). The catalysts were studied as powders using the gas treatment cell in hydrogen and oxygen atmospheres (Chapter 2 section 3.3). All X-ray data were conducted on station 9.3 at the SRS Daresbury laboratory, Warrington, England at the Pt L_{III} edge. The ring is operated with 2.0 GeV energy and 100 -250 mA ring current. All samples were run in October 2006 in transmission mode by other members of Prof. Russell's research group. The XAS data were analysed by the author using the Daresbury suite of analysis programmes: EXCALIB, EXBROOK & EXCURV98**.** Individual scans for each sample were summed and XANES spectra were acquired after pre-edge subtraction. The data then underwent background removal before the EXAFS data was theoretically fitted to a three shell model to acquire the number of Pt neighbours, bond distances, Debye-Waller factors and E_f. In the instances where oxygen neighbours were present a fourth shell was added to the model as shown below.

Theoretical Models used at the Pt L_{III} edge:

Three/Four shell: Pt-Pt_1 Pt-Pt_2 Pt-Pt_3 or Pt-O Pt-Pt_1 Pt-Pt_2 Pt-Pt_3

4. Results of *operando* XAS Experiments

4.1 Structural characterisation of 60% Pt/C and 40% Pt_3Co/C during time resolved potential steps under nitrogen by *operando* XAS

Structural characterisation of 60% Pt/C and 40% Pt_3Co/C during time resolved potential steps under nitrogen atmosphere was conducted to determine if this additional information could help explain the enhanced stability of PtCo alloys *vs*. Pt during potential cycles and potential holds under nitrogen atmosphere. In addition, structural characterisation was used to test the theory that the reason for enhanced activity for the ORR of alloys over Pt is a consequence of alloys exhibiting a delayed onset in OH / oxide formation (17, 18).

The XANES (X-ray absorption near edge structure) or white line region of the Pt L_{III} adsorption edge provides information regarding the d-electron occupancy of the metal particles. The XANES spectra at each applied potential under N_2 feed to the cathode were collected for 60% Pt/C and 40% Pt_3Co/C. The energy scales of the spectra were aligned by calibration to the Pt foil spectra collected simultaneously. No significant edge shifts were found, indicating that no global oxidation state change occurred at the applied potentials studied. The effects of the applied potential were further investigated by comparing the white line intensity at each applied cell potential. The intensities were normalised by dividing by the white line intensity at 0.125 V and the results are plotted in Figure 4 as a function of the potential.

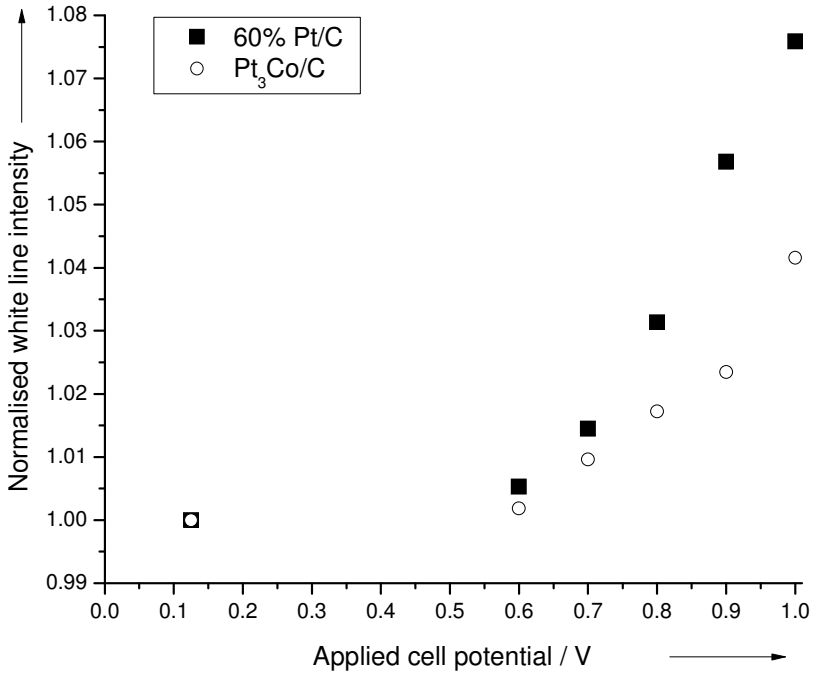

Figure 4. White line intensity at applied cell potential normalised to the white line intensity at 0.125 V for 60% Pt/C and 40% Pt_3Co/C in the transmission fuel cell at 65 °C at the Pt L_{III} edge with N_2 fed to cathode

Increasing the potential in 0.1 V increments from 0.6 V to 1.0 V, results in a progressive increase in white line intensity for the 60% Pt/C catalyst. This increase starts to occur at 0.6 V but is most significant at higher potentials in agreement with the increasing oxide formation seen in the cyclic voltammogram as shown in Figure 5.

The white line intensity (area) corresponds to vacancies in the d-electron band of the metal and, therefore, greater white line intensity indicates less metallic / more oxide character of the metal particles (13, 19). Such an increase in white line intensity with increasing potential has previously been observed for Pt/C as electrode layers in three electrode electrochemical cells with liquid electrolyte (20-22) and was similarly attributed to oxide formation. In comparison, the white line intensity for the 40% Pt_3Co/C alloy catalyst showed a smaller overall increase in white line intensity as a function of potential, with no change in intensity at 0.6 V. This is reflective of less oxide growth for the alloy catalyst and the shift in the onset of OH/oxide formation to higher overpotentials as seen in the cyclic voltammetry in Figure 5. Compared to the 60% Pt/C catalyst, a higher overpotential is required for oxide formation for the alloy catalyst.

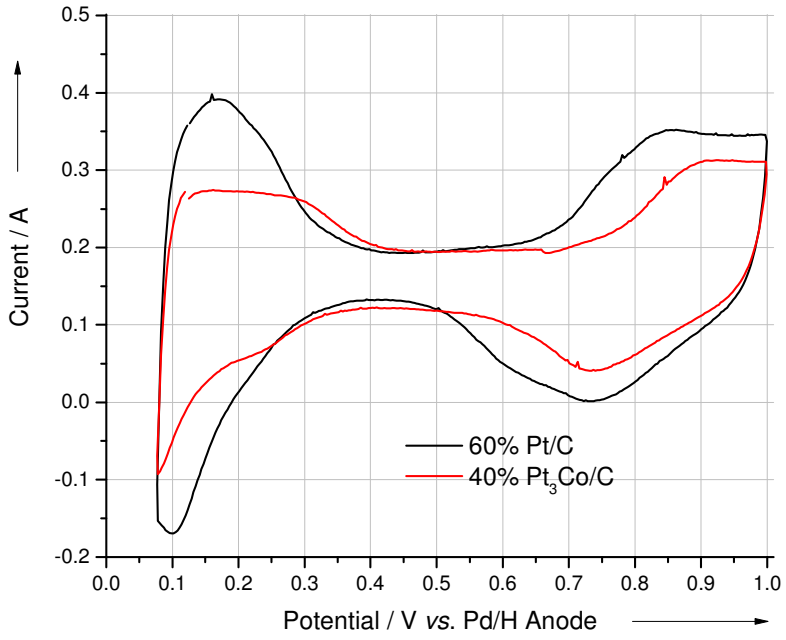

Figure 5. Cyclic voltammetry of 60% Pt/C (2.0 mg_{Pt} cm^{-2}) and 40% PtCo/C (3.3 mg_{Pt} cm^{-2}) measured in half cell mode in the XAS transmission fuel cell

The extent of platinum oxide formation with applied potential was also investigated for 60% Pt/C and 40% Pt_3Co/C under nitrogen atmosphere by analysis of the EXAFS (Extended X-ray absorption fine structure) region of the spectra collected during time resolved potential step experiments. Data were acquired as a function of time following potential steps from 0.125 V to 0.6, 0.7, 0.8, 0.9 or 1.0 V and back to 0.125 V. The data

were analysed and the fit parameters determined at given times during the potential stepping experiments. The fit parameters at 0.125 V (time = 0 s) and at the end of the upper potential limit hold (time = 384 s) are given in Table 1 for 60% Pt/C, and Table 2 for 40% Pt_3Co/C catalysts. Figure 6 shows the corresponding EXAFS data and theoretical fits for the 60% Pt/C catalyst and Figure 7 shows the data for the 40% Pt_3Co/C catalyst.

Table 1. Structural parameters for 60% Pt/C in the XAS transmission fuel cell at 0.125 V (time = 0 s) and at time = 384 s at range of upper potential limits in N_2.

Catalyst	Applied potential (V)	Absorber neighbour	N	R (Å)	$2\sigma^2$ (Å^2)	E_f (eV)	R_{EXAFS} (%)
60% Pt/C	0.125	Pt-Pt_1	7.9 (± 0.7)	2.75 (± 0.01)	0.012 (± 0.001)	-12.1 (± 1.3)	41.3
		Pt-Pt_2	2.3 (± 1.2)	3.89 (± 0.03)	0.008 (± 0.005)		
	0.6	Pt-Pt_1	7.6 (± 0.7)	2.74 (± 0.01)	0.012 (± 0.001)	-11.8 (± 1.3)	41.8
		Pt-Pt_2	1.4 (± 0.9)	3.84 (± 0.04)	0.008 (± 0.006)		
	0.7	Pt-Pt_1	6.8 (± 0.6)	2.74 (± 0.01)	0.012 (± 0.001)	-12.2 (± 1.5)	44.1
		Pt-O	0.6 (± 0.6)	2.07 (± 0.12)	0.047 (± 0.055)		
		Pt-Pt_2	1.9 (± 1.0)	3.90 (± 0.03)	0.008 (± 0.005)		
	0.8	Pt-Pt_1	6.7 (± 0.7)	2.74 (± 0.01)	0.013 (± 0.001)	-11.1 (± 1.5)	42.6
		Pt-O	0.7 (± 0.4)	2.02 (± 0.07)	0.025 (± 0.025)		
		Pt-Pt_2	2.3 (± 1.2)	3.88 (± 0.03)	0.009 (± 0.005)		
	0.9	Pt-Pt_1	7.0 (± 0.7)	2.75 (± 0.01)	0.013 (± 0.001)	-12.1 (± 1.4)	44.3
		Pt-O	0.9 (± 0.5)	2.02 (± 0.05)	0.030 (± 0.022)		
		Pt-Pt_2	2.5 (± 1.2)	3.89 (± 0.04)	0.010 (± 0.005)		
	1.0	Pt-Pt_1	6.1 (± 0.7)	2.75 (± 0.01)	0.013 (± 0.001)	-11.5 (± 1.6)	46.5
		Pt-O	1.1 (± 0.3)	2.01 (± 0.04)	0.018 (± 0.011)		
		Pt-Pt_2	2.0 (± 1.1)	3.89 (± 0.03)	0.009 (± 0.006)		

Table 2. Structural parameters for 40% Pt_3Co/C in the XAS transmission fuel cell at 0.125 V (time = 0 s) and at time = 384 s at range of upper potential limits in N_2.

Catalyst	Applied potential (V)	Absorber neighbour	N	R (Å)	$2\sigma^2$ (Å^2)	E_f (eV)	R_{EXAFS} (%)
40% Pt_3Co/C	0.125	Pt-Pt_1	7.5 (± 0.6)	2.72 (± 0.01)	0.013 (± 0.001)	-12.2 (± 0.9)	30.7
		Pt-Co	1.6 (± 0.3)	2.69 (± 0.01)	0.011 (± 0.003)		
		Pt-Pt_2	2.4 (± 1.1)	3.86 (± 0.03)	0.013 (± 0.005)		
	0.6	Pt-Pt_1	7.1 (± 0.7)	2.72 (± 0.01)	0.013 (± 0.001)	-12.1 (± 1.0)	32.7
		Pt-Co	1.6 (± 0.3)	2.68 (± 0.01)	0.011 (± 0.003)		
		Pt-Pt_2	2.6 (± 1.3)	3.86 (± 0.03)	0.015 (± 0.006)		
	0.7	Pt-Pt_1	7.2 (± 0.7)	2.72 (± 0.01)	0.013 (± 0.001)	-12.7 (± 0.9)	33.0
		Pt-Co	1.6 (± 0.3)	2.69 (± 0.01)	0.011 (± 0.003)		
		Pt-Pt_2	2.6 (± 1.4)	3.86 (± 0.04)	0.017 (± 0.007)		
	0.8	Pt-Pt_1	7.5 (± 0.6)	2.72 (± 0.01)	0.013 (± 0.001)	-12.3 (± 0.9)	31.1
		Pt-Co	1.6 (± 0.3)	2.69 (± 0.01)	0.012 (± 0.003)		
		Pt-Pt_2	2.5 (± 1.2)	3.86 (± 0.03)	0.017 (± 0.007)		
	0.9	Pt-Pt_1	7.1 (± 0.6)	2.73 (± 0.01)	0.013 (± 0.001)	-12.3 (± 0.9)	30.3
		Pt-Co	1.5 (± 0.3)	2.68 (± 0.01)	0.012 (± 0.003)		
		Pt-Pt_2	3.0 (± 1.5)	3.87 (± 0.03)	0.017 (± 0.007)		
		Pt-O	0.4 (± 0.2)	2.04 (± 0.06)	0.015 (± 0.019)		
	1.0	Pt-Pt_1	6.8 (± 0.7)	2.72 (± 0.01)	0.013 (± 0.001)	-12.2 (± 1.0)	32.9
		Pt-Co	1.6 (± 0.4)	2.68 (± 0.01)	0.012 (± 0.003)		
		Pt-Pt_2	3.3 (± 1.6)	3.85 (± 0.03)	0.018 (± 0.007)		
		Pt-O	0.5 (± 0.2)	2.00 (± 0.06)	0.018 (± 0.020)		

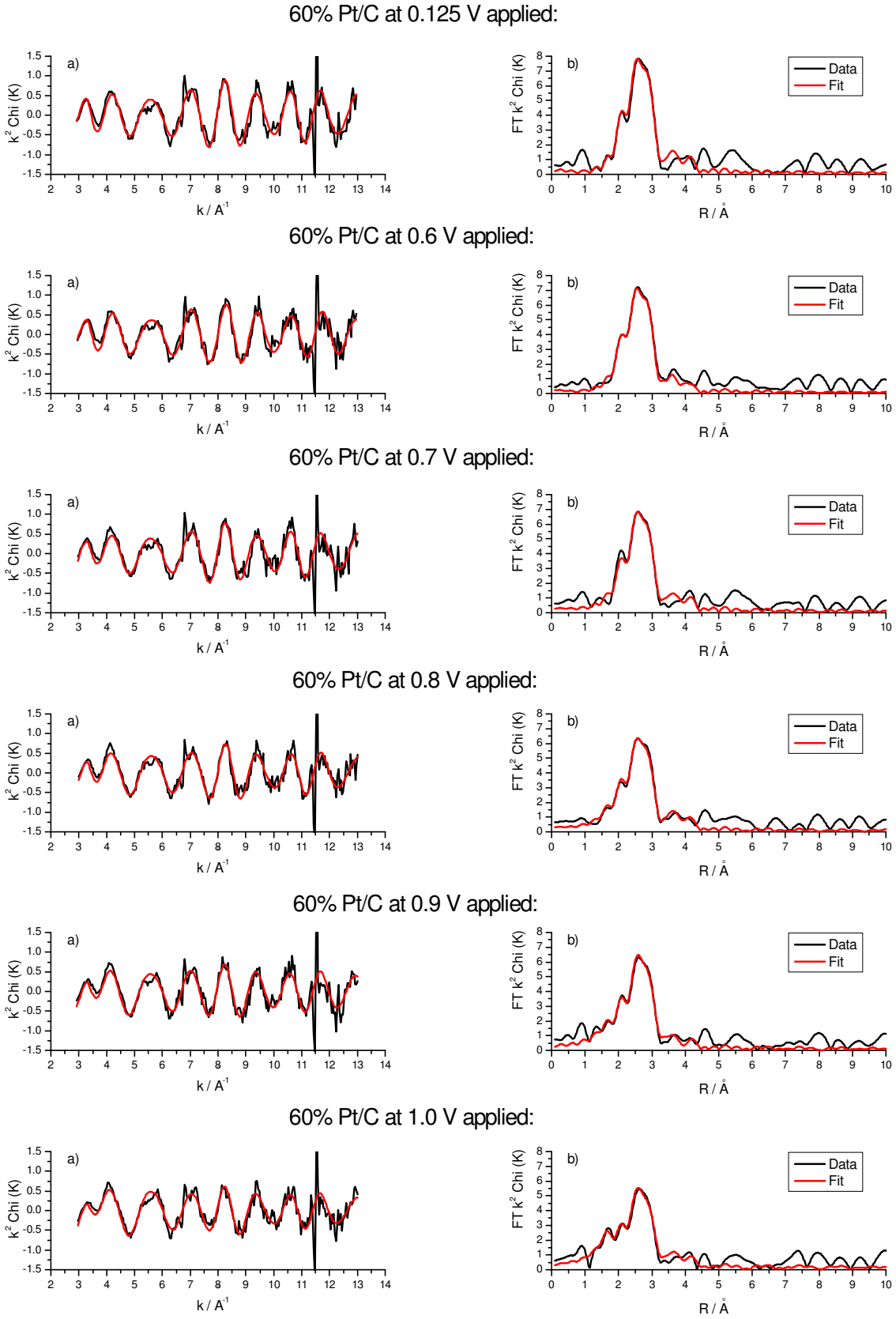

Figure 6. **k^2 weighted experimental a) EXAFS (black) and theoretical fit (red) plot and corresponding b) Fourier transforms for 60% Pt/C in the transmission XAS fuel cell at a range of applied potentials (Half cell)**

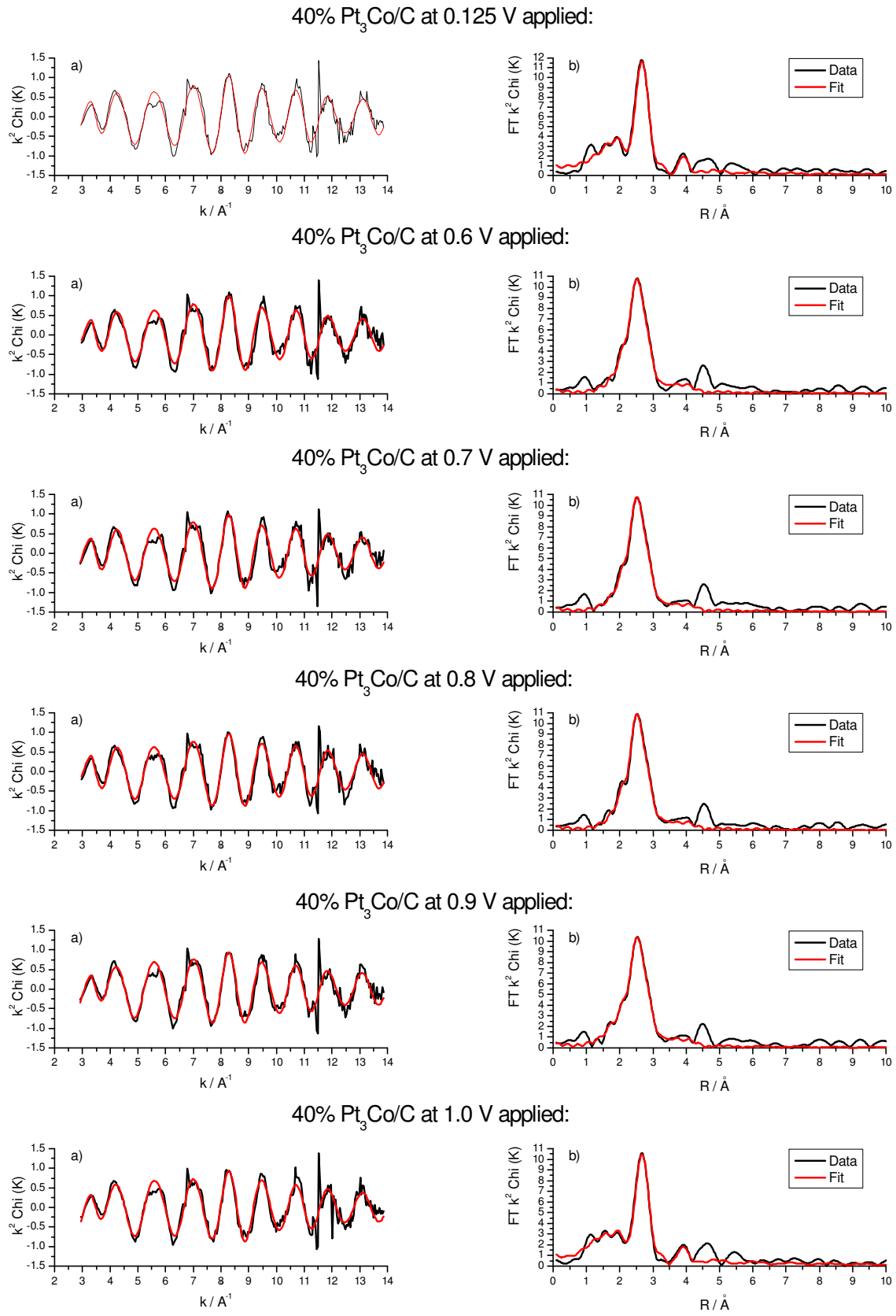

Figure 7. **k^2 weighted experimental a) EXAFS (black) and theoretical fit (red) plot and corresponding b) Fourier transforms for 40% Pt_3Co/C in the transmission XAS fuel cell at a range of applied potentials (Half cell)**

For both catalysts coordination numbers determined in the XAS transmission cell are in good agreement with the coordination numbers determined from powder sample measurements in H_2 atmosphere. The agreement is less well aligned with the samples in air atmosphere since the extent of the oxidation in the two environments is different (see Figure 10, for 2 nm Pt/C and Chapter 3, Tables 6 and 7 for 40% Pt_3Co/C alloy.) The % errors associated with the fit are higher in the transmission XAS cell than for the powder samples with the overall R_{EXAFS} value (< 47 transmission fuel cell, < 32 powder samples). Considering the shorter scan duration and lower signal to noise ratio of the data obtained, the theoretical fits for all catalysts were in good agreement with the experimental data.

Reported bond lengths for Pt-O bonds are 2.3 Å for Pt-OHH, 2.2 Å for Pt-OH, and 2.0 Å for Pt-O with adsorbed atomic oxygen and Pt-O in platinum oxides. Longer Pt-O bonds corresponding to place exchanged Pt-O have also been reported to occur at 3.1 and 3.5 Å (22). The fitted bond lengths of Pt-O in this work are all comparable within the error of the fit as 2.0 Å, suggesting adsorbed atomic oxygen and Pt-O in platinum oxides. However, it is noted that the error of some fits is large meaning that it is not possible distinguish between Pt-OH and Pt-O formation during oxidation.

The first shell Pt-Pt and Pt-O coordination numbers as a function of time for each of the cell potential steps for the 60% Pt/C catalyst are shown in Figure 8. While the errors associated with the fitting of individual data points are large (9-12%), this error is consistent across all data points, and therefore, general trends in the coordination numbers with the upper potential limit during potential steps can be interpreted. At the start of the experiment (at 0.125 V) the catalyst is fully reduced. Upon stepping to 0.6 V the catalyst remains reduced with no / little change in both the N(Pt-Pt) and N(Pt-O) coordination numbers being observed. However, stepping to higher potentials results in a progressive increase in Pt-O neighbours up to a maximum of 1.2 ± 0.4 for the 1.0 V step. This trend is in good agreement with the increase in white line intensity observed in the XANES analysis. A corresponding decrease in the Pt-Pt neighbours is also observed, indicating that Pt oxide formation disrupts the Pt-Pt bonding in the metal nano particle. This disruption is most significant at 1.0 V and is larger than the fitting error. The extent of disruption of the Pt-Pt shell is indicative of the thickness of the oxide layer. If a cuboctahedral particle shape is assumed a Pt-Pt coordination number of

8.0 (at 0.125 V) corresponds to 3.2 complete shells, whilst a coordination number of 6.0 (at 1.0 V) corresponds to 2.2 shells (23), indicating that oxide formation disrupts 1 shell, or the outer monolayer of surface atoms. This observation may be explained by the place exchange mechanism, where Pt–O is known to penetrate into the particle (24).

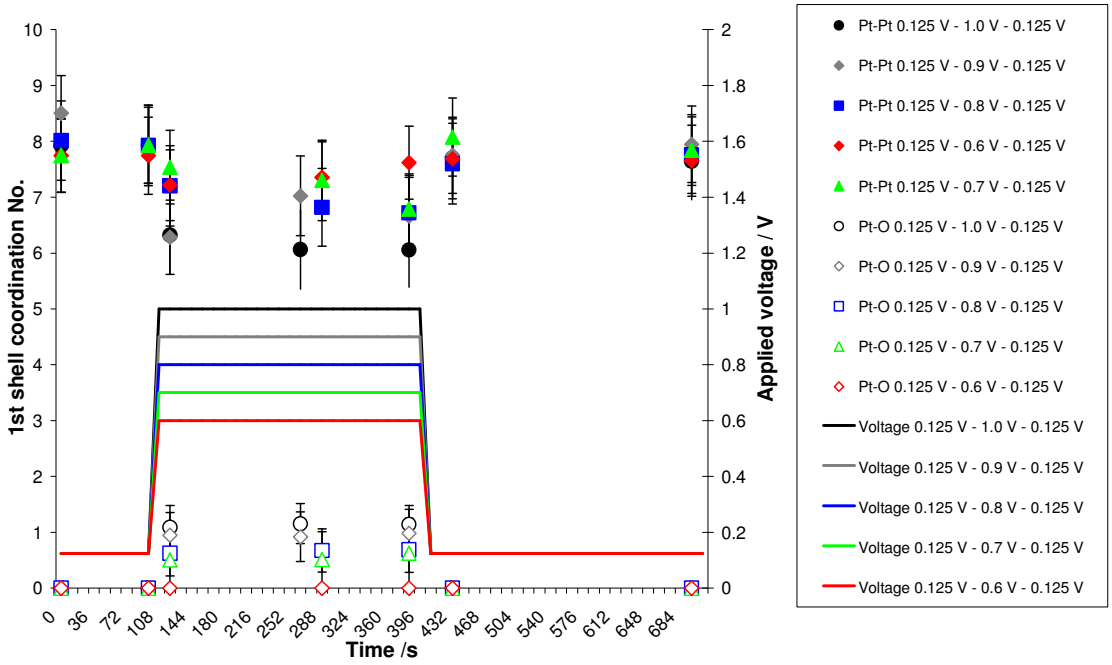

Figure 8. Variation in the 1st shell fitting parameters for 60% Pt/C during potential step from 0.125 V to 0.6, 0.7, 0.8, 0.9 and 1.0 V and back to 0.125 V in N_2

The rates of oxide formation and removal have been studied by several authors using energy dispersive EXAFS (EDE) (13, 23, 25, 26). In a study similar to that reported here, Allen *et al.* showed that complete reduction of oxide, equivalent to 2 shells thickness, (by assumption of a cuboctahedral particle shape (23) N(Pt-Pt) = 9.75 (5.3 shells) at 0.1 V and 8.25 (3.3 shells) at 1.2 V), was achieved within 100 s of stepping the potential of a Pt/C catalyst from 1.2 V to 0.1 V (10). Figure 8 shows that upon stepping the potential from the upper limit back to 0.125 V loss of the Pt-O neighbours and recovery of the Pt-Pt neighbours occurs within 20 s. The shorter time reported in the current study may be attributed the thinner oxide layer at 1.0 V than 1.2 V.

However, to enable further comment on the relative rates of oxide formation and removal improved time resolution is required, ideally on the sub second time scales reported in very recent work by Imai *et al.* (22), using energy dispersive XAS. In this

work EXAFS data was obtained during the oxidation of Pt/C during a potential step from 0.4 to 1.4 V *vs.* RHE in liquid electrolyte.

The first shell Pt-Pt, Pt-Co and Pt-O coordination numbers as a function of time and the cell potential for the 40% Pt_3Co/C catalyst are shown in Figure 9. Irrespective of the applied potential the Pt-Co coordination number remained unchanged at 1.5 ± 0.5. Pt-O neighbours were only found at potentials ≥ 0.9 V and the maximum Pt-O coordination number fitted at 1.0 V was 0.5 ± 0.2, in good agreement with the smaller increase observed in the white line intensity at this potential compared to the 60% Pt/C catalyst. A corresponding small decrease (0.7 units) in the Pt-Pt coordination occurs at 1.0 V, however, this change is comparable to the error of the fitting.

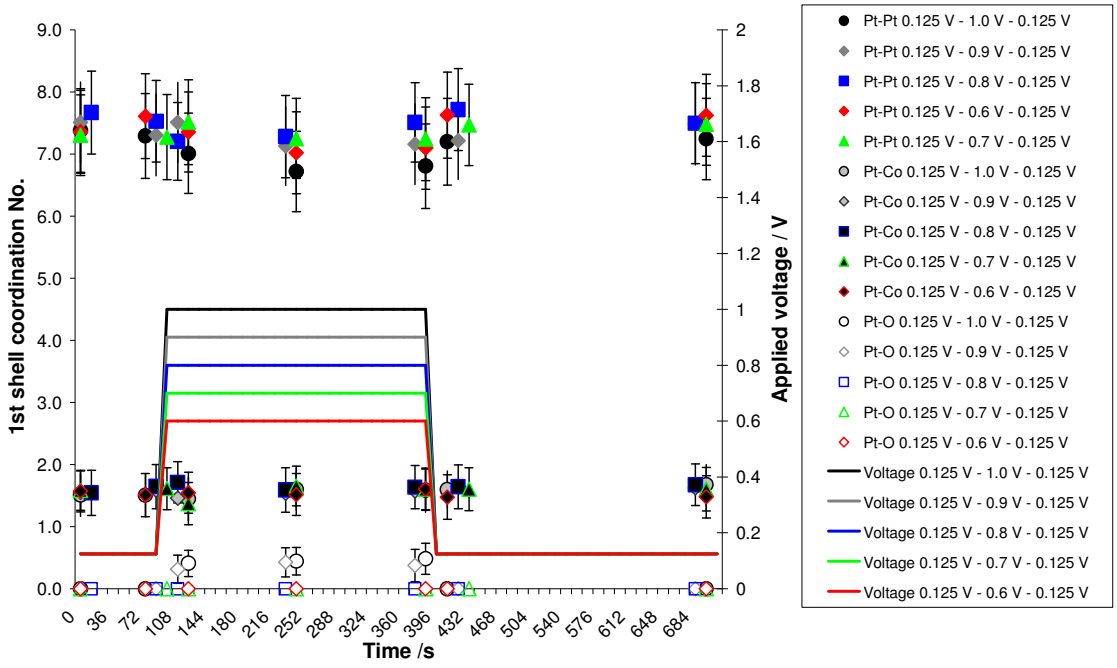

Figure 9. Variation in the 1st shell fitting parameters for 40% Pt_3Co/C during potential step from 0.125 V to 0.6, 0.7, 0.8, 0.9 and 1.0 V and back to 0.125 V in N_2

Compared to the 60% Pt/C catalyst the Pt_3Co/C catalyst required a higher overpotential for Pt-O neighbours to be fitted (onset in oxygen bond formation) during the potential step, and showed less particle disruption and fewer Pt-O bonds at the same applied potential. Less particle disruption at a given potential helps to explain the increased stability of the alloy catalyst over 2 nm Pt/C and at face value these results seem to support the theory that alloys are more active than Pt due to the delayed onset and

reduced extent of oxide formation. However, it is noted that the XAS parameters represent the per atom average coordination of all the platinum atoms in the sample and, therefore, consideration of the particle size of the catalyst is important.

4.2 The effect of particle size on XAS parameters

As stated previously, Pt L_{III} XAS provides the per atom average coordination environment of all the platinum atoms in the sample. The bulk to surface ratio of the material under investigation will, therefore, affect the coordination numbers and also the sensitivity for detection of species present at the surface layers of the particle.

To illustrate the effect of particle size and therefore bulk to surface ratio on the EXAFS fitting parameters a series of Pt/C catalysts with a range of particle sizes were studied under air and hydrogen using the gas treatment cell. Full tabulation of the theoretical fitting and Chi and FT plots are shown in the Electronic appendix and the data for the 4.7 nm and 7.7 nm diameter particle sizes were previously shown in Chapter 3. The data were fitted to a three shell model under hydrogen with a fourth Pt-O shell in air. The quality of the fits were high for $R \leq 4.5$ Å, with the goodness of fit parameter in the range $21.6 \leq R_{EXAFS} \leq 29.9$.

Figure 10 shows the effect of particle size (measured by XRD) on the first shell Pt-Pt and Pt-O coordination numbers in hydrogen (reduced) and air (as prepared) atmospheres. In hydrogen no Pt-O neighbours were measured so all catalysts are considered to be fully reduced. In air all but the largest particle size Pt catalyst have Pt-O neighbours. Larger particles have greater Pt-Pt coordination numbers and, in air, the lower Pt-O coordination number. This is a consequence of the increasing bulk to surface ratio with increasing particle size and/or a decrease in the extent of the oxidation of the particle. It is noted that once a critical particle size has been reached (> 4 nm) further increase in particle size does not significantly increase the number of Pt-Pt 1^{st} shell neighbours. The same trend is observed for both the Pt-Pt 2^{nd} and 3^{rd} shells. However, the error associated with the fitting of these shells is greater so differences between catalysts are not as significant. In air compared to hydrogen the absolute Pt-Pt coordination number is lower. This effect is most significant for the smaller particles and as discussed previously, is attributed to the presence of a surface oxide that disrupts the Pt crystallite structure. No Pt-O neighbours were required to fit the data for the

largest particle size Pt catalyst in air, and, within the error, there is no change in Pt-Pt 1st shell neighbours compared to hydrogen atmosphere for this catalyst. This indicates that any surface oxide formed is not extensive enough to disrupt the structure of the crystallite.

The effect of particle size on the first shell Pt-Pt and Pt-O coordination numbers were modelled for a cuboctahedral particle by Benfield (23). Equation 1 shows the formulae for calculating the mean first-nearest-neighbour coordination number N_1 of atoms in a cuboctahedral cluster geometry (23). N_1 has been determined for particle sizes from 0.276 nm (m =1, shell, 1 atom) to 21.8 nm (m = 40 shells, 205479 atoms) and the predicted values are plotted in Figure 10. The theoretical number of Pt-O neighbours has been determined from calculation of the proportion of atoms in the particle that are surface atoms at each particle size, assuming one oxygen will bind to each surface Pt atom. These results are also shown in Figure 10.

$$N_1(Cuboctahedron) = \frac{12(m-1)(10m^2-14m+6)}{(2m-1)(5m^2-5m+3)} \qquad \textbf{Equation 1}$$

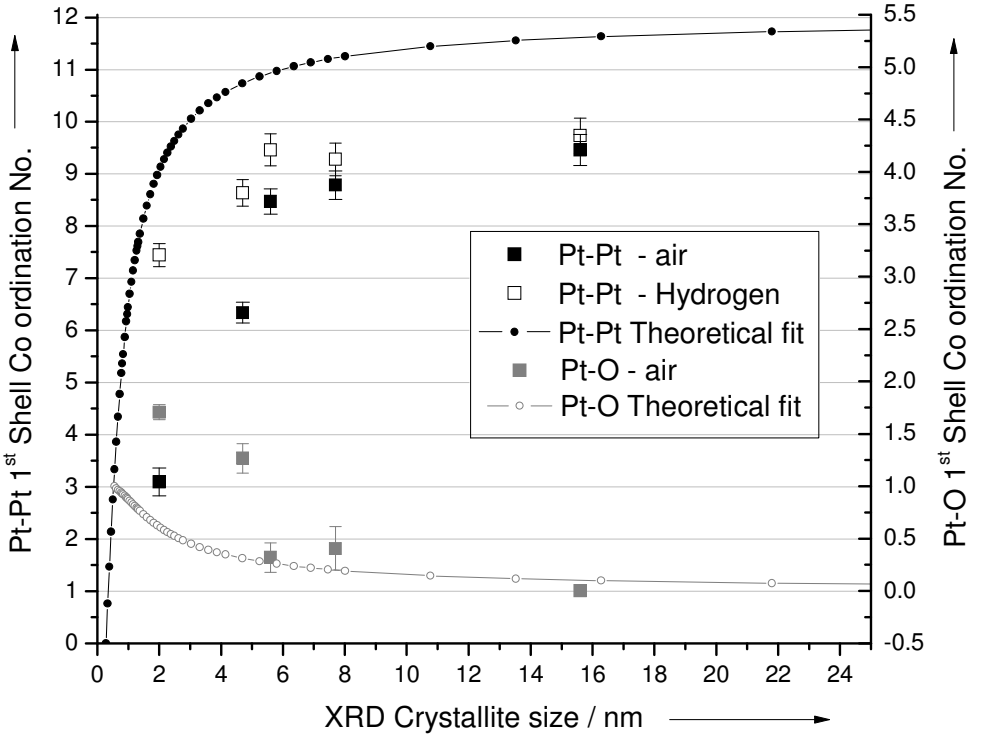

Figure 10. Effect of particle size on the Pt-Pt and Pt-O first shell coordination number of a series of Pt/C catalysts in hydrogen and air atmospheres

Comparison of the Benfield theoretical model to the fitting of the experimental EXAFS parameters plotted against the mean crystallite size determined by XRD, shows good agreement of the general trends for Pt-Pt and Pt-O coordination. However, in all cases the Pt-Pt_1 coordination number determined from the EXAFS is less than the Benfield model and the Pt-O coordination number is larger for the smallest particle sizes. These discrepancies may arise from deviation of the real catalyst from the assumptions of the Benfield model and the XRD measurement. It is unlikely that the catalysts are perfectly cuboctohedral as assumed in the theoretical model. The Benfield model does not allow for any ad-atoms or distortion of the shape that are likely to be present on the real catalysts. In addition the real catalysts have a distribution of particle sizes that will skew N_1. It should also be noted that the EXAFS parameters are plotted versus the mean crystallite size determined from XRD measurement. Due to the nature of this measurement technique, the mean crystallite size can be skewed by larger particles in the catalyst particle size distribution and particles without long range order will not be observed. The experimental data will therefore also have an error in the x-axis that is unknown. This error may also help account for some of the differences observed between the coordination numbers determined experimentally and those predicted using the Benfield model.

With regard to the sensitivity to detection of species present at the surface of the particle, decreased sensitivity is most significant for larger particles. This is a consequence of the higher bulk to surface ratio and is illustrated in the air data for the largest particle size catalyst in Figure 10. In this work this factor needs to be considered when fitting Pt-O neighbours. It is noted that for the Pt_3Co/ C alloy the error associated with the low Pt-O coordination number decreases the certainty that oxygen bonds are formed compared to the small particle size Pt/C catalyst with a higher Pt-O coordination number and comparable error.

To overcome the surface sensitivity limitation of XAS, a technique known as the Δμ technique has been applied in the literature to enable differences in surface structure to be observed (6, 25, 26). The technique analyses the difference XAS spectrum of the material before and after a change to the surface and relies on the fact that the imposed change affects only the surface layer of the material. In the consideration of the

potential stepping experiments conducted here it is noted that a change in the average Pt-Pt coordination occurs upon oxide formation disrupting the bulk of the particle. It is therefore inappropriate to apply the Δμ technique to this work.

In light of the limitations of the XAS methods as described above, differences observed in the onset of Pt-O bond formation and number of Pt-O neighbours at an applied potential between the 2 nm 60% Pt/C catalyst and the 5 nm 40% Pt_3Co/C catalyst described in section 4.1 need to be treated with caution. A fairer comparison would be to study a Pt/C and Pt_3Co/C alloy catalyst with comparable particle sizes. Attempts to do this included making a smaller particle size Pt_3Co/C catalyst. However, this proved unsuccessful due to the lower temperature firing used to limit particle growth resulting in a non-alloyed phase and poorly active catalyst. Instead a larger particle sized (5 nm) 40% Pt/C catalyst was studied.

4.3 *Operando* time resolved XAS of 40% Pt/C (5 nm)

The cyclic voltammetry profile of the 5 nm 40% Pt/C catalyst is shown in Figure 11 together with the profiles of the 60% Pt/C 2 nm catalyst and the 5 nm Pt_3Co/C alloy.

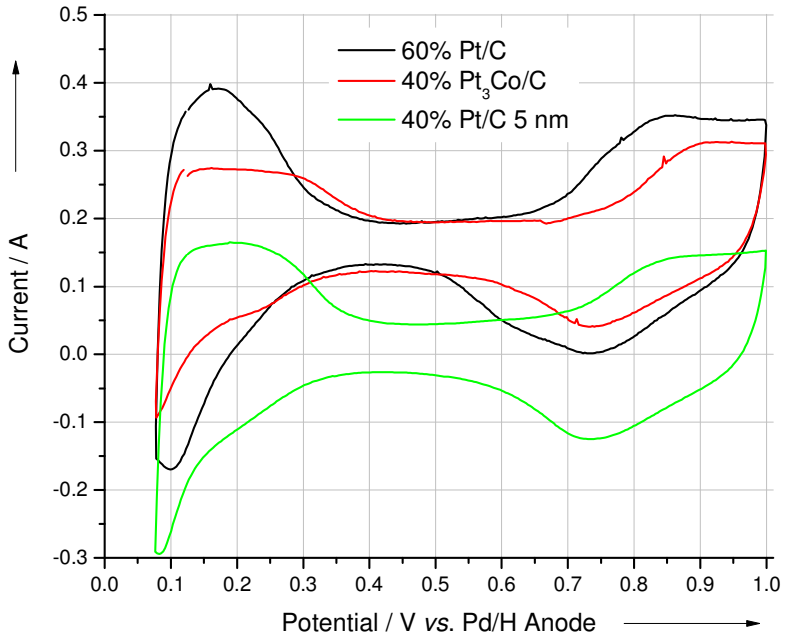

Figure 11. Cyclic voltammetry of 40% Pt/C 5 nm (2.4 mg_{Pt} cm^{-2}) measured in half cell mode in the XAS transmission fuel cell. Voltammetry of 60% Pt/C (2.0 mg_{Pt} cm^{-2}) and 40% PtCo/C (3.3 mg_{Pt} cm^{-2}) is shown for comparison

The shift to lower current observed for the 5 nm Pt/C catalyst is due to reduced hydrogen crossover in this MEA compared to the MEAs for the other catalyst samples. It can be seen that the onset of OH/oxide formation seen in the cyclic voltammetry is similar for the 5 nm Pt/C catalyst and the alloy.

XAS data were collected for a 40% Pt/C (5 nm) catalyst electrode as a function of time following potential steps under nitrogen atmosphere to allow direct comparison with the 40% Pt_3Co/C alloy. Due to problems with data collection the upper potential limit was only 0.9 V rather than 1.0 V.

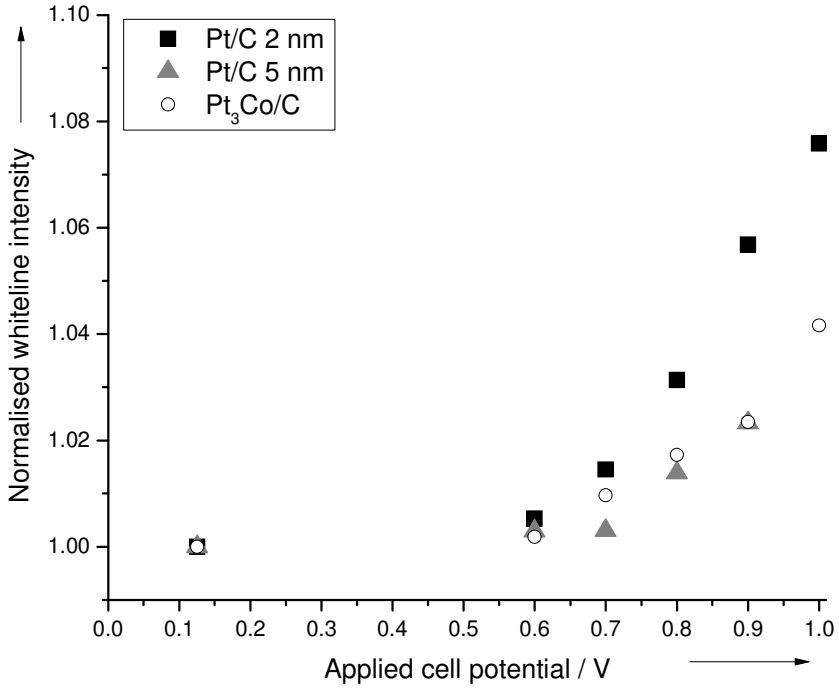

Figure 12. White line intensity at applied cell potential normalised to the white line intensity at 0.125 V for 60% Pt/C (2nm), 40% Pt/C (5nm) and 40% Pt_3Co/C in the transmission fuel cell at 65 °C at the Pt L_{III} edge with N_2 fed to cathode

XAS data were collected following potential steps and the white line intensities at the start potential (0.125 V) and at the end of the step to the upper potential limit were measured as described previously for the other catalysts. The normalised white line intensities are reported in Figure 12. The change in white line intensity and the onset of OH/oxide formation seen in the cyclic voltammetry (Figure 11) of the 40% Pt/C 5 nm catalyst is comparable to that observed for Pt_3Co/C alloy, with both these larger particle

size catalysts exhibiting a smaller change in white line intensity at all potentials compared to the 2 nm 60 % Pt/C. This result suggests less oxidation of the larger particles occurs at a given potential as seen for the powder samples.

Analysis of the EXAFS region of the spectra collected during time resolved potential step experiments was conducted and the fit parameters determined at given times during the potential stepping experiments. The fit parameters at 0.125 V (time = 0 s) and at the end of the upper potential limit hold (time = 384 s) are given in Table 3. The corresponding EXAFS data and theoretical fits are shown in Figure 13. As observed with the powder samples, increasing the catalyst particle size from 2 to 5 nm results in an increase in the Pt-Pt_1 coordination number. The R_{EXAFS} fit quality for the 5 nm Pt/C catalyst was comparable to the other catalysts studied in the transmission cell.

Table 3. Structural parameters for 40% Pt/C in the XAS transmission fuel cell at 0.125 V (time = 0 s) and at time = 384 s at range of upper potential limits in N_2.

Catalyst	Applied potential (V)	Absorber neighbour	N	R (Å)	$2\sigma^2$ (Å^2)	E_f (eV)	R_{EXAFS} (%)
40% Pt/C 5 nm	0.125	Pt-Pt_1	8.6 (± 0.4)	2.75 (± 0.01)	0.011 (± 0.001)	-11.4 (± 0.8)	32.4
		Pt-Pt_2	2.4 (± 1.1)	3.91 (± 0.03)	0.012 (± 0.005)		
	0.6	Pt-Pt_1	8.4 (± 0.5)	2.75 (± 0.01)	0.011 (± 0.001)	-11.7 (± 0.9)	33.2
		Pt-Pt_2	2.5 (± 1.1)	3.90 (± 0.03)	0.012 (± 0.005)		
	0.7	Pt-Pt_1	8.4 (± 0.5)	2.75 (± 0.01)	0.011 (± 0.001)	-12.2 (± 0.9)	32.9
		Pt-Pt_2	3.3 (± 1.4)	3.93 (± 0.03)	0.014 (± 0.005)		
	0.8	Pt-Pt_1	8.5 (± 0.5)	2.76 (± 0.01)	0.012 (± 0.001)	-11.4 (± 0.9)	33.7
		Pt-O	0.5 (± 0.4)	2.05 (± 0.09)	0.038 (± 0.040)		
		Pt-Pt_2	3.8 (± 1.5)	3.92 (± 0.01)	0.016 (± 0.005)		
	0.9	Pt-Pt_1	8.1 (± 0.5)	2.76 (± 0.01)	0.012 (± 0.001)	-11.9 (± 0.9)	33.7
		Pt-O	0.4 (± 0.2)	2.01 (± 0.06)	0.021 (± 0.028)		
		Pt-Pt_2	3.3 (± 1.3)	3.92 (± 0.03)	0.015 (± 0.006)		

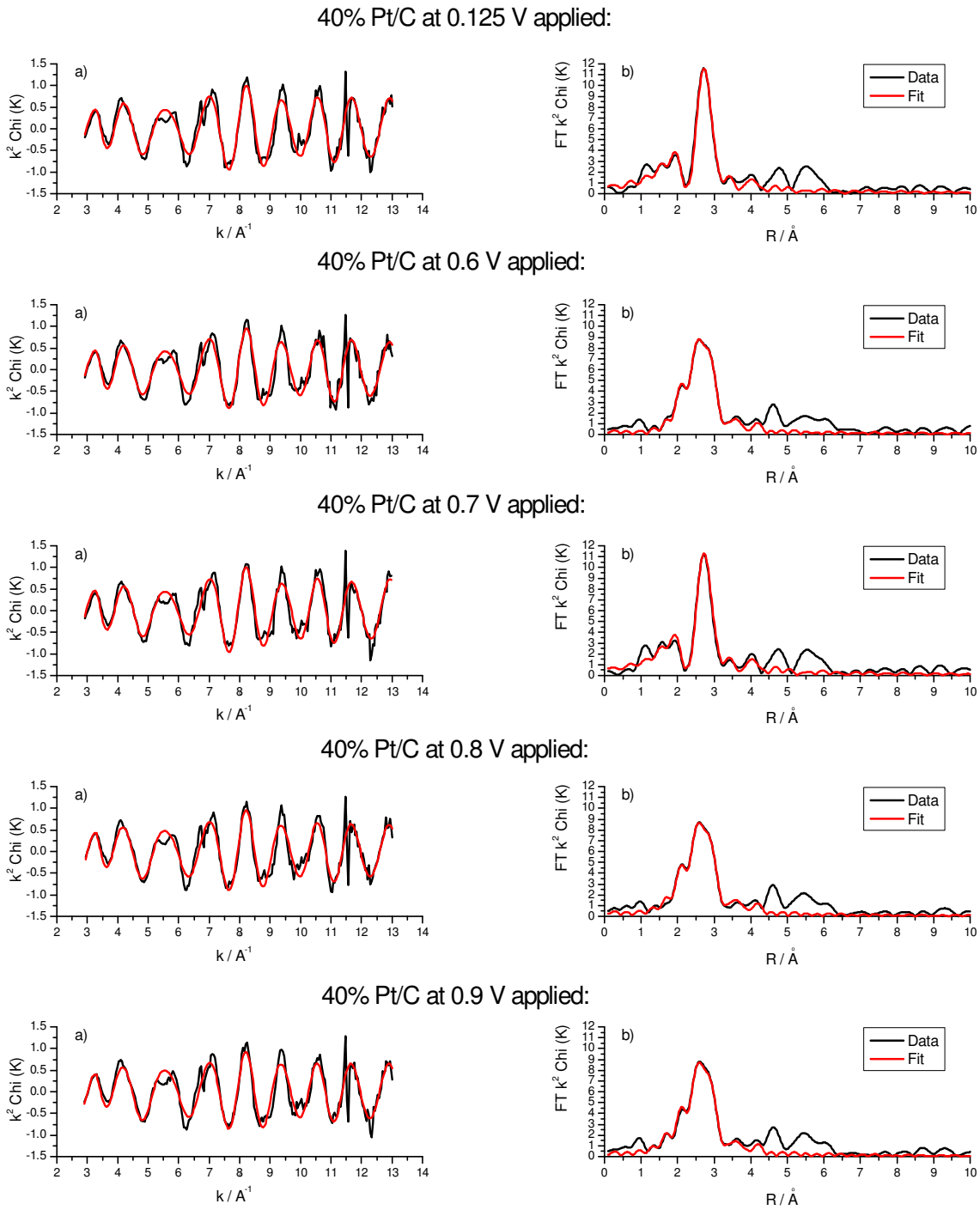

Figure 13. ***k*^{2} weighted experimental a) EXAFS (black) and theoretical fit (red) plot and corresponding b) Fourier transforms for 40% Pt/C in the transmission XAS fuel cell at a range of applied potentials (Half cell)**

A summary of the first shell Pt-Pt and Pt-O coordination numbers and corresponding cell potentials with time for 40% Pt/C are shown Figure 14. At potentials < 0.8 V the catalyst was reduced. Addition of oxygen neighbours to the fitting for the 0.8 V

potential step data gave a small improvement to the fit quality, but the error associated with the fit was high (e.g. Pt-O 0.5 ± 0.4), at 0.9 V the 5 nm Pt/C and PtCo/C alloy showed the same Pt-O coordination numbers and associated errors. Since the fit quality showed no improvement with addition of oxygen neighbours until 0.9 V for the alloy, the data suggest that the Pt_3Co/C catalyst remains oxide free over a wider potential range than the 5 nm Pt/C catalyst. However the evidence is not strongly compelling since the decreased surface sensitivity as a result of particle size could also account for the differences in the XAS results.

Figure 14 also shows the 5 nm Pt/C catalyst to exhibit a comparable decrease in the Pt-Pt coordination number on oxide formation to the Pt_3Co/C alloy indicating some particle disruption on oxide formation. As for the alloy the extent of disruption is significantly less compared to that seen for the 2 nm Pt/C catalyst. As discussed previously this helps explain why the larger particle size catalysts are more stable. However, the EXAFS characterisation does not provide further evidence for the enhance stability of the alloy over a comparable particle sized Pt catalyst.

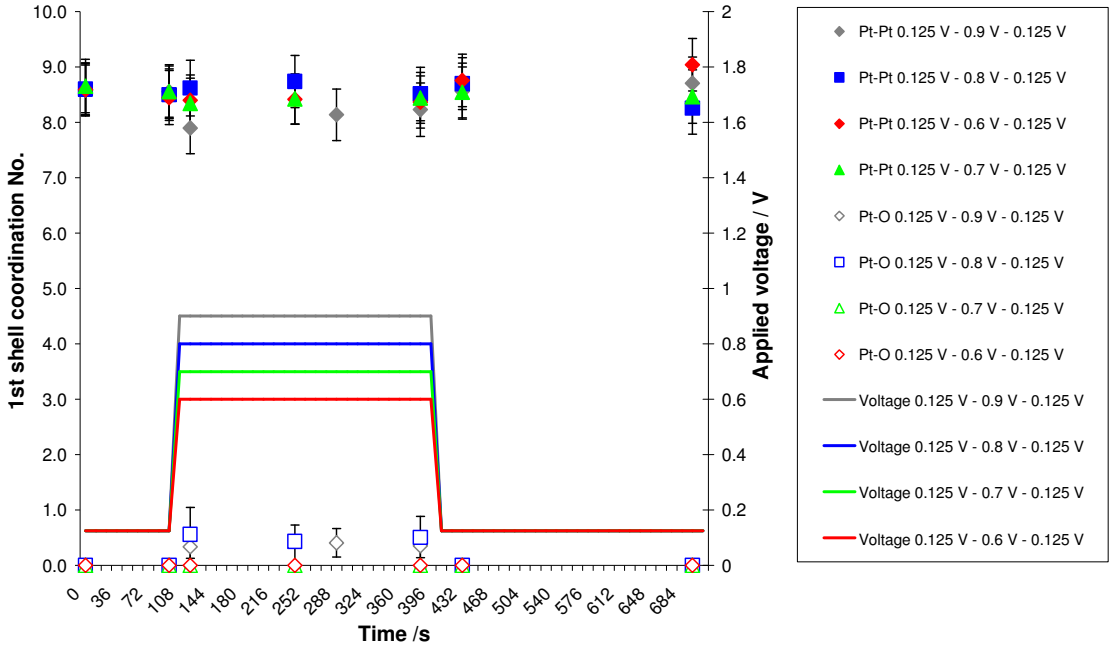

Figure 14. Variation in the first shell fitting parameters for 40% Pt/C during potential step from 0.125 V to 0.6, 0.7, 0.8, 0.9 and back to 0.125 V in N_2

As for the other materials studied, the time resolution of these experiments was found to be insufficient to all comment on the rates of oxide formation and removal.

4.4 Potential steps under fuel cell (oxygen) conditions

The time resolved potential step measurements, with XAS data collection, were also conducted with O_2 feed to the cathode to obtain structural information about the catalysts at OCV (~1.1 V) and during operation under load as the cathode underwent oxygen reduction. In this case the applied potential was stepped from OCV to 0.9, 0.8, 0.7, 0.6 V and back to OCV and the oxygen reduction current was recorded with time.

The arrows in Figure 15 show the 400 mV applied potential window studied and corresponding uncorrected performance curves for the three cathode catalysts. It is noted that the performance of the 2 nm Pt/C catalyst during the validation experiment is higher than the performance of the same catalyst at the synchrotron. The uncorrected performance of the 5 nm Pt/C and Pt_3Co/C catalysts are lower than the 2 nm Pt/C catalyst. These observations will be further discussed in section 4.4.1.

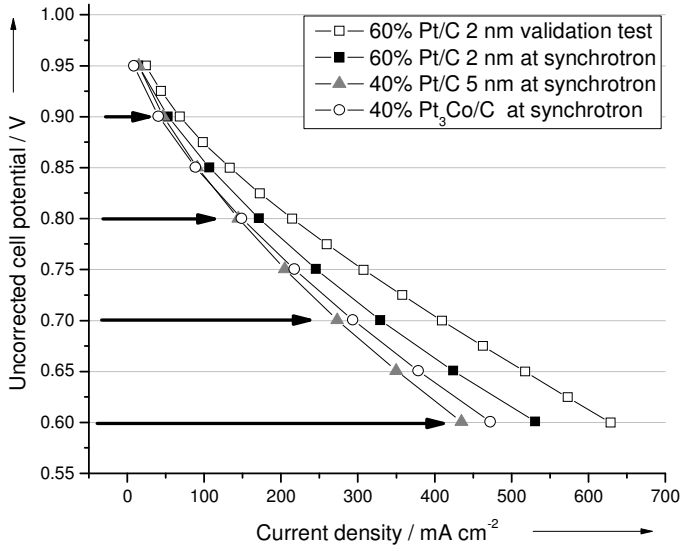

Figure 15. Polarisation curves for 2 nm 60% Pt/C, 5 nm 40% Pt/C and 40% Pt_3Co/C alloy collected during *operando* XAS experiments. Arrows illustrate the applied potentials used to study catalyst structure by XAS during the ORR. For comparison the validation test data for the 2 nm Pt catalyst is shown

Both the XANES and EXAFS data were obtained and analysed for all three catalyst materials. In all cases the maximum white line intensity occurred at OCV. The change in whiteline intensity as a consequence of drawing load from the cell is shown in Figure 16. The white line intensity at each applied potential was normalised to the intensity at OCV. Upon applying a potential of 0.9 V to the cell, a decrease in intensity is observed similar in magnitude (0.01) to that seen in recent work by Witkowska *et al.* during *in situ* fuel cell measurements at room temperature and atmospheric pressure for a PtCo/C catalyst (12). The 60% Pt/C catalyst shows a further decrease in intensity with increasing load, again with similar magnitude of change to that reported by Witkowska *et al.* However, in contrast to this work, the white line intensity of the 40% Pt_3Co/C and 5 nm Pt/C catalysts remained very similar irrespective of applied potential and therefore current drawn from the fuel cell. It is noted that in all cases the change in white line intensity is very small compared to the changes observed under N_2 (half cell conditions).

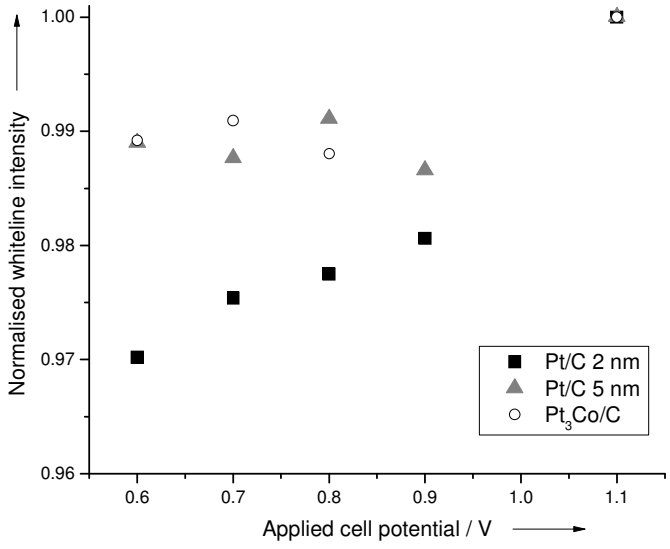

Figure 16. Variation white line intensity at applied cell potential normalised to the white line intensity at OCV for 60% Pt/C (2 nm), 40% Pt/C (5 nm) and 40% Pt_3Co/C in the transmission fuel cell at 65 °C at the Pt L_{III} edge with O_2 fed to cathode

The structural parameters obtained from fitting of the EXAFS data at OCV, 0.9 and 0.6 V applied for the three catalysts are tabulated in Table 4 and the corresponding EXAFS data and theoretical fits are shown in Figures 16-18. In the FT plots in

Figure 16 a large peak is observed at 1 Å, this is likely to be due to non-optimal background subtraction. Differences observed in Figures 17 and 18 between the OCV data and the 0.6 V and 0.9 V data arise due to the OCV data only being shown for one data set (0.9 V or 0.6 V) and the fact that within individual data sets the same background was applied, however, between data sets the background subtraction was similar but not identical. In all different data sets EXAFS analysis showed that Pt-O neighbours are present at all potentials during the potential step experiment and that the Pt-O bond length was similar to that seen under N_2 atmosphere, indicating that the oxide species formed in N_2 are indistinguishable from those formed in O_2 atmosphere and during the ORR. In agreement with the XANES analysis the EXAFS structural parameters (Pt-Pt and Pt-O co ordination numbers and bond lengths) did not change significantly irrespective of the applied voltage / current drawn from the cell. Further discussion on the fitting parameters and comparison of the effect of atmosphere will be provided in section 4.2.2

Table 4. Structural parameters for 2 nm and 5 nm Pt/C catalysts and the Pt_3Co/C alloy in the XAS transmission fuel cell during fuel cell operation (O_2).

Catalyst	Applied potential (V)	Absorber neighbour	N	R (Å)	$2\sigma^2$ (Å^2)	E_f (eV)	R_{exafs} (%)
60% Pt/C 2 nm	0 (OCV)	Pt-Pt_1	5.4 (± 0.7)	2.74 (± 0.01)	0.012 (± 0.002)	-10.4 (± 1.9)	49.7
		Pt-O	1.1 (± 0.3)	1.98 (± 0.03)	0.008 (± 0.007)		
		Pt-Pt_2	0.9 (± 0.6)	3.87 (± 0.03)	0.003 (± 0.006)		
	0.9	Pt-Pt_1	5.6 (± 0.6)	2.74 (± 0.01)	0.013 (± 0.001)	-10.9 (± 1.8)	46.2
		Pt-O	1.0 (± 0.3)	2.00 (± 0.04)	0.018 (± 0.012)		
		Pt-Pt_2	1.3 (± 0.9)	3.88 (± 0.04)	0.007 (± 0.007)		
	0.6	Pt-Pt_1	5.8 (± 0.7)	2.74 (± 0.01)	0.013 (± 0.002)	-11.1 (± 1.8)	52.2
		Pt-O	0.9 (± 0.3)	1.98 (± 0.04)	0.012 (± 0.011)		
		Pt-Pt_2	1.2 (± 0.7)	3.86 (± 0.03)	0.003 (± 0.005)		
40% Pt_3Co/C	0 (OCV)	Pt-Pt_1	6.5 (± 0.7)	2.72 (± 0.01)	0.013 (± 0.001)	-11.3 (± 1.0)	32.7
		Pt-Co	1.6 (± 0.4)	2.68 (± 0.02)	0.012 (± 0.003)		
		Pt-Pt_2	2.5 (± 1.0)	3.86 (± 0.02)	0.012 (± 0.004)		
		Pt-O	0.6 (± 0.2)	2.00 (± 0.04)	0.016 (± 0.014)		
	0.9	Pt-Pt_1	6.6 (± 0.7)	2.73 (± 0.01)	0.014 (± 0.001)	-11.5 (± 1.0)	32.1
		Pt-Co	1.5 (± 0.3)	2.68 (± 0.01)	0.011 (± 0.003)		
		Pt-Pt_2	3.0 (± 1.3)	3.86 (± 0.02)	0.016 (± 0.006)		
		Pt-O	0.7 (± 0.3)	2.00 (± 0.04)	0.023 (± 0.017)		
	0.6	Pt-Pt_1	7.0 (± 0.6)	2.73 (± 0.01)	0.013 (± 0.001)	-12.5 (± 0.9)	32.0
		Pt-Co	1.4 (± 0.3)	2.68 (± 0.02)	0.013 (± 0.003)		
		Pt-Pt_2	2.5 (± 1.3)	3.86 (± 0.03)	0.017 (± 0.007)		
		Pt-O	0.7 (± 0.3)	2.00 (± 0.04)	0.024 (± 0.016)		
40% Pt/C 5 nm	0 (OCV)	Pt-Pt_1	7.5 (± 0.5)	2.76 (± 0.01)	0.011 (± 0.001)	-11.8 (± 1.0)	36.0
		Pt-O	0.5 (± 0.2)	2.02 (± 0.04)	0.010 (± 0.012)		
		Pt-Pt_2	3.4 (± 1.6)	3.93 (± 0.03)	0.018 (± 0.008)		
	0.9	Pt-Pt_1	7.9 (± 0.5)	2.76 (± 0.01)	0.012 (± 0.001)	-11.4 (± 1.0)	32.6
		Pt-O	0.6 (± 0.2)	1.99 (± 0.05)	0.018 (± 0.015)		
		Pt-Pt_2	3.1 (± 1.3)	3.92 (± 0.03)	0.014 (± 0.005)		
	0.6	Pt-Pt_1	7.6 (± 0.5)	2.75 (± 0.01)	0.011 (± 0.001)	-10.9 (± 1.0)	33.7
		Pt-O	0.5 (± 0.2)	2.00 (± 0.05)	0.015 (± 0.015)		
		Pt-Pt_2	2.7 (± 1.4)	3.92 (± 0.03)	0.015 (± 0.007)		

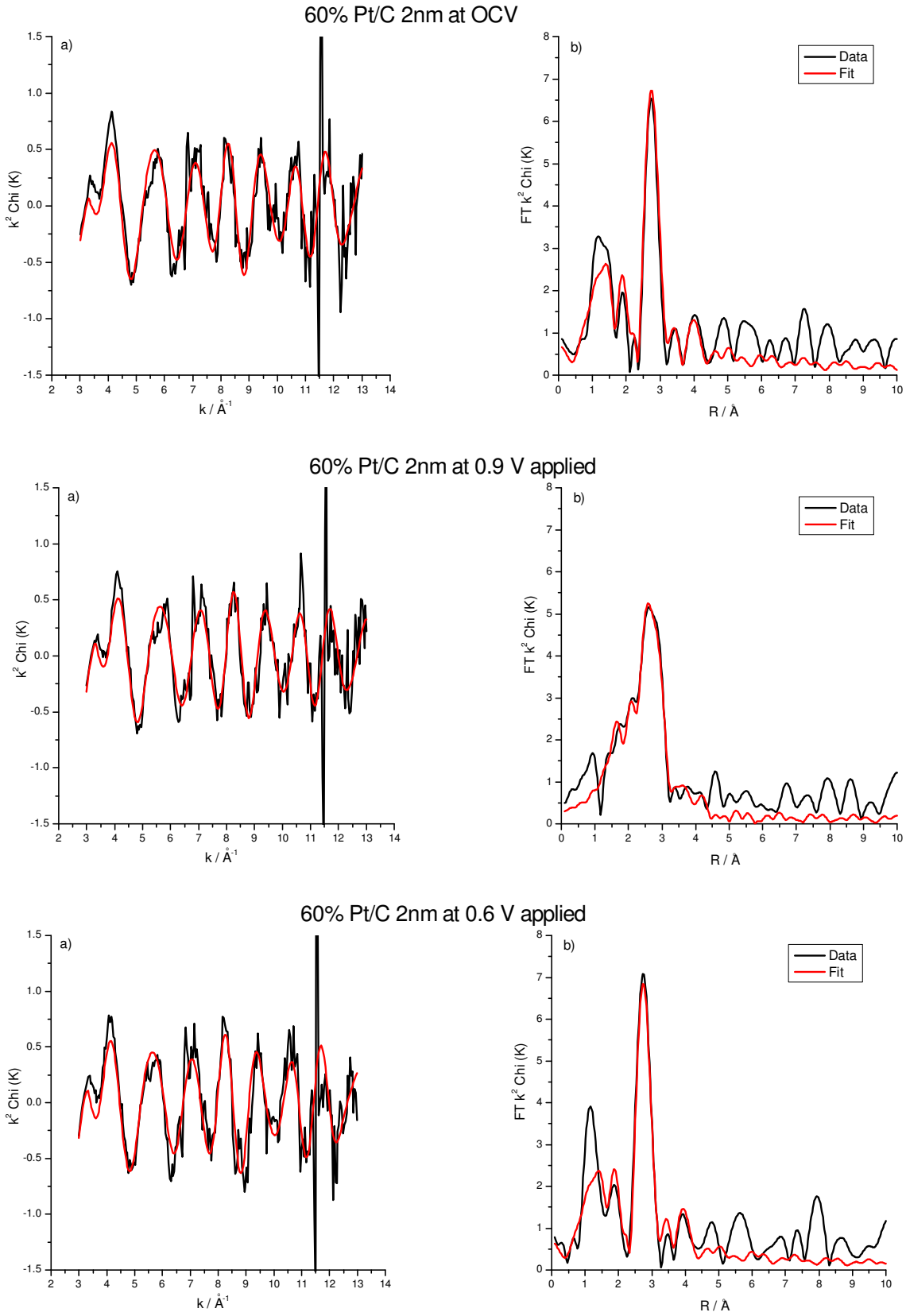

Figure 17 **k^2 weighted experimental a) EXAFS (black) and theoretical fit (red) plot and corresponding b) Fourier transforms for 60% Pt/C in the transmission XAS fuel cell at a range of applied potentials (Fuel cell)**

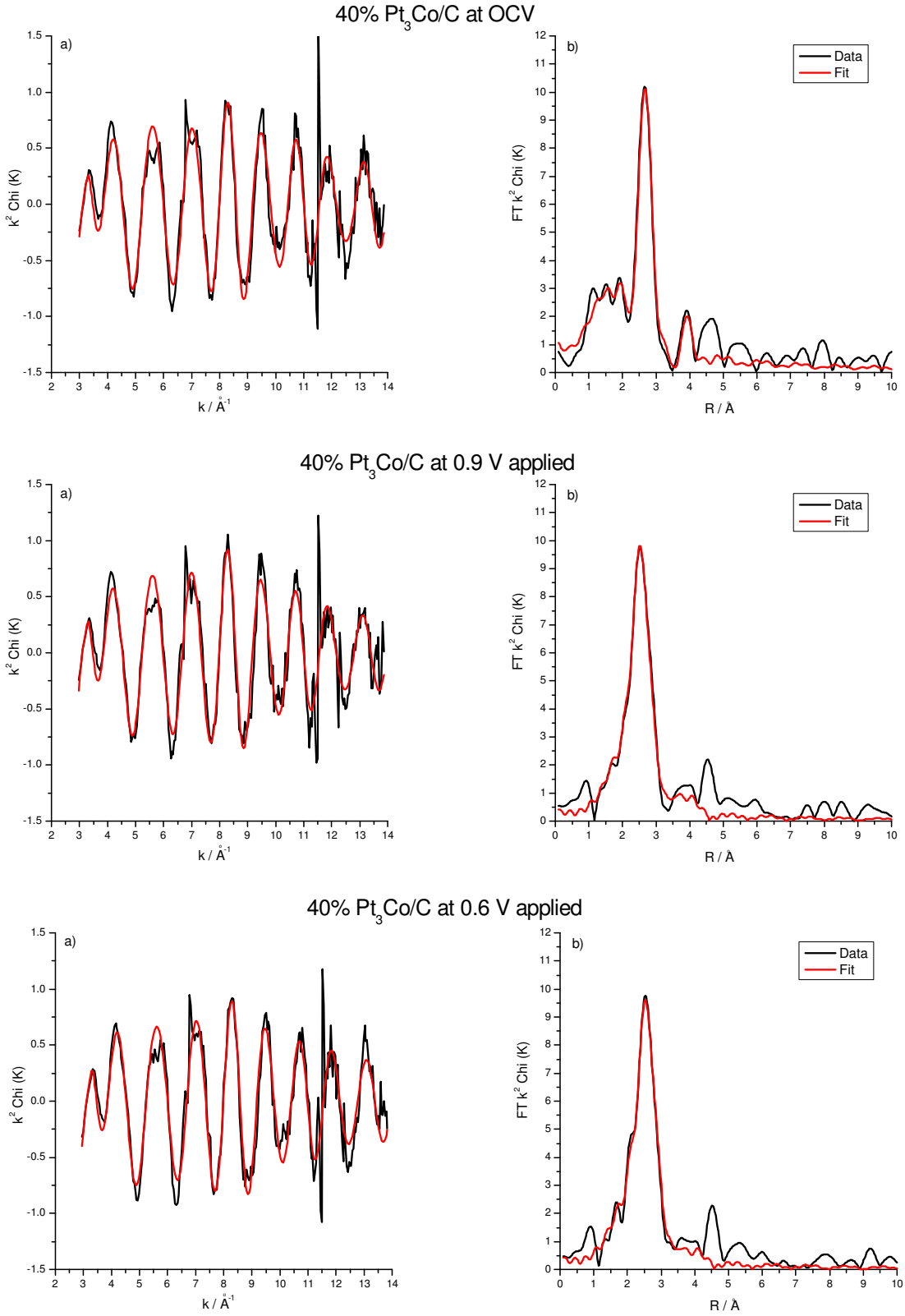

Figure 18. **k^2 weighted experimental a) EXAFS (black) and theoretical fit (red) plot and corresponding b) Fourier transforms for 40% Pt_3Co/C in the transmission XAS fuel cell at a range of applied potentials (Fuel cell)**

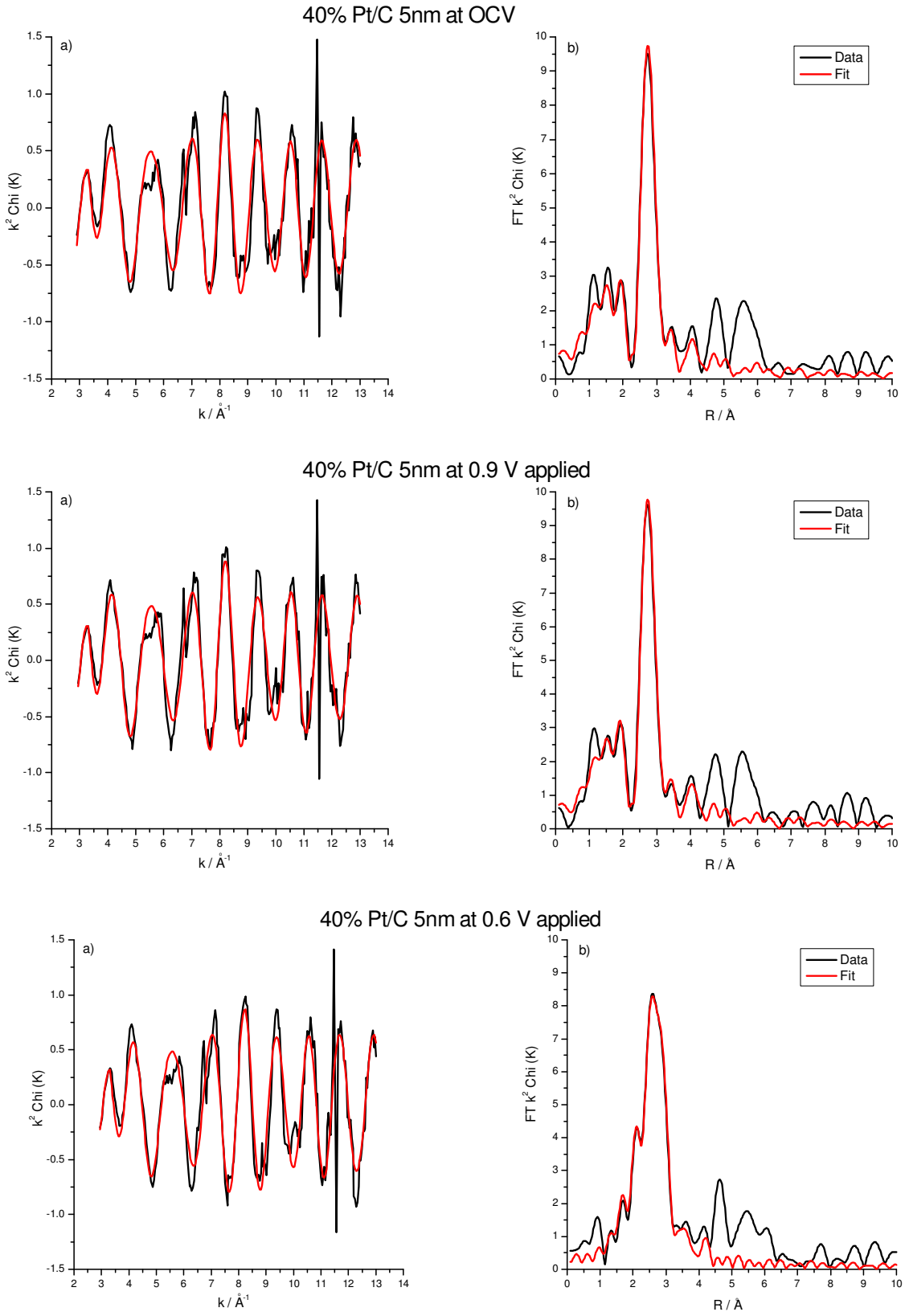

Figure 19. **k^2 weighted experimental a) EXAFS (black) and theoretical fit (red) plot and corresponding b) Fourier transforms for 40% Pt/C in the transmission XAS fuel cell at a range of applied potentials (Fuel cell)**

4.4.1 Cell performance during XAS experiments

To validate the premise that structural parameters obtained during XAS measurements are representative of the fuel cell operating under realistic conditions, the cell performance was measured during the XAS measurements in O_2. These tests were performed after the potential stepping experiments under nitrogen atmosphere were conducted. The cell resistance was measured at an applied potential of 0.8 V and was found to be 2.5 - 3 times (0.5-0.6 Ω cm^{-2}) higher than that observed during the validation experiments described in section 2. This increase is thought to be a consequence of the long periods (up to 6 hrs) under drying conditions during the N_2 potential hold testing conducted at the beamline. This explains the observed lower performance seen in Figure 15. Validation testing did not consider the impact of the N_2 atmosphere testing times on catalyst performance. In addition due to the limited time available for synchrotron experiments it was impractical (and thought unnecessary) to condition the MEA for more than the ten potentiostatic conditioning cycles described in Chapter 2 section 2.2.5. (which may have been in error).

The measured cell voltage was corrected using the measured cell resistance at 0.8 V. The very high resistance meant that rather than obtaining data over a true cathode potential range of 0.6 to 0.9 V, the data was only obtained over cathode potentials of approximately 0.82 V to 0.92 V. It is perhaps not surprising then that no structural change is observed in the XAS measurements as a function of the load. The corresponding iR correction for the data collected under N_2 was $\leq$ 20 mV as the currents were much smaller, therefore a larger potential window was able to be studied.

To check the performance of all catalysts during XAS measurements an oxygen polarisation curve was obtained using the conditioning procedure. The uncorrected cell voltage data is shown in Figure 15. To obtain the cathode performance the data was corrected for the measured resistance at 0.8 V and the hydrogen crossover of ~13 mA cm^{-2} (this is ten times higher than in validation experiments. See Chapter 5 for possible explanation). The anode polarisation could not be accounted for as it was not measured under the operating conditions at the beamline, but the same anode was used in all cases and validation experiments showed that the Pd/C anode did not result in deviation in performance from the Pt/C anode in the kinetic region (Figure 2). Figure 20

shows the corrected performance for all catalysts and a comparison with the performance obtained of the 60% Pt/C MEA during the validation experiments.

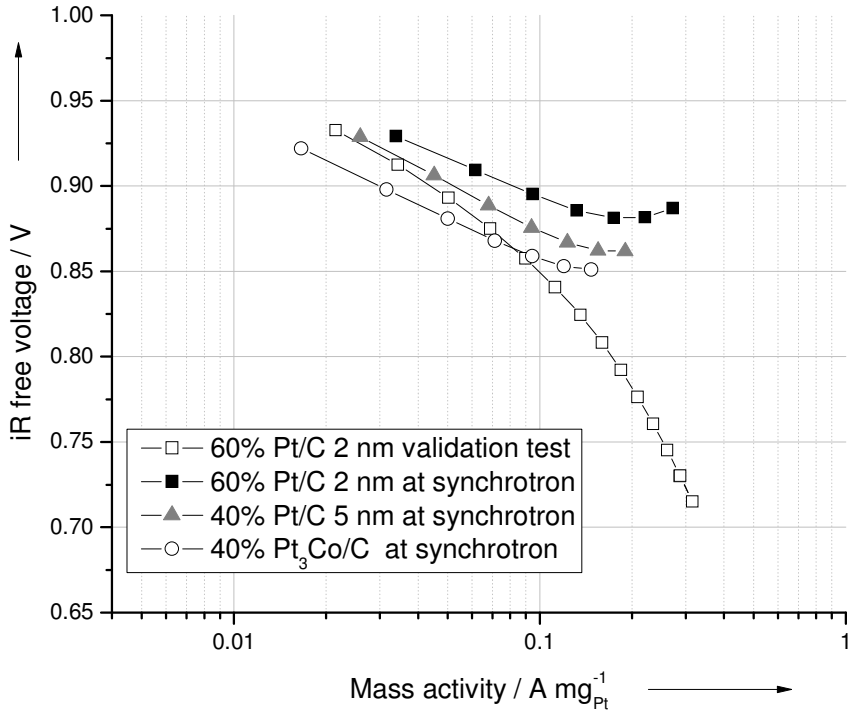

Figure 20. iR free fuel cell mass activity performance at the synchrotron of MEAs with 60% Pt/C, 40% Pt/C and 40% Pt_3Co/C cathodes with 2.0, 2.4 and 3.3 $mg_{Pt}\,cm^{-2}$ loading respectively. For comparison the mass activity of a 60% Pt/C MEA tested in the validation experiments is shown. All MEAs were prepared with the same 10% Pd/C anode, Nafion 115 and tested with H_2 anode gas and O_2 cathode gas at 60 ml min^{-1}, 10 psi, 65 °C

Figure 20 shows that the expected performance was not achieved at the synchrotron for all MEAs. The 60% Pt/C 2 nm MEA has higher performance than the validation test, the 40% Pt/C 5 nm MEA shows comparable performance to the validation test, but lower performance than the 2 nm Pt/C catalyst tested under more comparable conditions at the synchrotron. From the results presented in Chapter 3, Figure 1, it is expected that the mass activity of these two catalysts should be the same. The difference between the 2 nm Pt/C MEAs is likely to be the consequence of the very high resistance measured at the synchrotron and the data generated at the synchrotron using the conditioning scans rather than the full polarisation with longer equilibration times (see Chapter 2 section 2.2.4).

Figure 20 also shows that the 40% Pt_3Co/C alloy catalyst does not retain the expected two times mass activity benefit over the Pt/C catalysts and has lower performance than all the Pt only MEAs. It is also noted that despite no applied anode polarisation correction all synchrotron tested MEAs show non linear Tafel behaviour at high mass activities (high current densities) indicating over correction of the voltage. This over correction arises from only having one resistance value at 0.8 V to correct data at all potentials. While valid at low currents close to 0.8 V the correction factor is too high at high currents, since under these conditions increased water generation occurring at the cathode is likely to improve layer and membrane hydration and consequently decrease the cell resistance. The poorer performance of the 5 nm Pt/C and Pt_3Co/C alloy at the synchrotron is thought to be a layer thickness effect. The layer thickness of the 5 nm Pt/C catalyst is significantly thicker than for the 60% Pt/C catalyst due to both difference in carbon content of the catalyst and the absolute metal loading on the electrode (2.4 $mg_{Pt}\,cm^{-2}$). For the alloy even higher loadings were used to enable Co K edge measurement (section 4.4). The very low performance of the Pt_3Co/C alloy catalyst suggests there is poor utilisation of the catalyst layer and parts of the catalyst are not active for oxygen reduction, the same is true, but to a lesser extent, for the 5 nm Pt/C catalyst.

4.4.2 The effect of atmosphere on catalyst structure

Figure 21 compares the EXAFS first shell fitting parameters obtained for 60% Pt/C (2 nm) at OCV as a function of iR free cathode potential under both half cell (N_2) and fuel cell (O_2) conditions. The corresponding applied potentials are 0.8 V and 0.9 V under nitrogen and 0.6 and 0.9 V under oxygen. The iR free cathode potential has been calculated using the resistance value measured at 0.8 V. Under the drying conditions used during half cell testing this correction factor is thought to be a representative way of determining the cathode potential and, due to the low currents correction has little impact on the cathode potential. As discussed in section 4.4.1, under fuel cell conditions the 0.8 V correction factor is valid for high potentials, but is an overcorrection at low applied potentials/high current densities. It is therefore noted the oxygen data at 0.6 V applied, ~0.85 iR free, is best compared to the nitrogen data at ~0.8 V.

For 60% Pt/C (2 nm) during oxygen reduction a decrease in the Pt-Pt first shell coordination number occurs compared to the catalyst at a comparable potential under half cell conditions. Interestingly a similar number of Pt-O neighbours are present in both environments, although the Pt-Pt coordination numbers are different. This observation suggests a variation in the morphology (shape) of the particles in the presence of O_2. It has been suggested by Teliska *et al.* (28) that the chemisorption of atomic oxygen causes the platinum particles to become flatter, though this was thought unlikely by Teliska *et al.*. A flattening of the particles in oxygen *vs.* nitrogen atmosphere is a possible structural that would fit the observed differences in this work.

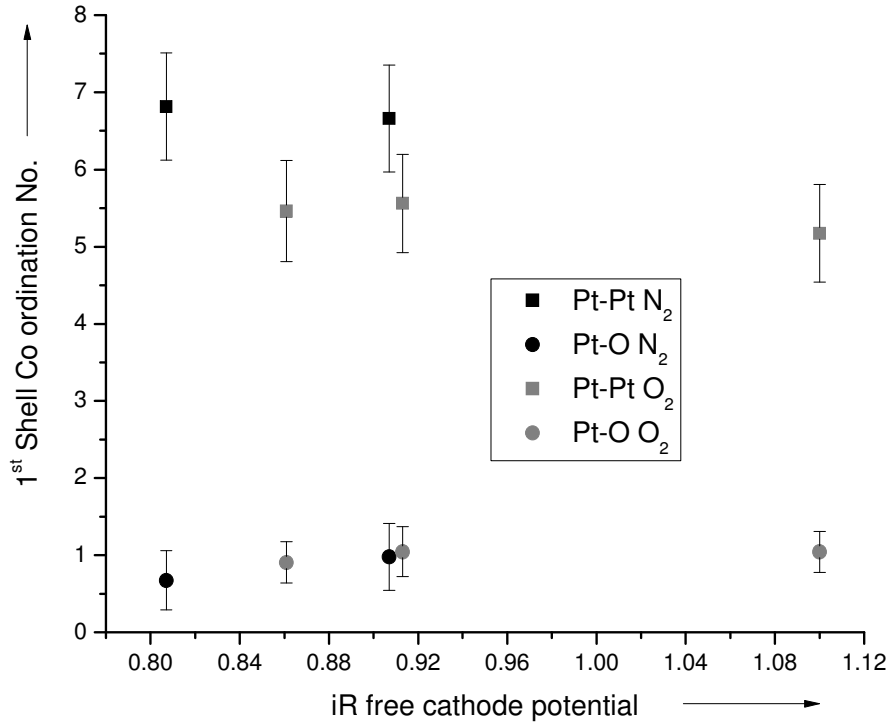

Figure 21. The effect of cell conditions on the first shell neighbours at comparable iR free cathode potentials for 60% Pt/C (2 nm)

The corresponding plots for the 5 nm 40% Pt/C catalyst and 40% Pt_3Co/C alloy are shown in Figure 22 and Figure 23. Similar Pt-Pt, Pt-O and Pt-Co co ordination numbers are observed in both cell environments. A small decrease in Pt-Pt neighbours is observed in O_2 for Pt/C at ~0.8 V but no change is observed at ~0.9 V. No observable changes in the structures of 5 nm Pt/C and the PtCo/C alloy were found with variation of either the cell potential or environment.

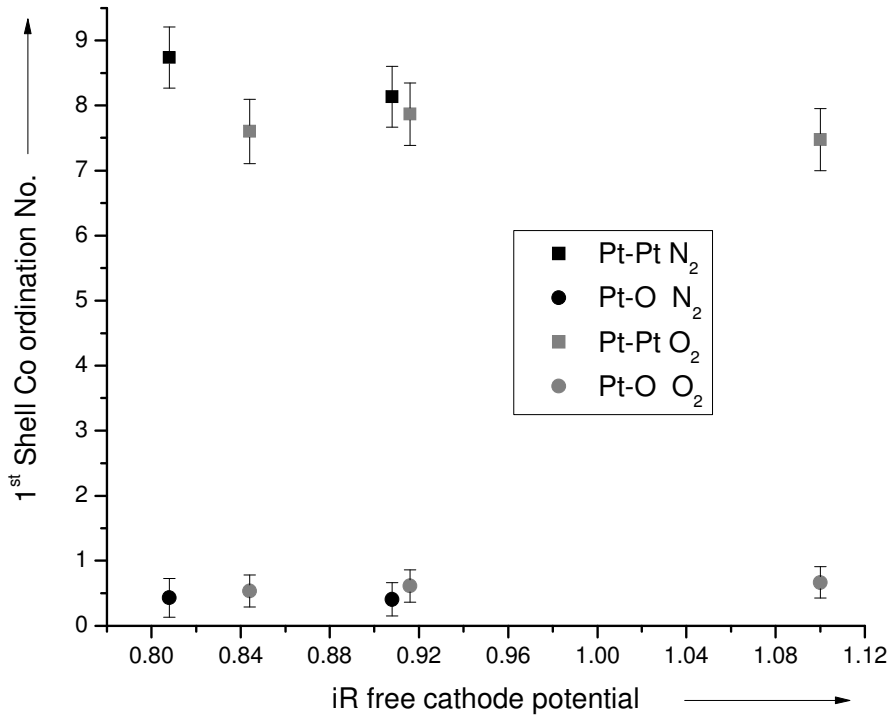

Figure 22. The effect of cell conditions on the first shell neighbours at comparable iR free cathode potentials for 40% Pt/C (5 nm)

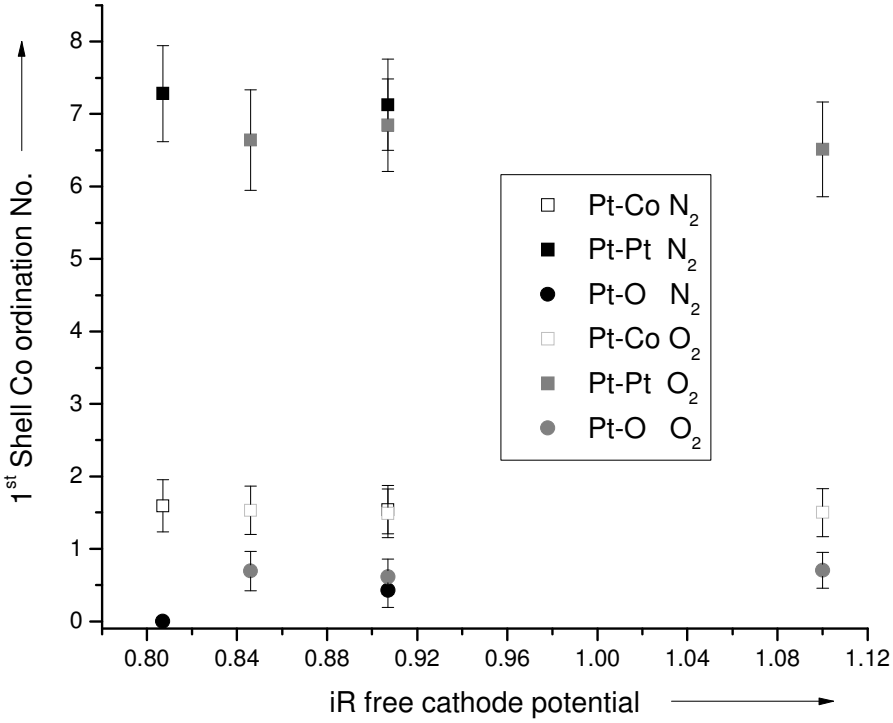

Figure 23. The effect of cell conditions on the first shell neighbours at comparable iR free cathode potentials for 40% Pt_3Co/C

4.5 Co K edge Experiments

To enable full characterisation of the PtCo/C alloy catalyst and to study the effect of acid leaching on catalyst structure during fuel cell operation XAS data collection at the Co K edge (7.709 keV) is desirable. *Operando* measurements at the Co K edge with the version II plate design used for Pt L_{III} edge experiments proved impossible in both transmission and fluorescence modes even with the beam signal optimised to maximum through the ionisation chambers. However, if the MEA was tested *ex-situ* a reasonable edge jump and signal was obtained. This indicated that the graphite plates were too thick were blocking the X-rays at this edge. To counter this problem, the graphite plate was completely removed from the beam path by drilling a hole 3 mm x 3 mm square hole though the plate into the flow field channel. To ensure a gas and watertight seal a kapton window (with low X-ray absorbance) was glued into a recess made in each graphite plate. A graphite insert was positioned over the recess to ensure optimum cell compression. The new plate design (version III) is shown in Figure 24.

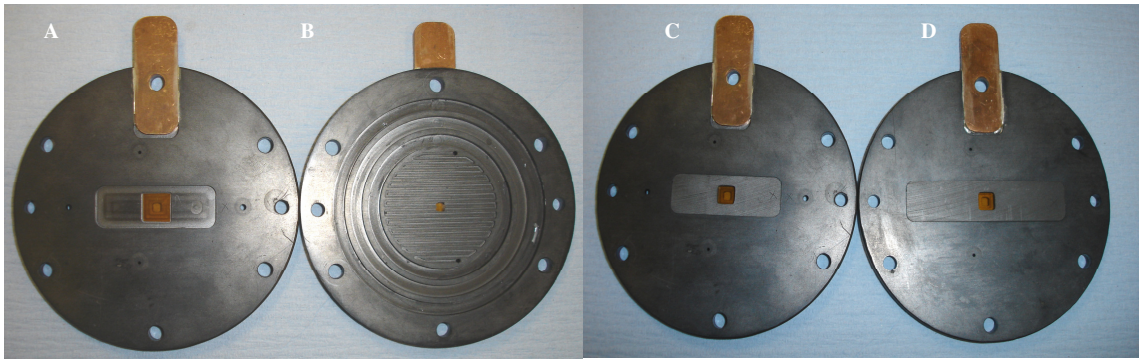

Figure 24. EXAFS transmission fuel cell plate version III (A) Anode plate showing recess and kapton window (B) Cathode plate flow field view (C) Anode plate with graphite insert (D) Cathode plate with graphite insert

Whilst the design modification facilitated XAS measurement, complete removal of the graphite plate in the region of the window may have some unavoidable implications for the MEA. In this region electrical contact is removed, gas may by-pass the window area / part of the MEA and water may build up during testing. These factors will all affect catalyst utilisation and may explain why the MEA performance of a 0.4 $mg_{Pt}\,cm^{-2}$ Pt/C MEA is lower with the version III design than the version II design as shown in Figure 25. In addition the cell resistance was higher for the version III design. This is likely to

be due to the lack of compression in the window region. The same trends were also observed for the PtCo/C alloy catalyst.

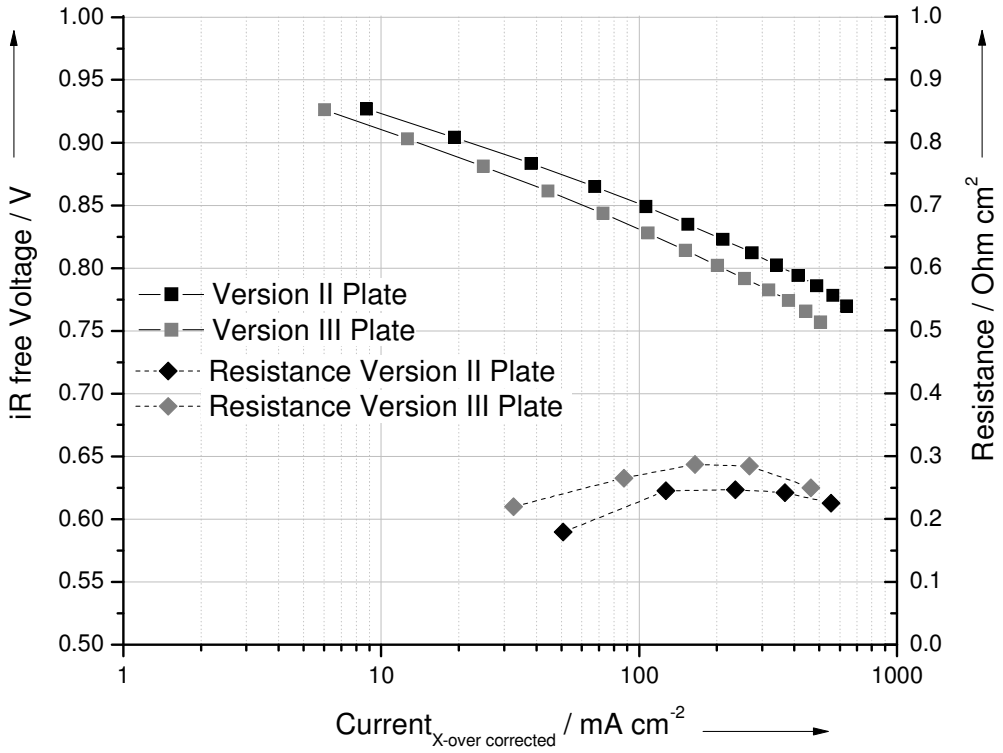

Figure 25. Comparison of fuel cell performance in Version II EXAFS transmission cell and Version III transmission cell for MEA: Anode Pt/C, cathode Pt/C, Nafion 115 tested in duplicated with H_2 anode gas O_2 cathode gas at 60 ml min^{-1}, 10 psi, 65 °C

Co K edge XAS data were collected for both the Pt_3Co/C alloy and the acid leached Pt_3Co/C using MEAs with a Pt loading of 3.3 $mg_{pt}\,cm^{-2}$ and corresponding Co loading of $\leq$ 1.1 $mg_{Co}\,cm^{-2}$. Despite the new plate design the XAS data quality during the short acquisition times of the potential stepping experiments was insufficient to obtain analysable EXAFS data. Example spectra are shown in Figure 26. It can be seen that the edge jump in the raw data is small (0.4) with little definition in the EXAFS region. The edge jump is less than half that measured for both samples at the Pt L_{III} edge during *operando* experiments and for powder samples at the Co K edge. In addition, it can be seen that both the Chi and Fourier transform plots are noisy. Attempts to fit the data resulted in poor fit values, with $R_{EXAFS} > 58$. For the acid leached samples the lower Co concentration resulted in a further decrease in data quality. The results of these

experiments are therefore not presented and no comment on the effect of acid leaching on the catalyst structure under operating conditions can be provided. Possible ways of obtaining this information will be discussed in Chapter 5, section 5.

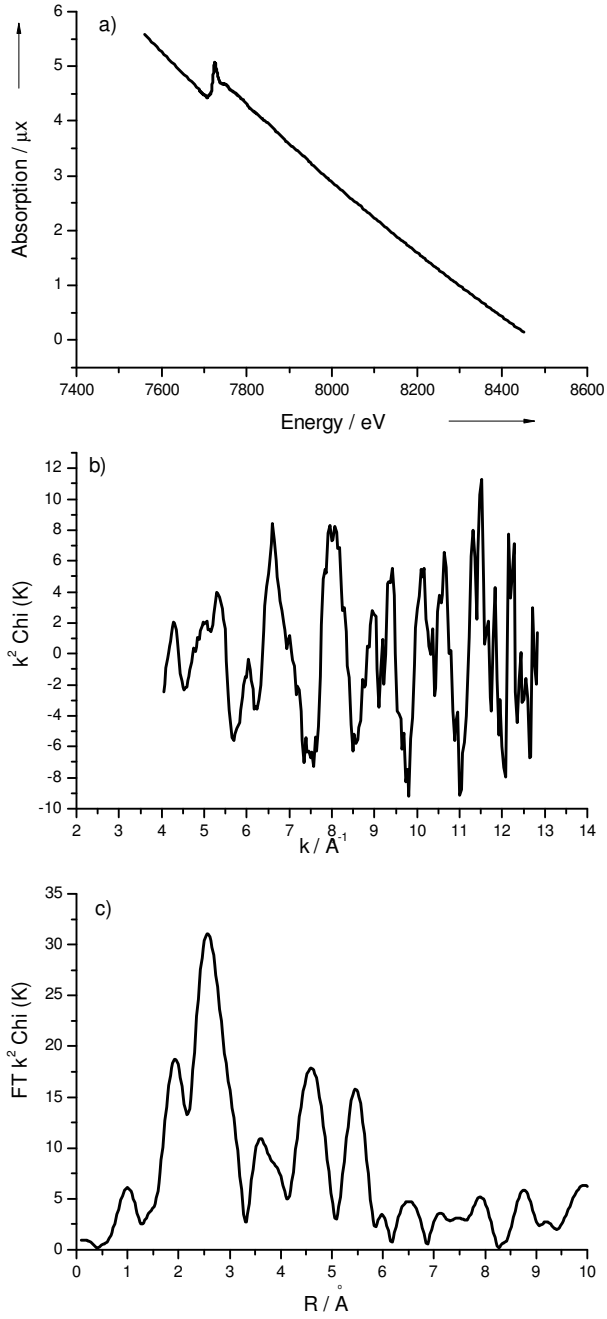

Figure 26. Example Co K edge data for 40% Pt_3Co/C at 1.1 mg_{Co} cm^{-2} a) XAS spectrum b) Chi plot and c) Fourier transform plot

5. Conclusions

A fuel cell capable of allowing *operando* XAS of fuel cell cathode catalysts operating under realistic conditions has been successfully validated. In validation experiments with low loaded MEAs the activity benefit of a Pt_3Co/C alloy catalyst over Pt/C was observed as expected from experiments using fuel cells of more conventional design. *Operando* XAS experiments performed at the Pt L_{III} adsorption edge in transmission mode have been conducted for a 60% Pt/C, 40% Pt_3Co/C cathode catalysts and 40% Pt/C with comparable particle size to the alloy. Structural information from XAS has been correlated to catalyst performance in nitrogen and oxygen. For 60% Pt/C XANES and EXAFS analysis show that under nitrogen the extent of oxide coverage increases with increasing potential up to 1.0 V. EXAFS analysis shows a corresponding decrease in Pt-Pt coordination corresponding to particle disruption by oxide growth. In comparison, the alloy catalyst required a higher overpotential before the onset in oxide formation under nitrogen and fewer Pt-O neighbours at each applied potential. The lack of structural change was found to be a consequence of particle size and insensitivity to the surface changes of the XAS technique compared to the electrochemical measurement.

To enable direct comparison between Pt/C and the Pt_3Co/C alloy a Pt/C catalyst with comparable particle size to the alloy catalyst was also studied. Under N_2 both catalysts required an applied potential of > 0.8 V before Pt-O neighbours could be fitted, with the alloy requiring potentials of 0.9 V. The increase in the potential at which oxides are formed has been previously invoked as an explanation for the enhanced activities of alloys for the ORR (17, 18). However, evidence of this effect from the XAS experiments is not strongly compelling in this work, due to the large fitting errors observed and the decreased surface sensitivity for detection of surface species for these larger particle sized catalysts. Unlike the small particle size 60% Pt/C catalyst little disruption to the particle structure occurs on oxide formation at 1.0 V. This may in part help explain the increased stability observed for the larger particle materials as reported in Chapter 3.

For all catalysts no change in coordination number was observed under oxygen at OCV or during oxygen reduction at applied potentials down to 0.6 V. For the 2 nm 60% Pt/C catalyst the same number of Pt-O neighbours and a lower Pt-Pt first shell coordination

number is observed in oxygen compared to nitrogen at the same iR free cathode potential. This was attributed to a difference in particle morphology between the active state whilst undergoing oxygen reduction and the oxidised state at similar potentials under nitrogen. No strong evidence for the same effect was observed for the 5 nm 40% Pt/C and 40% Pt_3Co/C catalyst within the fitting errors.

The high resistance values measured during XAS measurements result in a perturbation (~100 mV) in cathode potential under oxygen. Analysis of catalytic performance during *operando* XAS measurements highlights possible catalyst utilisation issues, likely to be a consequence of the thick layers used, especially for the 5 nm Pt/C and 40% Pt_3Co/C catalysts. This means the catalysts are not behaving as expected in a conventional fuel cell and brings into question how representative the XAS fitting parameters are of the catalyst operating under idealised, realistic fuel cell conditions. Proposed methods / modifications to the experimental design to overcome these problems will be discussed in Chapter 5.

In all cases the time scale of the potential stepping experiments did not allow the processes of oxide formation and removal to be measured at intermediate points. To achieve greater time resolution a different experimental approach was required. The results obtained using this approach are described in Chapter 5.

References

1. S. L. Hudson, S. C. Ball, K. B. Blaney, G. H. Chouchelamane, S. G. Fiddy, I. Harvey, P. Sivasubramaniam, B. C. Tessier, B. R. C. Theobald, D. Thompsett and A. E. Russell, *ECS Transactions*, **16**, 1395 (2008).
2. R. A. Lampitt, L. P. L. Carrette, M. P. Hogarth and A. E. Russell, *Journal of Electroanalytical Chemistry*, **460**, 80 (1999).
3. W. E. O'Grady and D. C. Koningsberger, *Electrochemical Society Extended Abstracts*, **88-1**, 513 (1988).
4. J. McBreen, W. E. O'Grady, K. I. Pandya, R. W. Hoffman and D. E. Sayers, *Langmuir*, **3**, 428 (1987).
5. M. E. Herron, S. E. Doyle, S. Pizzini, K. J. Roberts, J. Robinson, G. Hards and F. C. Walsh, *Journal of Electroanalytical Chemistry*, **324**, 243 (1992).
6. S. Maniguet, R. J. Mathew and A. E. Russell, *Journal of Physical Chemistry B*, **104**, 1998 (2000).

7. E. Principi, A. Di Cicco, A. Witkowska and R. Marassi, *Journal of Synchrotron Radiation*, **14**, 276 (2007).
8. C. Roth, N. Martz, T. Buhrmester, J. Scherer and H. Fuess, *Physical Chemistry Chemical Physics*, **4**, 3555 (2002).
9. R. J. K. Wiltshire, C. R. King, A. Rose, P. P. Wells, M. P. Hogarth, D. Thompsett and A. E. Russell, *Electrochimica Acta*, **50**, 5208 (2005).
10. P. G. Allen, S. D. Conradson, M. S. Wilson, S. Gottesfeld, I. D. Raistrick, J. Valerio and M. Lovato, *Journal of Electroanalytical Chemistry*, **384**, 99 (1995).
11. R. Viswanathan, G. Y. Hou, R. X. Liu, S. R. Bare, F. Modica, G. Mickelson, C. U. Segre, N. Leyarovska and E. S. Smotkin, *Journal of Physical Chemistry B*, **106**, 3458 (2002).
12. A. Witkowska, S. Dsoke, E. Principi, R. Marassi, A. Di Cicco and V. R. Albertini, *Journal of Power Sources*, **178**, 603 (2008).
13. A. E. Russell and A. Rose, *Chemical Reviews*, **104**, 4613 (2004).
14. J. McBreen, W. E. Ogrady and K. I. Pandya, *Journal of Power Sources*, **22**, 323 (1988).
15. H. A. Gasteiger, J. E. Panels and S. G. Yan, *Journal of Power Sources*, **127**, 162 (2004).
16. S. C. Ball, S. L. Hudson, B. R. C. Theobald and D. Thompsett, *ECS Transactions*, **11**, 1267 (2007).
17. V. R. Stamenkovic, B. Fowler, B. S. Mun, G. F. Wang, P. N. Ross, C. A. Lucas and N. M. Markovic, *Science*, **315**, 493 (2007).
18. V. Stamenkovic, T. J. Schmidt, P. N. Ross and N. M. Markovic, *Journal of Physical Chemistry B*, **106**, 11970 (2002).
19. C. Roth, N. Benker, M. Mazurek, F. Scheiba and H. Fuess, *Applied Catalysis A-General*, **319**, 81 (2007).
20. A. E. Russell, S. Maniguet, R. J. Mathew, J. Yao, M. A. Roberts and D. Thompsett, *Journal of Power Sources*, **96**, 226 (2001).
21. H. Yoshitake, O. Yamazaki and K. Ota, *Journal of the Electrochemical Society*, **141**, 2516 (1994).
22. H. Imai, K. Izumi, M. Matsumoto, Y. Kubo, K. Kato and Y. Imai, *Journal of the American Chemical Society*, **131**, 6293 (2009).
23. R. E. Benfield, *Journal of the Chemical Society-Faraday Transactions*, **88**, 1107 (1992).
24. R. M. Darling and J. P. Meyers, *Journal of the Electrochemical Society*, **150**, A1523 (2003).
25. M. Teliska, V. S. Murthi, S. Mukerjee and D. E. Ramaker, *Journal of the Electrochemical Society*, **152**, A2159 (2005).
26. T. M. Arruda, B. Shyam, J. M. Ziegelbauer, S. Mukerjee and D. E. Ramaker, *Journal of Physical Chemistry C*, **112**, 18087 (2008).

Chapter 5. Probing the structure of Operating Fuel Cell Cathode Catalysts Using XAS – Part II

1. Introduction

In Chapter 4, results of XAS investigations using the transmission XAS fuel cell were reported. Scanning EXAFS was used, with a 10 s scan duration followed by a 2 s delay to allow the position of the monochromator to be reset before the next scan commenced. This Quick EXAFS experiment retains the point-by-point data acquisition of conventional scanning EXAFS, whilst improving the time resolution by optimisation of the speed of movement of the monochromator (1). While changes in catalyst structure from unreduced to oxidised were observed, the scanning nature of the experiment gave insufficient time resolution to study the intermediate steps in the oxide formation and removal process. Equally, mechanistic insight into the oxygen reduction reaction could not be obtained. Such studies require the time resolution to be further improved.

Improved time resolution can be achieved using Energy Dispersive EXAFS (EDE). EDE uses a 'bent' monochromator to instantaneously illuminate the sample with a focussed X-ray beam containing the desired spread of energies. Data acquisition on the millisecond time scale is therefore possible (1, 2). Using EDE with a 10 s time resolution, Allen *et al*. conducted an *in situ* experiment to follow Pt oxide formation during a potential step from 0.1 V to 1.2 V with N_2 feed to the cathode. Pt oxide removal was also studied by stepping the potential back to 0.1 V (3). Analysis of the XANES white line intensity and EXAFS allowed quantification of the rates of oxide formation and removal. In addition, the authors were able to propose a model of oxide formation for small particles that differed to that occurring on bulk electrodes and showed that restructuring of the Pt particles occurs during oxide formation and removal (3).

Understanding the mechanism of oxide growth on platinum achieved by potential cycling or potentiostatic holding is important, since it is well established that an oxide film on the surface can affect the mechanism and kinetics of surface processes (4). The presence of an oxide can have several effects, including: altering the thermodynamics of the reaction at the double layer; changing the electronic properties of the metal surface;

inhibiting charge transfer; and influencing the adsorption behaviour of reaction intermediates and/or products at the catalyst surface, potentially causing a site blocking effect (4). All of these factors have implications for the ORR (5, 6).

The mechanism for oxide formation is still under debate, with several mechanistic pathways proposed (4). From cyclic voltammetry, a general consensus exists where Pt-OH_{ads} forms at low overpotentials (~ 0.8 V *vs*. RHE), followed by Pt-O and PtO_2 formation at higher potentials. At potentials corresponding to a critical surface coverage of oxygen species (~ 1.0 V *vs*. RHE), the formation of subsurface oxygen species occurs and leads to the hysteresis observed in the voltammetry of Pt. This process, first proposed by Reddy *et al*. in 1968, is known as place exchange (7). Conway *et al.* proposed a model of oxide film formation in which the first step requires OH to adsorb on the Pt surface. OH is generated via oxidation of water molecules. Subsequently place exchange occurs, forming a subsurface HO-Pt quasi-3D lattice that deprotonates to form Pt-O (8, 9). Based on electrochemical quartz crystal microbalance data, this mechanism was questioned by Birss *et al.*, since no mass change corresponding to OH_{ads} or deprotonation was observed in their work (4, 10). AC voltammetry measurements by Harrington *et al.* also did not find evidence for the electrosorption of OH and instead a mechanism in which a direct two electron oxidation of Pt by reaction with a water molecule was proposed (11). More recently, based on cyclic voltammetry, electrochemical quartz crystal nanobalance and Auger electron spectroscopy measurements, Jerkiewicz *et al.* also concluded OH_{ads} was not involved in the mechanism of oxide growth (4, 12). A mechanism was proposed in which the first step involved the direct electro-adsorption of a water molecule resulting in a chemisorbed oxygen on the Pt surface and release of two hydrated protons. In a subsequent step in a quasi-3D lattice was formed comprising of Pt^{2+} and O^{2-} through the place exchange process (4, 12).

The layer thickness or quantity of oxide, q, per cm^2 of oxide films grown on Pt as a function of time at an applied potential, has been shown to follow logarithmic growth laws (5, 8, 12-14). Studies show that increasing potential, time at a given potential, and temperature all lead to increased layer thickness (5, 8, 12-14). In the work of Conway *et al.* (8) and Jerkiewicz *et al.* (12), q is determined by integration of the current associated with the removal of the oxide film grown during a given time period, t, at given

potential and temperature. Plots of q *vs.* log t or q^{-1} *vs.* log t have been shown to demonstrate linear dependence over a given thickness range (8, 12). Jerkiewicz *et al.* demonstrated that logarithmic growth is followed for up to one monolayer oxide thickness and inverse-logarithmic growth for thicker oxide films (12).

In this Chapter, findings from *operando* studies of a 2 nm diameter 60% Pt/C fuel cell catalyst using EDE are reported. In this work, significantly improved time resolution is used to provide mechanistic insight and structural characterisation during the oxidation and reduction of the Pt particles at a range of upper potential limits with N_2 feed. In addition, the Pt catalyst was studied during fuel cell operation with O_2 feed. A 40% PtCo/C and a 40% Pt/C catalyst with comparable particle size were also studied as was the effect of temperature on the rate of oxide formation and removal by conducting the experiments at a cell temperature of 35 °C and 65 °C.

2. Experimental

The MEAs studied were identical to those described in Chapter 4, section 3. The cell design and gas delivery system used was identical to that which has previously been described in Chapter 4. The version III plate design was used (see Chapter 4, Figure 18) to eliminate the interfering graphite absorbance, thereby improving the signal to noise ratio. The cell potential was controlled using an Eco Chemie Autolab PGSTAT 30 in conjunction with an Eco Chemie 20 Amp Booster. Measurements were conducted at cell temperatures of 65 °C and 35 °C. In both cases the incoming gases were humidified by use of MSAs and a circulating water bath set at 85 °C. Where measurements were conducted at 35 °C, the water circulation by-passed the water channels in the cell. Such low temperature measurements were conducted following failure of one of the graphite plates that make up the cell body during the experimental run at the ESRF. Potential step experiments in fuel cell mode were conducted at 10 psi with 60 ml min^{-1} H_2 at the anode and O_2 at the cathode. During potential stepping experiments in half cell mode, the cell operating conditions were: 60 ml min^{-1} H_2 at the anode with no applied pressure, and 60 ml min^{-1} N_2 at the cathode at 5 psi. As in the case of the lower temperature measurements mentioned above, these conditions differ from those reported in Chapter 4 and were used due to the plate failure.

2.1 XAS data collection and analysis

Experiments were conducted on beamline ID24 at the ESRF, Grenoble. The experimental set-up on the beamline is shown in Figure 1and Figure 2. Use of the EDE monochromator allowed collection of a XAS spectrum every 6.6 ms. To improve data quality, 15 spectra were summed giving a data set every 0.1 s. Oxide formation and removal were studied at the cathode under N_2 during potential steps from 0.125 V to 0.6, 0.7, 0.8, 0.9, 1.0, 1.1, 1.2, 1.3 and 1.4 V and back to 0.125 V *vs*. H_2 anode. In addition, the fuel cell was operated with O_2 at the cathode and the ORR studied during a potential step from OCV to 0.9 V and 0.6 V applied, followed by relaxation to OCV. To achieve reproducible timings, the XAS detector was triggered by the potentiostat. XAS spectra were recorded at the Pt L_{III} edge over an energy range of 11400-12330 eV (calibrated using a Pt foil reference from scanning XAS, see Chapter 2, section 2.3). Due to the nature of the EDXAS set-up, it is not possible to simultaneously record a Pt foil reference spectra for energy calibration. The sample stage must be moved to the foil position and a separate measurement made. Pt foil spectra were recorded every few experiments or ~ every 30 minutes, whichever was sooner.

Again, due to the nature of the EDXAS set-up, I_0 is also not simultaneously recoded before each measurement. The stage was therefore moved to obtain either I_0 using a dummy cell or I_0 with the beam just passing through air to allow a background calibration. The I_0 cell was fabricated from a Pd/C-only MEA sandwiched between two sheets of Kapton film to simulate the absorbance of the MEA without platinum. In addition, an air path I_0, (I_0 air) was also used. It was found that a better calibration was achieved using I_0 air (this is likely to be due to sample inhomogeneity in both the I_0 cell and the actual MEA under test) and therefore I_0 air was measured at the start of every experiment and was used for calibration.

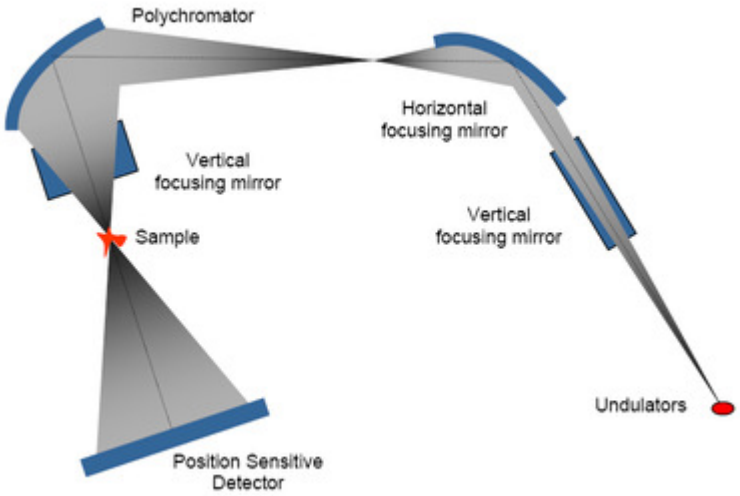

Figure 1. **Schematic view of the optical layout of the Energy Dispersive X-ray Absorption Spectroscopy beamline ID24 at the ESRF (15)**

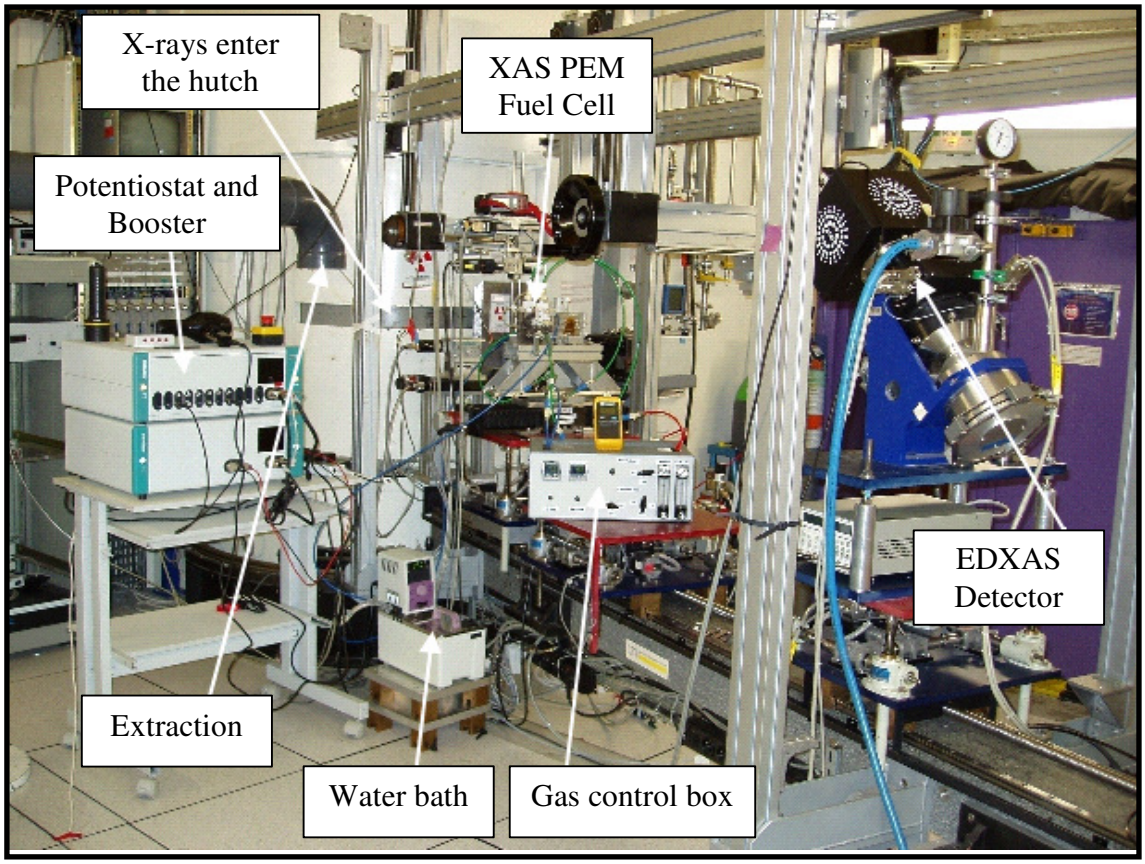

Figure 2. **Photograph of experimental set-up on ID24 at the ESRF**

4. Results of *operando* energy dispersive XAS experiments

The use of EDE compared to scanning XAS results in increased complexity when studying fuel cell catalysts. Ideally the bent crystal of the monochromator will result in a very small focussed spot on the sample. In reality this spot is large enough (~10 μm diameter) that the various X-ray energies each sample slightly different areas of the sample (2). The sample must therefore exhibit a high degree of spatial homogenetity over, as a minimum, the dimension of the focused beam for good quality data (1). The highly dispersed nature of the Pt nanoparticles supported on carbon, and the non-uniform carbon fibre and membrane components of the MEA, leads to some observable spatial inhomogeneity. The quality of the data was also compromised by the fact that the monochromator on ID24 is not well suited to study the Pt L_{III} edge, which is at the lower end of the bandwidth allowed. Together with the problems associated with sample inhomogenatity, this meant that only the XANES region of the spectra were of sufficient quality for analysis.

4.1 Half cell potential stepping experiments N_2 atmosphere

4.1.1 60% Pt/C 2nm

The EDE data was converted from detector position to an energy scale by calibration to a platinum foil reference collected both during the EDE experiments that had been energy calibrated using a platinum foil spectrum collected during scanning XAS experiments at the SRS Daresbury UK. No background correction was applied to the raw data but the data was cropped to isolate the XANES region. The Pt L_{III} XANES spectra for the 2 nm 60% Pt/C catalyst are plotted as a function of time following a potential step from 0.125 V to 1.2 V and back to 0.125 V at 65 °C in Figure 3. As can be clearly seen the white line intensity (peak maximum at 11564 eV) increases on stepping to 1.2 V and then falls back upon returning to 0.125 V. As can be seen in Figure 3, the time resolution of this work is sufficient to allow the changes in XANES intensity to be observed in real time. As discussed previously, the increased white line accompanies formation of the surface oxide and the return to the starting condition, removal of this oxide. The feature at 11580 eV also changes during the potential step. As the potential is increased, this peak decreases in intensity. When the potential is returned to 0.125 V, the peak intensity increases to a similar magnitude to that before

the potential stepping event. It is also noted that no change in edge position, and therefore no change in global oxidation state (bulk oxidation of the metal nanoparticles), occurs during the potential step and, therefore, the oxide appears to be restricted to the surface.

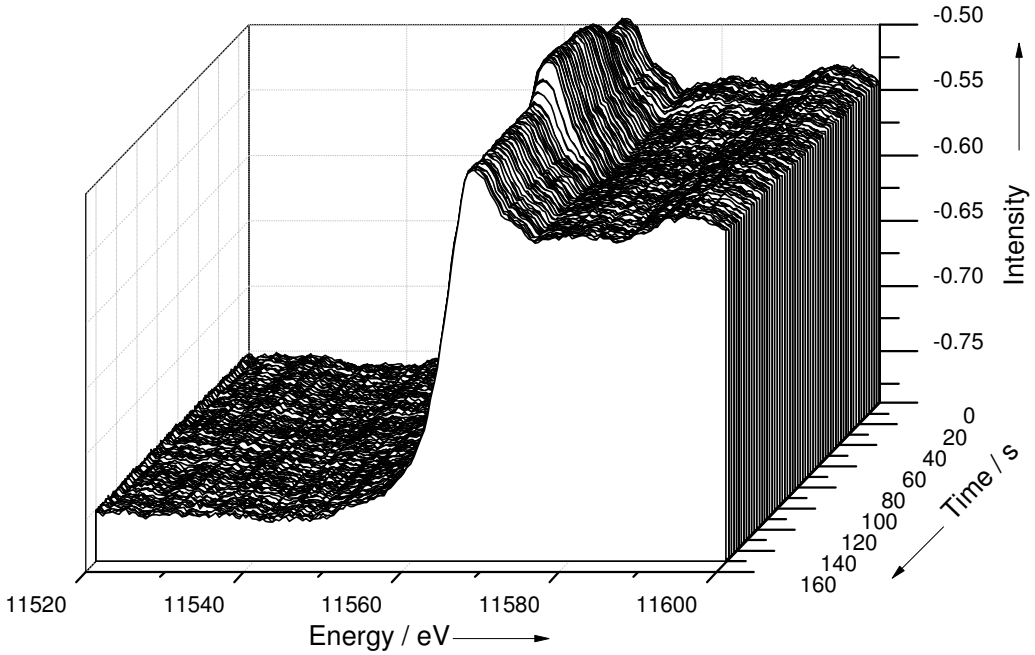

Figure 3. Pt L_{III} edge XANES spectrum of 60% Pt/C obtained *operando* in the XAS fuel cell undergoing a potential step from 0.125 V to 1.2 V at 20 s and back to 0.125 V at 80 s under N_2 at 65 °C

To allow comparison between experiments with different upper potential limits, the magnitude of the white line intensity change has been calculated with respect to time. This was achieved by subtracting the intensity of the pre edge region (at 11540 eV) from the maximum of the white line (at 11564 eV) for each scan, followed by normalising to the average intensity of the first 100 data points (10 s worth of data at 0.125 V) to give a normalised white line intensity (I). The changes in normalised white line intensity with time for potential stepping experiments at 65 °C from 0.6 to 1.2 V are shown in Figure 4. An increase in white line intensity is observed after stepping to potentials greater than 0.9 V, and the magnitude of the white line change increases with increasing upper potential limit. This corresponds to the formation of more Pt-O bonds (greater oxide coverage) at higher potential. Such an increase in white line intensity with increasing potential has previously been observed for Pt/C as electrode layers in

liquid electrolyte filled electrochemical cells in the literature (16-18) and in Chapter 4. In Chapter 4, section 4.1, the observed increase in white line intensity occurred at potentials greater than 0.7 V for this MEA, which is 0.2 V lower than in the EDXAS measurements. Possible reasons for these differences will be outlined later in this chapter.

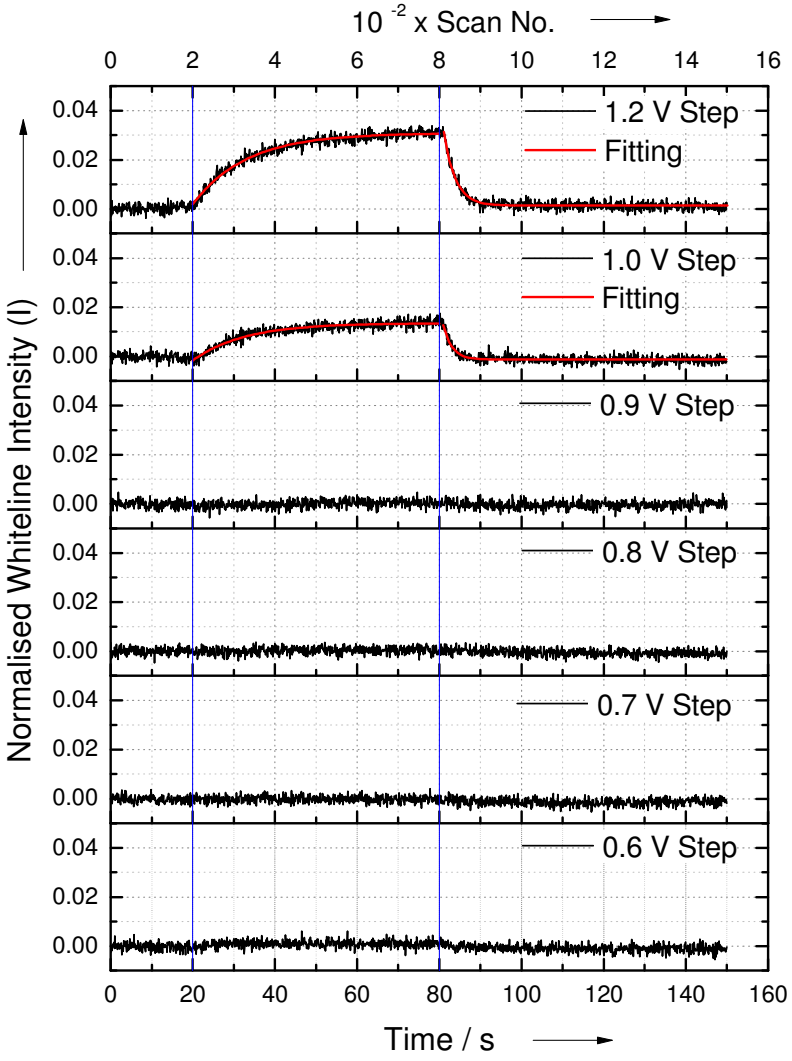

Figure 4. **Variation in white line intensity for 60% Pt/C following potential steps from 0.125 V to a range of upper potential limits at 20 s and back to 0.125 V at 80 s under N_2 at 65 °C (blue lines denote times of the potential steps). Exponential fitting of the experimental data is shown (red lines)**

Unlike the scanning XAS experiments conducted at the SRS, the use of EDE in this work has allowed sufficient time resolution to be able to follow, in real time, the

white line response due to changes in applied potential. These changes correspond to both platinum oxide growth (white line increase) and platinum oxide removal (white line decrease) for the potential steps to and from 1.0 V and 1.2 V.

To determine the rates of white line intensity change, the data have been fitted to an exponential function, Equation 1, in which I_i and I_f are respectively the initial and final values of I, *t* is time (in seconds) and τ is the time constant. In this work, the potential steps result in a sudden shift from the steady state defined by the experimental conditions, $1/\tau$ may therefore be considered as a relaxation time defining the change in the white line intensity as a consequence of the perturbation on the system. A larger $1/\tau$ value corresponds to a faster change in white line intensity, i.e. a more rapid formation or removal of oxide on platinum.

$$\mathbf{I = I_f - (I_f - I_i)\exp(-t/\tau)} \qquad \textbf{Equation 1}$$

This treatment has been previously reported by Nagai *et al*. (19) for changes in white line intensity corresponding to changes in particle size (sintering/redispersion) for Pt/Al_2O_3 and Pt/CeZrY mixed oxide catalysts. In this case the perturbation to the system was caused by changing the temperature and $1/\tau$ was defined as the speed of the Pt redispersion.

In this work an increase in the white line intensity occurred as soon as the potential was stepped to the upper potential limit, therefore the data were fitted from 20 s to 80 s corresponding to the time period when the potential was held at the upper limit. The potential step down to 0.125 V was fitted from 81 s to the end of the experiment. This start point was chosen because, after the potential step occurred, there was a delay of 1 s before the decrease in white line intensity commenced. The fitting results are shown as the red lines in Figure 4. The $1/\tau$ values from the fitting of the white line increase and decrease are reported in Table 1. The increase in white line intensity shows no dependence on potential while the corresponding decrease in white line intensity was found to be potential dependent and occurred significantly faster than the white line increase (4.6 time faster when stepping back from 1.2 V and 5.9 times faster when stepping back from 1.0 V).

Table 1. Fitted relaxation times for changes in the while line intensity for 60 % Pt/C 2 nm undergoing potential steps at 65 °C	
Potential Step	$1/\tau$ / s^{-1}
0.125 V to 1.0 V	0.08 ± 0.003
0.125 V to 1.2 V	0.08 ± 0.003
1.0 V to 0.125 V	0.46 ± 0.03
1.0 V to 0.125 V	0.35 ± 0.01

These results suggest oxide growth and removal occur by different mechanisms, in agreement with the irreversibility observed in the cyclic voltammetry (7). The slow rate and potential independence of oxide growth suggests this process is mass transport limited, while for oxide removal the increased removal rate with increased potential indicates that the process is limited by kinetics of the chemical reaction step, not mass transport. In very recent work by Imai *et al.* (18), the oxidation of Pt/C during a potential step from 0.4 to 1.4 V *vs.* RHE in liquid electrolyte by EDXAS with 0.9 s time resolution was reported. In this work EXAFS data was obtained and it is reported that with time, formation of different oxide species occur. In the first 30 s after the potential step a Pt-O bond attributed to either Pt-OH or Pt-OHH is seen to increase and then by 50 s, decrease in conjunction with formation of a bond assigned to Pt-O in 2 or 3D oxides formed by place exchange. It is also widely reported that the extent of place exchange is greater at higher potentials (7, 8, 12). It is therefore probable that the catalyst structure formed after the 60 s 1.0 V hold is different to the structure after the 60 s 1.2 V hold. It is also noted that the quantity or extent of platinum oxidation also increases with increasing upper potential limit. The differences observed in the removal rate may therefore be the consequence of different species undergoing the reaction.

The time lag of 1 s observed before the white line intensity change occurs during the reduction reaction has not previously been reported and is only seen here as a consequence of the improved time resolution obtained in this work. The delay implies that another process occurs before reduction of the oxide can commence. Since no delay is observed for oxide growth on a reduced Pt surface, it is postulated that the oxide covered Pt catalyst requires a longer time to charge than the reduced surface, and hence the effect of the applied potential does not occur instantaneously. This theory can not be corroborated with the current measured during the potential steps, since the time taken to reach the maximum current value after the potential is applied is the same for the reduced and oxidised surfaces. An alternative explanation for a time lag before removal, as proposed by Allen *et al.*, is that a gross rearrangement of the particle structure is

required before the reduction process can commence (3). Without the corresponding EXAFS information obtained simultaneously, it is not possible to comment if a structural change accounts for the time delay.

The effect of temperature on oxide formation and removal rates was also studied for the 2 nm 60% Pt/C catalyst by repeating the half cell potential stepping experiments at a cell temperature of 35 °C, using a new MEA. As at 65 °C, the intensity of white line was found to track the changes in the applied potential. The changes observed in the normalised white line intensity (I) with time during potential steps at 35 °C are shown in Figure 5. At 35 °C, an increase in the white line intensity occurs at all potentials greater than 0.7 V. With increasing upper potential limit, an increase in the magnitude of the white line change is observed. These results are in good agreement with the data collected at the SRS at 65 °C (detailed in Chapter 4), but as shown earlier at 65 °C in the EDXAS measurements, no change in white line intensity was observed until a potential of 1.0 V. This difference is thought to arise due to effects of the X-ray beam combined with the effect of temperature on the membrane.

The greater intensity of the X-ray beam and the small focal spot size at the ESRF was found to cause degradation of the Nafion membrane with time. Increases in white line intensity upon stepping the potential to the higher values were observed initially, but when repeat measurements were made some time later, the catalyst remained in the reduced state. When the beam spot position was moved to a different area of the sample which had not previously been exposed to the beam, the expected white line changes were once again observed. This apparent deactivation of regions of the catalyst seemed to occur more rapidly if the catalyst was operated at higher temperature. Under these conditions the measured (global) hydrogen crossover was also found to be higher. Accordingly it is proposed that degradation of the membrane by the X-ray beam resulted in localized thinning or even pinholing of the membrane, thereby exposing the cathode catalyst in the exposed region to much greater hydrogen crossover. This in turn suppresses the oxidation of Pt and therefore, although globally the catalyst was still responding to changes in potential, it remained reduced in the observation area. At 65 °C, data were collected for the 0.6 to 0.9 V potential steps sequentially before moving to a new region of the membrane for each of the 1.0 V and 1.2 V experiments. It is therefore possible that the 0.8 V and 0.9 V data is suffering from membrane

degradation and consequently not showing the same response observed at the lower temperature or at the SRS. Once the membrane degradation problem was identified, the beam was not left on the sample between measurements to try to preserve membrane integrity. The number of repeat measurements was increased to try to ensure that the response of the catalyst was not changing with time. However, it should be noted that it is not possible to know the amount of hydrogen crossover occurring in the measurement region during any measurement, or the extent to which the observed response of the white line may have been perturbed by hydrogen crossover.

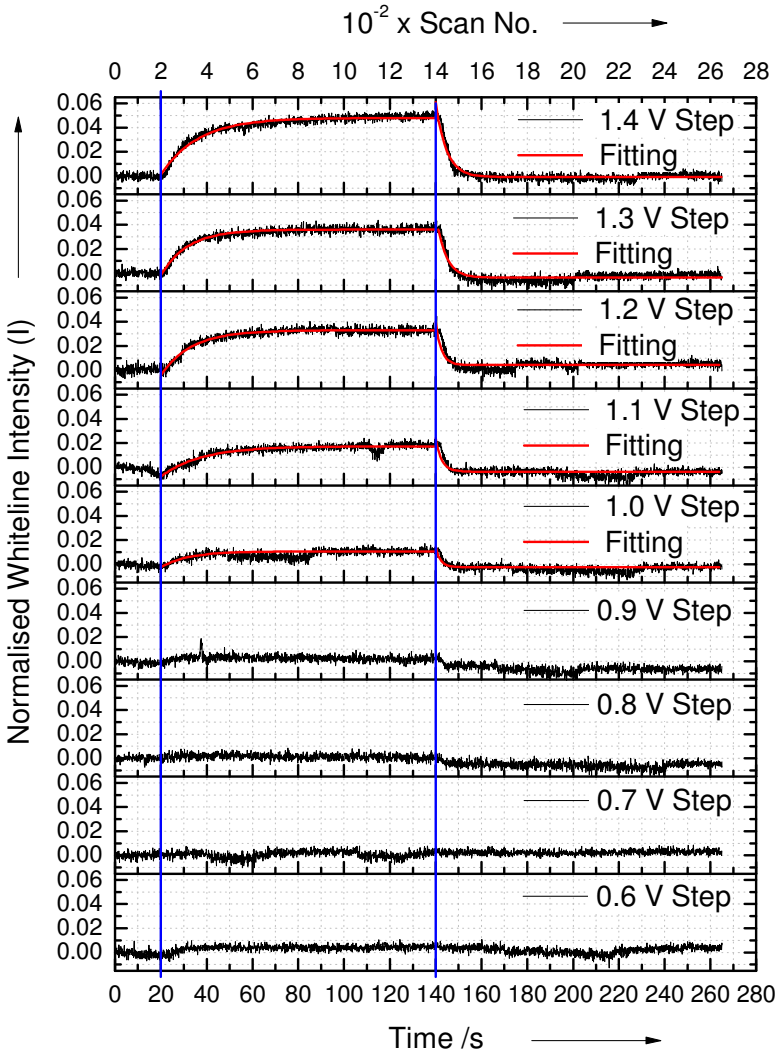

Figure 5. **Variation in white line intensity for 60% Pt/C following potential steps from 0.125 V to a range of upper potential limits at 20 s and back to 0.125 V at 140 s under N_2 at 35 °C (blue lines denote times of the potential steps). Exponential fitting of the experimental data is shown (red lines)**

The variation in white line intensities following potential steps at 35 °C are shown in Figure 5 together with the fitting using Equation 1 (red lines). The fitted 1/τ values for the white line increase and decrease (oxide formation and removal), with applied potential are shown in Figure 6 along with the values at 65 °C. No effect of temperature on the rate of change of the white line is observed. This may be a consequence of hydrogen crossover dominating or limiting the oxidation and removal processes.

As can be seen in Figure 6 the results obtained at 35 °C are consistent with those at 65 °C. The 1/τ value for the white line increase (oxide formation) is potential independent, whilst the value for white line decrease (oxide removal) is potential dependent. The higher the upper potential limit, the slower the rate of oxide removal. Across the potential range, oxide removal occurs between four and six times faster than oxide growth.

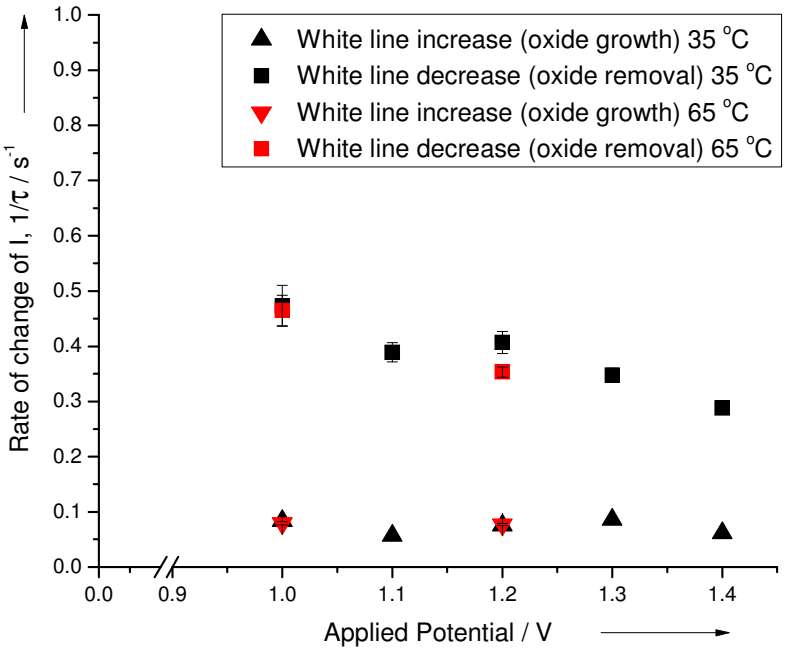

Figure 6. Effect of temperature on rate of change of white line intensity for 2 nm Pt/C undergoing potential steps under half cell conditions

4.1.2 40% Pt_3Co/C and 5 nm Pt/C

As in Chapter 4, 40% Pt_3Co/C and a 40% Pt/C catalysts of comparable particle size to the alloy were also studied to enable consideration of the effect of alloying on oxide formation and removal. The changes in white line intensity during the potential steps

and exponential fitting at the two temperatures are shown in Figure 7a/b and Figure 8a/b for the 40% Pt_3Co/C alloy and 40% Pt/C catalyst respectively. As for the 2 nm 60% Pt/C catalyst, the potential at which changes in the white line intensity occurred was lower at 35 °C than at 65 °C, for both catalysts. As in Chapter 4, the alloy and comparable particle size platinum catalyst showed very similar changes in white line response. Both catalysts exhibited an increase in white line intensity at potentials of 0.9 V or higher at 35 °C, and 1.1 V or higher at 65 °C. The higher the upper potential limit, the greater the extent of white line change observed.

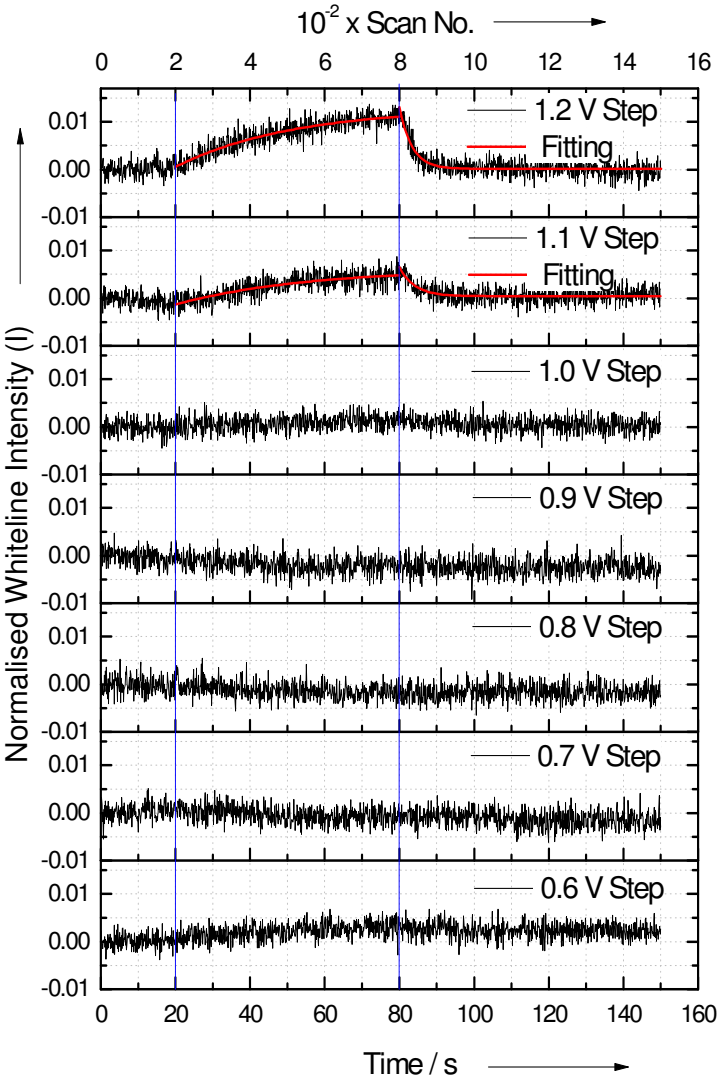

Figure 7a. **Variation in white line intensity for 40% Pt_3Co/C following potential steps from 0.125 V to a range of upper potential limits at 65 °C (blue lines denote time of the potential steps). Exponential fitting of the experimental data is shown (red lines)**

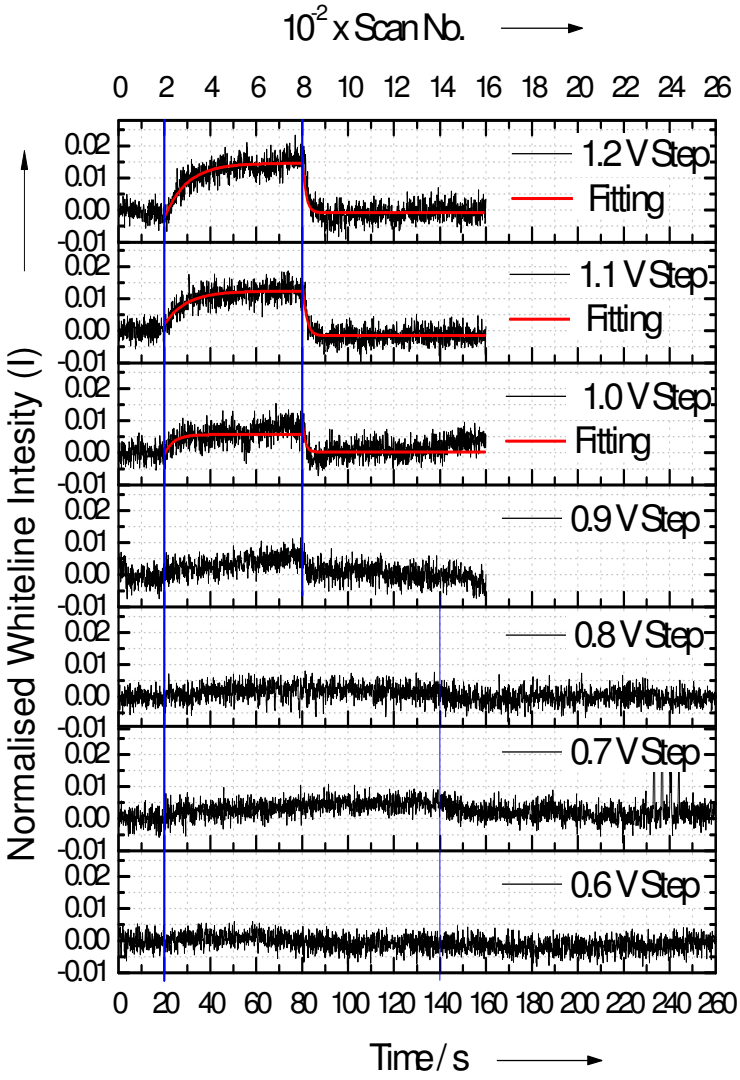

Figure 7b. **Variation in white line intensity for 40% Pt_3Co/C following potential steps from 0.125 V to a range of upper potential limits at 35 °C (blue lines denote time of the potential steps). Exponential fitting of the experimental data is shown (red lines)**

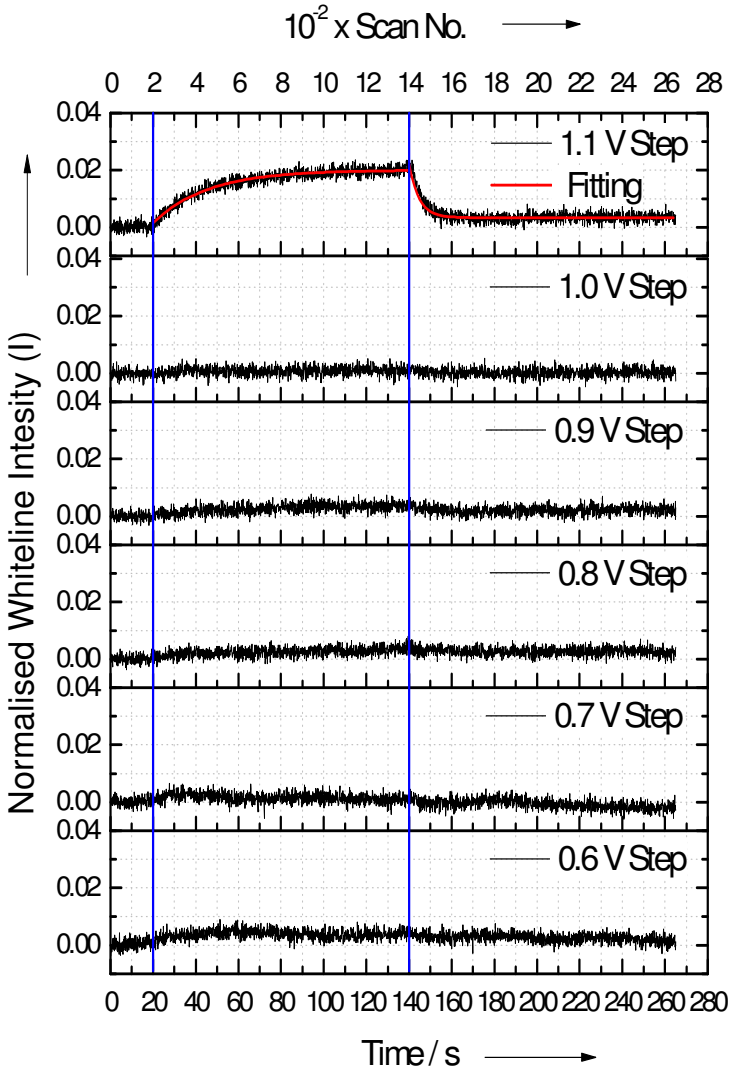

Figure 8a. **Variation in white line intensity for 5 nm 40% Pt/C following potential steps from 0.125 V to a range of upper potential limits at 65 °C (blue lines denote times of the potential steps). Exponential fitting of the experimental data is shown (red lines)**

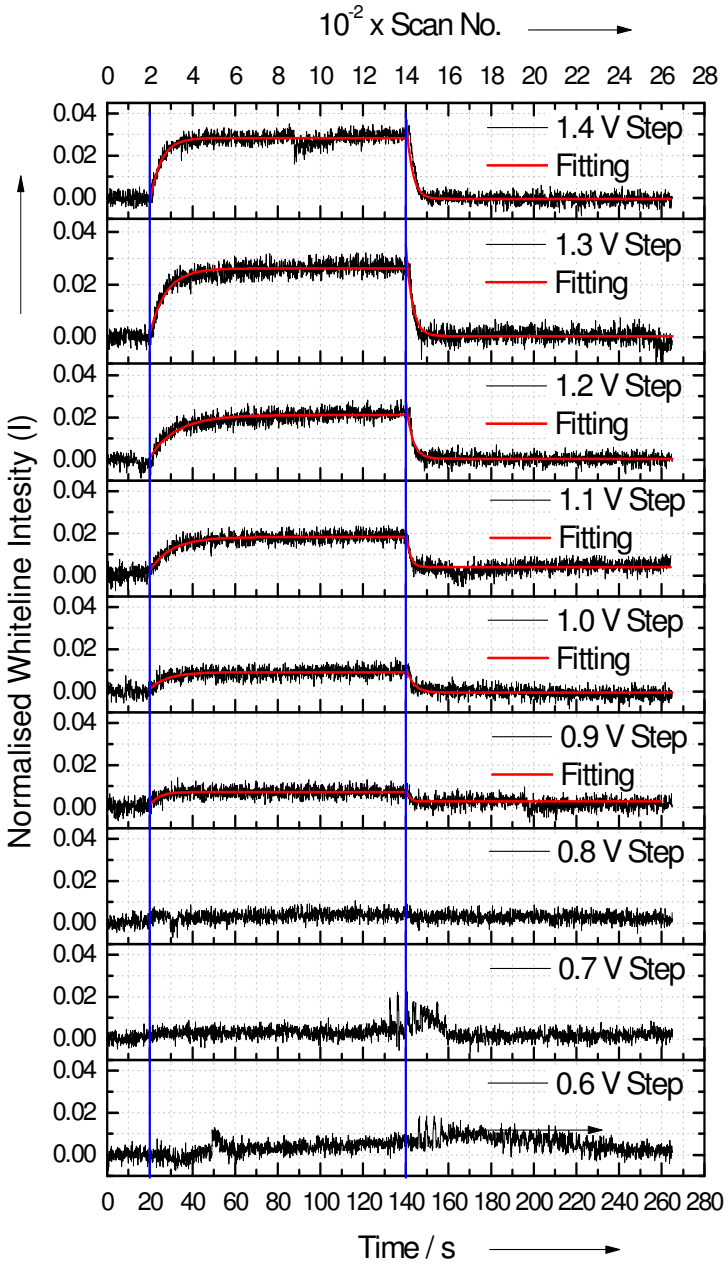

Figure 8b. Variation in white line intensity for 5 nm 40% Pt/C following potential steps from 0.125 V to a range of upper potential limits at 35 °C (blue lines denote times of the potential steps). Exponential fitting of the experimental data is shown (red lines)

As observed for the 2 nm Pt/C catalyst, the 1/τ values obtained for the white line decrease (oxide removal) are greater than those for oxide formation and at lower temperature, as shown in Figure 9. The faster relaxation time constants (1/τ) obtained at lower temperature are attributed to the decrease in the hydrogen crossover at lower

temperature. Due to the uncertainty about the integrity of the membrane during the tests, and the impact on the extent of oxide formation and removal, it is not considered appropriate to draw conclusions about differences between the PtCo/C alloy and Pt/C catalysts.

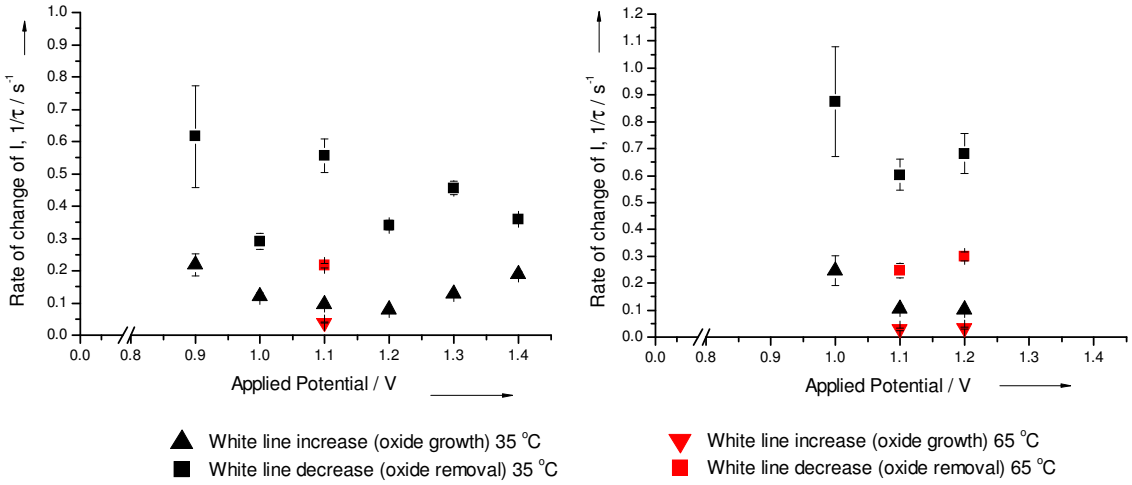

Figure 9. **Effect of temperature on rate of change of white line intensity for a) 40% PtCo/C and b) 5 nm 40% Pt/C undergoing potential steps half cell**

4.2 XAS characterisation during the ORR

The XANES was also collected during potential steps under fuel cell operating conditions with oxygen at the cathode. The potential was stepped from OCV (~1.1 V) to 0.9 V (applied) after a 5 s OCV hold, then the applied potential removed after a further 60 s and the cell allowed to relax to OCV. The same experiment was conducted with a potential step to 0.6 V (applied). The XANES spectrum and oxygen reduction current were recorded for each potential stepping event for 2 nm 60% Pt/C. This experiment was not conducted with the other catalysts due to safety concerns, after it was realised that the X-ray beam was causing membrane degradation and therefore significantly increasing the risk of cell fire.

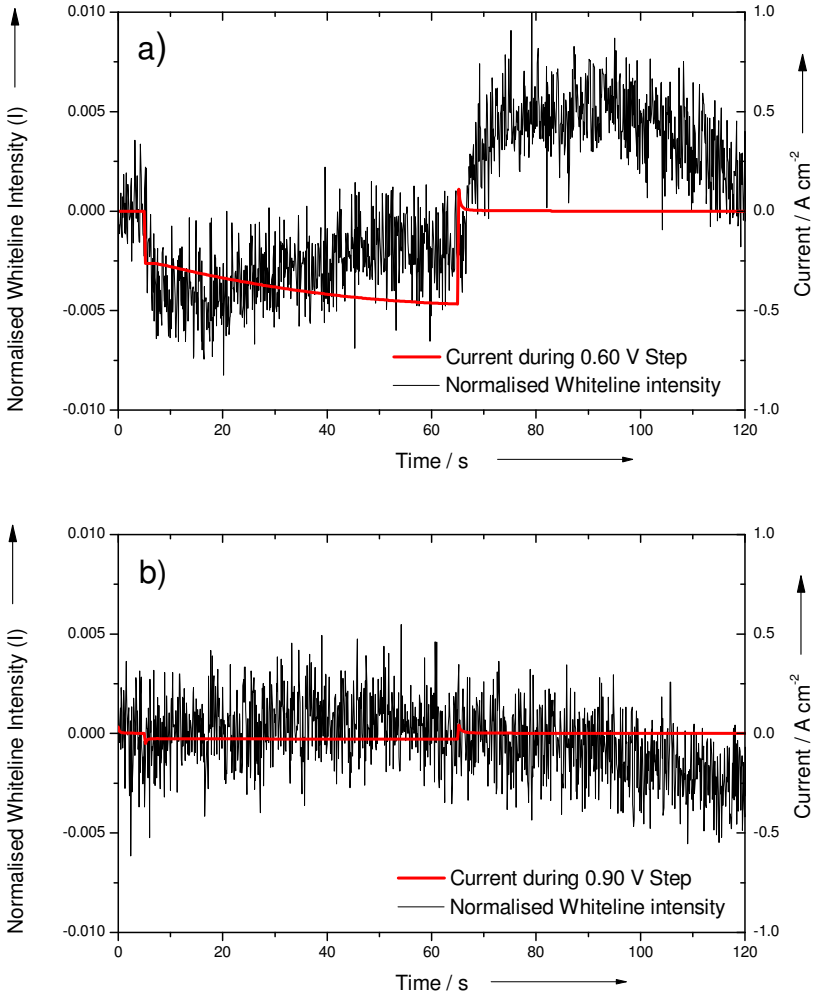

Figure 10. Variation in white line intensity for 2 nm 60% Pt/C following potential steps from OCV to a) 0.6 V and b) 0.9 V applied at 65 °C The corresponding oxygen reduction current is shown (red lines)

The white line intensity responses normalised to the first 40 data points at OCV, during the potential stepping experiments from OCV to 0.6 V and 0.9 V (applied) are shown in Figure 10 a) and b). As expected, a larger oxygen reduction current is drawn from the cell when 0.6 V is applied to the cell compared to 0.9 V. The applied potentials of 0.9 V and 0.6 V correspond to cathode potentials of approximately 0.95 V and 0.85 V, after correction is made for the measured membrane resistance at 0.8 V, as previously described in Chapter 4. It is noted that, the observed changes in the normalised white line intensity are less than that observed during the half cell experiments under nitrogen atmosphere.

During the 0.9 V potential stepping experiment, application of the applied potential at 5 s results in a spike in the current corresponding to double layer charging. This current decays to a steady state value, corresponding to the oxygen reduction current. At 65 s the applied potential is removed and the system relaxes to OCV. Double layer charging is observed in the current response and within 10 s the cell voltage has returned to OCV and the measured current, now indicative of the hydrogen crossover current, is the same as it was before the potential stepping event. Throughout the experiment the white line intensity does not change significantly and therefore it is concluded that the number of Pt-O species are comparable at OCV and when a small current is drawn at a potential near the OCV. At 100 s a decrease in intensity is seen, which is also seen for the 0.6 V experiment.

During the 0.6 V potential stepping experiment, significantly more current (4-5 times) is drawn from the cell than at 0.9 V. The oxygen reduction current increases with time at 0.6 V. This is likely to be the consequence of improved hydration of the catalyst layer due to formation of water during ORR. After 50 s the rate of increase of current slows and approaches a stable value. Unlike the 0.9 V test, potential stepping to 0.6 V results in a change in white line intensity. Compared to potential stepping events in N_2, this change is small. As the potential of 0.6 V is applied to the cell, the white line intensity rapidly decreases. Decreasing white line intensity correlates to the Pt having higher d electron occupancy, and therefore fewer bonds to oxygen, than at OCV. A possible explanation for this trend is that bound / surface absorbed oxygen species undergo reduction before repopulation with dissociated gas phase O_2 can occur. With time, under increasing load, the white line intensity increases towards the OCV intensity but remains at a value less than at OCV. This suggests that as ORR continues more of the Pt electron density is donated / used during the ORR. This could be the consequence of better hydration increasing the catalyst utilisation and / or number of Pt-O bonding interactions. The changes in white line intensity tracks the changes in ORR current. When the rate of increase in white line intensity occurs most rapidly the change in ORR current also occurs most rapidly, in addition, when the white line intensity appears to stabilise the current also stabilises.

When the applied potential was removed, the potential returned to > 1.0 V within 5 s. For the remainder of the experiment, the potential continued to increase towards the

OCV value. After the applied potential is removed, the current response becomes positive, corresponding to double layer charging. The current then decays to the hydrogen crossover value 10 s after the applied potential was removed. Within the same time frame, the white line intensity increases to that of OCV and continues to increase to a maximum value. A decrease in intensity is then observed, starting around 100 s, and by the end of the experiment the intensity approaches that at the start of the experiment. It is postulated that these changes may be associated with the hydration of the catalyst layer and / or population of the catalyst with oxide species (OH_{ads}, O_{ads} and place exchange O to form the oxide) at the OCV. After a prolonged period undergoing ORR, the wetted catalyst layer is more readily oxidised. With time at OCV, the catalyst layer drys out, and correspondingly the system returns to a similar state to that at the start of the potential stepping event.

5. Discussion and future directions

5.1 Oxide formation and removal

The timescale of the energy dispersive measurements has allowed changes in the electronic configuration of platinum, tracked by changes in white line intensity, to be followed during both Pt-O bond forming reactions and during reduction of these oxide species. By applying Equation 1 to the normalised white line intensity during the oxidative and reductive potential steps, the rate of change in white line intensity and therefore speeds of both oxide formation and removal have been determined.

In agreement with the literature (16, 17), a larger white line change, corresponding to more oxide formation, occurred at higher potential when the cell was operating with nitrogen feed to the cathode. Due to the effect of hydrogen crossover, the reported effect of temperature on oxide formation could not be confirmed. Changes in white line intensity, corresponding to oxide formation, have also been reported by Allen *et al.* An initial rapid change was observed, followed by relatively slow change (3). This is in good agreement with this work. In the work of Allen *et al.*, the oxidation kinetics were fitted to a logarithmic function (3), however, a rate of oxide growth was not reported and therefore a comparison of their results with this work is not possible.

The rates of oxide removal were determined by Allen *et al.* by fitting a single exponential function (3), as in this work. The rates reported in this work are a factor of ten faster than those reported by Allen *et al*. This difference is attributed to a combination of the following factors. Firstly, the duration of the potential is hold at the upper limit is significantly longer in the experiments by Allen *et al.* and the operating temperature is higher (300 s hold at 1.2 V at 80 °C *vs*. 60 s hold at 65 °C in this work). Due to the nature of the oxide growth process, the Pt catalyst will have a thicker oxide layer after the longer hold time at increased temperature (5, 8, 12-14). This may influence the rate of oxide removal, since it has been demonstrated as shown in Figure 6 that the removal rates decrease when more oxide is grown and when more place exchange occurs. In addition, in the work of Allen *et al*., the data is fitted from the change in the potential to the end of the experiment (300 s). In this work the reduction process is fitted over a shorter time frame. This is due to the observed time lag between the potential step and the response of the white line intensity, a shorter experiment duration, and significantly more data points at short times. All of these factors will impact on the observed rate. It is also noted that the loading of Pt on the carbon support, carbon type, Nafion content, layer fabrication techniques, platinum loading, cell hardware and conditions in the two experiments differ. These factors can affect catalyst layer thickness, hydration and utilisation, with the cathode layers of Allen *et al*. thought to be significantly thicker than those used in this work (20). The Pt oxidation process under half cell conditions is thought to be initiated by reaction with water (7, 8, 12), and the electrical conductivity of the layer is also affected by hydration, therefore the water content of the layer will also affect the observed rate. Another difference is that the anode catalyst used by Allen *et al*. contains Pt. The white line response observed is therefore the superposition of the reactions occurring on both the anode and cathode. Finally, the exact form of the exponential fitting applied by Allen *et al.* is not reported, therefore, it is unclear if the kinetic information obtained is directly comparable.

5.2 Towards more realistic Fuel Cell operation – Cell modifications

The transmission cell design used in this work has enabled XAS to be measured on fuel cell catalysts during fuel cell operation. In Chapter 4, EXAFS analysis allowed changes in catalyst structure to be observed, while in Chapter 5, improved time resolution enabled the rates of oxide formation and removal to be studied.

The opposing requirements for high quality XAS data and optimum, realistic fuel cell performance, have been highlighted in this work. This conflict has resulted in the study of a narrow potential window on the cathode and uncertainty about the catalyst utilisation for the thicker catalyst layers. In light of these results, a number of possible design modifications will now be discussed and evaluated for: improving the scope of data obtainable; the effect on data quality; and whether study of the catalyst under more realistic fuel cell operating conditions can be achieved.

Design modifications that result in a reduction in the cell performance losses would significantly improve the scope of data obtainable (larger potential window probed on the cathode), and allow study of the catalysts under more realistic operation. With the current cell design, cell resistance is a major source of performance loss with resistances measured using the current interrupt method being up to five times higher in the non-ideal test conditions at the synchrotron than for conventional cell designs.

Improving the cell compression should reduce cell resistance. This is difficult to achieve in the window region where XAS measurements are conducted, since the thinning or complete removal of the graphite flow field plate on both sides of the cell results in nothing for the MEA to be compressed against. Some improvement may be obtained if the area immediately surrounding the thinned region is compressed more efficiently, for example by improving the screw fixings, moving them closer to the window region, or by using a bladder system that uses compressed air to hydraulically press the plates together. This type of system is used in conventional fuel cell designs and typically is found to provide more even compression across the MEAs than screw fixings, however, for an XAS cell it would require modification such that it does not block the X-ray pathway.

Reducing the intrinsic resistance of the membrane would also reduce cell resistance. This may be achieved by reducing the thickness of the Nafion membrane. This however is not preferable, since it is now known that the X-ray beam can damage the membrane causing ‘pin holing’, causing a safety risk. Also from a practical view point, achieving rapid cell assembly without gas leakage, a key requirement for efficient time usage on the beamline, is significantly easier if thicker membranes are used. An alternative would be to use a membrane with a lower EW than Nafion 115 (1100 g mol^{-1} of SO_3^-) and

hence higher conductivity, but with comparable thickness. One possible alternative would be to use Flemion T with an EW of 1000 g mol^{-1} of SO_3^-. This has the same thickness as Nafion 115, (~120 µm), but marginally higher conductivity of 79 *vs.* 71 mS cm^{-1} (21). To improve conductivity further would require in-house casting of lower EW ionomers to the desired thickness. While physically possible, these membranes are not commercially available or very representative of the types of membranes typically used in fuel cell applications. On balance, changing the membrane is not viable for these types of experiments.

Improving the flow of electrons through the catalyst layer can also reduce the cell resistance. One way this may be achieved is by reducing catalyst layer thickness. The use of thinner layers on the anode is viable if the wt% of Pd on carbon is increased. Doubling the wt% Pd to 20% from 10% would reduce the anode layer thickness by half. Increasing the wt% Pd further is also synthetically possible without having a detrimental effect on the catalyst dispersion using in-house preparation methods at Johnson Matthey. Due to the requirement for high sample concentrations, the scope to reduce layer thickness on the cathode is limited. It may be possible to increase the wt% of the catalyst as described above, and to support the catalyst on an alternative carbon support that has different packing properties and results in a thinner layer structure. However, changing the carbon support will also have a knock on effect on other parameters that may be detrimental to fuel cell performance, including the catalyst preparation, dispersion, and water handling of the catalyst layer. Thinner layers will also help improve the water handling properties of the MEA (layer + membrane) that will in turn help to decrease the cell resistance.

The hydration of the catalyst layers and membrane are key contributors to both cell resistance and catalyst utilisation. If the catalyst is not in good electrical contact because the layer is dry, then the active sites of the catalyst can become isolated and therefore effectively switched off. This is thought to be the reason why the PtCo alloy catalyst and large particle size Pt catalyst do not show the expected catalytic performance in the *operando* XAS cell. The water flux in the cell is controlled by the amount of water generated in the catalyst layer during the ORR, and also by externally added water from the humidification of the incoming gas streams. The current humidification system uses MSAs. The active area of the MSAs is smaller than the MEA active area, and they do

not give any control over the % humidity and are therefore non-ideal. The humidifers are made from PTFE that acts as a 'heat sink', decreasing the overall cell temperature.

The humidification system could be improved by increasing the MSA active area and changing the material(s) they are made from, or ideally by using a more sophisticated design. Designs typically used in more conventional fuel cells have the incoming gases bubbled through heated water, and the water temperature and residence time of the gas results in a tuneable humidification system. Such a system would need to be removed from the incoming X-ray beam, and if the humidified gas needs to be piped to the cell then any pipework would need to be sufficiently lagged or heated to prevent any cold spots where liquid water could condense and accumulate. A careful balance of the amount of water supplied to the fuel cell would need to be considered. If the layer were to become too wet, mass transport losses by flooding would become significant, and liquid water accumulation in the window region would cause noise in the XAS data, while the system running too dry may result in utilisation issues. A tuneable humidification system would enable an optimum balance to be achieved, and would also allow the effect of % humidity on the catalyst structure to be studied.

The anode polarisation is also a significant factor in reducing the potential window on the cathode that can be studied. This loss may be reduced by increasing the number of active sites for hydrogen oxidation, but as previously discussed, simply increasing the catalyst loading would be detrimental in terms of layer thickness effects. It would therefore be preferable to increase the wt% Pd/C used on the anode as the loading may be increased without increasing layer thickness. Increasing the cell temperature may also increase reaction rate, reduce the anode polarisation, and improve the cathode cell performance. This would be viable if an alternative humidification system is employed that did not act as a heat sink, and if an alterative heating system was added to the cell such as cartridge heaters/pads. As with the other modifications, these heaters must not block the incoming or outgoing X-ray pathway. Another option would be to consider using an alternative catalyst to Pd on the anode that has improved hydrogen oxidation kinetics. An alternative is to use Pt as in conventional fuel cell systems. However, Pt on the anode would interfere with the Pt signal that is being collected on the cathode, so could only be used if the Pt was removed from the anode in the region that is being studied. This has been done by others (22), but problems with current distribution in the

region of the window caused by removing Pt in this area have been described (23). A solution would be to fabricate an anode layer that contained Pd/C in the window region and Pt/C covering the rest of the active area.

Another significant issue, both in terms of deactivation of the catalyst under test and safety, is hydrogen crossover as a consequence of operational temperature and membrane failure during exposure to the X-ray beam. This issue was particularly problematic during the EDXAS experiments at the ESRF where a small focal spot size and high flux beam were used. In light of the damage caused to the membrane, only limited testing under O_2 was conducted and the degradation resulted in uncertainty in the amount and rate of oxide formation/removal. In order to reduce / remove this issue the exposure time of the membrane in the beam must be limited and the focal spot size could be increased therefore decreasing the beam intensity. Using a thicker membrane would also be beneficial in terms of reducing hydrogen crossover and reducing pin holing, however, thicker membranes would lead to increased CI resistance and would move the MEA structure still further from conventional MEA systems.

Other factors that would improve the cell performance include: increasing the cell temperature (as previously discussed); increasing the O_2 partial pressure (by increasing the cell pressure); and eliminating any contaminates that would poison the catalyst. The pressure used during the testing is not unrealistic for conventional fuel cell systems and safety concerns as a consequence of gas leakage for the drilled pates would be more significant at higher pressures. Also the chance of poisoning in the current system is very low, since high purity gases are used (99.99%) and DI water is used in the cell. Therefore the gas purity and pressure conditions used in this work are both reasonable and realistic.

The major deviation from realistic fuel cell operation with the current cell design is the need to use high catalyst loadings on the cathode in order to be able to obtain sufficient signal to noise in the XAS data. A solution would be to use fluorescence detection as in the research group's previous cell design (24). In these experiments, catalyst loadings of 0.4 $mg_{Pt}\,cm^{-2}$ were used, in line with typical loadings used in conventional fuel cell research. Fluorescence detection would allow realistic loadings, and therefore significantly reduce the performance losses and increase the potential window over

which the cathode can be studied. However, conducting the time resolved potential stepping experiments with fluorescence detection would prove challenging with the current beamline technology. In addition, the geometry of the window in the fuel cell would need to be altered to obtain the maximum solid angle possible for detection of the entire XAS energy range. For the energy dispersive experiments, obtaining the time resolution achieved in this work is currently not possible (2). This is because the beam needs to be spatially resolved for fluorescence detection. To achieve this an approach developed by Pascarelli (25) (1999) known as 'Turbo EXAFS' uses a moving slit to scan across the broad band of energies provided by the dispersive monochromator. In recent work on the Pt L_{III} edge, a time resolution of ~1 s and 6 s was achieved, however only XANES has been achieved on this timescale (2, 19, 26). Further developments are required before fluorescence may be used to study these systems with sub-second time resolution. Until this time, the inherent problem of requiring high catalyst loadings when combining the fuel cell with time resolved XAS will persist.

5.3 Challenges of studying Pt/C and Pt_3Co/C using *operando* XAS

A key objective of this work was to study and compare both Pt/C and PtCo/C catalysts. To synthetically achieve alloying, high temperatures are required which in turn results in a large particle size for alloys *vs.* Pt/C. The scope of the data obtainable for alloys was therefore reduced, since XAS probes the per-atom average and alloys, due to the larger particle size, have a higher bulk to surface ratio than Pt/C. Consequently, the surface sensitivity of the XAS technique was reduced and the % error associated with the fitting of the Pt-O neighbours was high. To try to allow direct comparison between the alloy and Pt/C, a heat treated Pt catalyst was used with similar particle size to the alloy. Within the error associated with the experimental fitting, both the alloy and Pt catalysts behaved the same way during the potential stepping experiments with 12 s time resolution. It is uncertain if the alloy and heat treated Pt catalyst genuinely behave the same way or if any differences are masked by the averaging nature of the technique. This is an intrinsic problem with using XAS to study large particle sized catalysts and is a key finding from this work. Improving the XAS data quality would decrease the EXAFS fitting errors and would help to mitigate this problem, and may also allow improved differentiation between large particle Pt and PtCo alloys.

In addition to optimal data fitting, improving the XAS data quality would also increase the scope of the data obtainable. Increasing the signal to noise ratio sufficiently would allow the study of low energy edges such as Co K-edge, and improved beamline set-up would allow the acquisition of EXAFS data for the energy dispersive experiments conducted at the ESRF, Grenoble. Improvements in signal to noise ratio could be achieved by increasing the XAS scan duration or by combining multiple scans, however this decreases the time resolution of the data. Further removing interfering elements from the X-ray pathway would also maximise the XAS signal. Some benefit may be achieved by using thinner gas diffusion layers and membranes in the MEA, however the layers used in this work are representative of commercial MEA components, so this option is not preferred. Decreasing the catalyst layer thickness would remove interfering carbon absorbance from the catalyst support. One way to achieve this would be to use lower loaded electrodes, however, this would also reduce the concentration of metal on the electrode, magnifying the polarisation of the anode and decreasing the concentration of the absorbing metal (Pt or Co) on the cathode hence reducing the XAS signal. A more effective way to decrease carbon absorbance and layer thickness is to increase the wt% metal in the catalyst layer. This would decrease the wt% C while increasing the wt% metal in the catalyst. On the cathode, this would have the additional benefit of increasing the XAS signal by increasing the Pt and Co concentration. On the anode, this approach would decrease the carbon absorbance, but overall prove to be detrimental due to the difference in absorption coefficient at the Pt L_{III} edge for carbon and Pd (C = 1.455 $cm^2\ g^{-1}$ Pd = 76.53 $cm^2\ g^{-1}$). A 1% decrease in C absorbance would correspond to ~50% increase in Pd absorbance. On the anode, decreasing the Pd absorbance would be more beneficial, however this is not viable due to the anode activation issue.

Only XANES information was obtainable from the energy dispersive experiments conducted at the ESRF Grenoble. This was related to the nature of how the EDE experiment is conducted, the monochromator, and the non-homogeneous nature of the MEA samples. Newton (26) has shown for Pd catalysts that defocusing the beam averages over more of the local non-uniformities within the sample, and using a reference that mimics the sample closely can improve the obtainable data range significantly and remove structure due to polychromator glitches and scattering of support materials. In this work an MEA containing no Pt was used as a reference,

however, due to poor homogeneity and mismatch between the reference MEA and test MEA, the data quality was found to be worse using the reference MEA than using air alone. Increasing the focal spot size further is also not possible at this beamline due to the nature of the optics available.

The XAS detector also limits the spatial resolution and measurable energy range. In this work a state of the art FReLoN camera was used on the most modern beamline available, therefore in this respect the best possible quality XAS data was obtained. It should be noted however, that this beamline is not optimised for the types of experiments undertaken (2). In the future a new purpose built beamline (I20 XAS3) at the Diamond light source will become available (late 2009/early 2010) and by late 2010 will be operational for *operando* time-resolved X-ray spectroscopy studies (27). This beamline will employ the latest technology in optics and detector systems, including new Si and Ge based 'XSTRIP' detectors, (28, 29). This detector system should not only improve the spectral resolution, and hence XAS quality, but will also allow access to even faster time resolution.

6. Conclusions

In this work, energy dispersive XAS has been used to probe the oxidation and reduction of Pt/C under N_2 and during ORR. The time resolution was sufficient to allow calculation of the rate of oxide growth and removal. Oxide removal occurred faster than growth, indicative of a different mechanism. During the ORR, a change in Pt electronic configuration occurs compared to OCV when significant load is drawn from the cell. The strong correlation in current response and white line intensity provided insight into the electronic configuration of Pt and mechanistic insight into the ORR.

Significantly, prolonged exposure to the X-ray beam was found to degrade the membrane, preventing oxidation of the catalyst in the region of degradation. This is thought to be the consequence of increased hydrogen crossover forming a reducing environment in the observation area. Uncertainty about the extent of hydrogen crossover, and amount and rate of oxide formation prevented comparison between Pt and alloy catalyst materials.

References

1. M. A. Newton, A. J. Dent and J. Evans, *Chemical Society Reviews*, **31**, 83 (2002).
2. M. A. Newton, *Journal of Synchrotron Radiation*, **14**, 372 (2007).
3. P. G. Allen, S. D. Conradson, M. S. Wilson, S. Gottesfeld, I. D. Raistrick, J. Valerio and M. Lovato, *Journal of Electroanalytical Chemistry*, **384**, 99 (1995).
4. G. Jerkiewicz, G. Vatankhah, J. Lessard, M. P. Soriaga and Y. S. Park, *Electrochimica acta*, **49**, 1451 (2004).
5. A. Sun, J. Franc and D. D. Macdonald, *Journal of the Electrochemical Society*, **153**, B260 (2006).
6. A. Damjanovic, *Journal of the Electrochemical Society*, **138**, 2315 (1991).
7. P. A. Christensen and A. Hamnett, *Techniques and Mechanisms in Electrochemistry*, Chapman and Hall (1994).
8. B. E. Conway, B. Barnett, H. Angerstein-Kozlowska and B. V. Tilak, *Journal of Chemical Physics*, **93**, 8361 (1990).
9. Angerste.H, B. E. Conway and W. B. A. Sharp, *Journal of Electroanalytical Chemistry*, **43**, 9 (1973).
10. V. I. Birss, M. Chang and J. Segal, *Journal of Electroanalytical Chemistry*, **355**, 181 (1993).
11. M. E. van der Geest, N. J. Dangerfield and D. A. Harrington, *Journal of Electroanalytical Chemistry*, **420**, 89 (1997).
12. M. Alsabet, M. Grden and G. Jerkiewicz, *Journal of Electroanalytical Chemistry*, **589**, 120 (2006).
13. V. I. Birss and A. Damjanovic, *Journal of the Electrochemical Society*, **130**, 1688 (1983).
14. A. Damjanovic, A. T. Ward, B. Ulrick and M. Ojea, *Journal of the Electrochemical Society*, **122**, 471 (1975).
15. ESRF ID24 Dispersive EXAFS Beamline: http://www.esrf.eu/UsersAndScience/Experiments/ElectStructMagn/ID24, in (2009).
16. A. E. Russell, S. Maniguet, R. J. Mathew, J. Yao, M. A. Roberts and D. Thompsett, *Journal of Power Sources*, **96**, 226 (2001).
17. H. Yoshitake, O. Yamazaki and K. Ota, *Journal of the Electrochemical Society*, **141**, 2516 (1994).
18. H. Imai, K. Izumi, M. Matsumoto, Y. Kubo, K. Kato and Y. Imai, *Journal of the American Chemical Society*, **131**, 6293 (2009).
19. Y. Nagai, K. Dohmae, Y. Ikeda, N. Takagi, T. Tanabe, N. Hara, G. Guilera, S. Pascarelli, M. A. Newton, O. Kuno, H. Y. Jiang, H. Shinjoh and S. Matsumoto, *Angewandte chemie*, **47**, 9303 (2008).
20. M. S. Wilson and S. Gottesfeld, *Journal of Applied Electrochemistry*, **22**, 1 (1992).
21. Y. G. Chun, D. H. Peck, C. S. Kim and D. R. Shin, *Journal of New Materials for Electrochemical Systems*, **4**, 31 (2001).
22. C. Roth, N. Martz, T. Buhrmester, J. Scherer and H. Fuess, *Physical Chemistry Chemical Physics*, **4**, 3555 (2002).
23. A. E. Russell and A. Rose, *Chemical Reviews*, **104**, 4613 (2004).
24. R. J. K. Wiltshire, C. R. King, A. Rose, P. P. Wells, M. P. Hogarth, D. Thompsett and A. E. Russell, *Electrochimica Acta*, **50**, 5208 (2005).

25. S. Pascarelli, T. Neisius and S. De Panfilis, *Journal of Synchrotron Radiation*, **6**, 1044 (1999).
26. M. A. Newton, *Chemical Society Reviews*, **37**, 2644 (2008).
27. Website, Diamond Light Source Ltd. Beamlines | I20: http://www.diamond.ac.uk/Home/Beamlines/I20.html, in (2009).
28. J. Headspith, G. Salvini, S. L. Thomas, G. Derbyshire, A. Dent, T. Rayment, J. Evans, R. Farrow, C. Anderson, J. Cliche and B. R. Dobson, *Nuclear Instruments & Methods in Physics Research Section A-Accelerators Spectrometers Detectors and Associated Equipment*, **512**, 239 (2003).
29. G. Salvini, J. Headspith, S. L. Thomas, G. Derbyshire, A. Dent, T. Rayment, J. Evans, R. Farrow, S. Diaz-Moreno and C. Ponchut, *Nuclear Instruments & Methods in Physics Research Section A-Accelerators Spectrometers Detectors and Associated Equipment*, **551**, 27 (2005).

Chapter 6. Activation of $PtCo_3$

1. Introduction

To enable economically viable commercialisation of proton exchange membrane fuel cells (PEMFCs) for automotive applications, more active catalysts are required. Candidate materials must demonstrate a four times activity benefit over commercial Pt materials in operational MEAs allowing sufficient reduction in Pt loading and therefore cost (1). The application of electrochemical dealloying to modify catalyst surface properties as an effective method for synthesising active fuel cell catalysts was first presented in 2007 by Strasser *et al.,* at the 212th meeting of the Electrochemical Society (2-4) and as a communication in the Journal of the American Chemical Society (5). This modern electrochemical method, and those used to modify catalyst surfaces by addition of Pt monolayers, are based on the ancient methods of surface metal galvanic displacement and surface metal depletion gilding. Pre-Columbian goldsmiths modified the surface properties and changed the appearance of cheap metal alloys to make them appear as if they consisted of pure gold (4, 6). Surface metal galvanic displacement resulted in a uniform coating of a thin layer of gold on top of copper sheets by treatment in heated baths of gold salts.

Over the past decade, a modern galvanic displacement method has been applied to fuel cell catalysts in which platinum monolayers have been coated on non-platinum core materials, via galvanic displacement of a layer of Cu surface atoms to form catalysts with a core shell structure also known as Pt monolayer catalysts (7-10). These materials have been demonstrated to decrease cost by replacing platinum in the centre of the particles with a cheaper core. In addition, the underlying core material can influence the electronic and geometric properties of the platinum overlayer, resulting in activity enhancement for the ORR over pure platinum materials. This class of materials represents a promising approach to development of new fuel cell cathode materials and is the topic of much current research (6, 10).

The method of surface metal depletion gilding is an alternative method for creating an enriched outer layer. Historically, bimetallic ingots of Cu and Au were repeatedly annealed and pickled to first increase the surface composition with Cu and subsequently deplete Cu from the surface by chemical dissolution. The modern take on this method

presented by Strasser *et al.* selectively dissolves Cu from PtCu bimetallic compounds until a multi-layer Pt-rich shell forms. This is achieved using voltammetric dealloying of the catalyst, in which the catalyst is repeatedly electrochemically cycled to high (up to 1.2 V vs. RHE) potentials inducing Cu dissolution (4, 6).

Catalysts were prepared by Strasser's group by impregnating a pre-formed 30% Pt/C catalyst with Cu to yield $Pt_{75}Cu_{25,}$ $Pt_{50}Cu_{50}$ and $Pt_{25}Cu_{75}$ alloy precursors after annealing at 600, 800 and 950 ºC (4, 6, 11). The $Pt_{75}Cu_{25}$ catalysts exhibited a single alloy phase by XRD while the $Pt_{50}Cu_{50}$ exhibited at least two bimetallic alloy phases when annealed at 600 ºC and was found to be single phase at 950 ºC. XRD showed all $Pt_{25}Cu_{75}$ materials to be multiphase, with the 600 ºC material containing unalloyed Cu. Generally the higher the annealing temperature the better alloyed the catalyst. The catalysts were then studied as thin films on a graphite rotating disc electrode. The as prepared materials exhibited voltammetry features assigned to Cu at the surface of the catalyst, including suppressed hydride features and anodic peaks assigned to Cu (~0.3 V *vs*. RHE) and Cu atoms on Pt at higher potentials (~0.3-0.7 V *vs*. RHE) (2, 4-6). After application of the dealloying procedure of 200 cycles from 0.05 to 1.2 V at 500 mV s^{-1}, all materials lost the features assigned to Cu and a displayed a voltammetric profile equivalent to that of pure platinum. After dealloying, the composition of the selected catalysts was determined and the oxygen reduction activity measured (4, 6, 11). Results are detailed in Table 1.

Table 1. Comparison of nominal and final compositions and dealloyed ORR activities at 900 mV *vs*. RHE of PtCu catalysts. Reproduced from (6).

Catalyst	Nominal Composition at.%		Annealing Temperature / ºC	Pt mass activity / A mg_{Pt}^{-1}	Specific activity / µA cm_{Pt}^{-2}	Surface area / m^2 g_{Pt}^{-1}	Composition after dealloying at.%	
	Pt	Cu					Pt	Cu
1	25	75	600	0.53	644	89	79	21
2	25	75	950	0.35	788	45	80	20
3	50	50	600	0.51	596	86	-	-
4	50	50	950	0.11	428	27	-	-
5	75	25	600	0.27	360	75	86	14
6	75	25	950	0.03	234	13	81	19

Catalysts 1, 2 and 3 in Table 1 showed a four to five times activity improvement over a pure Pt catalyst, meeting the DoE activity requirements. Catalyst 5 shows the previously reported up to 3 times activity benefit for Pt_3X catalysts, while a lower activity than Pt

is reported for catalyst 6. The compositions of catalysts 1, 2 and 6 are very similar after dealloying, however, the catalytic mass and specific activities are dramatically different.

The authors attribute the high activity of the dealloyed $Pt_{25}Cu_{75}$ catalysts to the catalyst structure formed upon dealloying. The origin of enhanced ORR activity is not induced by an increased surface area (Raney catalysts), but is thought to be due to modified geometric and electronic properties of the Pt-enriched nanoparticle shell analogous to the core shell/Pt monolayer catalysts previously discussed (6). It is hypothesised that enhanced activity is the result of a reduced Pt-Pt distance near the particle surface, stabilised by the lattice of the contracted core (12). Evidence for a core shell structure has recently been confirmed by anomalous small angle X-ray scattering experiments (6, 13).

In addition to demonstration of activity enhancement using rotating disc measurements, Strasser *et al.* have also demonstrated up to a four fold activity enhancement over platinum in MEAs after application of a dealloying and washing procedure to exchange Cu^{+2} ions adhered to the $–SO_3^-$ groups in the electrolyte matrix (3, 13, 14). An *ex situ* chemically leached catalyst with very similar composition showed enhanced activity over Pt, but a lower mass activity than the *in situ* dealloyed catalyst (3).

As described in Chapter 3, the presence of leached base metals within the MEA structure can have severe and detrimental effects on catalytic performance. The dealloying procedure results in significant quantities of dissolved Cu within the MEA, and is therefore a concern. In 2009, Strasser *et al.* sought to address this issue by using a combined scanning electron microscope/electron probe microanalysis study of *in situ* voltammetric dealloying in MEAs (14). Cu was found to readily leach on ink manufacture. After *in situ* dealloying at 100 mV s^{-1} from 0.5-1.0 V for up to 300 cycles, large amounts of Cu were observed in the membrane and some Cu had migrated to the anode layer. The consequence on performance was stated to be catastrophic. After ion exchange by MEA disassembly, washing in 1 M H_2SO_4 at 80 ºC for 1 hr followed by repeated washing in DI water and MEA drying, the Cu content in the MEA was reduced and the activity benefit realised (14).

1.1 Aims of this work

In light of the results of Strasser *et al.,* preparation and characterisation of a Co version of the electrochemically dealloyed catalyst was undertaken. Co was chosen as the base metal as good activity has previously been observed for the $Pt_{75}Co_{25}$ alloy. Co is also known to readily leach, so should easily be dealloyed using the electrochemical dealloying approach. This material was subsequently tested for activity and comparison made to conventionally prepared PtCo alloys and the literature values reported for PtCu systems. XAS measurements were also conducted to investigate relationships between activity and structure.

2. Experimental Detail

2.1 Catalyst precursor preparation and characterisation

Two $PtCo_3$/C precursor catalysts with nominal atomic composition $Pt_{25}Co_{75}$/C have been prepared by annealing at 600 and 950 °C in H_2/N_2. Samples of each of the two precursor materials were repeatedly chemically acid leached to give two further materials. The Pt and Co content of the resulting leachate was determined using ICP-MS. A detailed description of the catalyst preparation can be found in Chapter 2 section 1.1. XAS characterisation was conducted on the precursor catalysts and the catalysts formed after each stage of the acid leaching to study the effect of chemical dealloying on catalyst structure. XAS was collected on the powder samples using the gas treatment cell at the SRS Daresbury laboratory station 9.3 at the Pt L_{III} and Co K edge. The XAS data analysis using the methods described in Chapter 2 section 3.3. Briefly, individual scans for each sample were summed and XANES spectra were acquired after pre-edge subtraction. The background was then removed to obtain EXAFS spectra and the data were fitted to the structural models shown:

Structural Models used at the Pt L_{III} edge:

Four shell: Pt-Pt_1 Pt-Co Pt-Pt_2 Pt-Pt_3/Pt-Co_2

Five shell: Pt-Pt_1 Pt-Co Pt-Pt_2 Pt-Pt_3 Pt-O

Structural Models used at the Co K edge:

Two shell: Co-Co_1 Co-Pt_1

Five shell: Co-Co_1 Co-Pt_1 Co-O Co-Co_2 Co-Pt_2

The four new catalyst materials were also characterised by assay, CO chemisorption, XRD and TEM, as described in Chapter 2 section 4.

2.2 Electrochemical Dealloying

The catalysts were fabricated into electrode layers by screen printing/brush coating at 0.4 $mg_{Pt}\,cm^{-2}$ loading. Electrodes were vacuum filled before electrochemical dealloying of the four catalyst materials was conducted *ex situ* in the liquid electrolyte, by application of the stability testing procedure from 0.6-1.0 V and 0.6-1.2 V (Chapter 2 section 2.1.2). Cyclic voltammetry, ICP-MS and TEM were used to characterise structural changes occurring. In addition, electrochemical dealloying was conducted *in situ* within the MEA. Two different cell hardware designs were required to enable catalyst coated membrane (CCM) removal and washing. A CCM at ~0.2 $mg_{Pt}\,cm^{-2}$ loading of the $PtCo_3$/C catalysts at the cathode and 0.1 $mg_{Pt}\,cm^{-2}$ Pt/C anode loading and V3 membrane was fabricated and a BOL performance test conducted using one cell hardware. The catalyst was dealloyed according to the procedure in Chapter 2, section 2.2.4. The CCM was then boiled in 1 M H_2SO_4 and washed in water before performance testing in alternative cell hardware to consider the effect of dealloying on catalytic activity.

For comparative purposes 40% Pt_3Co/C and Pt/C catalysts were also studied.

All data in this chapter is based on a one off batch of synthesised catalyst and no repeat characterisation, XAS or electrochemical measurements were performed.

3. Results

3.1 Preparation and characterisation of $PtCo_3$/C catalysts

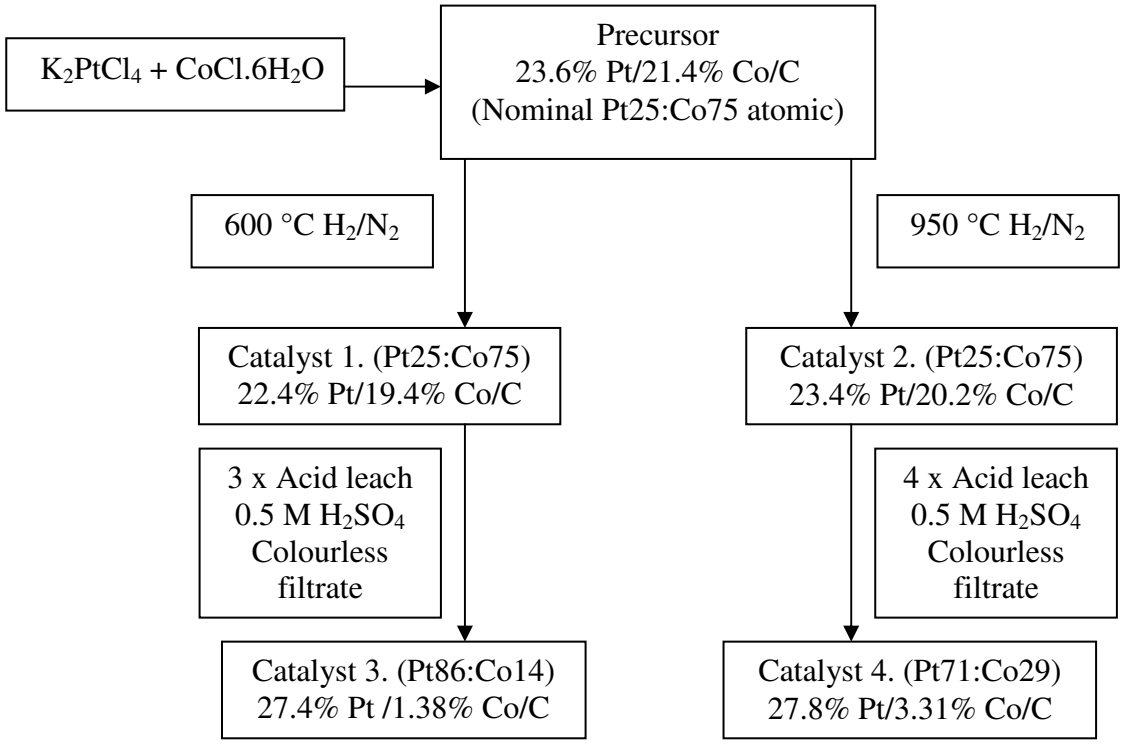

Figure 1. Preparation summary of four new PtCo catalysts

A summary of the catalyst preparation method and the assay results for the four catalyst materials is shown in Figure 1. ICP-MS analysis of the filtrate obtained after the co-deposition of Pt and Co to form the precursor indicated complete deposition occurred during the preparation. Catalyst 1 was prepared by annealing the PtCo (25:75) precursor at 600 °C and Catalyst 2 prepared by annealing at 950 °C. Catalysts 3 and 4 were prepared by acid leaching Catalysts 1 and 2.

During the acid leaching experiments, addition of the 500 ml 0.5 M H_2SO_4 to 10 g of Catalysts 1 and 2 at room temperature resulted in gas evolution and an immediate colour change of the solution to purple/pink indicating that Co is readily lost from the catalyst on reaction with acid according to Equation 1.

$Co + 2H^+ \rightarrow Co^{2+} + H_2$ (g) **Equation 1**

Repeated acid leaching was undertaken until no pink colouration persisted after the 24 hr leaching experiment. After each successive leach, ICP-MS analysis of the leachate was performed to quantify the amount of Pt and Co removed from the catalyst. Negligible loss of Pt occurred during leaching, however, significant amounts of Co were removed from both catalysts. Calculation based on the assay of Catalysts 1 and 2 and the ICP-MS results for each successive loss equates to 100 % removal of Co from Catalyst 1 to form Catalyst 3 and 86.6 % removal from Catalyst 2 to form Catalyst 4. Based on the assay results detailed in Figure 1, these figures are known to be an overestimate of Co removal. This discrepancy is likely to be due to the loss of catalyst during the filtering and drying process, however the ICP-MS trends are consistent with the assay results. Co is more readily lost from Catalyst 1 in three successive leaches than from Catalyst 2 after four acid leaching experiments. This is probably because Catalyst 1 is less well alloyed and has a higher surface area and proportion of smaller particles than Catalyst 2.

XRD and TEM analysis were performed on the four catalyst materials. The degree of alloying and the particle size was determined by the Johnson Matthey analytical department.

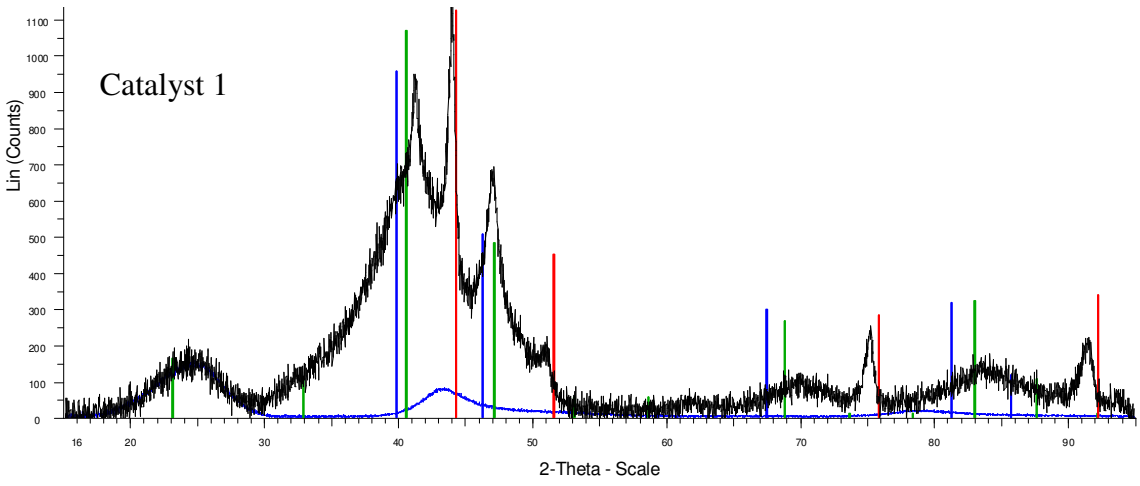

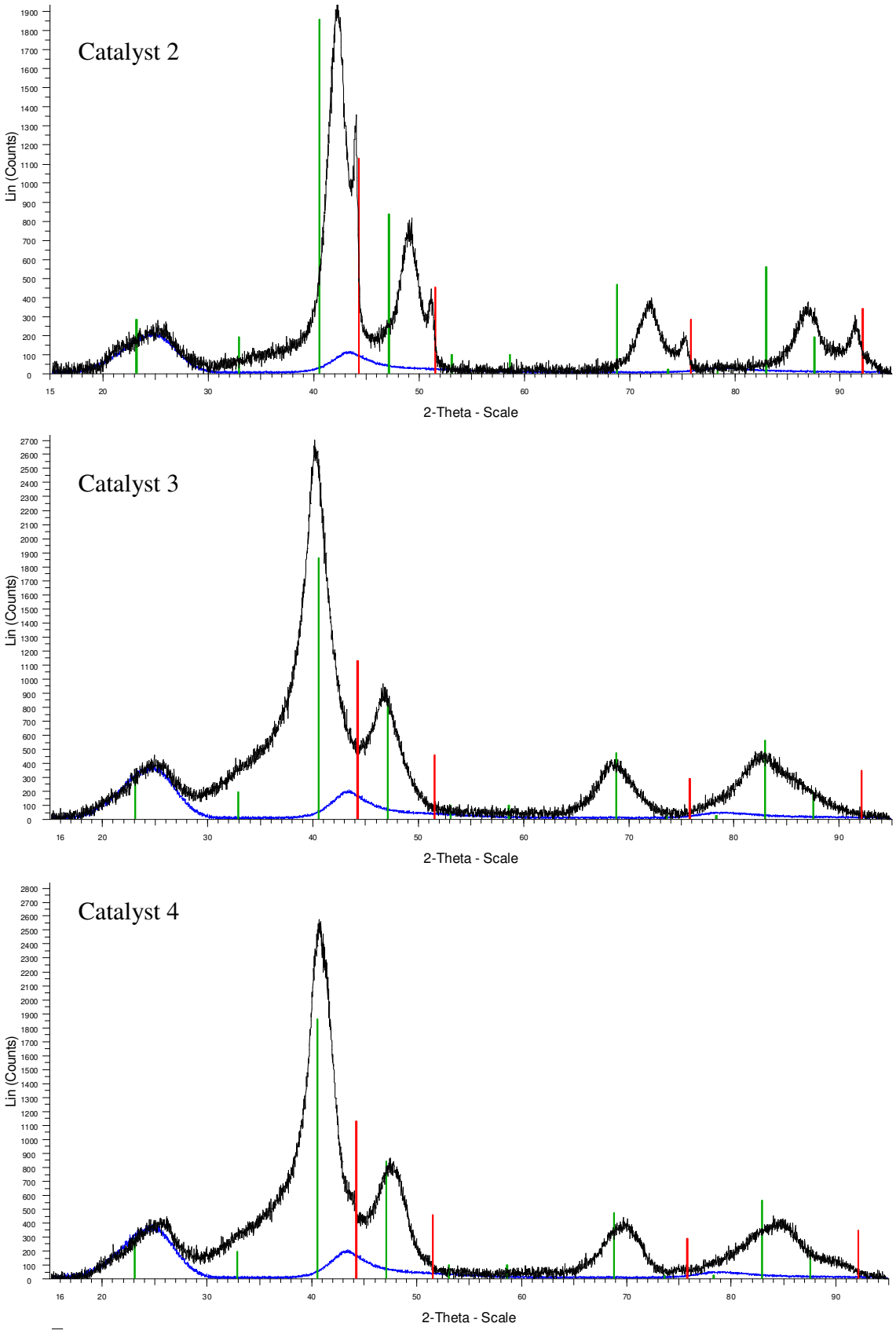

Figure 2. XRD patterns for Catalysts 1, 2, 3 and 4. (Black line – catalyst trace, Blue line – carbon trace, Diffraction pattern bars: Green – Cubic Platinum Cobalt Pt_3Co, Blue – Cubic Platinum, Red – Cubic Cobalt

Figure 2 shows the XRD diffraction patterns for Catalysts 1, 2, 3 and 4. The low temperature annealing used to make Catalyst 1 results in the catalyst being mainly amorphous with two poorly crystalline cubic phases identified as Co and Pt_3Co, however, no exact match to the ICDD data base (release 2003) values were possible. This is thought to be due to the crystalline phases not being fully formed. The non-crystalline nature of Catalyst 1 meant that lattice parameter and crystallite size information could not be calculated. Annealing at the higher temperature of 950 °C to form Catalyst 2 gave a material with two alloyed phases: one major Pt rich phase, similar but not an exact match to document data (15) for Pt_3Co (which gave a lattice parameter of a = 3.668Å); and a trace amount of a Co rich PtCo phase close in lattice parameters to cubic cobalt (Co, PDF No 00-015-0806). A trace (< 4%) amount of amorphous material was also observed.

After acid leaching to form Catalysts 3 and 4, XRD analysis showed both catalysts to be mainly composed of a poorly crystalline cubic phase close in lattice parameters to platinum cobalt (Pt_3Co PDF No 00-029-0499). The observed pattern is slightly shifted from the documented data, and slightly shift compared to each other. This is most likely due to the stoichometric differences known from the assay results. A minor amount of amorphous material is also present in for both catalysts.

The lattice parameters and crystallite sizes were calculated for Catalysts 2-4 using Reitveld analysis. All particle size information is summarised in Table 2, and Figure 3 shows the correlation between the XRD determined lattice parameter and the atomic %Pt for Catalysts 2-4 determined from catalyst assay. Acid leaching Catalyst 2 results in loss of the two phases to form one more Pt rich phase. Catalyst 3 is also single phase and is further enriched in Pt than Catalyst 4, in agreement with increased Co removal upon leaching. For comparison, the change in XRD lattice parameter with Pt composition from the literature (16) is shown. The lattice parameters determined for Catalysts 2-4 show good agreement with this trend.

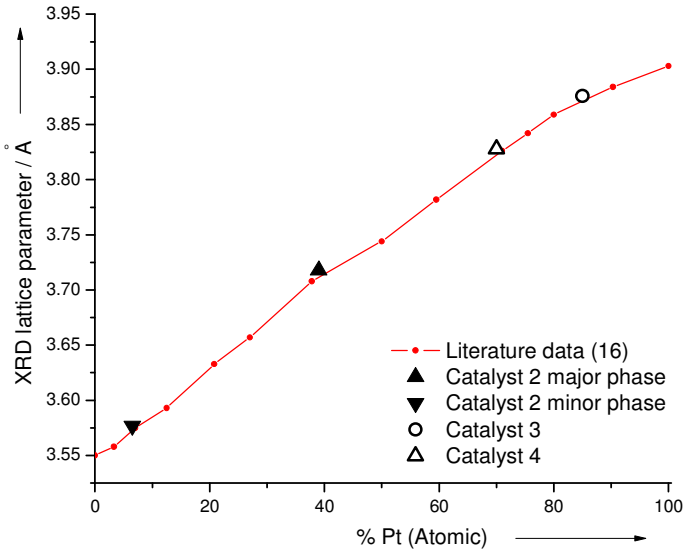

Figure 3. Correlation of assay composition and XRD lattice parameter for Catalysts 2-4 and literature (16) Co, PtCo and Pt catalysts

Catalyst particle sizes and compositional information was also determined using TEM. Figure 4 shows TEM images for all of the catalysts consist of both large and small particles and compositional analysis from EDAX line scan shows good correlation with XRD phase assignment.

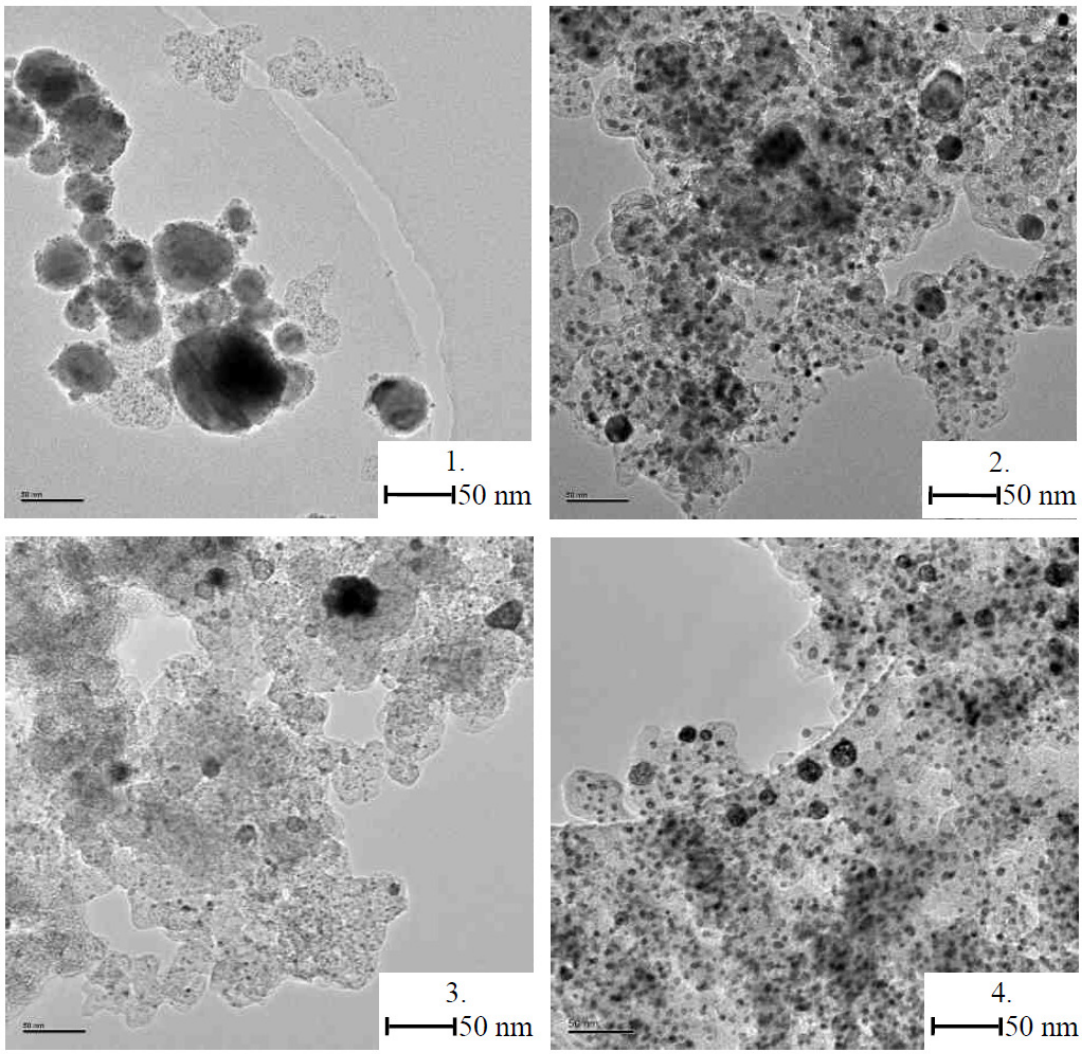

Figure 4. **TEM images of Catalysts 1, 2, 3 and 4. 50 nm scale bar**

Particle size distributions and compositions are summarised in Table 2. The effect of annealing temperature and leaching is clearly shown to alter the catalyst morphology. In agreement with XRD analysis, Catalyst 1 showed no evidence of alloying. EDAX and particle size analysis showed the catalyst is comprised of Co rich particles of 30-50 nm diameter and unalloyed Pt and Co particles of 1.5-2.5 nm diameter. The higher temperature annealing to form Catalyst 2 resulted in Co rich particles of 20-40 nm diameter and Pt rich particles of 5-8 nm diameter. Acid leaching Catalyst 1 to form Catalyst 3 resulted in the loss of the largest Co rich particles, resulting in Catalyst 3 exhibiting 20 nm diameter PtCo particles with varying PtCo composition and 1.4-3.0 nm diameter particles with uniform PtCo composition. Acid leaching Catalyst 2 to form Catalyst 4 gave a distribution of particles 20-80 and 4-6 nm in diameter, all with a uniform PtCo composition.

Table 2. XRD and TEM particle sizes and CO chemisorption results for Catalysts 1-4

Catalyst	Composition Wt. % Pt	Co	TEM composition and particle size	XRD mean crystallite size / nm	Surface area / $m^2\ g_{Pt}^{-1}$ (dispersion)	Composition At. % Pt	Co
1 600 ºC	22.4	19.4	Co rich particles: 30-50 nm Unalloyed Pt+Co: 1.5-2.5 nm	Not determined	97 (39%)	25	75
2 950 ºC	23.3	20.2	Co rich particles: 20-40 nm Pt rich particles: 5-8 nm	16 and 3.3	25 (10%)	25	75
3 600 ºC	27.4	1.38	Varying composition Pt&Co particles: 20 nm Uniform composition Pt&Co particles: 1.4-3.0 nm	2.2	74 (30%)	86	14
4 950 ºC	27.8	3.31	Uniform composition Pt&Co particles: 20-80 and 4-6 nm	2.4	50 (21%)	71	29

Particle size information for each catalyst determined by XRD and TEM is shown in Table 2, together with the catalyst surface areas determined by CO chemisorption. For Catalyst 2 there is a mismatch between the XRD and TEM particle sizes, with the XRD mean crystallite sizes being lower that those observed in the particle size distribution measured by TEM. The same trend is seen for Catalyst 4. Good agreement between the XRD and TEM particle size information is observed for the smaller particle sizes for Catalysts 3 However, the presence of two separate particle size distributions and the very large particles in Catalysts 3 and 4 are not evident from the XRD analysis.

The platinum surface area and dispersion of the catalysts were measured by CO chemisorption, assuming a one to one binding configuration of CO to Pt and no adsorption of CO on Co. Results are shown in Table 2. Catalyst 1 has a relatively high platinum surface area of 97 $m^2 g_{Pt}^{-1}$ and dispersion of 39%, indicating that significant amounts of the Pt in the catalyst are accessible at the surface of the particles. This is consistent with the presence of ~2 nm diameter particles in this catalyst. Increasing the annealing temperature for Catalyst 2 results in a decrease in surface area and dispersion compared to Catalyst 1. This is due to increased particle size of the smallest particles compared to Catalyst 1. The improved alloying at higher temperature may also enable a redistribution of metal within the particle, e.g. surface segregation. After leaching Catalyst 1 to form Catalyst 3, the surface area and dispersion decreases. This suggests, as a consequence of the leaching, that fewer Pt atoms are now accessible at the surface. This could occur if Pt was lost from the particles by dissolution. ICP-MS results show some dissolution occurs, but at low levels. Interestingly, the opposite trend is observed after acid leaching Catalyst 2 where a doubling of the surface area and dispersion occurs for Catalyst 4. This would indicate that leaching results in exposure of more Pt at the surface and or an increase in surface to bulk ratio of Pt. This would occur if Co is removed from both the small and larger particles upon leaching and is consistent with the compositional analysis from both XRD and TEM. This enrichment of the particles with Pt on removal of base metal is analogous to the effect described by Strasser *et al.* for high activity, dealloyed PtCu particles. However, the observed increase in surface area may also indicate the formation of a Raney surface.

3.2 XAS characterisation of the effect of chemical acid leaching

Assay, XRD and TEM have shown repeated chemical acid leaching of Catalysts 1 and 2 to form Catalysts 3 and 4 results in loss of Co. For both catalysts, most Co was removed during the first leaching experiment (~90% and ~75% of Co in the catalyst removed for Catalysts 1 and 2 respectively from ICP-MS analysis), then the amount of Co removed with each successive leach decreased. The concentration of Co removed during the second leach was fifty times less for Catalyst 1 and eight times less for Catalyst 2. This was further reduced by four times and three times for the third leaching experiment, and

the final leaching experiment for Catalyst 2 still removed some Co, but the amount was two times lower that that removed in the previous leaching experiment. This trend suggests initially it is easy to remove Co that is either not well alloyed or at the particle surface, then removing Co from deeper within the particle is more difficult. To investigate this hypothesis, XAS at the Pt L_{III} and Co K edges was measured on catalyst powders recovered after each successive leaching experiment.

Figure 5 and Figure 6 show the chi and Fourier transform plots at the Pt L_{III} edge for the acid leaching of Catalyst 1 to form Catalyst 3 in hydrogen and air atmospheres. The corresponding data for acid leaching Catalyst 2 to form Catalyst 4 is shown in Figure 7 and Figure 8. The chi and Fourier transform plots for Catalysts 1-4 at the Co K edge in hydrogen and air atmospheres is shown in Figure 9 and Figure 10. It is noted that the spikes observed in the data at $k \sim 11.3$ Å^{-1} are an artifact of the monochromator. The theoretical fitting results for both leaching experiments at both edge and atmospheres are detailed in Table 3 to Table 6.

The theoretical fits for the acid leaching of Catalyst 2 to form Catalyst 4 were in general in good agreement with the experimental data, $R_{EXAFS} < 38$. However, the fit quality for the acid leaching of Catalyst 1 to form Catalyst 3 showed a poorer fit quality especially in air atmosphere and notably a very poor fitting was achieved for Catalyst 1 at the Co K edge in hydrogen $R_{EXAFS} = 60$. The poor fit quality may be both a combination of a very non homogeneous sample composition and/or noise associated with a poor formation of the pellet and the requirement for longer scan duration. Unfortunately repeat measurements were unable to be completed during the timescale of this work to clarify the reason for poor fit quality.

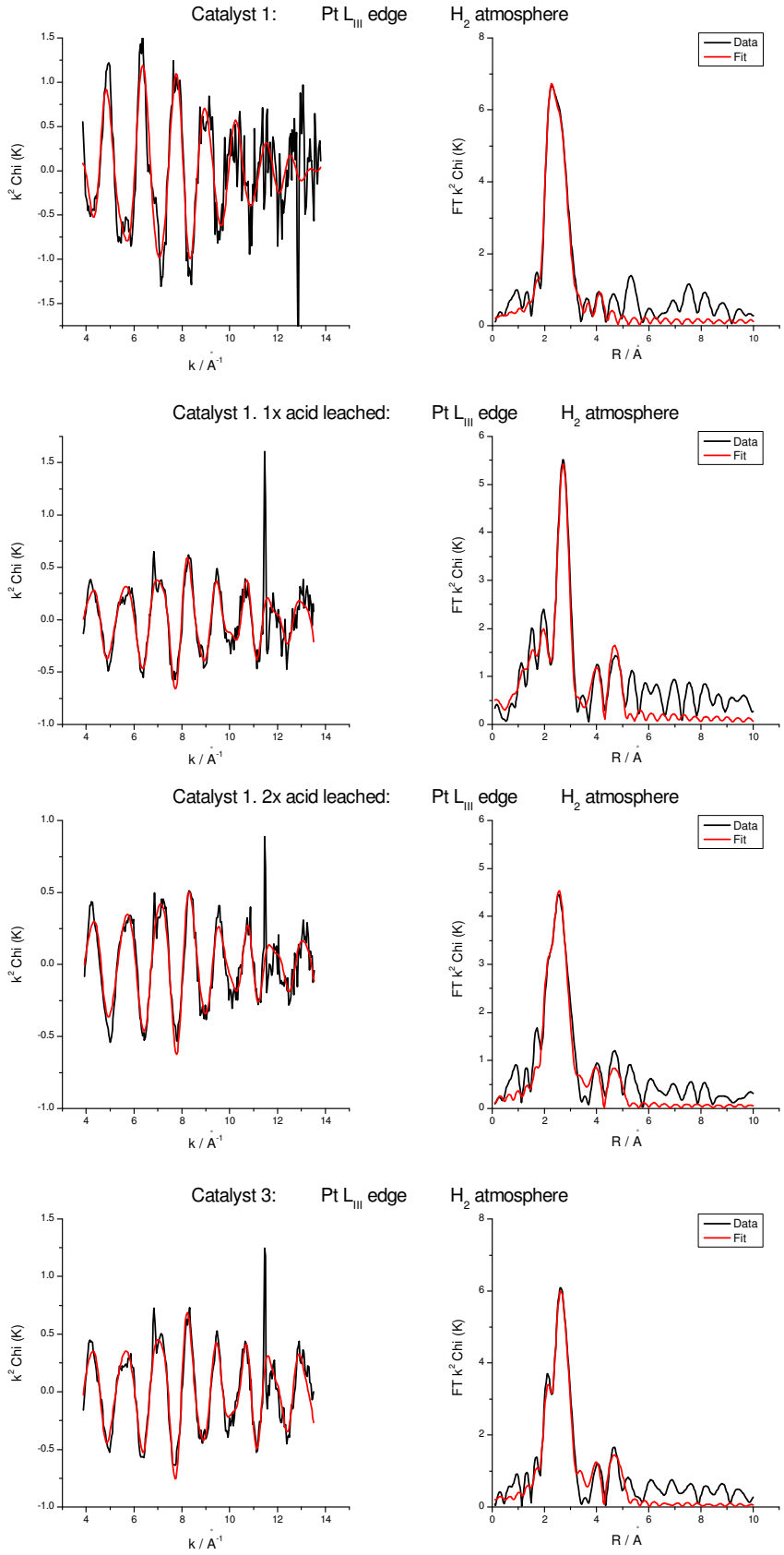

Figure 5. **k^2 weighted experimental chi data (black) and theoretical fit (red) plot and k^2 weighted experimental Fourier transform data (black) and theoretical fit (red) plot for sequential acid leaching of Catalyst 1 to for Catalyst 3 at the Pt L_{III} in H_2**

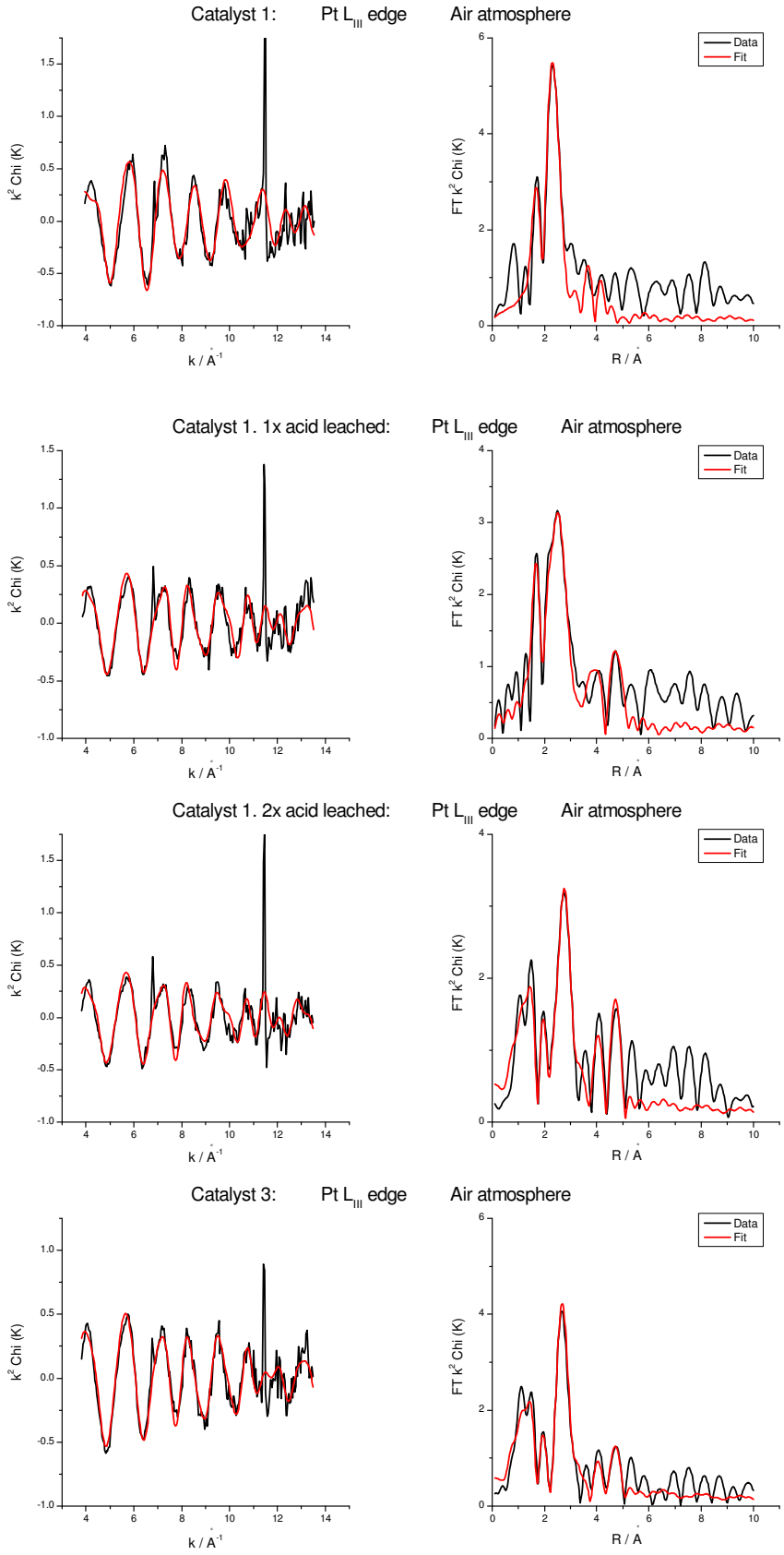

Figure 6. **k^2 weighted experimental chi data (black) and theoretical fit (red) plot and k^2 weighted experimental Fourier transform data (black) and theoretical fit (red) plot for sequential acid leaching of Catalyst 1 to for Catalyst 3 at the Pt L_{III} in air**

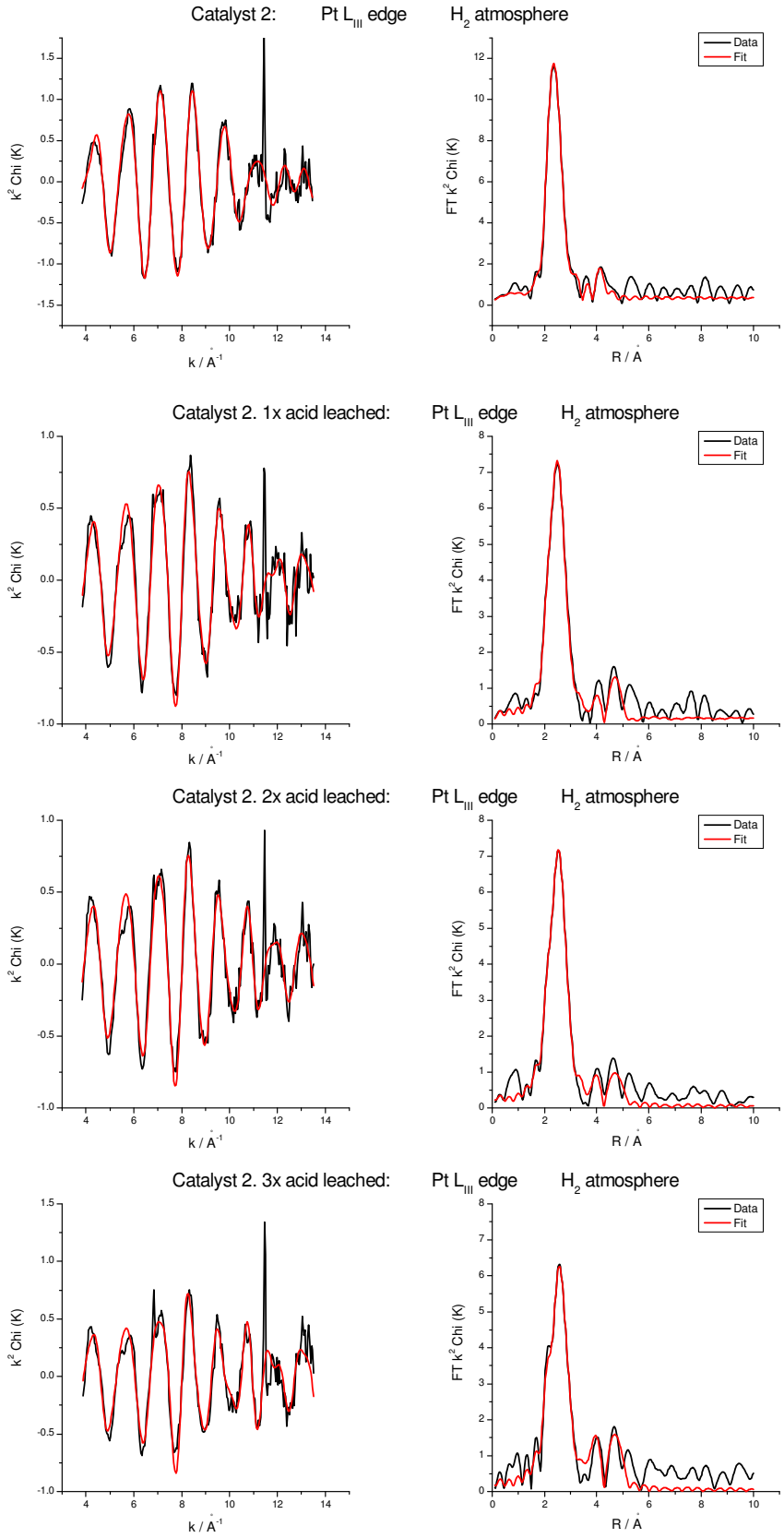
Catalyst 2: Pt L_{III} edge H_2 atmosphere
Data
Fit
k^2 Chi (K)
k / Å^{-1}
FT k^2 Chi (K)
R / Å
Catalyst 2. 1x acid leached: Pt L_{III} edge H_2 atmosphere
Catalyst 2. 2x acid leached: Pt L_{III} edge H_2 atmosphere
Catalyst 2. 3x acid leached: Pt L_{III} edge H_2 atmosphere

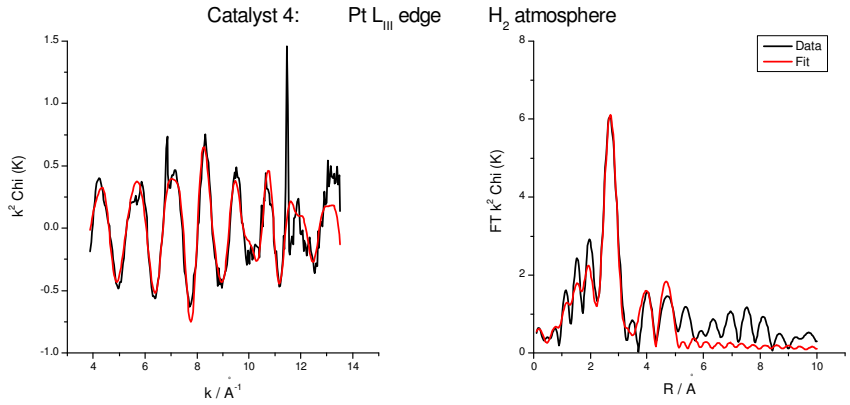

Figure 7. **k^2 weighted experimental chi data (black) and theoretical fit (red) plot and k^2 weighted experimental Fourier transform data (black) and theoretical fit (red) plot for sequential acid leaching of Catalyst 2 to for Catalyst 4 at the Pt L_{III} in H_2**

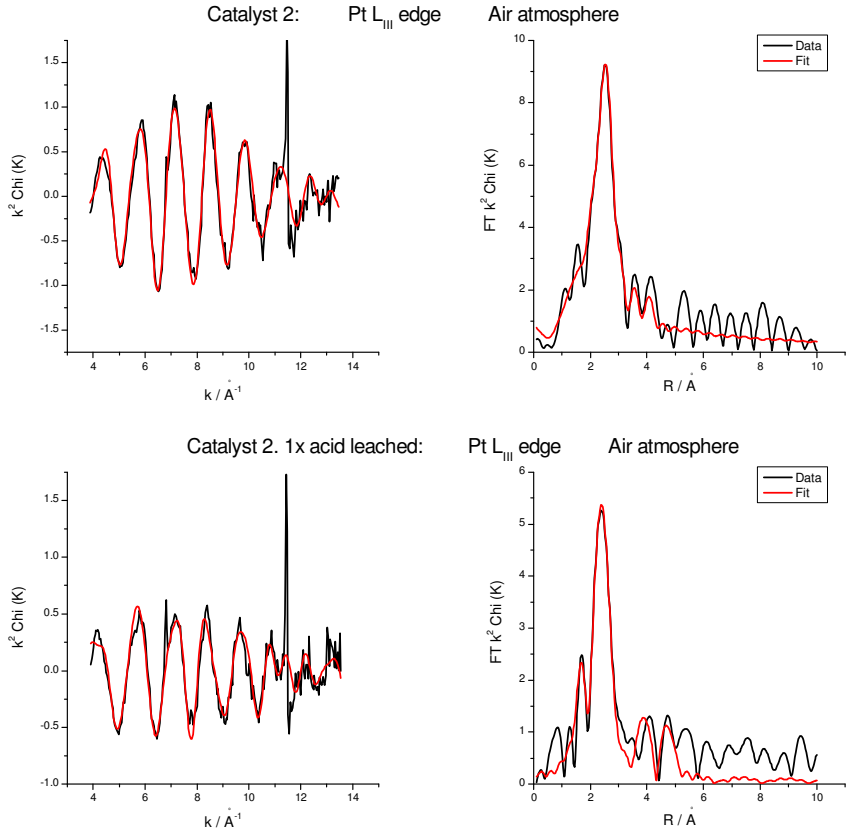

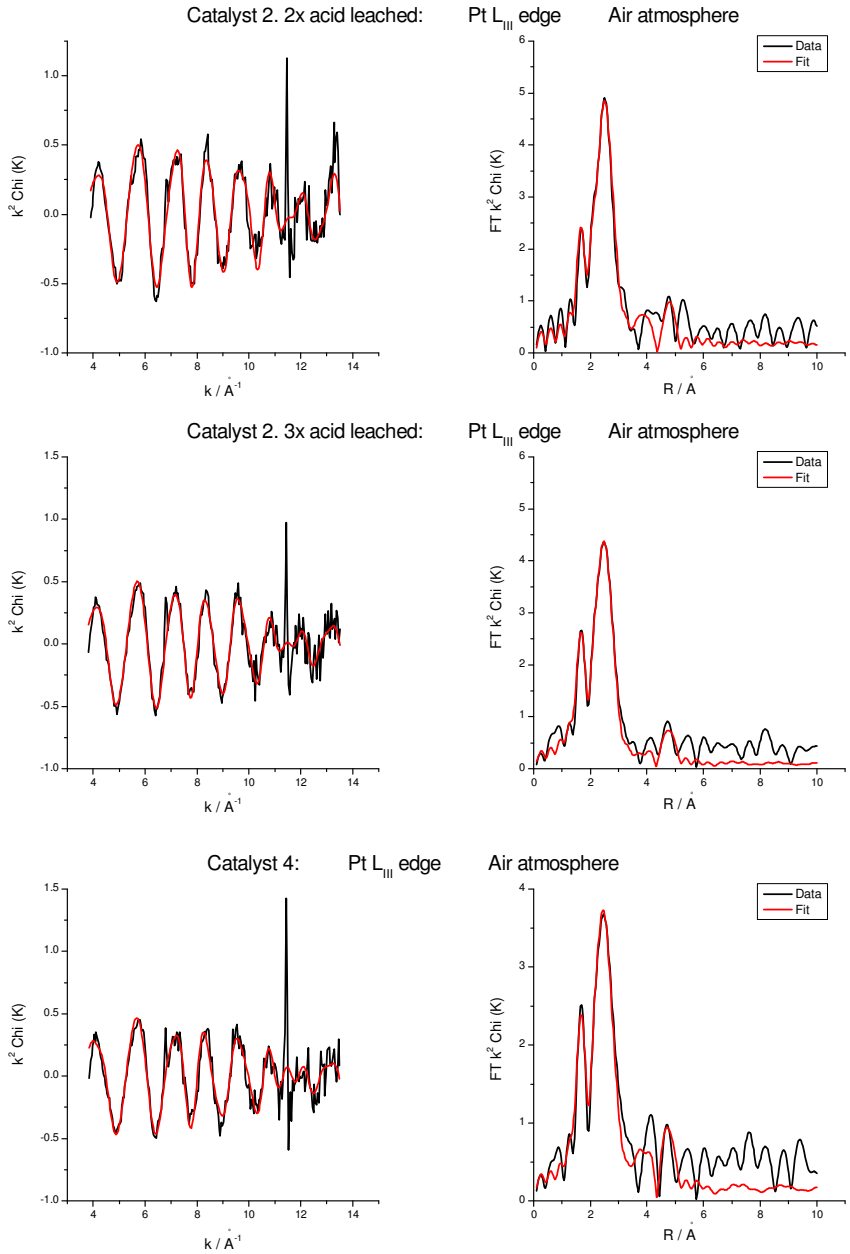

Figure 8. **k^2 weighted experimental chi data (black) and theoretical fit (red) plot and k^2 weighted experimental Fourier transform data (black) and theoretical fit (red) plot for sequential acid leaching of Catalyst 2 to for Catalyst 4 at the Pt L_{III} in air**

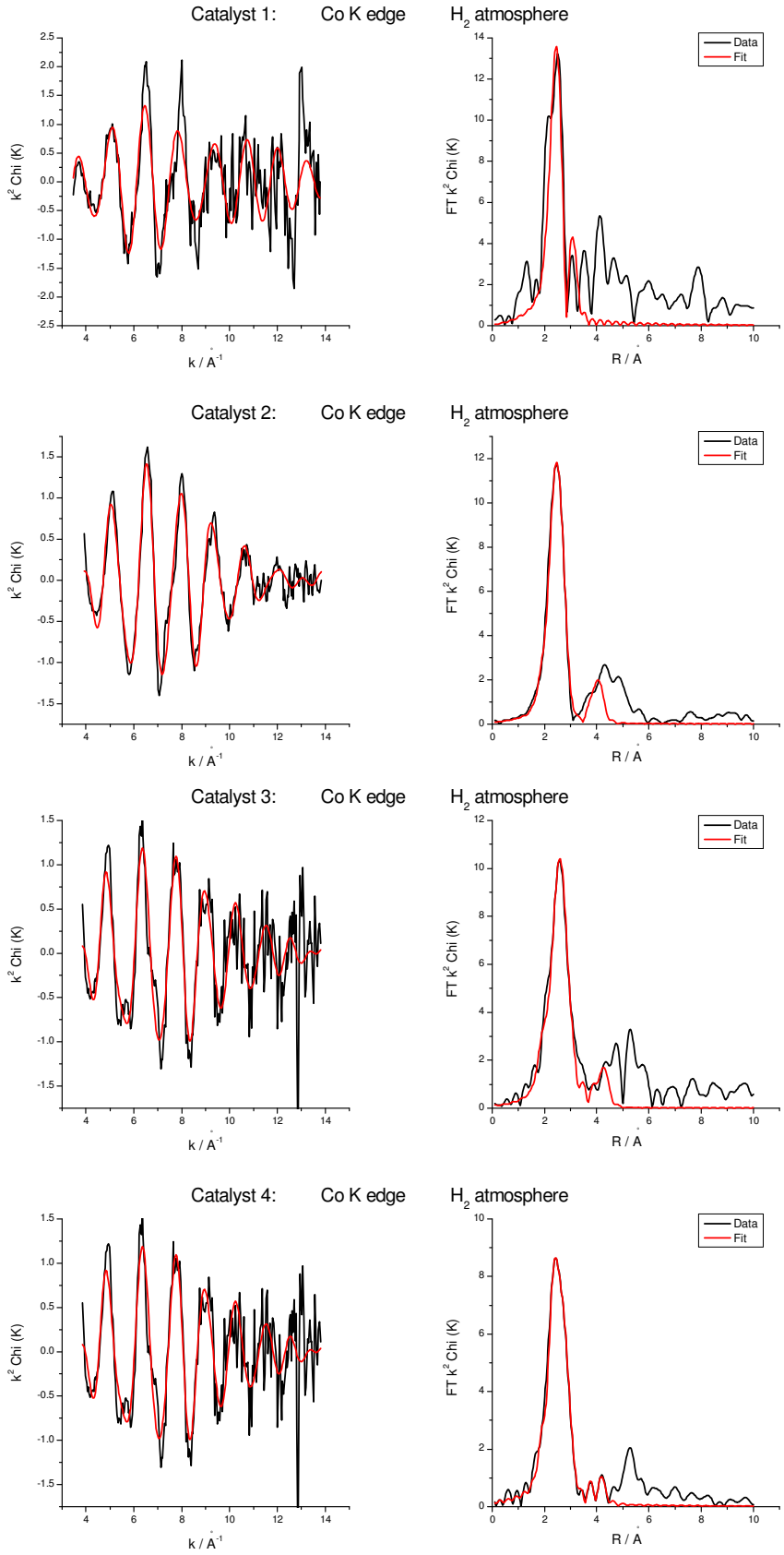

Figure 9. **k^2 weighted experimental chi data (black) and theoretical fit (red) plot and k^2 weighted experimental Fourier transform data (black) and theoretical fit (red) plot for Catalysts 1-4 at the Co K edge in H_2**

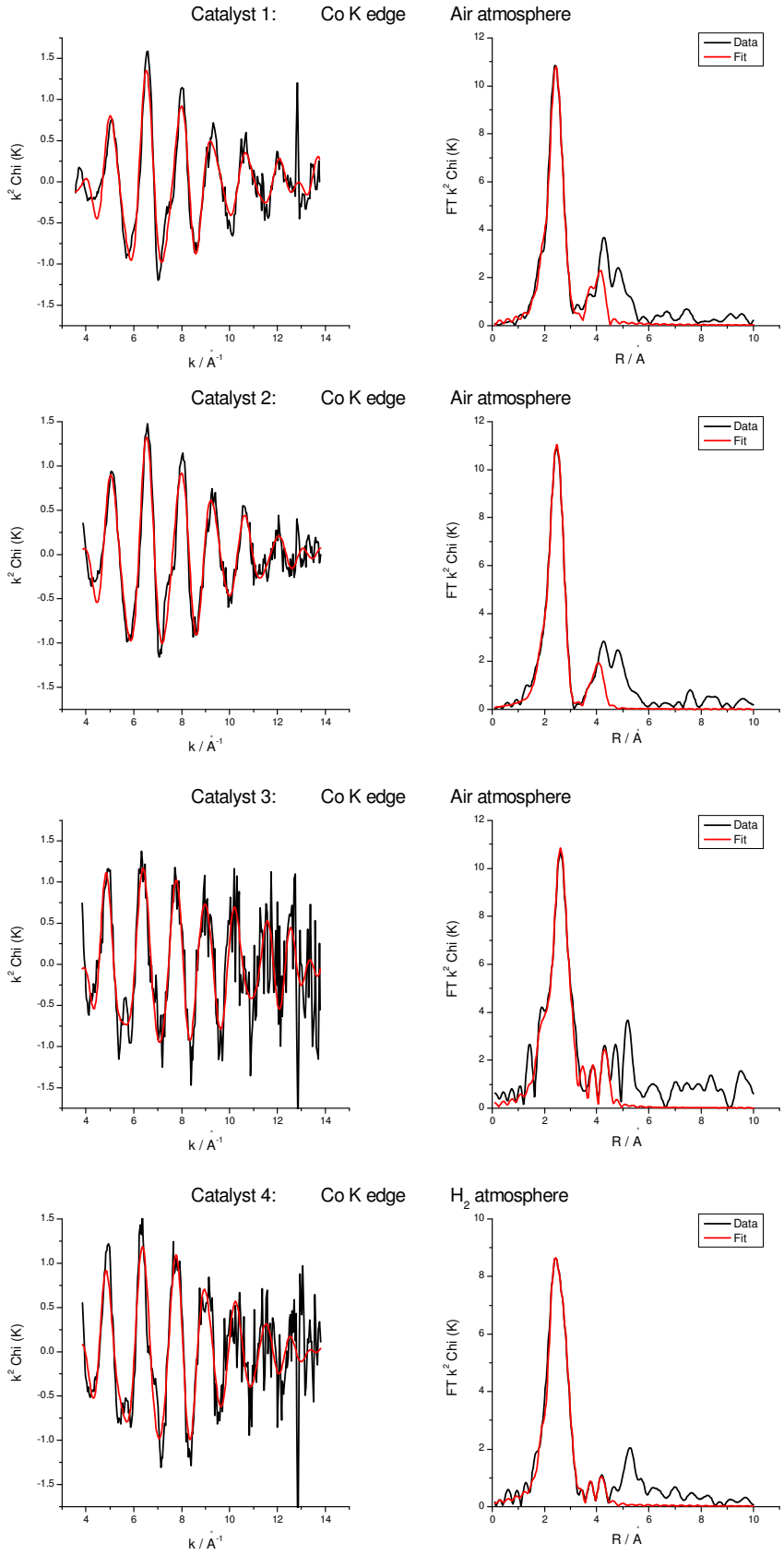

Figure 10. **k^2 weighted experimental chi data (black) and theoretical fit (red) plot and k^2 weighted experimental Fourier transform data (black) and theoretical fit (red) plot for Catalysts 1-4 at the Co K edge in air**

Table 3. Structural parameters obtained by fitting the Pt L_{III} and Co K edges EXAFS data in H_2 for Catalyst 1 during sequential acid leaching to form Catalyst 3

Edge	Catalyst	Absorber neighbour	N	R (Å)	$2\sigma^2$ (Å^2)	E_f (eV)	R_{exafs} (%)
Pt L_{III}	Catalyst 1	Pt-Pt_1	3.4 (± 0.4)	2.73 (± 0.01)	0.012 (± 0.001)	- 9.7 (± 1.5)	31.4
		Pt-Co	2.2 (± 0.2)	2.59 (± 0.01)	0.012 (± 0.001)		
		Pt-Pt_2	2.3 (± 1.2)	3.90 (± 0.03)	0.010 (± 0.004)		
		Pt-Co_2	1.1 (± 0.8)	4.00 (± 0.05)	0.008 (± 0.009)		
Co K	Catalyst 1	Co-Co	4.4 (± 0.5)	2.53 (± 0.01)	0.013 (± 0.002)	- 10.2 (± 2.7)	60.0
		Co-Pt_1	2.0 (± 0.9)	2.80 (± 0.02)	0.008 (± 0.003)		
Pt L_{III}	Catalyst 1 after 1 x acid leach	Pt-Pt_1	3.6 (± 0.5)	2.74 (± 0.01)	0.012 (± 0.001)	- 10.3 (± 2.2)	36.8
		Pt-Co	0.8 (± 0.3)	2.63 (± 0.03)	0.013 (± 0.004)		
		Pt-Pt_2	1.3 (± 0.6)	3.88 (± 0.03)	0.006 (± 0.003)		
		Pt-Pt_3	4.0 (± 1.5)	4.76 (± 0.02)	0.010 (± 0.003)		
Pt L_{III}	Catalyst 1 after 2 x acid leach	Pt-Pt_1	3.5 (± 0.4)	2.72 (± 0.01)	0.013 (± 0.001)	- 9.2 (± 1.7)	34.9
		Pt-Co	1.0 (± 0.2)	2.60 (± 0.02)	0.015 (± 0.003)		
		Pt-Pt_2	1.3 (± 0.6)	3.88 (± 0.03)	0.009 (± 0.004)		
		Pt-Pt_3	2.4 (± 1.0)	4.74 (± 0.03)	0.010 (± 0.004)		
Pt L_{III}	Catalyst 1 after 3 x acid leach = Catalyst 3	Pt-Pt_1	5.1 (± 0.4)	2.74 (± 0.01)	0.012 (± 0.001)	- 10.8 (± 1.5)	31.0
		Pt-Co	0.7 (± 0.2)	2.61 (± 0.03)	0.016 (± 0.005)		
		Pt-Pt_2	1.7 (± 0.7)	3.89 (± 0.02)	0.009 (± 0.003)		
		Pt-Pt_3	4.0 (± 1.3)	4.75 (± 0.02)	0.009 (± 0.002)		
Co K	Catalyst 1 after 3 x acid leach = Catalyst 3	Co-Co_1	2.2 (± 0.4)	2.59 (± 0.02)	0.011 (± 0.002)	- 2.9 (± 2.2)	47.5
		Co-Pt_1	3.0 (± 0.7)	2.67 (± 0.02)	0.012 (± 0.002)		
		Co-O	0.7 (± 0.4)	2.03 (± 0.04)	0.008 (± 0.011)		
		Co-Co_2	2.2 (± 1.1)	4.07 (± 0.04)	0.007 (± 0.006)		
		Co-Pt_2	2.9 (± 1.4)	3.94 (± 0.03)	0.008 (± 0.006)		

Table 4. Structural parameters obtained by fitting the Pt L_{III} and Co K edges EXAFS data in Air for Catalyst 1 during sequential acid leaching to form Catalyst 3

Edge	Catalyst	Absorber neighbour	N	R (Å)	$2\sigma^2$ ($Å^2$)	E_f (eV)	R_{exafs} (%)
Pt L_{III}	Catalyst 1	Pt-Pt_1	0.7 (± 0.6)	2.64 (± 0.04)	0.014 (± 0.009)	- 8.3 (± 2.9)	43.9
		Pt-Co	1.9 (± 0.3)	2.57 (± 0.02)	0.012 (± 0.002)		
		Pt-Pt_2	2.0 (± 1.3)	3.89 (± 0.03)	0.006 (± 0.005)		
		Pt-Pt_3	1.2 (± 0.8)	3.98 (± 0.04)	0.005 (± 0.007)		
		Pt-O	0.8 (± 0.2)	1.97 (± 0.03)	0.004 (± 0.004)		
Co K	Catalyst 1	Co-Co_1	3.1 (± 0.2)	2.52 (± 0.01)	0.013 (± 0.001)	- 9.6 (± 1.5)	38.8
		Co-Pt_1	0.8 (± 0.5)	2.66 (± 0.04)	0.015 (± 0.009)		
		Co-O	0.7 (± 0.2)	2.00 (± 0.03)	0.011 (± 0.009)		
		Co-Co_2	2.4 (± 0.6)	3.97 (± 0.02)	0.008 (± 0.004)		
		Co-Pt_2	1.1 (± 0.3)	3.83 (± 0.02)	0.002 (± 0.002)		
Pt L_{III}	Catalyst 1 after 1 x acid leach	Pt-Pt_1	1.8 (± 0.4)	2.71 (± 0.02)	0.011 (± 0.002)	- 10.9 (± 3.2)	43.7
		Pt-Co	0.8 (± 0.2)	2.61 (± 0.03)	0.012 (± 0.004)		
		Pt-Pt_2	1.3 (± 0.8)	3.89 (± 0.04)	0.006 (± 0.004)		
		Pt-Pt_3	2.6 (± 1.4)	4.75 (± 0.04)	0.007 (± 0.003)		
		Pt-O	0.8 (± 0.2)	1.99 (± 0.04)	0.005 (± 0.004)		
Pt L_{III}	Catalyst 1 after 2 x acid leach	Pt-Pt_1	1.9 (± 0.5)	2.75 (± 0.02)	0.012 (± 0.003)	- 12.8 (± 3.0)	44.7
		Pt-Co	0.8 (± 0.2)	2.61 (± 0.03)	0.011 (± 0.004)		
		Pt-Pt_2	1.4 (± 0.9)	3.91 (± 0.04)	0.008 (± 0.005)		
		Pt-Pt_3	2.5 (± 1.1)	4.76 (± 0.03)	0.006 (± 0.003)		
		Pt-O	0.7 (± 0.2)	2.00 (± 0.03)	0.005 (± 0.004)		
Pt L_{III}	Catalyst 1 after 3 x acid leach = Catalyst 3	Pt-Pt_1	2.0 (± 0.4)	2.72 (± 0.01)	0.011 (± 0.002)	- 13.3 (± 2.0)	33.4
		Pt-Co	0.8 (± 0.2)	2.63 (± 0.02)	0.011 (± 0.003)		
		Pt-Pt_2	0.8 (± 0.4)	3.91 (± 0.03)	0.007 (± 0.005)		
		Pt-Pt_3	2.1 (± 0.9)	4.77 (± 0.03)	0.009 (± 0.003)		
		Pt-O	1.2 (± 0.1)	2.01 (± 0.02)	0.010 (± 0.003)		
Co K	Catalyst 1 after 3 x acid leach = Catalyst 3	Co-Co_1	2.0 (± 0.4)	2.60 (± 0.02)	0.011 (± 0.003)	- 4.3 (± 2.2)	51.6
		Co-Pt_1	3.4 (± 0.8)	2.66 (± 0.02)	0.012 (± 0.002)		
		Co-O	0.9 (± 0.4)	2.01 (± 0.04)	0.008 (± 0.008)		
		Co-Co_2	2.7 (± 0.2)	4.04 (± 0.03)	0.006 (± 0.006)		
		Co-Pt_2	4.3 (± 1.6)	3.93 (± 0.02)	0.007 (± 0.003)		

Table 5. Structural parameters obtained by fitting the Pt L_{III} and Co K edges EXAFS data in H_2 for Catalyst 2 during sequential acid leaching to form Catalyst 4

Edge	Catalyst	Absorber neighbour	N	R (Å)	$2\sigma^2$ (Å^2)	E_f (eV)	R_{exafs} (%)
Pt L_{III}	Catalyst 2	Pt-Pt_1	2.4 (± 0.5)	2.69 (± 0.01)	0.012 (± 0.002)	- 12.2 (± 1.2)	23.1
		Pt-Co_1	3.9 (± 0.3)	2.60 (± 0.01)	0.011 (± 0.001)		
		Pt-Pt_2	3.9 (± 1.5)	3.91 (± 0.03)	0.008 (± 0.003)		
		Pt-Co_2	2.6 (± 1.1)	4.03 (± 0.03)	0.008 (± 0.005)		
Co K	Catalyst 2	Co-Co_1	3.4 (± 0.2)	2.52 (± 0.01)	0.013 (± 0.001)	- 3.7 (± 1.3)	30.4
		Co-Pt_1	1.1 (± 0.3)	2.62 (± 0.02)	0.010 (± 0.002)		
		Co-O	0.6 (± 0.2)	2.02 (± 0.03)	0.015 (± 0.010)		
		Co-Co_2	2.4 (± 0.7)	3.95 (± 0.03)	0.013 (± 0.006)		
		Co-Pt_2	1.7 (± 1.0)	3.80 (± 0.04)	0.010 (± 0.005)		
Pt L_{III}	Catalyst 2 after 1 x acid leach	Pt-Pt_1	3.8 (± 0.4)	2.72 (± 0.01)	0.012 (± 0.001)	- 11.8 (± 4.3)	26.3
		Pt-Co_1	1.9 (± 0.2)	2.63 (± 0.01)	0.012 (± 0.001)		
		Pt-Pt_2	0.7 (± 0.4)	3.89 (± 0.03)	0.006 (± 0.004)		
		Pt-Pt_3	3.1 (± 1.0)	4.73 (± 0.02)	0.009 (± 0.002)		
Pt L_{III}	Catalyst 2 after 2 x acid leach	Pt-Pt_1	4.5 (± 0.4)	2.72 (± 0.01)	0.012 (± 0.001)	- 12.0 (± 1.2)	26.4
		Pt-Co_1	1.5 (± 0.2)	2.63 (± 0.01)	0.013 (± 0.002)		
		Pt-Pt_2	1.4 (± 0.6)	3.89 (± 0.02)	0.011 (± 0.004)		
		Pt-Pt_3	3.0 (± 1.0)	4.75 (± 0.02)	0.011 (± 0.003)		
Pt L_{III}	Catalyst 2 after 3 x acid leach	Pt-Pt_1	4.6 (± 0.5)	2.73 (± 0.01)	0.012 (± 0.001)	- 10.9 (± 1.6)	32.6
		Pt-Co_1	1.1 (± 0.3)	2.62 (± 0.02)	0.014 (± 0.003)		
		Pt-Pt_2	1.8 (± 0.6)	3.89 (± 0.02)	0.007 (± 0.003)		
		Pt-Pt_3	3.8 (± 1.1)	4.75 (± 0.02)	0.008 (± 0.002)		
Pt L_{III}	Catalyst 2 after 4 x acid leach = Catalyst 4	Pt-Pt_1	4.2 (± 0.6)	2.72 (± 0.01)	0.012 (± 0.001)	- 10.6 (± 2.0)	37.2
		Pt-Co_1	1.0 (± 0.3)	2.62 (± 0.03)	0.016 (± 0.005)		
		Pt-Pt_2	2.0 (± 0.9)	3.87 (± 0.03)	0.008 (± 0.003)		
		Pt-Pt_3	3.8 (± 1.5)	4.75 (± 0.03)	0.008 (± 0.003)		
Co K	Catalyst 2 after 4 x acid leach = Catalyst 4	Co-Co_1	2.6 (± 0.2)	2.52 (± 0.01)	0.014 (± 0.001)	- 1.7 (± 1.3)	32.2
		Co-Pt_1	1.9 (± 0.3)	2.65 (± 0.01)	0.010 (± 0.001)		
		Co-O	0.4 (± 0.2)	1.99 (± 0.04)	0.008 (± 0.008)		
		Co-Co_2	1.6 (± 0.7)	3.94 (± 0.03)	0.013 (± 0.007)		
		Co-Pt_2	1.7 (± 0.7)	3.82 (± 0.03)	0.009 (± 0.005)		

Table 6. Structural parameters for obtained by fitting the Pt L_{III} and Co K edges EXAFS data in Air for Catalyst 2 during sequential acid leaching to form Catalyst 4

Edge	Catalyst	Absorber neighbour	N	R (Å)	$2\sigma^2$ (Å^2)	E_f (eV)	R_{exafs} (%)
Pt L_{III}	Catalyst 2	Pt-Pt_1	1.8 (± 0.6)	2.66 (± 0.02)	0.012 (± 0.003)	- 11.3 (± 1.5)	26.7
		Pt-Co_1	3.6 (± 0.3)	2.59 (± 0.01)	0.011 (± 0.001)		
		Pt-Pt_2	2.8 (± 1.3)	3.90 (± 0.03)	0.007 (± 0.004)		
		Pt-Co_2	2.3 (± 1.0)	4.02 (± 0.03)	0.008 (± 0.006)		
Co K	Catalyst 2	Co-Co_1	3.3 (± 0.2)	2.52 (± 0.01)	0.014 (± 0.001)	- 4.4 (± 1.4)	32.4
		Co-Pt_1	0.8 (± 0.3)	2.59 (± 0.02)	0.010 (± 0.003)		
		Co-O	0.5 (± 0.2)	1.98 (± 0.03)	0.009 (± 0.008)		
		Co-Co_2	2.4 (± 0.7)	3.96 (± 0.03)	0.013 (± 0.005)		
		Co-Pt_2	1.2 (± 0.8)	3.80 (± 0.04)	0.007 (± 0.005)		
Pt L_{III}	Catalyst 2 after 1 x acid leach	Pt-Pt_1	1.5 (± 0.5)	2.70 (± 0.02)	0.012 (± 0.003)	- 10.8 (± 2.5)	38.3
		Pt-Co	1.6 (± 0.3)	2.61 (± 0.02)	0.011 (± 0.002)		
		Pt-Pt_2	1.6 (± 1.0)	3.90 (± 0.04)	0.007 (± 0.004)		
		Pt-Pt_3	2.5 (± 1.6)	4.75 (± 0.04)	0.008 (± 0.004)		
		Pt-O	0.7 (± 0.2)	1.99 (± 0.04)	0.007 (± 0.006)		
Pt L_{III}	Catalyst 2 after 2 x acid leach	Pt-Pt_1	2.7 (± 0.4)	2.69 (± 0.01)	0.011 (± 0.001)	- 10.7 (± 2.5)	32.7
		Pt-Co	1.0 (± 0.2)	2.60 (± 0.02)	0.012 (± 0.003)		
		Pt-Pt_2	1.1 (± 0.7)	3.86 (± 0.04)	0.007 (± 0.004)		
		Pt-Pt_3	1.8 (± 1.2)	4.76 (± 0.04)	0.007 (± 0.004)		
		Pt-O	0.7 (± 0.2)	1.99 (± 0.03)	0.006 (± 0.004)		
Pt L_{III}	Catalyst 2 after 3 x acid leach	Pt-Pt_1	2.2 (± 0.4)	2.71 (± 0.01)	0.012 (± 0.002)	- 13.2 (± 2.0)	31.8
		Pt-Co	1.0 (± 0.2)	2.62 (± 0.02)	0.011 (± 0.002)		
		Pt-Pt_2	0.4 (± 0.4)	3.90 (± 0.06)	0.006 (± 0.008)		
		Pt-Pt_3	1.5 (± 0.8)	4.76 (± 0.03)	0.007 (± 0.004)		
		Pt-O	0.7 (± 0.1)	2.00 (± 0.02)	0.005 (± 0.003)		
Pt L_{III}	Catalyst 2 after 4 x acid leach = Catalyst 4	Pt-Pt_1	2.0 (± 0.5)	2.72 (± 0.02)	0.013 (± 0.002)	- 12.2 (± 3.0)	38.4
		Pt-Co	0.9 (± 0.2)	2.62 (± 0.02)	0.011 (± 0.003)		
		Pt-Pt_2	1.1 (± 0.8)	3.90 (± 0.04)	0.009 (± 0.005)		
		Pt-Pt_3	2.0 (± 1.3)	4.75 (± 0.04)	0.008 (± 0.004)		
		Pt-O	0.8 (± 0.2)	2.00 (± 0.03)	0.007 (± 0.005)		
Co K	Catalyst 2 after 4 x acid leach = Catalyst 4	Co-Co_1	2.4 (± 0.2)	2.53 (± 0.01)	0.014 (± 0.001)	- 3.5 (± 1.6)	30.1
		Co-Pt_1	2.0 (± 0.3)	2.63 (± 0.01)	0.010 (± 0.001)		
		Co-O	0.6 (± 0.2)	1.96 (± 0.02)	0.011 (± 0.007)		
		Co-Co_2	1.2 (± 0.6)	3.97 (± 0.05)	0.017 (± 0.013)		
		Co-Pt_2	0.7 (± 0.6)	3.78 (± 0.03)	0.007 (± 0.005)		

Despite the poor quality of fit in some cases, the over all trends observed in the XAS data show Co loss during leaching. The change in first shell coordination number at the Pt L_{III} edge with leaching in hydrogen atmosphere are shown in Figure 11 for acid leaching of Catalyst 1 and Figure 12 for the acid leaching of Catalyst 2. A similar trend is observed in air but the associated errors are larger. In good agreement with the ICP-MS results, the largest loss of Co occurs during the first leach. With subsequent acid leaching the removal of Co decreases as shown by a smaller change in the Pt-Co coordination number. For the acid leaching of Catalyst 1 to form Catalyst 3 (Figure 11) a significant reduction in Pt-Co neighbours occurs after 1 x acid leach and there after further acid leaching results in little change in the Pt-Co coordination number. When considering the Pt-Pt coordination number little change is observed until after third leach to form Catalyst 3 when an increase in Pt-Pt neighbours is observed. At the Co K edge a poor fit quality is observed for Catalyst 1 however, a general trend showing a reduction in Co-Co neighbours and an increase in Co-Pt neighbours post leaching is observed in both hydrogen and air. It is also noted that the Co-Co bond distance are shorter (~2.53 Å) than those observed for the Pt_3Co alloy reported in Chapter 3 (~2.67 Å) and that the bond length increases slightly (~2.60 Å) after acid leaching. These results suggest that acid leaching readily removes large amounts of Co without have significant impact of the regions of the sample containing Pt. This is likely to be due to removal of Co from unalloyed particles and is in good agreement with both findings from XRD and TEM.

Figure 12 shows the effect of acid leaching Catalyst 2 to form Catalyst 4. In this instance a progressive decrease in Pt-Co neighbours occurs with each leach. The largest decrease occurs after 1x acid leach then with each subsequent leach a smaller decrease in Pt-Co coordination number occurs. This is in good agreement with the ICP-MS results. Correspondingly the Pt-Pt coordination number increases with each sequential leaching experiment. This indicates that the acid leaching removes Co that is associated with Pt atoms. At the Co K edge a decrease in Co-Co coordination number is observed after leaching, however the Co-Co bond length remains similar (~2.52-2.53 Å). These observations may be the consequence of the improved alloying at the increased temperature used to form Catalyst 2.

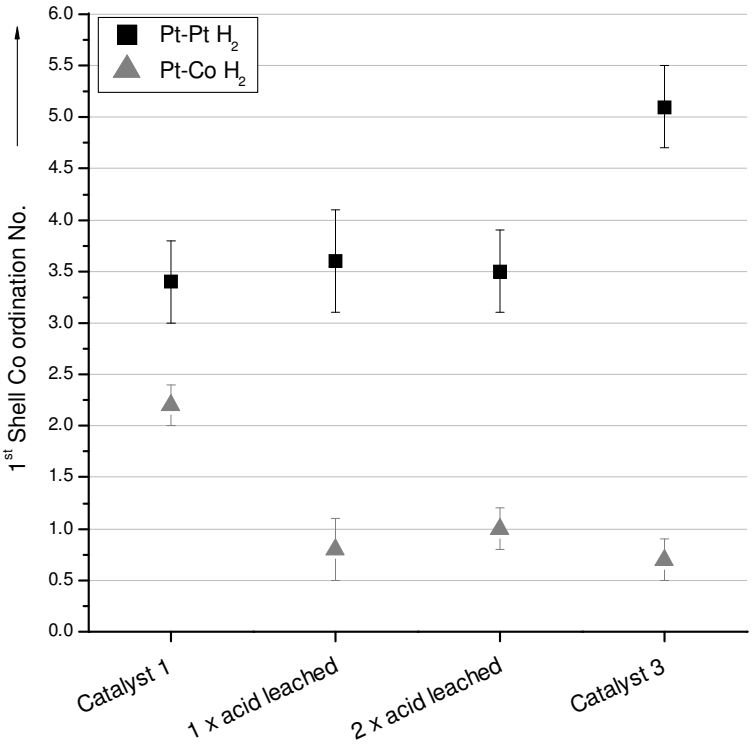

Figure 11. Summary of the fitted coordination number of first shell neighbours during sequential acid leaching of Catalyst 1 to form Catalyst 3 at the Pt L_{III} edge in H_2

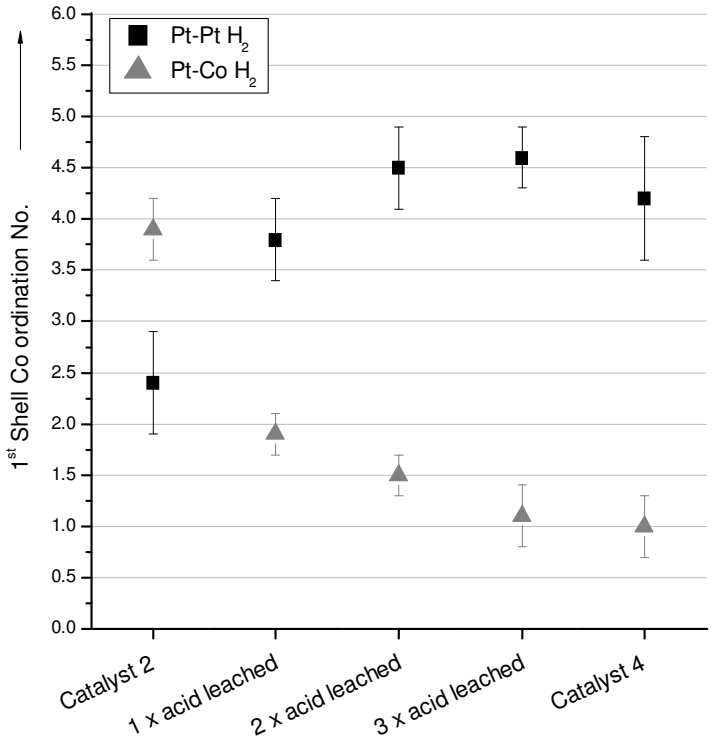

Figure 12. Summary of the fitted coordination number of first shell neighbours during sequential acid leaching of Catalyst 2 to form Catalyst 4 at the Pt L_{III} edge in H_2

3.3 Electrochemcial dealloying

3.3.1 *Ex situ* liquid electrolyte experiments

Catalysts 1-4 were electrochemically dealloyed by cycling from 0.6-1.0 V and 0.6-1.2 V. The upper potential limits of 1.0 and 1.2 V were chosen to match those reported by Strasser *et al.* (4, 6, 14) and to allow direct comparison with the results obtained for Pt_3Co/C catalysts discussed in Chapter 3. Conducting the dealloying in liquid electrolyte also enabled both Co and Pt dissolution to be monitored.

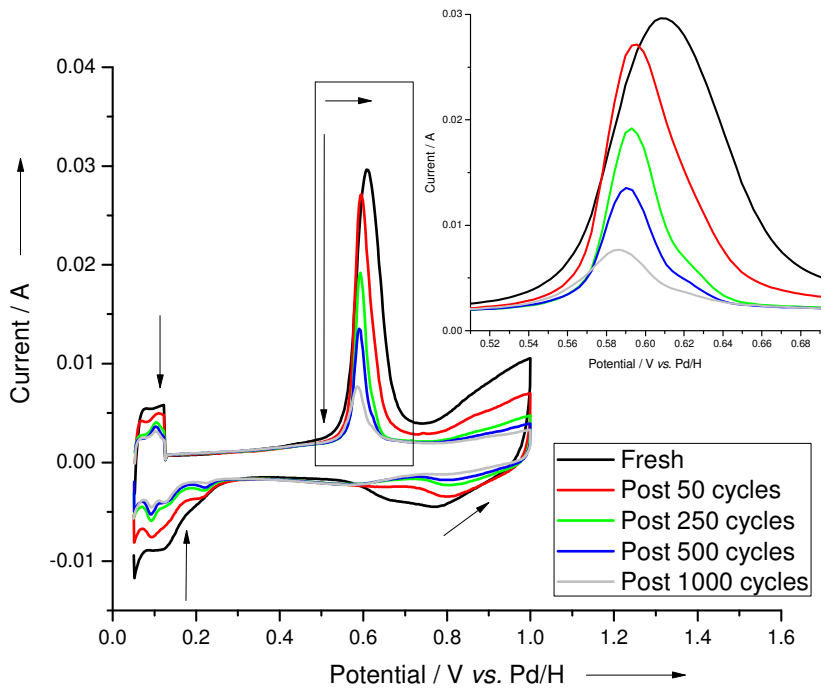

Figure 13. CO oxidation voltammetry of Catalyst 1 during 0.6-1.2 V cycling

The BOL ECA areas for Catalysts 1-4 were determined from the BOL CO oxidation voltammetry as 81, 44, 75, 57 $m^2_{Pt}\,g^{-1}_{Pt}$ respectively. This trend is in good agreement with the metals areas determined by CO chemisorption. Cyclic voltammetry was used to follow changes occurring to the catalyst during potential cycling. For all catalysts, as the cycle number increases, the magnitude of the current across the voltammogram decreases and the hydrogen adsorption/desorption peaks become more well defined. This effect is more significant during 0.6-1.2 V cycling. An example CO oxidation voltammogram for Catalyst 1 during the 0.6-1.2 V cycling regime is shown in Figure 13. For all catalysts except Catalyst 3, the CO oxidation peak sharpens and the onset

shifts to higher overpotentials, indicating that as the catalyst is cycled it becomes harder to oxidise adsorbed CO on the surface. For Catalyst 3, the peak sharpening is observed, however the CO oxidation onset does not change during the test.

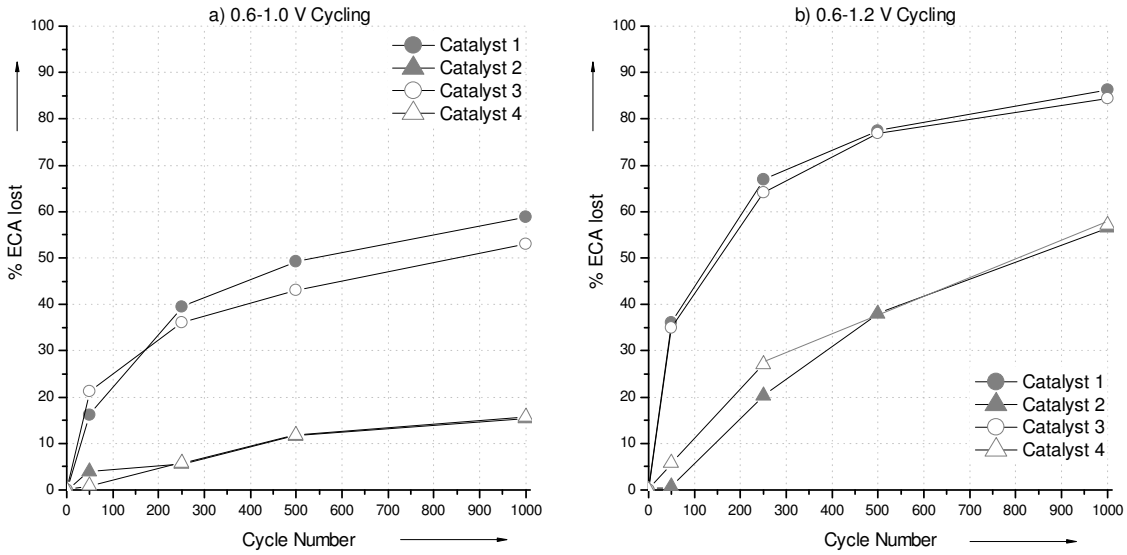

Figure 14. %ECA loss with cycle no. for Catalysts 1-4 during a) 0.6-1.0V and b) 0.6-1.2 V cycles

The % ECA loss for Catalysts 1-4 with cycle number during both cycling regimes determined from the CO oxidation voltammetry is shown in Figure 14. All catalysts exhibited ECA loss with 0.6-1.2 V cycling resulting in greater ECA loss for all catalysts. In both cycling regimes, the same ECA trends are observed. Catalysts 1 and 3 (low temperature annealed as prepared and leached) were found to be least stable, with Catalyst 1 losing slightly more ECA over 1000 cycles. Catalysts 2 and 4 (high temperature annealed as prepared and leached) were significantly more stable than Catalysts 1 and 3 and had very similar ECA loss during cycles. The increased stability of Catalysts 2 and 4 is thought mainly to be a consequence of the larger particle size of the smallest particles in the catalyst compared to Catalyst 1 and 3 (See Table 2). In addition, the improved alloying at higher temperature may also contribute to the enhanced stability. For both catalyst pairs (1 & 3, and 2 & 4), the Co content of the catalyst does not significantly affect the ECA stability. This observation can be explained by considering the %Co removed from the catalyst with cycle, as shown in Figure 15.

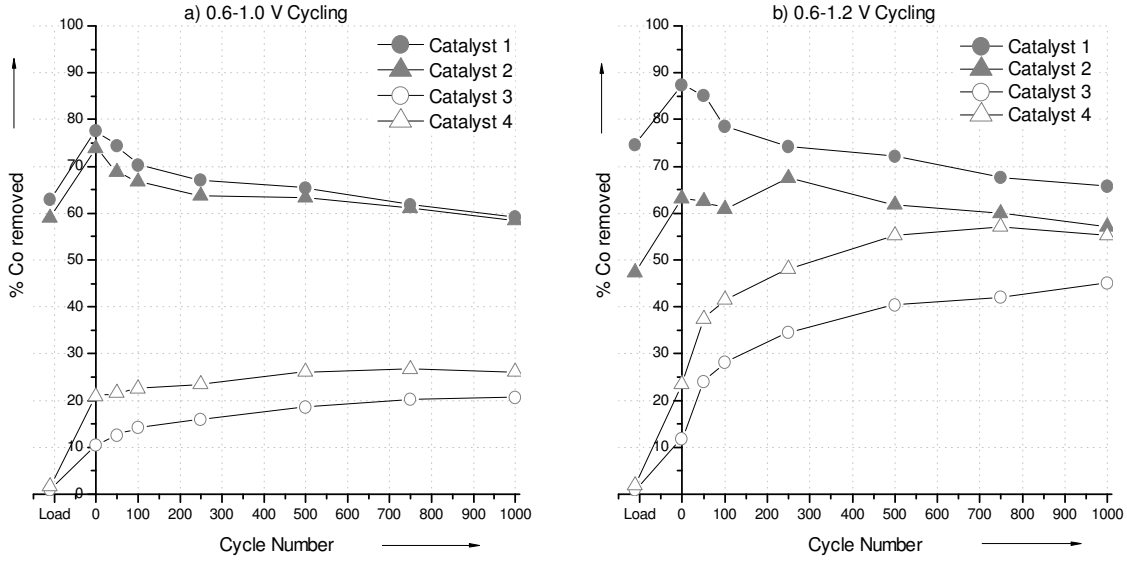

Figure 15. % Co removed with cycle no. for Catalysts 1-4 during a) 0.6-1.0 V and b) 0.6-1.2 V cycles

For Catalysts 1 and 2 (low and high temperature annealed as prepared), before any cycling has occurred, significant quantities of Co have been leached from the catalysts into the electrolyte. This leaching occurred when the electrode buttons were placed into the hot acid (80 °C) and during the equilibration period whilst degassing occurred (~20 minutes) before any electrochemical measurements were run. The amounts of Co removed into the solution at this stage are represented in Figure 15 by the "load" data point. The electrolyte sample taken at "0 cycles" was after the BOL cyclic voltammetry and CO oxidation voltammetry was conducted. In all cases, an increase in Co removed is observed indicating the initial voltammetry characterisation causes some Co loss. Before electrochemical cycling, the Co content of the catalyst pairs are therefore very similar. It is therefore not surprising that the ECA loss trends for both sets of materials are also similar. For Catalysts 1 and 2, electrochemical cycling does not significantly further increase the amount of Co found in solution, in fact a slight decrease is observed. This is likely to be the consequence of a dilution effect when sampled electrolyte is replaced by fresh acid throughout the test.

Cycling results in increasing Co loss for both Catalysts 3 and 4 (acid leached) with more Co removal from Catalyst 4 under both cycling regimes. This may be the consequence of Catalyst 4 having a higher initial Co content than Catalyst 3. Co loss is observed to

be potential dependent, with more Co removal occurring at the higher upper potential limit. As discussed in Chapter 3, this is likely to be a consequence of increased place exchange at higher potentials, facilitating Co removal.

Pt dissolution into the electrolyte with cycles was also observed. After 1000 0.6-1.0 V cycles, ≤ 1.3 %Pt in the catalysts was removed. Cycling to 1.2 V resulted in increased Pt dissolution with 6, 14, 9 and 10% loss for Catalyst 1-4 respectively. Unexpectedly, more dissolution occurred from the larger particle sized Catalysts 2 and 4, both of which, lost less ECA. This suggests the dominant mechanisms of ECA loss for the catalyst pairs may differ. To consider ECA loss mechanisms and to study structural changes occurring as a consequence of electrochemical dealloying, TEM analysis of the cycled electrodes was performed.

Bright field and High Angle Annular Dark Field (HAADF z-contrast) images for Catalysts 1-4 post 0.6-1.0 V and 0.6-1.2 V cycling are shown in Figure 16. Electrochemical cycling caused a change in the catalyst particle size distribution, composition and structure. The very large Co rich particles present in some of the catalysts before cycling (especially Catalyst 1) were not present after cycling, with all catalysts now exhibiting a mono modal particle size distribution. The average particle sizes of Catalysts 1 and 3 increased after cycling, with loss of the particles under 2.5 nm leaving post cycled samples with a 2.5-4.0 nm particle size range after 0.6-1.0 V cycling and 5-8 nm range after 0.6-1.2 V cycling. Ostwald ripening of the catalyst particles therefore accounts for a significant proportion of ECA loss for Catalysts 1 and 3. For Catalyst 2, electrochemical cycling from 0.6-1.0V or 0.6-1.2 V did not change the particle size distribution. A slight increase in particle size was seen for Catalyst 4, with the distribution increasing from 4-6 nm in the as prepared catalyst to 5-6 nm post 0.6-1.0 V cycling and 6-7 nm post 0.6-1.2 V cycling. This small shift in particle size distribution indicates Ostwald ripening occurs but is not a dominant mechanism of ECA loss. For Catalysts 2 and 4 (high temperature annealed and acid leached), cycling to both 1.0 V and 1.2 V resulted in the formation of a core shell type structure, denoted by particles in the HAADF images of Figure 16 having a bright outer ring around a darker centre. Catalyst 3 (low temperature annealed and acid leached) showed core shell formation only after the more aggressive 1.2 V cycling regime where Co dissolution levels were increased.

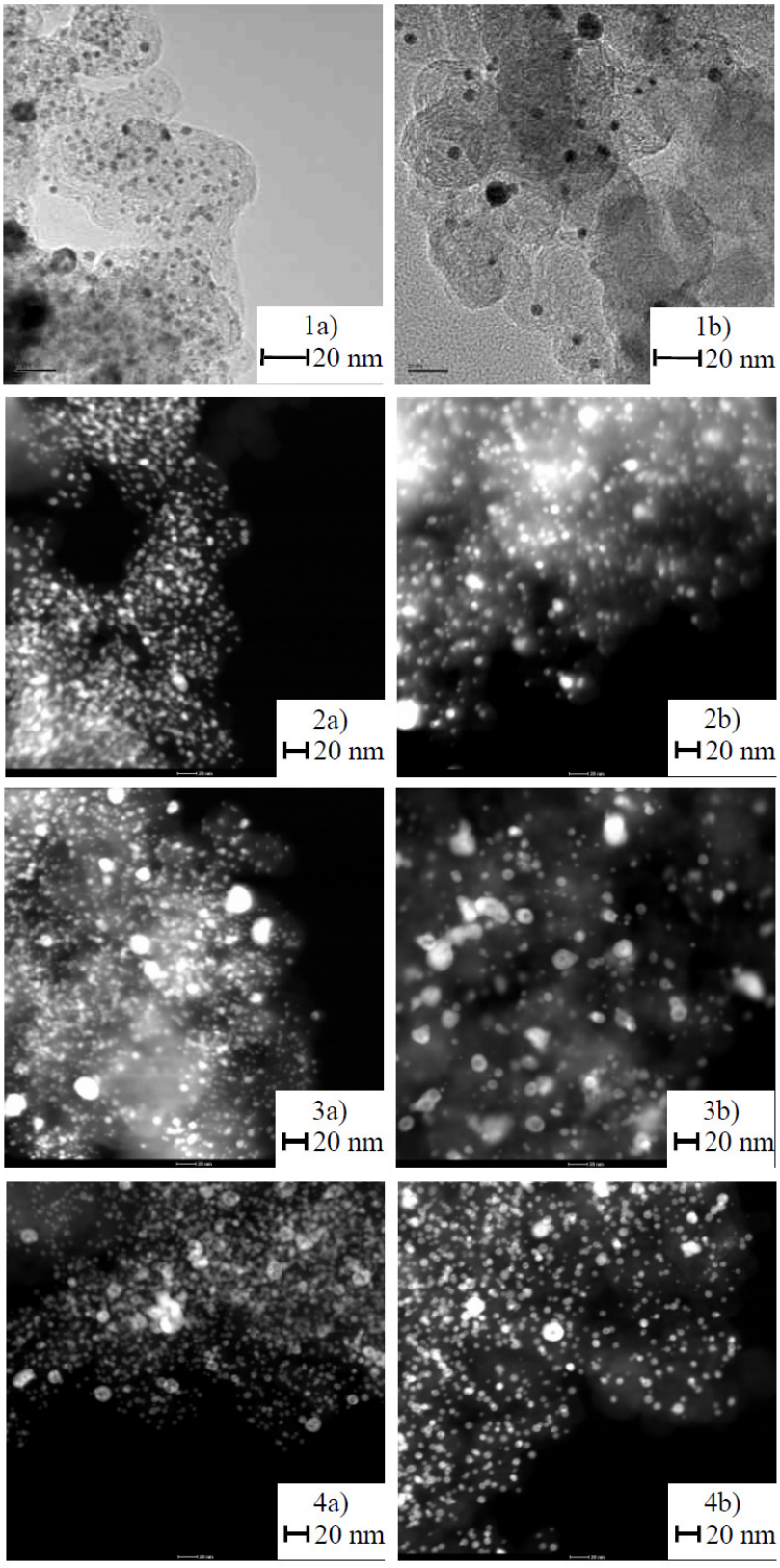

Figure 16. Bright Field and High Angle Annular Dark Field (HAADF) TEM images for Catalysts 1-4 after a) 0.6-1.0 V and b) 0.6-1.2 V cycling

EDAX line scan analysis across the particles of post cycled Catalyst 1 and Catalyst 3 after 0.6-1.0 V cycling showed no variation of the Pt and Co distribution across the particle diameter. For the other samples, EDAX line scan analysis across the particles clearly shows an enrichment of the Pt signal at the edge of the particles and background levels of Co, while in the centre of the particles a high Co signal is observed with a corresponding depletion in Pt signal. A representative EDAX analysis of two particles with core shell structure for Catalyst 3 after 1.2 V cycling is shown in Figure 17. The Pt shell thickness was also measured, by hand, directly from the TEM images by the author, using Digital Micrograph software. The thickness of the Pt shell of the 17 nm diameter particle in Figure 17 was 6 nm. This shell thickness corresponds to 71% of the particle radius. Assuming a metallic Pt radius of 0.138 nm (17) and that the thickness of one Pt layer is equal the diameter of a Pt atom, the core shell particle has a Pt shell 21-22 Pt layers thick.

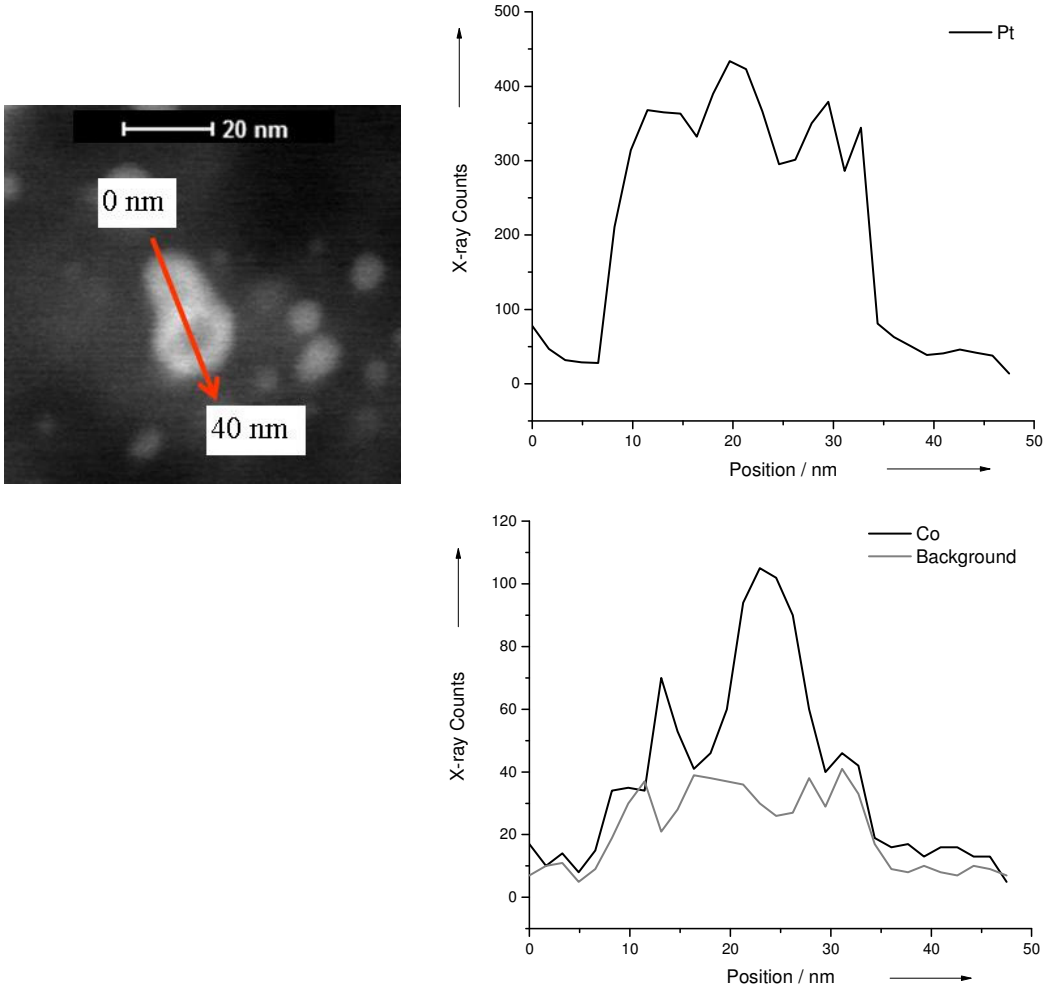

Figure 17. HAADF TEM image and EDAX line scan analysis of core shell particles in Catalyst 3 after 0.6-1.2 V cycling

The thickness of the Pt shells were also determined for a selection of particles, with a range of particle sizes, in images 3b), 4a) and 4b) Figure 16. Results are plotted in Figure 18. It can be seen that the *ex situ* dealloying procedure has produced core shell particles with a multi-layer Pt shell structure. With increasing particle size, a thicker Pt shell is formed. On average, the Pt shell thickness of particles in Catalyst 3 after 0.6-1.2 V cycling was 73% of the particle radius. For Catalyst 4 after cycling from 0.6-1.0 V, the average shell thickness equates to 61% of the particle radius. Cycling to the higher upper potential limit of 1.2 V results in an increase in the average shell thickness to 79% of the particle radius. This is consistent with a higher % Co removal during 0.6-1.2 V cycling. In addition to Co leaching, the Pt shell formation may arise due to re-precipitation of dissolved Pt species as a consequence of cycling. At higher upper potentials more dissolution and particle growth is observed that may in turn lead to the observed thicker Pt shells.

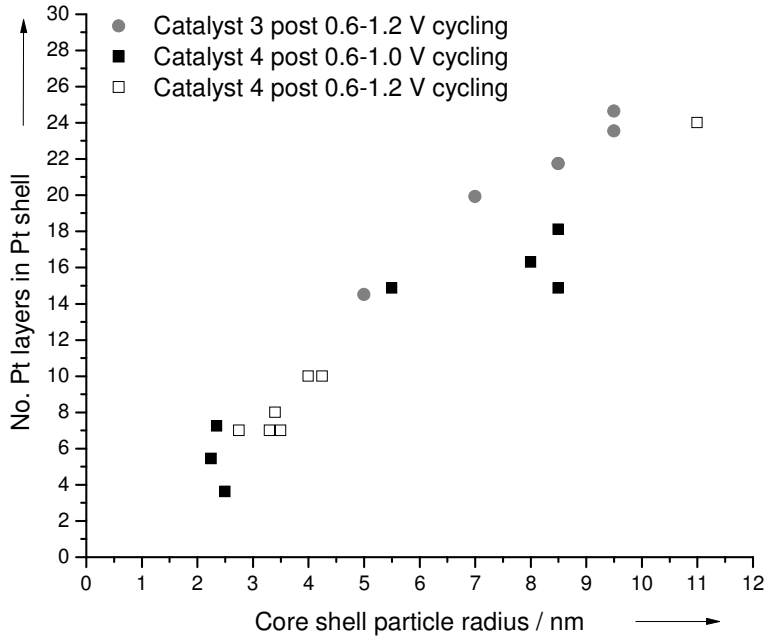

Figure 18. Measured Pt shell thickness for selected core shell particles in images 3b), 4a) and 4b) Figure 16

The TEM results demonstrate that the dealloying procedure results in catalyst particles with a multi-layer, Pt-rich shell and bimetallic cores. This structure for PtCu systems has been reported to have enhanced activity for the ORR (6). A reason proposed for activity enhancement is the retention of the contracted lattice of Pt despite removal of the base metal (12), for the $Pt_{25}Cu_{75}$/C catalyst reported in Table 1 the d-spacing is reported to be 2.09-2.21 Å (11) and from the atomic composition the lattice parameter is 3.697 Å (16).To probe if the contracted lattice is present in the shell of the PtCo core shell structures, high resolution TEM was attempted on selected particles and fringes were obtained. Figure 19 shows a representative HRTEM image. The d-spacings measured from the TEM image are consistent with platinum. Further, there was no indication of a change in the d-spacing in the centre of the particle despite the observed lattice contraction seen by XRD of the fresh catalysts. This may indicate that the orientation of the cobalt core was unsuitable for this imaging technique or that the d-spacing of Pt and PtCo are too similar to be able to distinguish them using this technique.

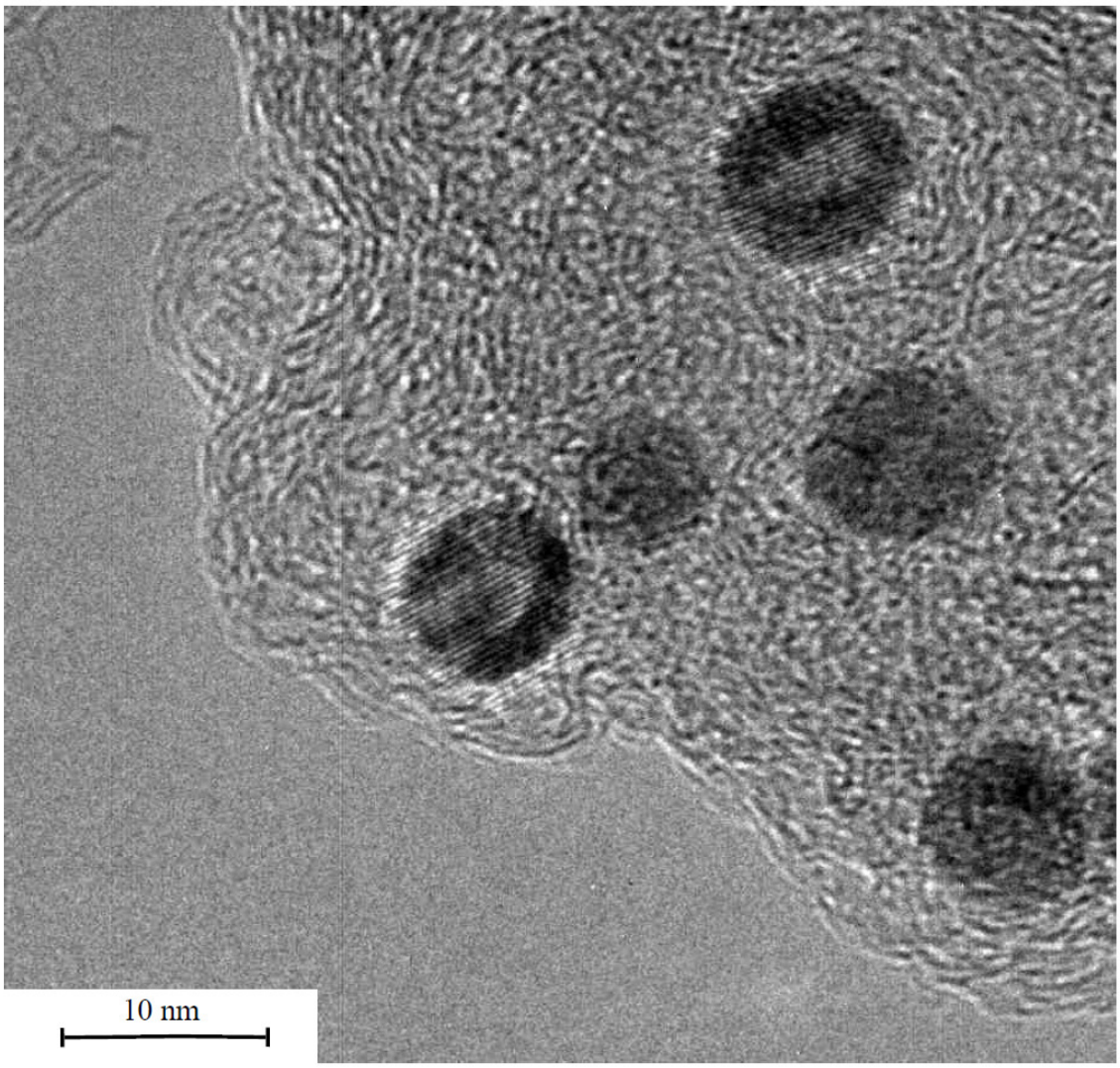

Figure 19. High resolution TEM image of Catalyst 4 after 0.6-1.2 V cycling

3.3.2 *In situ* dealloying in MEAs

The beginning of life performances at 270 kPa_{abs} of CCMs prepared from Catalysts 1-4 and a comparable 30% Pt/C catalyst at similar Pt loading (0.1-0.2 mg_{Pt} cm^{-2}) are shown in Figure 20.

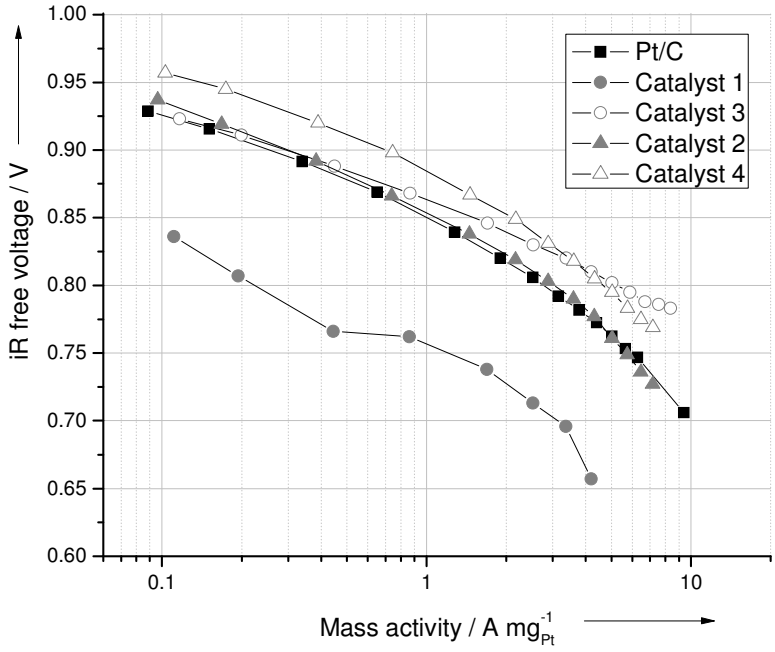

Figure 20. BOL iR free fuel cell mass activity performance of CCMs with Catalysts 1-4 cathodes with 0.1-0.2 mg_{Pt} cm^{-2} loading and Pt/C, 0.1 mg_{Pt} cm^{-2} anodes. All CCMs were prepared with V3 membrane and tested in the Mark 4 cell at 100% RH, 80 °C, 270 kPa_{abs}. For comparison the mass activity of 30% Pt/C is shown

Catalysts 2 and 3 have comparable performance to the Pt/C catalyst at BOL. Catalyst 1 has significantly poorer performance than the Pt/C catalyst. The sample was unable to support the current ranges used in the standard conditioning procedures and automated polarisation measurements. The oxygen polarisation was therefore run manually over a reduced current range. This poor performance is characteristic of insufficient active sites for reaction and / or mass transport limitations and is likely to be the consequence of the significant amounts of unalloyed Co in the sample leaching under operation. The highest performance (a three fold improvement over the Pt/C catalyst at 900 mV) is observed for Catalyst 4. In both cases, the chemical acid leaching treatment to form

Catalysts 3 and 4 significantly improves the catalytic performance compared to the unleached precursor material. After BOL performance testing, the CCMs were electrochemically cycled according to the procedure in Chapter 2, section 2.2.4.

During the dealloying procedure, changes to the catalyst were monitored by cyclic voltammetry. In all cases, no significant change to the voltammetry profile was observed, indicating that the cycling procedure does not cause any significant electrochemical area change that would be indicative of Raney surface formation or Pt dissolution and sintering. After dealloying, the CCM was removed from the cell and acid washed according to the procedure in Chapter 2, section 2.2.3. The acidified washings were analysed by ICP-MS for Pt and Co content. Dealloying and washing was found to remove 0.6-0.8% Pt from Catalysts 2-4 based on the cathode loading, while 1.3% of the Pt was removed from the CCM of Catalyst 1. Catalyst 1 also showed very high levels of Co removal, calculation suggested all of the Co in the layer was removed by dealloying and washing. This very easy loss of Co from the catalyst particles into the MEA structure helps explain the very poor performance observed for this catalyst at BOL. Co was also removed from the other catalysts. 65% Co was removed from Catalyst 2. Less Co was removed from the better alloyed, lower Co containing catalysts. 2.4% was removed from Catalyst 3 and 4.8 % from Catalyst 4. Compared to the *ex situ* dealloying experiments, less Co was removed over 1000 *in situ* cycles (except for Catalyst 1), however the same Co stability trends for the catalysts were observed. This result is in line with *ex situ* cycling being more aggressive than *in situ* MEA cycling, as previously discussed in Chapter 3. It is possible therefore that the core shell structures observed after *ex situ* cycling were not formed during *in situ* dealloying.

The activity of Catalysts 1-4 after de-alloying and acid washing are shown in Figure 21. For comparative purposes, the activity of Catalyst 4 and a Pt/C catalyst that underwent the same acid washing and refabrication procedure but no electrochemical cycling are shown. After dealloying, all catalysts show increased performance *vs*. the washed Pt/C catalyst. Catalyst 3 showed a two fold improvement at 900 mV, while Catalysts 1 and 2 showed a three fold improvement. The highest performance benefit of 3.2 times that observed for Pt/C was observed for Catalyst 4. To check if the activity enhancements observed after the dealloying and washing procedure were a consequence of the electrochemical cycling, Catalyst 4 was tested after only undergoing the washing

procedure. Comparing Catalyst 4 washed and dealloyed, an activity enhancement is observed after de-alloying. At 900 mV this equates to a 20% increase. This suggests that the dealloying procedure is required to 'activate' the catalyst, as reported by Strasser *et al* (4, 6). ICP-MS analysis of the acid washings indicates the activity benefit is likely to be the result of the two fold increase in Co removed from the CCM as a consequence of dealloying, compared to washing alone. It is unknown if this Co removal corresponds to core shell formation or if all the dealloyed Co in the MEA has been removed by the acid washing procedure. It is therefore unclear if the optimum catalytic activity has been measured. To confirm this, post mortem analysis of the MEA by TEM cross section and EMPA cross sectional mapping would be required.

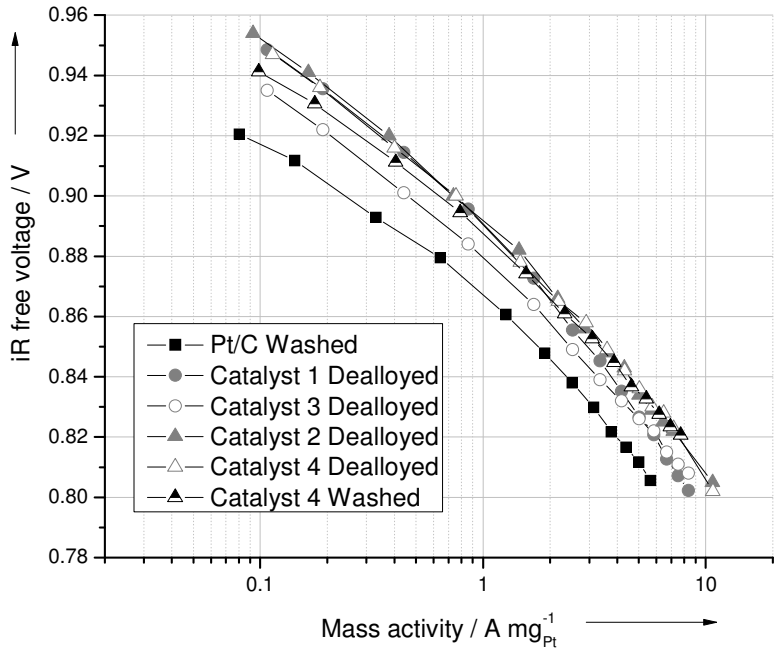

Figure 21. **iR free fuel cell mass activity performance after *in situ* dealloying of CCMs with Catalysts 1-4 cathodes with 0.1-0.2 mg_{Pt} cm^{-2} loading and Pt/C, 0.1 mg_{Pt} cm^{-2} anodes. All CCMs were prepared with V3 membrane and tested in the Generic Screener Cell at 100% RH, 80 °C, 270 $kPa_{abs.}$ For comparison the mass activity of 30% Pt/C and Catalyst 4 that had undergone the washing procedure are shown**

4. Discussion

4.1 Activation of Pt_3Co

The BOL activity of $PtCo_3$/C was found to be platinum like or, where significant quantities of unalloyed Co were present, poorer than platinum. Co removal *via* chemical acid leaching, was found to improve performance. *In situ* dealloying resulted in further catalyst activation.

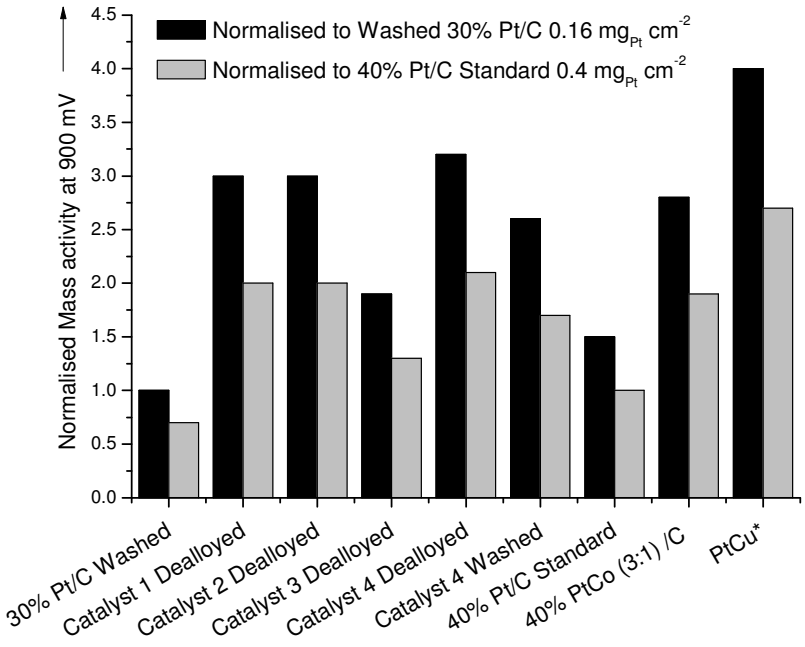

Figure 22. Mass activity performance at 900 mV comparison of dealloyed Catalysts 1-4 ($PtCo_3$) with Pt_3Co and literature dealloyed $PtCu_3$ catalysts (14) * PtCu activities normalised to reported low loading 30% Pt/C and high loading 45%Pt/C values

Figure 22 summarises the mass activity enhancements observed for the $PtCo_3$ derived materials. Activities were normalised to both a 30% Pt/C catalyst at the same metal loading, that had undergone the same acid washing procedure as the $PtCo_3$ derived materials, and a standard 40% Pt/C catalyst, at the higher metal loading of 0.4 $mg_{Pt}\,cm^{-2}$, fabricated as a conventional MEA. For comparison a Pt_3Co/C alloy at 0.4 $mg_{Pt}\,cm^{-2}$ loading fabricated as a conventional MEA is shown, as are the results for

the dealloyed PtCu system reported by Strasser *et al.* (14). Normalised activities have been used to enable comparison of the PtCo systems with PtCu systems reported in the literature that have been tested in different cell hardware and under differing operating conditions. The PtCu results have been normalised to the activity values reported by Strasser *et al.* for a 30% Pt/C MEA at comparable loading and a 45% Pt/C standard MEA at 0.3 $mg_{Pt}\,cm^{-2}$ (14).

Compared to both Pt/C catalysts in MEA tests, all the dealloyed materials show activity enhancement with Catalyst 3 showing the lowest performance, Catalyst 1 and 2 having comparable performance and Catalyst 4 the highest performance. The activity enhancement observed is more modest when comparing to the 40% Pt/C standard 0.4 $mg_{Pt}\,cm^{-2}$ MEA than the 30%Pt/C MEA that had also undergone the same washing procedure and was at a comparable loading to the dealloyed catalysts. This may be the consequence of the differences in the catalyst composition and layer thickness (mass transport and water management properties) of this MEA and the fact that the MEA has not undergone the mechanically stressful dealloying, washing and refabrication process. Compared to the Pt_3Co/C alloy Catalyst 3 showed lower activity, Catalysts 1 and 2 have comparable activity and Catalyst 4 shows a modest activity enhancement. As for the PtCu systems, dealloying the PtCo systems results in a performance enhancement, but the magnitude of the enhancement is less for PtCo than that reported for PtCu. In comparison with the normalised values for the PtCu system, the best performance from Catalyst 4 corresponds to 80% of the reported activity of the PtCu catalyst. Numerous reasons may be speculated for the lower activity observed for PtCo than PtCu. The XRD lattice parameters observed by Strasser *et al.* for $Pt_{25}Cu_{75}$ systems are 3.697Å (11, 16). This value is lower than those observed for the PtCo catalysts (Figure 3) (3.828 and 3.876 Å), meaning less contraction of the Pt lattice occurs in the PtCo systems, which in turn, may be less favourable for the ORR. In addition, HRTEM does not show evidence for the geometric effect described by Strasser *et al*., however, a lattice contraction cannot be confirmed for the core of the particle, indicating that the resolution of the technique may be insufficient to observe this effect. Non-optimum precursor catalyst or core shell formation may also explain lower activity. TEM results on the *ex situ* dealloyed samples show core shell structure formation. Due to the differences in ECA loss and %Co removal observed in the liquid electrolyte and MEA environments, it is not known if the desired core shell structure was formed during *in situ* dealloying. In

addition, it has not been demonstrated that the washing procedure has removed all dissolved Co from the MEA structure, therefore Co contamination within the MEA leading to mass transport issues cannot be discounted. Equally, the non-optimised layer structure used in the MEA may also mean the maximum activity benefit for the PtCo has not been observed. Further optimisation experiments are required to determine if the activity measured for the dealloyed PtCo systems represents the maximum activity obtainable and if dealloyed PtCo catalysts are intrinsically less active than PtCu systems.

5. Conclusions

Four new PtCo catalysts have been prepared and characterised, and the effects of dealloying using chemical acid leaching and electrochemical cycling on catalyst structure and activity have been studied. Catalyst 1 was prepared by annealing a $PtCo_3$/C precursor at 600 °C and Catalyst 2 prepared by annealing at 950 °C. Catalysts 3 and 4 were prepared by acid leaching Catalysts 1 and 2 respectively. The low temperature firing used to make Catalyst 1 resulted in an unalloyed material with both large and small particles, while firing at 950 °C to form Catalyst 2 gives two alloyed phases, one Pt rich and one Co rich. Again two particle size distributions are observed by TEM. After successive acid leaching, both Catalyst 3 and 4 are single phase. Acid leaching removed different amounts of Co from the precursors. Catalyst 3 lost more Co than Catalyst 4 in fewer acid leaching experiments, as a consequence of the poorer alloying observed for the precursor Catalyst 1 compared to the better alloyed Catalyst 2. The resultant composition of the leached catalysts is similar to PtCo 3:1 alloys that have been previously tested and have been found to show enhanced activity for ORR over Pt only catalysts, however unlike the PtCo 3:1 alloys the new materials all have both large and small particles from TEM.

At BOL only Catalyst 4 showed enhanced activity over Pt/C. After dealloying, all new catalysts showed activity enhancement over Pt/C, with Catalysts 1 and 2 having comparable activity to a PtCo 3:1 alloy. Catalyst 4 showed enhanced activity over a PtCo 3:1 alloy, however, the activity benefit observed was lower than that reported by Strasser *et al*. for dealloyed PtCu systems that have been reported to meet DoE activity targets. TEM analysis after *ex situ* dealloying showed electrochemical cycling resulted

in formation of catalyst particles with core shell structure. It is not known if the same structures are formed during *in situ* dealloying experiments, however *in situ* electrochemical dealloying was found to remove more Co compared to acid washing alone and was required for catalyst activation.

Preparation of dealloyed catalysts *in situ* resulted in the highest catalytic activity, however the dealloying process is known to contaminate the MEA with significant quantities of base metal. This has been show to lead to poor catalytic performance (very low BOL performance for Catalyst 1 and catastrophic activity loss after dealloying (14) reported by Strasser *et al.*). Chemical acid leaching followed by *in situ* dealloying of $PtCo_3$ has been shown to lead to a modest activity enhancement over a conventional Pt_3Co/C alloy, however, the complex methodology of the dealloying and washing process is impractical for large scale applications making these materials less commercially attractive. Only if the dealloyed materials are found to retain the activity enhancement during long term activity and durability tests, or if improved synthesis methods could lead to improved performance, would a dealloyed $PtCo_3$/C system be a viable candidate material for fuel cell applications.

References

1. H. A. Gasteiger, S. S. Kocha, B. Sompalli and F. T. Wagner, *Applied Catalysis B-Environmental*, **56**, 9 (2005).
2. S. Koh, C. Yu and P. Strasser, *ECS Transactions*, **11**, 205 (2007).
3. P. Mani, R. Srivastava, C. Yu and P. Strasser, *ECS Transactions*, **11**, 933 (2007).
4. P. Strasser, S. Koh and C. Yu, *ECS Transactions*, **11**, 167 (2007).
5. S. Koh and P. Strasser, *Journal of the American Chemical Society*, **129**, 12624 (2007).
6. P. Strasser, S. Koha and J. Greeley, *Physical Chemistry Chemical Physics*, **10**, 3670 (2008).
7. R. R. Adzic, J. Zhang, K. Sasaki, M. B. Vukmirovic, M. Shao, J. X. Wang, A. U. Nilekar, M. Mavrikakis, J. A. Valerio and F. Uribe, *Topics in Catalysis*, **46**, 249 (2007).
8. S. R. Brankovic, J. X. Wang and R. R. Adzic, *Electrochemical and Solid State Letters*, **4**, A217 (2001).
9. M. Shao, K. Sasaki, N. S. Marinkovic, L. Zhang and R. R. Adzic, *Electrochemistry Communications*, **9**, 2848 (2007).
10. M. B. Vukmirovic, J. Zhang, K. Sasaki, A. U. Nilekar, F. Uribe, M. Mavrikakis and R. R. Adzic, *Electrochimica acta*, **52**, 2257 (2007).

11. S. Koh, N. Hahn, C. F. Yu and P. Strasser, *Journal of the Electrochemical Society*, **155**, B1281 (2008).
12. P. Mani, R. Srivastava and P. Strasser, *Journal of Physical Chemistry C*, **112**, 2770 (2008).
13. C. F. Yu, S. Koh, J. E. Leisch, M. F. Toney and P. Strasser, *Faraday Discussions*, **140**, 283 (2008).
14. R. Srivastava, P. Mani and P. Strasser, *Journal of Power Sources*, **190**, 40 (2009).
15. K. H. J. Buschow, P. G. Vanengen and R. Jongebreur, *Journal of Magnetism and Magnetic Materials*, **38**, 1 (1983).
16. W. B. Pearson, *A Handbook of Lattice Spacings and Structures of Metals and Alloys*, Pergamon Press (1964).
17. N. A. Lange, *Lange's Handbook Of Chemistry*, McGraw-Hill (1985).

Chapter 7. Conclusions

The aim of this work was to compare a Pt/C catalyst, typical of commercially available materials, with a series of Pt_xCo_y/C catalysts, with a view to gaining an increased understanding of the desirable catalytic features that result in enhanced ORR activity and increased stability that have previously been reported for PtCo/C catalysts. Proposed explanations of the activity enhancement observed for platinum alloys over platinum only catalysts include both geometric and electronic effects such as: the effect of Pt-Pt interatomic distance (1, 2), the proportion of low index planes (3, 4), inhibition of OH_{ads} and oxide formation (5-10), surface roughening (11, 12), the alloying atoms being involved in the ORR (12) and electronic effects resulting in changing the electronic structure of the Pt 5d-band (13-16). Evidence for these effects seen in this work will now be discussed together with proposed reasons for the enhanced stability of PtCo/C catalysts.

To explore the origins of activity and stability enhancement for Pt_3Co/C catalysts over Pt/C, the mechanisms of catalyst deactivation were investigated. Loss of catalytic performance has been observed for both Pt/C and Pt_3Co/C alloy catalysts as a consequence of electrochemical cycling between the reduced and oxidised states and, in this work, it has been shown that *ex situ* acid leaching of the Pt_3Co/C alloy also resulted in loss of the alloying activity benefit leaving the leached catalyst with comparable activity to that observed for a platinum only catalysts of similar particle size.

Characterisation of the as prepared materials by XRD and XAS showed alloy formation for the Pt_3Co/C catalyst and a decreased Pt-Pt interatomic distance compared to Pt/C, meaning that both the geometric and electronic properties of the Pt/C and Pt_3Co/C catalysts differ. For the acid leached Pt_3Co/C catalyst no change in the XRD lattice parameter or increase in the Pt-Pt interatomic bond distance was observed despite the catalyst being less active. This result indicates that either these factors are not critical to the catalytic activity or more likely, that the XRD and XAS techniques provide information on the bulk structure such that the relatively small changes in the surface as a consequence of acid leaching are not detected. For catalysts however, it is the properties of the near surface that will dominate the observed catalytic activity.

Cyclic voltammetry of the as prepared catalysts found no evidence of a delayed onset (shift to more positive potentials) in OH_{ads}/oxide formation for the Pt_3Co/C catalyst compared to Pt/C, as has previously been proposed as an explanation of the observed activity enhancement (9, 10). However, differences were observed between the catalysts. More oxide per unit catalyst surface area was formed at a given upper potential limit on Pt_3Co/C compared to Pt/C but this oxide was removed at a lower overpotential. Under fuel cell operation at a given potential the alloy catalyst may therefore have more catalytic sites available for the ORR or the oxygen species on those sites may be more readily removed when compared to Pt/C. This proposal was investigated using *operando* XAS and will be discussed further later. After electrochemical cycling or acid leaching of the Pt_3Co/C catalyst, the oxide formation and removal properties of the alloy became more similar to that of a platinum only catalyst, with the largest changes observed after electrochemical cycling from 0.6-1.2 V 1000 times.

Electrochemical cycling to a higher upper potential limit was found to result in more electrochemical area loss for both Pt/C and Pt_3Co/C alloy catalysts. In the fuel cell this would correspond to fewer sites remaining available for reaction and, therefore, a decrease in catalytic activity. Larger particles were found to be more stable to electrochemical area loss under potentiostatic cycling regimes than smaller particles, with the Pt_3Co/C catalysts exhibiting an additional alloying benefit at a given particle size. From *operando* XAS measurements, catalysts with larger particles have been demonstrated to experience less particle disruption upon oxide formation. This effect is thought to help prevent ECA loss since fewer atoms within the particle are subject to dissolution. The additional stability seen for the Pt_3Co/C catalyst is thought to be the consequence of sacrificial leaching of the Co (evidenced by ICP-MS of the electrolyte and changes in Pt-Co and Co-Co coordination number from XAS measurements) helping maintain platinum electrochemical area during cycling. In fact, a slight increase in ECA was observed initially for the Pt_3Co/C catalysts during cycling and in electrochemical cycling experiments in the MEA (conducted prior to this work (17, 18)) an initial activity increase was also observed. It is proposed that the ECA increase (and therefore performance increase) is a consequence of removal of surface Co leaving either a more roughened platinum surface or platinum skin surface. A measurement of

the surface composition following this initial conditioning phase, such as XPS or LEIS or perhaps ASAXS (19, 20) is required to provide further conformation. Subsequent cycling removes larger quantities of Co and correspondingly ECA loss and performance loss occurs. It was found that removal of a critical percentage of Co (25%) from the catalysts resulted in the onset of ECA loss.

Changes in the catalyst structure as a consequence of electrochemical cycling were studied by cyclic voltammetry, TEM and in the case of the Pt_3Co/C, XAS was conducted pre- and post cycling. Electrochemical area loss mechanisms were found to differ for Pt/C 2 nm and Pt_3Co/C. The mechanisms of Ostwald ripening and Pt dissolution were found to result in ECA loss for the 2 nm Pt/C catalysts while the Pt_3Co/C catalyst was found to be more stable with the ECA loss observed corresponding to either Ostwald ripening or coalescence of catalyst particles and Pt and Co dissolution. XAS of the catalyst post cycling also showed a change in catalyst structure. Co removal was observed and this process resulted in disruption of a larger proportion of the catalyst particle compared to *ex situ* acid leaching of the catalyst despite similar amounts of Co removal. This increased disruption was attributed to the cycling facilitating the rearrangement of atoms via oxide formation, place exchange and the possibility of Ostwald ripening occurring under these conditions. For both acid leached and electrochemically cycled Pt_3Co/C catalysts formation of a percolated structure would fit the XAS observation that the Co had O neighbours, however, the presence of dissolved Co oxide trapped within the porous electrode structure can not be discounted. The observed structural changes (Co removal from the outer most layers of the catalyst particle) compared to the as prepared Pt_3Co/C catalyst, may therefore help explain the activity loss observed for the Pt_3Co/C catalyst post cycling or acid leaching. These results strongly indicate that reterntion of sufficient Co at or near the surface of the catalyst particles appears to be critical to maintaining the activity enhanced over platinum only catalysts. To further understand this requirement experiments could be conducted to determine how the removal of Co by acid leaching and electrochemical cycling affects the electronic properties of the catalyst. It is suspected that removal of Co results in loss of the desirable Pt 5d-band properties that occur as a consequence of alloying. This proposal could be tested by conducting XAS measurements of the catalysts on both the Pt L_{II} and L_{III} edges and determining the number of unoccupied d-electron states. Alternatively computational modelling of the catalysts could be used.

To further explore the origins of the activity and stability enhancement observed for the Pt_3Co/C catalysts over Pt/C, the relationship between catalyst activity and structure has been studied by conducting XAS on the catalysts operating in the fuel cell environment. To enable the *operando* studies to be conducted a specially adapted fuel cell was built and validated. The cell design enabled the catalysts to be studied during time resolved potential step experiments with 12 s and 0.1 s time resolution. The catalysts were studied with nitrogen cathode feed gas to investigate the effect of potential and temperature on the processes of oxide formation and removal and during operation at OCV and under load with oxygen as the cathode feed gas.

The data obtained with 12 s time resolution, whilst of sufficient quality to determine the extent of oxide formation as a function of potential, did not provide enough detail to discriminate between Pt-OH_{ads} and Pt-O formation during the oxidation of the catalyst particles. Higher overpotentials were required to form an oxide on the 40% Pt_3Co/C catalyst as evidenced by both the cyclic voltammetry of the MEA and the XAS results, compared to the 60% Pt/C 2 nm catalyst. However, for the XAS results, this effect was more likely to be a consequence of larger Pt_3Co/C particle size, which made the XAS spectra relatively insensitive to surface oxide formation. When comparing the 40% Pt_3Co/C catalyst to a Pt/C catalyst of comparable particle size little difference was observed, with only a 0.1 V difference being found. In all cases the time scale of the potential stepping experiments did not allow the processes of oxide formation and removal to be measured at intermediate points. To achieve greater time resolution energy dispersive XAS experiments were conducted.

Potential stepping experiments under nitrogen conducted with 0.1 s time resolution enabled study of changes in the white line intensity corresponding to oxide formation and removal in real time. It was not possible however, to obtain EXAFS data at this time resolution due to sample in-homogeneity and beam line constraints. The effect of upper potential limit and temperature were investigated for 60% Pt/C 2 nm, 40% Pt/C 5 nm and the 40% Pt_3Co/C catalyst. Fitting of the normalised while line intensity for each potential step allowed the relaxation constants for oxide formation and removal to be determined. For all catalysts oxide removal occurred faster than growth, indicating a different mechanism. For 60% Pt/C (2 nm) the rate of oxide formation was found to be

potential independent, while oxide removal was found to be potential dependent, with a slower rate after potential holds at higher upper potential limits. The potential dependence correlates with increased oxide formation at higher potentials. In addition, during oxide removal, a 1 s delay was observed before the white line intensity decrease commenced. To understand the origins of this observation and to allow further comment on the processes of oxide formation and removal EXAFS analysis is required to characterise any structural changes occurring during the experiment.

Significantly, prolonged exposure to the X-ray beam was found to degrade the membrane, preventing oxidation of the catalyst during the 0.1 s EDXAS measurements. The membrane degradation (thinning/pinholing) increased hydrogen crossover in the observation area. Uncertainty about the extent of hydrogen crossover, and the amount and rate of oxide formation prevented comparison between platinum and alloy catalyst materials. In addition, the effect of temperature on the oxide formation and removal processes could not easily be studied due to differences in the amount of hydrogen crossover with temperature.

The membrane degradation issue also prevented study of the 40% Pt_3Co/C catalyst with oxygen feed, however, the effect of fuel cell operation under two different loads was investigated for the 60 % Pt/C catalyst. Compared to the experiments with 12 s time resolution where no change in the EXAFS fitting parameters were observed, the improved time resolution of the energy dispersive XAS experiment allowed changes in the platinum electronic configuration to be observed. On application of the 0.6 V applied potential (representing a significant load) a decrease in white line intensity was observed. This change was attributed to bound / surface absorbed oxygen species undergoing reduction before repopulation with dissociated gas phase O_2 can occur. Other changes in white line response were thought to correlate to changes in hydration of the MEA.

The 5 nm Pt/C and 40% Pt_3Co/C catalysts were also studied during fuel cell operation using XAS with 12 s time resolution. However, as for the 60% Pt/C catalyst, no change in coordination number was observed under oxygen at OCV or during oxygen reduction at applied potentials down to an applied potential of 0.6 V. The high resistance of the cell meant that this 0.6 V only represented a ~100 mV perturbation of the actual cathode

potential. Analysis of catalytic performance during *operando* XAS measurements highlights possible catalyst utilisation issues, likely to be a consequence of the thick layers used, especially for the 5 nm Pt/C and 40% Pt_3Co/C catalysts. This means that under operation the catalysts are not behaving as expected in a conventional fuel cell and brings into question how representative the XAS fitting parameters are of the catalyst operating under idealised, realistic fuel cell conditions. Proposed methods / modifications to the experimental design to overcome these problems were discussed in Chapter 5.

To meet targets for automotive applications a further increase in activity over that of the 40% Pt_3Co/C catalysts is required. Electrochemical dealloyed $PtCu_3$/C catalysts have recently been shown to meet these activity targets (19). In light of this, four new $PtCo_3$/C catalyst materials were prepared and evaluated for ORR activity before and after activation by electrochemical dealloying. Catalyst 1 was prepared by annealing a $PtCo_3$/C precursor at 600 °C and Catalyst 2 prepared by annealing at 950 °C. Catalysts 3 and 4 were prepared by acid leaching Catalysts 1 and 2. The resultant composition of the leached catalysts is similar to PtCo 3:1 alloys previously found to show enhanced activity for ORR over Pt only catalysts however XAS analysis of the catalysts showed the materials exhibited a different structure. Unlike the 40% Pt_3Co/C catalysts, the activity of the $PtCo_3$/C catalysts increased after acid leaching/washing and electrochemical cycling. Acid leaching was found to remove significant quantities of Co from the catalyst including unalloyed material. It was shown that although acid leaching of the catalysts resulted in an increased activity compared to the as prepared materials, the maximum activity was obtained after the electrochemical dealloying procedure. After dealloying, Catalyst 4 showed a modest activity enhancement over a PtCo 3:1 alloy, however, the activity benefit observed was lower than that reported by Strasser *et al*. for dealloyed PtCu systems (19).

The *ex situ* dealloying procedure used was the same as the electrochemical cycling procedure used to study catalyst deactivation of the 40% Pt_3Co/C catalyst. Differences in the starting compositions of the $PtCo_3$/C catalyst materials the cycling resulted in a different particle structure compared to the cycled 40% Pt_3Co/C catalyst. For all catalysts except Catalyst 1 (low temperature annealed $PtCo_3$/C) TEM analysis after *ex situ* dealloying showed that electrochemical cycling resulted in formation of catalyst

particles with core shell structure. The thickness of the outer platinum shell increased after cycling to the higher upper potential limit of 1.2 V and the shell was found to be thicker for particles of larger diameter. XAS experiments were not conducted on the dealloyed catalysts. However, TEM line scan analysis showed that no Co remained within the outer most layers of the catalyst particles. Assuming a similar structure is formed in the MEA dealloying test, it is interesting to note that the catalysts exhibit increased activity for the ORR compared to Pt/C, while for the PtCo 3:1 alloys Co removal from the outer layers results in loss of the activity benefit. The activity benefit observed for dealloyed materials is proposed by *Strasser et al*. (21) to be the consequence of the result of a reduced Pt-Pt distance near the particle surface, stabilised by the lattice of the contracted core. In this work, no evidence for this geometric effect could be observed using HRTEM.

It is not known if the same core shell structures were formed during *in situ* dealloying experiments where the activity of the catalyst was measured, however, based on the knowledge that cycling in liquid electrolyte accelerates changes in catalyst structure compared to the MEA environment it is possible that the same structures were not formed. This may be a possible reason why the observed activity enhancement of the dealloyed $PtCo_3$/C catalysts was less than those reported by Strasser *et al*. (19) for dealloyed PtCu systems. Other reasons including less favourable lattice contraction were discussed in Chapter 6.

The effect of Co contamination in the MEA has been shown to detrimentally affect performance and raises concerns over the long term use of base metal containing catalysts in fuel cell MEAs. Co loss has been shown to occur for both the PtCo 3:1 catalyst, with Co loss also initiating ECA loss. For the 1:3 systems loss of large quantities of base metal into the MEA is required for activation. Removing Co from the MEA has been demonstrated by washing the MEA, however, it is not known if all contamination was removed or if further Co loss under longer term operation will occur and remove the activity benefit.

To meet targets for automotive applications this study has shown that larger particles are required for enhanced stability and that alloying can improve both activity and stability to ECA loss. The activity enhancement of the alloy catalysts evidenced in this

work are the consequence of the alloying element (Co) favourably perturbing both the geometric and electronic properties of the platinum catalyst. To maintain catalytic activity, it has been shown that improved retention of the alloying metal in the active catalyst is required both to retain activity and to prevent MEA contamination. In addition, to enable commercialisation a further increase in activity or reduction in platinum content is required.

References

1. V. Jalan and E. J. Taylor, *Journal of the Electrochemical Society*, **130**, 2299 (1983).
2. V. Jalan and E. J. Taylor, *Journal of the Electrochemical Society*, **130**, C125 (1983).
3. M. Teliska, V. S. Murthi, S. Mukerjee and D. E. Ramaker, *Journal of the Electrochemical Society*, **152**, A2159 (2005).
4. C. W. B. Bezerra, L. Zhang, H. S. Liu, K. C. Lee, A. L. B. Marques, E. P. Marques, H. J. Wang and J. J. Zhang, *Journal of Power Sources*, **173**, 891 (2007).
5. V. Stamenkovic, T. J. Schmidt, P. N. Ross and N. M. Markovic, *Journal of Physical Chemistry B*, **106**, 11970 (2002).
6. V. R. Stamenkovic, B. Fowler, B. S. Mun, G. F. Wang, P. N. Ross, C. A. Lucas and N. M. Markovic, *Science*, **315**, 493 (2007).
7. S. Mukerjee, S. Srinivasan, M. P. Soriaga and J. McBreen, *Journal of the Electrochemical Society*, **142**, 1409 (1995).
8. D. S. Strmcnik, P. Rebec, M. Gaberscek, D. Tripkovic, V. Stamenkovic, C. Lucas and N. M. Markovic, *Journal of Physical Chemistry C*, **111**, 18672 (2007).
9. U. A. Paulus, A. Wokaun, G. G. Scherer, T. J. Schmidt, V. Stamenkovic, N. M. Markovic and P. N. Ross, *Electrochimica Acta*, **47**, 3787 (2002).
10. V. Stamenkovic, T. J. Schmidt, P. N. Ross and N. M. Markovic, *Journal of Electroanalytical Chemistry*, **554**, 191 (2003).
11. M. T. Paffett and S. Gottesfeld, *Journal of the Electrochemical Society*, **135**, C348 (1988).
12. M. T. Paffett, K. A. Daube, S. Gottesfeld and C. T. Campbell, *Journal of Electroanalytical Chemistry*, **220**, 269 (1987).
13. I. Chorkendorff and J. W. Niemantsverdriet, *Concepts of Modern Catalysis and Kinetics*, WILEY-VCH (2003).
14. V. Stamenkovic, B. S. Mun, K. J. J. Mayrhofer, P. N. Ross, N. M. Markovic, J. Rossmeisl, J. Greeley and J. K. Norskov, *Angewandte Chemie-International Edition*, **45**, 2897 (2006).
15. V. R. Stamenkovic, B. S. Mun, M. Arenz, K. J. J. Mayrhofer, C. A. Lucas, G. F. Wang, P. N. Ross and N. M. Markovic, *Nature Materials*, **6**, 241 (2007).

16. R. R. Adzic, J. Zhang, K. Sasaki, M. B. Vukmirovic, M. Shao, J. X. Wang, A. U. Nilekar, M. Mavrikakis, J. A. Valerio and F. Uribe, *Topics in Catalysis*, **46**, 249 (2007).
17. S. C. Ball, S. L. Hudson, B. R. C. Theobald and D. Thompsett, *ECS Transactions*, **3**, 595 (2006).
18. S. Ball, S. Hudson, B. Theobald and D. Thompsett, *ECS Transactions*, **1**, 141 (2006).
19. P. Strasser, S. Koha and J. Greeley, *Physical Chemistry Chemical Physics*, **10**, 3670 (2008).
20. C. F. Yu, S. Koh, J. E. Leisch, M. F. Toney and P. Strasser, *Faraday Discussions*, **140**, 283 (2008).
21. P. Mani, R. Srivastava and P. Strasser, *Journal of Physical Chemistry C*, **112**, 2770 (2008).

Chapter 4 – Electronic Appendix

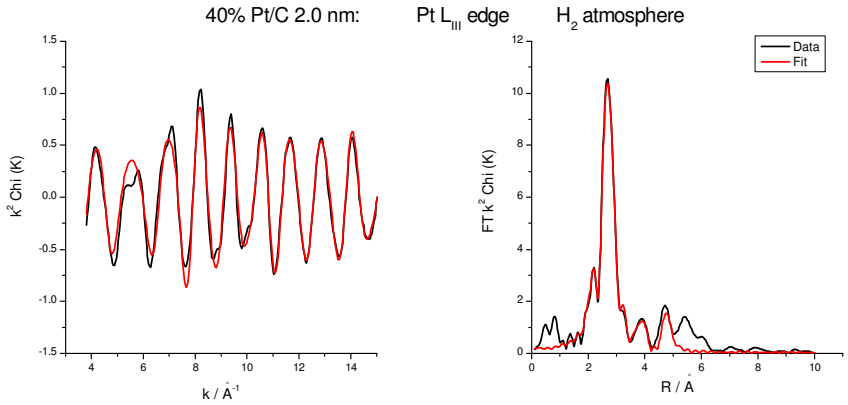

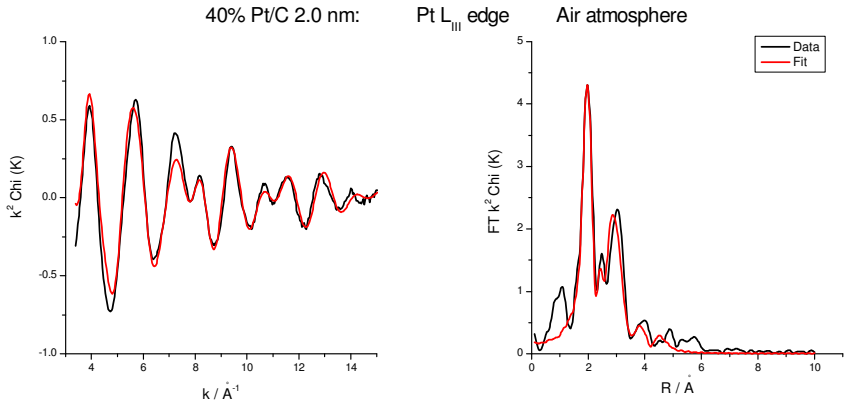

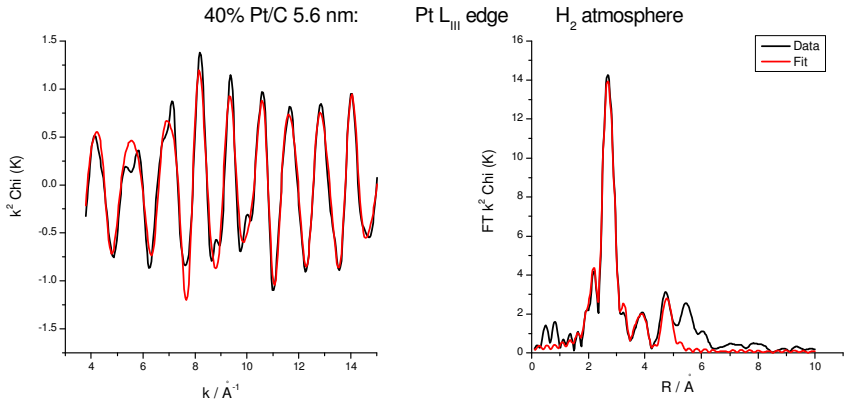

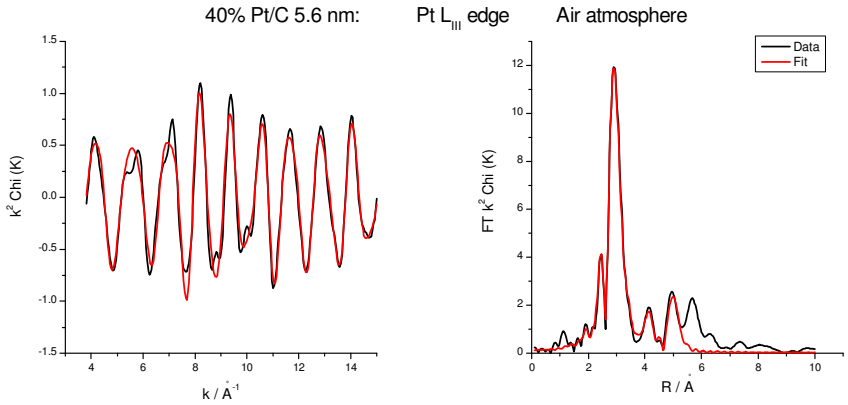

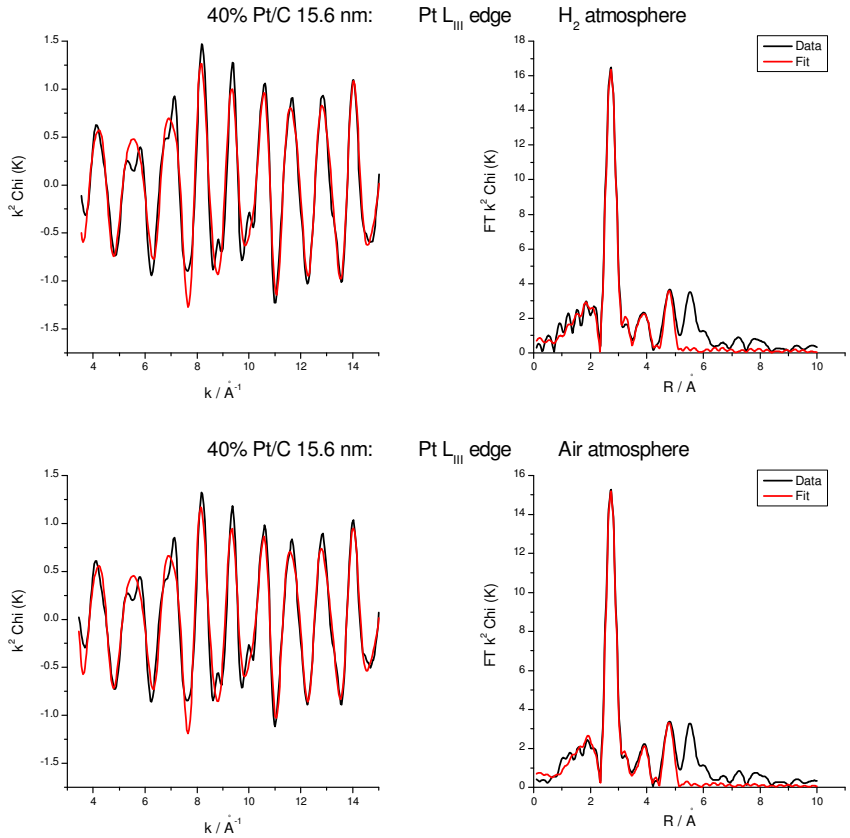

k^2 weighted experimental chi data (black) and theoretical fit (red) plot and k^2 weighted experimental Fourier transform data (black) and theoretical fit (red) plot for the 40% Pt/C 2.0 nm, 5.6 nm and 15.6 nm catalysts at the Pt L_{III} in H_2 and air

Structural parameters Pt/C catalysts obtained by fitting the Pt L_{III} EXAFS data in Air.

Edge	Catalyst	Absorber neighbour	N	R (Å)	$2\sigma^2$ (Å^2)	E_f (eV)	R_{exafs} (%)
Pt L_{III}	Pt/C 2.0 nm	Pt-O Pt-Pt_1 Pt-Pt_2	1.7 (± 0.1) 3.1 (± 0.3) 9.4 (± 1.8)	2.01 (± 0.01) 2.75 (± 0.01) 3.89 (± 0.02)	0.006 (± 0.001) 0.017 (± 0.001) 0.047 (± 0.007)	-15.4 (± 0.7)	29.9
Pt L_{III}	Pt/C 5.6 nm	Pt-O Pt-Pt_1 Pt-Pt_2 Pt-Pt_3	3.0 (± 0.1) 8.5 (± 0.2) 4.7 (± 0.9) 5.9 (± 0.9)	1.98 (± 0.04) 2.76 (± 0.01) 3.90 (± 0.01) 4.79 (± 0.01)	0.012 (± 0.001) 0.012 (± 0.001) 0.017 (± 0.002) 0.011 (± 0.001)	-13.0 (± 0.6)	21.7
Pt L_{III}	Pt/C 15.6 nm	Pt-Pt_1 Pt-Pt_2 Pt-Pt_3	9.5 (± 0.3) 3.4 (± 0.8) 7.5 (± 1.2)	2.76 (± 0.01) 3.91 (± 0.01) 4.80 (± 0.01)	0.011 (± 0.001) 0.012 (± 0.002) 0.011 (± 0.001)	-12.2 (± 0.6)	25.0

Structural parameters for Pt/C catalysts obtained by fitting the Pt L_{III} EXAFS data in H_2.

Edge	Catalyst	Absorber neighbour	N	R (Å)	$2\sigma^2$ ($Å^2$)	E_f (eV)	R_{exafs} (%)
Pt L_{III}	Pt/C 2.0 nm	Pt-Pt_1	7.4 (± 0.2)	2.76 (± 0.01)	0.011 (± 0.001)	-11.7 (± 0.6)	21.6
		Pt-Pt_2	2.2 (± 0.5)	3.90 (± 0.01)	0.012 (± 0.002)		
		Pt-Pt_3	4.1 (± 1.0)	4.79 (± 0.01)	0.012 (± 0.002)		
Pt L_{III}	Pt/C 5.6 nm	Pt-Pt_1	9.5 (± 0.3)	2.76 (± 0.01)	0.011 (± 0.001)	-12.4 (± 0.7)	24.3
		Pt-Pt_2	3.8 (± 0.9)	3.90 (± 0.01)	0.012 (± 0.002)		
		Pt-Pt_3	7.4 (± 1.3)	4.79 (± 0.01)	0.011 (± 0.002)		
Pt L_{III}	Pt/C 15.6 nm	Pt-Pt_1	9.7 (± 0.3)	2.76 (± 0.01)	0.010 (± 0.001)	-12.4 (± 0.7)	26.3
		Pt-Pt_2	3.9 (± 0.9)	3.91 (± 0.01)	0.011 (± 0.002)		
		Pt-Pt_3	7.8 (± 1.4)	4.80 (± 0.01)	0.012 (± 0.002)		

Plan and side views of the graphite plates and compression plates for both the anode (2 & 4) and cathode (1&3) sides of the cell. Version II design.

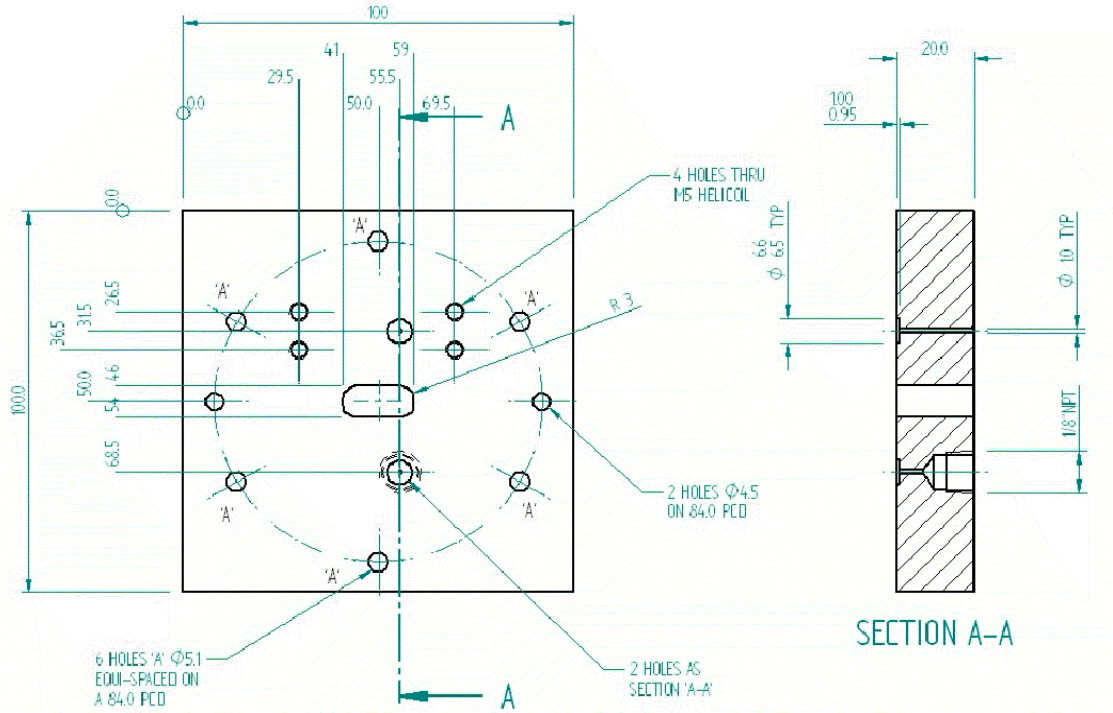

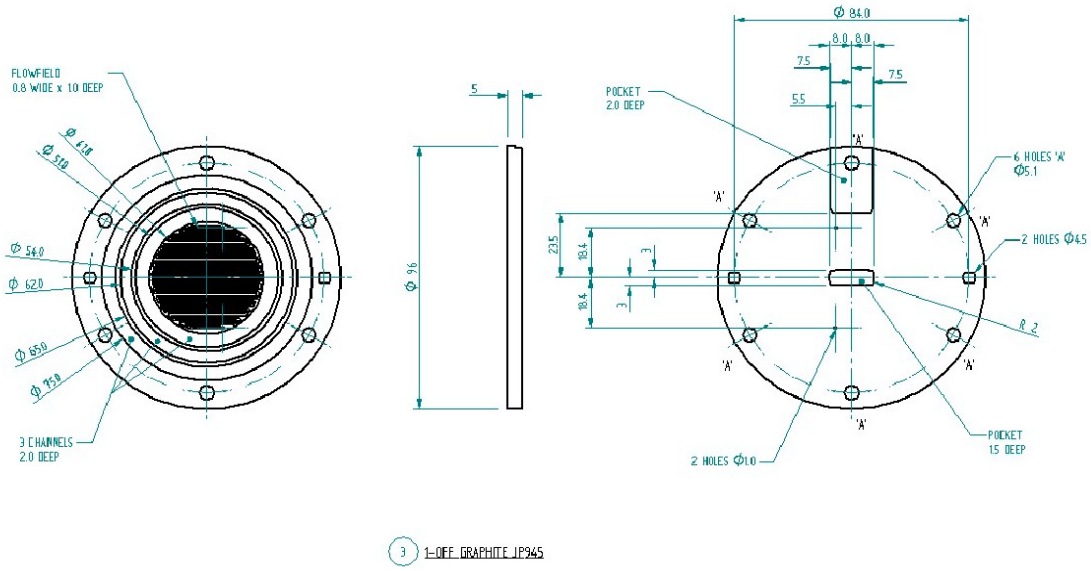

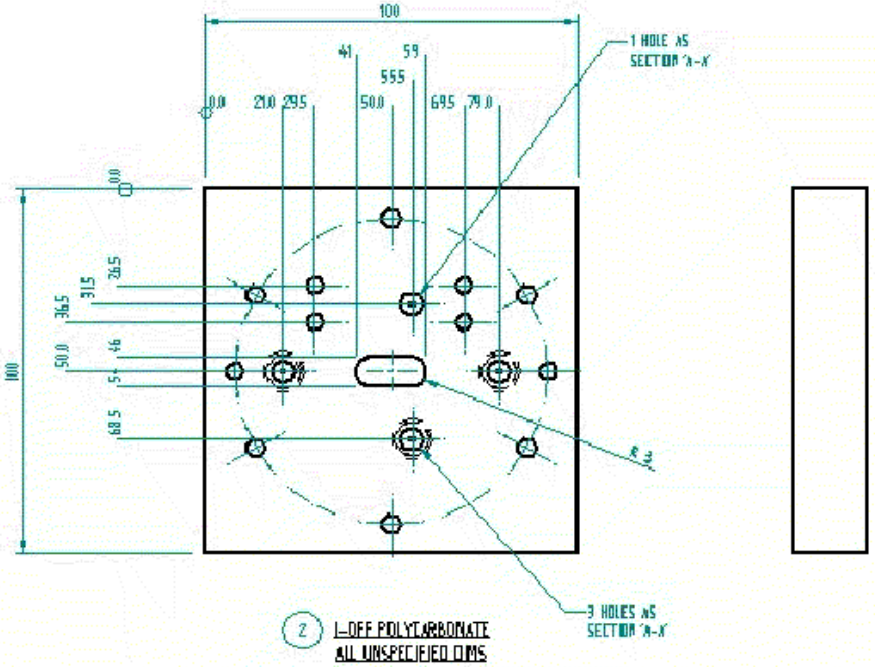

2 1-OFF POLYCARBONATE
ALL UNSPECIFIED DIMS
AS PER ITEM 1

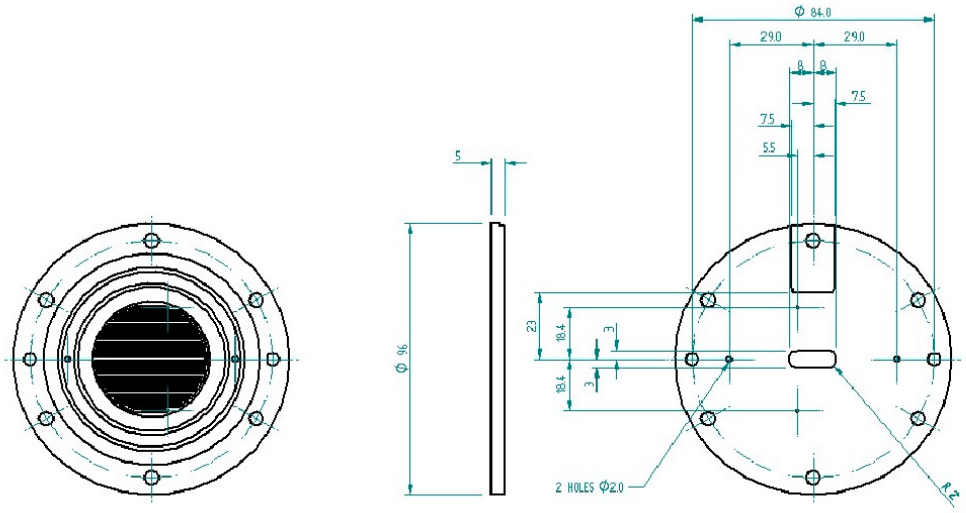

4 1-OFF GRAPHITE JP945
ALL UNSPECIFIED DIMS
AS PER ITEM 3